Integral modeling of liquid films sheared by a gas flow

Gianluca Lavalle

▶ **To cite this version:**

Gianluca Lavalle. Integral modeling of liquid films sheared by a gas flow. Fluids mechanics [physics.class-ph]. ISAE - Institut Supérieur de l'Aéronautique et de l'Espace, 2014. English. ⟨NNT : ⟩. ⟨tel-01139899⟩

HAL Id: tel-01139899

https://theses.hal.science/tel-01139899v1

Submitted on 7 Apr 2015

HAL is a multi-disciplinary open access archive for the deposit and dissemination of scientific research documents, whether they are published or not. The documents may come from teaching and research institutions in France or abroad, or from public or private research centers.

L'archive ouverte pluridisciplinaire **HAL**, est destinée au dépôt et à la diffusion de documents scientifiques de niveau recherche, publiés ou non, émanant des établissements d'enseignement et de recherche français ou étrangers, des laboratoires publics ou privés.

HAL Authorization

THÈSE

En vue de l'obtention du

DOCTORAT DE L'UNIVERSITÉ DE TOULOUSE

Délivré par *l'Institut Supérieur de l'Aéronautique et de l'Espace (ISAE)*

Présentée le *15/12/2014* **par**

GIANLUCA LAVALLE

Integral modeling of liquid films sheared by a gas flow

JURY

LAURENT LIMAT	Membre du Jury
STÉPHANE POPINET	Rapporteur
CHRISTIAN RUYER-QUIL	Rapporteur
FRANÇOIS CHARRU	Directeur de thèse
CLAIRE LAURENT	Co-directeur de thèse
JEAN-PAUL VILA	Encadrant de thèse

École doctorale et spécialité : *MEGEP - Dynamique des fluides*
Unité de Recherche : *ONERA - DMAE/MH*
Directeur de Thèse : *François CHARRU*
Co-directeur de Thèse : *Claire LAURENT*

Gianluca Lavalle
Integral modeling of liquid films sheared by a gas flow

COLOPHON
This thesis was typeset using the LaTeX typesetting system with the book class. The body text is set to 11pt. Typographical decisions were based on the recommendations given by Bringhurst [13], according to which reader's comfort has been taken care of, by leaving appropriate room on left and right sides to place the thumbs. The package LayAureo of F. Busdraghi with option *big* was used to wide the page layout. All drawings are created with MATLAB, Inkscape and Gnuplot.

Version for reviewers: October 29, 2014
Final version: February 17, 2015

However, at the time that Penrose produced his theorem,
I was a research student desperately looking for a problem
with which to complete my Ph.D. thesis.
(S. Hawking - A brief history of time)

Ai miei genitori.

Acknowledgements

This Ph.D. has been a great experience for me, definitely not because it has been easy and without difficulties, not at all! Seneca gives a kind of answer to this matter in *De Providentia*.

I carried out this work at the DMAE of the Onera-Toulouse in collaboration with the IMFT, starting from October 2011. Many people deserve to be mentioned here because of their support.

Firstly, I am very grateful to my advisor F. Charru for his solid guide during these years. I appreciated his concern about the successful conclusion of my work. We had regular meetings and I must admit I always felt having learnt many things when leaving his office. I also deeply thank C. Laurent, particularly for her sincere support during the writing of this manuscript, and for several suggestions to make this work being better. This thesis would not have been the same without the support of J.-P. Vila. I feel indebted to him for his crucial contribution, and I kindly remember many hours of discussions spent together.

I am also grateful to the jury that evaluated my work. I would like to express my gratitude to L. Limat, for stimulating comments during my Ph.D. defense, and to the two reviewers: S. Popinet and C. Ruyer-Quil for having read my manuscript with care, regard and analysis. Their suggestions made this manuscript being more rich and more solid. I had the chance to meet C. Ruyer-Quil during the GdR Film Cisaillés, and I honestly owe a lot to him.

I gratefully acknowledge also G. Dietze, who I met during the GdR Film Cisaillés. Apart from providing me with several data to compare my work to his, he gave me fruitful suggestions and kind listening of general matter.

I would like to remember the DMAE, where I spent a pleasant time during these years. My gratitude goes to all researchers and technicians of the department. Many thanks are due to P. Gajan and G. Casalis for their administrative and scientific support. I also really thank all Ph.D. students: Ghislain, who helped me in the achievement of this work, Baptiste, Rémi, Valentin, Bertrand, Henry, Jegan, Motta, ... and the other researchers: Davide, Jean-Mathieu, Olivier, Olivier and Lucas, ... I would like to thank also my office mates: Anne, Julien, Julie, Charlotte, Isabelle, and Jean-Michel who was in the office next to mine. I also express my thank to IMFT and INSA departments. Finally, I am very grateful to A. Carles-Bailhé for her help and listening during these years.

I cannot forget all my friends here in Toulouse. It was a pleasure to share the experience of the Ph.D. with Paulo and Gerardo, and to spend a lot of time together in the downtown. I also thank Rémi, for showing me the wine testing in the region and for having forced me in doing weird sports. I also remember Tiziana, Lia, Luigi, Elisa, Tomek, ... for all the time together. My daily lunch at ISAE would not have been the same without Syed, Khairol, Azeddine, Nico, William and Cheng, and of course Paulo and Sara.

Un ringraziamento speciale va appunto a Sara. Con il suo ascolto e i suoi consigli, e con gli innumerevoli discorsi riguardanti il dottorato è stata importantissima per me durante questo percorso. Il resto non posso di certo racchiuderlo in due righe.

Ringrazio anche mio fratello Marco, sempre vicino nei momenti cruciali con i suoi consigli e il suo aiuto, e per aver partecipato alla mia discussione. Ringrazio anche Rossella e Andrea per il loro spirito e il loro supporto, e Viola per la capacità con cui riesce a distrarmi così facilmente.

Infine ringrazio i miei genitori, a cui dedico con cuore questo lavoro, perché sanno tutto quello che mi è costato.

Gianluca Lavalle
Toulouse, 17 February 2015

Contents

1 Introduction **1**

2 Review of long-wave modeling **5**
2.1 Literature survey 5
2.1.1 Gravity-driven liquid films 5
2.1.2 Liquid films sheared by a gas flow 8
2.2 The governing equations 10
2.3 Modeling of gravity-driven thin liquid films 11
2.3.1 Nusselt's solution 11
2.3.2 The long-wave theory 12
2.3.3 Benney's non-linear equation 14
2.3.4 Shkadov's model 15
2.3.5 Ruyer-Quil & Manneville's model 16
2.3.6 Luchini & Charru's model 18
2.4 Modeling of two-layer channel flows 19
2.4.1 Long-wave theory 20
2.4.2 Tilley's non-linear equation 21
2.4.3 Dietze & Ruyer-Quil's modeling 21
2.5 Review of long-wave linear stability analysis 22
2.5.1 Stability analysis of gravity-driven liquid films 22
2.5.2 Stability analysis of gravity-driven films with constant shear stress . 23
2.5.3 Stability analysis of two-layer flows 24
2.5.4 Stability analysis of the integral models for gravity-driven films . . . 24

3 Development of consistent shallow water equations for thin liquid films **27**
3.1 The governing equations 27
3.1.1 The dimensionless equations 29
3.2 Integration over the film thickness 30
3.3 The asymptotic expansion 31
3.3.1 Expansion at order zero 31
3.3.2 Expansion at order one 32
3.4 Closure of the integrated equations 33

3.5 Further considerations on shallow water equations . . . 34
3.5.1 The Galilean invariance principle . . . 35
3.5.2 The final system of shallow water equations . . . 35

4 Development of consistent shallow water equations for confined two-layer flows 37
4.1 The governing equations . . . 37
4.1.1 The dimensionless equations . . . 38
4.2 Integration over the film-gas thickness . . . 40
4.3 The asymptotic expansion . . . 40
4.3.1 Expansion at order zero . . . 41
4.3.2 Expansion at order one . . . 43
4.4 Closure of the two-layer integrated equations . . . 43
4.5 Discussions . . . 44

5 Linear stability analysis of one- and two-layer shallow water equations 47
5.1 The base state . . . 47
5.1.1 Film subject to interfacial pressure and shear stress . . . 47
5.1.2 Two-layer pressure-driven flow . . . 48
5.2 Linearization around the equilibrium state . . . 49
5.3 Thin liquid film stability analysis . . . 51
5.3.1 Falling film in a passive gas atmosphere . . . 52
5.3.2 Falling film with constant shear stress . . . 54
5.4 Two-layer flow stability analysis . . . 57
5.4.1 Comparison with Yih's results . . . 58

6 Development of numerical schemes in coupling shallow water and Navier-Stokes equations: the SWANS model 61
6.1 The general architecture . . . 62
6.1.1 Case study . . . 62
6.1.2 Two-layer flow and boundary conditions . . . 62
6.1.3 Computational technique . . . 64
6.2 Discrete one-layer depth-integrated equations . . . 65
6.2.1 Spatio-temporal discretization schemes . . . 67
6.2.2 The CFL condition for the augmented system of shallow water equations 69
6.3 Discrete compressible Navier-Stokes equations . . . 70
6.3.1 Low-Mach scheme description . . . 71
6.3.2 Viscous stress discretization . . . 73
6.3.3 Boundary conditions . . . 73
6.3.4 The stability criterion . . . 74
6.4 Coupling approach development . . . 74
6.4.1 Film to gas coupling . . . 76
6.4.2 ALE method development . . . 76
6.4.3 Gas to film coupling . . . 78
6.5 Additional remarks . . . 79
6.6 Conclusions . . . 79

7 Validation of the SWANS numerical schemes by analytical solutions and experiments 81
7.1 Shallow water code's validation . . . 81
7.1.1 Linear stability of gravity-driven films . . . 81
7.1.2 Comparison with Liu & Gollub's experiments . . . 83

7.2 Navier-Stokes code's validation 87
7.2.1 The ALE Poiseuille flow 87
7.3 Validation of the coupling technique 90
7.3.1 Shear stress and pressure gradient validation 91
7.4 Conclusions 92

8 Non-linear dynamics of two-layer flows: SWANS results and comparison with DNS analysis 95
8.1 Description of the horizontal test 95
8.1.1 Initial flow conditions 96
8.1.2 Non-linear dynamics 96
8.1.3 The SWANS model versus DNS analysis 98
8.1.4 The SWANS model versus the two-layer long-wave model 98
8.1.5 Analysis of compressibility effects 99
8.2 Vertical two-layer flow 102
8.2.1 The SWANS model versus DNS analysis 103
8.3 Effect of second-order dissipation in the film model 106

9 Conclusions and perspectives 111

A Integration of the boundary-layer equations 115

B Fields of the first-order expansion 117

C Dispersion relation coefficients 121

D Description of the Newton method 125

Bibliography 127

List of Figures

2.1 Development of waves on a vertical falling water film at $Re = 32.7$, without controlled perturbations at the inlet. Experiments of Park & Nosoko [63]. . 6

2.2 Waves on a vertical water film at $Re = 16.1$ for two different forcing frequencies: low frequency $f = 14.0\ Hz$ (left) and high frequency $f = 40.2\ Hz$ (right). Experiments of Nosoko & Miyara [58]. 7

2.3 Levels of modeling approximation for falling liquid films. 8

2.4 Sketch of a liquid film sheared by a gas flow and definition of the coordinate system. For falling films, $\tilde{u}_2 = 0$. 11

2.5 Definition of the geometry of a liquid film (index $k = 1$) sheared by a gas flow (index $k = 2$) in an inclined channel. 20

3.1 Road map of Chapter 3. 28

3.2 Sketch of a liquid film subject to interfacial shear stress and pressure, and the gravity. 29

4.1 Road map of Chapter 4. 38

4.2 Two-layer pressure-driven flow in a strongly confined channel: indices 1 and 2 identify liquid and gas phases, respectively. 39

5.1 Road map of Chapter 5. 48

5.2 Uniform flow of a gravity-driven liquid film down an inclined plane. 49

5.3 Uniform flow of a two-layer in an horizontal channel. 49

5.4 Uniform velocity profile of an air-water flow in a channel: $\tilde{Q} = 4.06 \cdot 10^{-4}\ m^2 s^{-1}$, $\tilde{L} = 26\ mm$, $\tilde{H} = 0.39\ mm$, $r = 0.001$ and $m = 0.01$. Dashed line is the flat interface. 50

5.5 Dispersion curves from (5.22) for a water-glycerin gravity-driven film down an inclined plane of $\beta = 6.4°$. Dimensionless numbers: $Re = 8.5$, $Fr = 0.316$, $We = 0.048$. Case with surface tension (solid line) and without surface tension (dashed line). 53

5.6 Neutral stability curve for gravity-driven water-glycerin films down a 6.4° inclined plane. Solid line: Orr-Sommerfeld theory; dashed line: first-order long-wave model of Chapter 3, subject to gravity only; squares: experiments of Liu, Paul and Gollub [48, 47]. 54
5.7 Equilibrium thickness versus shear stress from (5.26), for a water film down a $\beta = 4°$ inclined plane, and for several Reynolds numbers: $Re = 2$ dotted line, $Re = 6$ dash-dot line, $Re = 10$ solid line, $Re = 16$ dashed line. 56
5.8 Critical Reynolds number versus shear stress from (5.30) and (5.31), for a water film down a $\beta = 6°$ inclined plane. Dashed line is the limit of gravity-driven films, i.e. $\tau_i = 0$; dash-dotted line is the limit of an infinite τ_i. 56
5.9 Dispersion curves from (5.36) for an air-water system flowing in a confined channel neglecting the gravity: $\tilde{H} = 0.39\ mm$, $\tilde{h}_0 = 0.13\ mm$, $\tilde{u}|_h = 0.06\ m\ s^{-1}$. Dimensionless numbers: $Re_1 = 4.48$, $Re_2 = 36.8$, $Fr = 0.93$, $We = 0.002$. 58
5.10 Yih's two-layer configuration. 59

6.1 Sketch of the performed computational investigation. Indices 1 and 2 refer to liquid and gas phases, respectively. 61
6.2 Sketch of film (top) and gas (bottom) code geometries. In the background, dashed lines indicate the base configuration, i.e. Figure 6.1. 64
6.3 Sketch of the film mesh and definitions of periodic boundary conditions. . . 65
6.4 Input and output of the film code. 66
6.5 Sketch of the stencil of the film mesh, and definitions of variables at the interface. 67
6.6 Time evolution of the minimum characteristic velocity e^2 normalized with the initial value $e_{in} = 2.5 \cdot 10^{-4}\ m^2 s^{-2}$. Two-layer flow with dimensionless numbers: $Re_1 = 4.48$, $Re_2 = 36.8$, $Fr = 0.93$, $We = 0.002$, and geometry given by $\tilde{H} = 0.39\ mm$ and $\lambda = 26\ mm$. After 0.7 s periodic waves appear. 69
6.7 Sketch of the gas mesh and definitions of periodic boundary conditions. . . 71
6.8 Two different cell notations for the low-Mach scheme used in this work. . . 72
6.9 Sketch of the coupling methodology and time progress $n \longrightarrow n+1$. 75
6.10 Sketch of cell displacement through the ALE technique. Dashed lines indicate the starting orthogonal configuration. 77
6.11 Node displacements through the ALE technique at the interface liquid-gas. The dashed line indicates the uniform flow. 77
6.12 Film and gas mesh: coupling between the two codes and notations. 78

7.1 Temporal evolution of the dimensionless film thickness at imposed wavelength $\lambda = 70\ mm$, and convergence of three mesh sizes: 40 (circles), 80 (cross) and 160 (solid line) cells in the domain. Dimensionless numbers: $Re = 8.5$, $We = 0.048$, $Fr = 0.31$. 82
7.2 Temporal evolution of the dimensionless maximum film thickness h_M in the domain at imposed wavelength $\lambda = 70\ mm$, and convergence of three mesh sizes: 40 (circles), 80 (cross) and 160 (solid line) cells in the domain. Dimensionless numbers: $Re = 8.5$, $We = 0.048$, $Fr = 0.31$. 83
7.3 Wave celerity of a gravity-driven film of water-glycerin down a 6.4° inclined plane. Dimensionless numbers: $Re = 8.5$, $We = 0.048$, $Fr = 0.31$. Solid line: solution of the long-wave dispersion relation (5.22); squares: code SWANS. 83
7.4 Linear growth rate of a gravity-driven film of water-glycerin down a 6.4° inclined plane. Dimensionless numbers: $Re = 8.5$, $We = 0.048$, $Fr = 0.31$. Solid line: solution of the long-wave dispersion relation (5.22); squares: computational analysis. 84

7.5 Temporal wave dynamics and saturated waves, spatially periodic, of a falling water-glycerin film down a 6.4° inclined plane. Data correspond to Liu & Gollub experiments: $Re = 19.3$, $We = 35$, $f = 4.5\ Hz$ ($\lambda = 5\ cm$ in the performed computational analysis). 85

7.6 Shape of saturated waves of a falling water-glycerin film down a 6.4° inclined plane, at $t = 1.6\ s$. Data correspond to Liu & Gollub experiments: $Re = 19.3$, $We = 35$, $f = 4.5\ Hz$ ($\lambda = 5\ cm$ in the performed computational analysis). 85

7.7 Experiments of Liu & Gollub [47] for a falling water-glycerin film down a 6.4° inclined plane, at $Re = 19.3$ and $We = 35$. On the left, forcing frequency $f = 4.5\ Hz$, on the right $f = 7\ Hz$. 85

7.8 Temporal wave dynamics and saturated waves, spatially periodic, of a falling water-glycerin film down a 6.4° inclined plane. Data correspond to Liu & Gollub experiments: $Re = 19.3$, $We = 35$, $f = 7\ Hz$ ($\lambda = 3\ cm$ in the performed computational analysis). 86

7.9 Shape of saturated waves of falling water-glycerin film down a 6.4° inclined plane, at $t = 1.6\ s$. Data correspond to Liu & Gollub experiments: $Re = 19.3$, $We = 35$, $f = 7\ Hz$ ($\lambda = 3\ cm$ in the performed computational analysis). 86

7.10 Geometry of the plane Poiseuille flow. Channel length is $L_x = 1\ mm$ and the height is $L_y = 2r = 2\ mm$. 87

7.11 Poiseuille velocity profile at $t = 0.4\ s$ on a fixed grid and comparison with the exact solution. Squares: mesh 10x40; solid line: exact profile. 88

7.12 Sketch of the grid motion in the ALE plane Poiseuille flow, at the maximum amplitude. 89

7.13 Velocity profiles at $t = 0.4\ s$ for three different moving grids and comparison with the exact solution. Squares: mesh 10x40; circles: mesh 20x80; cross: mesh 40x160; solid line: exact profile. 90

7.14 Geometry of the horizontal channel, which is 13 mm long and 0.39 mm high. Scaling is 8 : 1 for the x-direction and 24 : 1 for the y-direction. Dotted line expresses the uniform flow. 91

7.15 Film thickness at $t = 0.03\ s$ from SWANS. Dimensionless numbers: $Re_1 = 8.7$, $Re_2 = 71.3$. Pressure drop: $\Delta p = 62\ Pa$. Mesh size: $\Delta_x = 81.2\ \mu m$, $\Delta_y = 10.8\ \mu m$. 92

7.16 Interfacial shear stress normalized with the uniform value $\tau_0 = 0.61\ Pa$, corresponding to film thickness of Figure 7.15. Solid line: asymptotic expansion; dashed line: code SWANS. Physical and numerical parameters in the caption of Figure 7.15. 92

7.17 Space evolution of the interfacial pressure gradient normalized with the uniform value $G_0 = 4769\ Pa\ m^{-1}$, corresponding to film thickness of Figure 7.15. Solid line: asymptotic expansion; dashed line: code SWANS. Physical and numerical parameters in the caption of Figure 7.15. 93

8.1 Geometry of the horizontal test from Dietze & Ruyer-Quil [25], with $L_x = 26\ mm$ and $H = 0.39\ mm$. Scaling is 5 : 1 for the x-direction and 24 : 1 for the y-direction. Dotted line expresses the equilibrium film thickness. 95

8.2 Time evolution of the film thickness normalized with the uniform flow. Dimensionless numbers: $Re_1 = 4.48$, $Re_2 = 36.8$, $Fr = 0.93$, $We = 2 \cdot 10^{-3}$. Uniform pressure gradient and shear stress: $G_0 = -\Delta p/L = 2461.5\ Pa\ m^{-1}$, $\tau_{i0} = 0.32\ Pa$. 97

8.3 Film thickness at $t = 0.75\ s$ normalized to the flat equilibrium value versus stream-wise direction normalized with the wavelength. Convergence in the x-direction for three different meshes. Solid line: mesh 4 in Table 8.2; dashed line: mesh 2; dotted line: mesh 1. Physical parameters are detailed in the caption of Figure 8.2. 97

8.4 Film thickness at $t = 0.75\ s$ normalized to the flat value versus stream-wise direction normalized with the wavelength. Convergence in the y-direction for two different meshes. Solid line: mesh 3 in Table 8.2; dotted line: mesh 2. Physical parameters are detailed in the caption of Figure 8.2. 97

8.5 Traveling wave in the channel, and comparison between DNS of Dietze & Ruyer-Quil (dashed line), Figure 7(a) of [25], and SWANS (solid line). Physical parameters are detailed in the caption of Figure 8.2. DNS data courtesy of G. Dietze. 98

8.6 Space evolution of film thickness normalized to the flat value. Comparison between the two-layer long-wave model of Dietze & Ruyer-Quil (dashed line) and SWANS (solid line). Physical parameters are detailed in the caption of Figure 8.2. Data of the two-layer long-wave model courtesy of G. Dietze. . . 100

8.7 Space evolution of interfacial shear stress normalized to the uniform condition. Comparison between the two-layer long-wave model of Dietze & Ruyer-Quil (dashed line), Figure 8(c) of [25] after appropriate scaling, and SWANS (solid line). Physical parameters are detailed in the caption of Figure 8.2. Data of the two-layer long-wave model courtesy of G. Dietze. 100

8.8 Space evolution of interfacial pressure gradient normalized to the uniform condition. Comparison between the two-layer long-wave model of Dietze & Ruyer-Quil (dashed line), Figure 8(b) of [25] after appropriate scaling, and SWANS (solid line). Physical parameters are detailed in the caption of Figure 8.2. Data of the two-layer long-wave model courtesy of G. Dietze. . . 100

8.9 Gas velocity profiles (normalized at the uniform flow: interface locates at $y/H = 1/3$). 101

8.10 Time evolution of the film thickness normalized with the equilibrium film state obtained by means of the two-layer depth-integrated equations of Chapter 4. Physical parameters are detailed in the caption of Figure 8.2. 101

8.11 (top) Mach number contour in the gas phase. (bottom) Density contour ($kg\ m^{-3}$), or pressure contour, in the gas phase. The liquid film is white. . 102

8.12 Geometry sketch (with a 10 : 1 scaling) of the vertical test, where $L_x = 5.2\ mm$ and $H = 6.37\ mm$. Dotted line expresses the equilibrium film thickness. 103

8.13 Time evolution of normalized film thickness for the vertical flow. Dimensionless numbers: $Re_1 = 16.5$ and $Re_2 = 1972$, $Fr = 5.65$, $We = 0.021$. Uniform flow: $\tau_{i0} = 0.03\ Pa$, $u_0|_h = 0.15\ m\ s^{-1}$. 104

8.14 Film thickness versus normalized wavelength at $t = 0.235\ s$. Convergence of two different meshes. Solid line: mesh 6 in Table 8.3, circles: mesh 5 in Table 8.3. Physical parameters are detailed in the caption of Figure 8.13. . 104

8.15 Gas velocity profiles at $t = 0.25\ s$. Convergence of three different meshes. Solid line: mesh 7 in Table 8.3; dashed line: mesh 6; dotted line: mesh 5. Physical parameters are detailed in the caption of Figure 8.13. 104

8.16 Film thickness time evolution. Comparison between SWANS (solid line) and DNS provided by G. Blanchard by means of Slosh (dashed line). Physical parameters are detailed in the caption of Figure 8.13. 105

8.17 Film thickness time evolution after shifting in time the solution of SWANS. Comparison between SWANS (solid line) and DNS provided by G. Blanchard by means of Slosh (dashed line). Physical parameters are detailed in the caption of Figure 8.13. 105

8.18 Film thickness space evolution of saturated non-linear waves. Comparison between SWANS (solid line) and DNS provided by G. Blanchard by means of Slosh (dashed line). Physical parameters are detailed in the caption of Figure 8.13. 106

8.19 Film thickness time evolution. Comparison between SWANS (solid line) by adding the dissipative term $2\partial_{xx}q$, and DNS provided by G. Blanchard by means of Slosh (dashed line). Physical parameters are detailed in the caption of Figure 8.13. 107

8.20 Film thickness space evolution of the traveling wave. Comparison between SWANS (dotted line) by adding the dissipative term $2\partial_{xx}q$, and DNS provided by G. Blanchard by means of Slosh (dashed line). Solid line is solution by SWANS without second-order dissipative contribution. Physical parameters are detailed in the caption of Figure 8.13. 107

8.21 Interfacial shear stress space evolution. Comparison between SWANS (dotted line) by adding the dissipative term $2\partial_{xx}q$ and without (solid line). Physical parameters are detailed in the caption of Figure 8.13. 108

8.22 Interfacial pressure gradient space evolution. Comparison between SWANS (dotted line) by adding the dissipative term $2\partial_{xx}q$ and without (solid line). Physical parameters are detailed in the caption of Figure 8.13. 108

8.23 Film thickness time evolution of the horizontal two-layer flow. Comparison between SWANS (dotted line) by adding the dissipative term $2\partial_{xx}q$ and DNS provided by Dietze & Ruyer-Quil with OpenFOAM (dashed line). Solid line is solution by SWANS without second-order dissipative contribution. Physical parameters are detailed in the caption of Figure 8.2. 109

FR1 Film liquide mince, soumis à la gravité et un champs imposé pour le cisaillement et la pression. 137

FR2 Écoulement bi-couche dans une conduite étroite. 138

FR3 Solution de la relation de dispersion pour un film d'eau-glycerine tombant le long d'un plan incliné de $\beta = 6.4°$. Nombres adimensionnés : $Re = 8.5$, $Fr = 0.316$, $We = 0.048$. Courbes avec tension de surface (ligne en traits pleins) et sans (ligne en pointillés). 139

FR4 Représentation de la géométrie du code film (en haut) et du code gaz (en bas). La ligne en pointillés sur le fond illustre la configuration de base. . . . 140

FR5 Représentation de la méthodologie de couplage et progression en temps $n \longrightarrow n+1$. 141

FR6 Evolution temporelle de l'épaisseur du film normalisé avec l'état uniforme. Nombres adimensionnés : $Re_1 = 4.48$, $Re_2 = 36.8$, $We = 2 \cdot 10^{-3}$. Gradient de pression et cisaillement uniforms : $G_0 = -\Delta p/L = 2461.5\ Pa\ m^{-1}$, $\tau_{i0} = 0.32\ Pa$. 142

FR7 Épaisseur du film dans la conduite. Comparaisons entre la DNS de Dietze & Ruyer-Quil (ligne en pointillés), Figure 7(a) de [25], et SWANS (ligne en traits pleins). La description des paramètres physiques se trouve dans la Figure FR6. 143

FR8 Évolution spatiale du cisaillement. Comparaisons entre le modèle double St. Venant de Dietze & Ruyer-Quil (ligne en pointillés), Figure 8(c) de [25], et SWANS (ligne en traits pleins). La description des paramètres physiques se trouve dans la Figure FR6. 143
FR9 Évolution spatiale du gradient de pression. Comparaisons entre le modèle double St. Venant de Dietze & Ruyer-Quil (ligne en pointillés), Figure 8(b) de [25], et SWANS (ligne en traits pleins). La description des paramètres physiques se trouve dans la Figure FR6. 143
FR10 Évolution temporelle de l'interface après décalage de la solution SWANS. Comparaison entre la DNS de G. Blanchard avec le code Slosh (ligne en pointillés), et SWANS (ligne en traits pleins). Nombres adimensionnés : $Re_1 = 16.5$ et $Re_2 = 1972$. État uniforme : $\tau_{i0} = 0.03\ Pa$, $u_0|_h = 0.15\ m\ s^{-1}$. 144
FR11 Évolution spatiale de l'onde périodique. Comparaison entre la DNS de G. Blanchard avec le code Slosh (ligne en pointillés), et SWANS (ligne en traits pleins). La description des paramètres physiques se trouve dans la Figure FR10. 144

List of Tables

2.1 Leading-order closure models for three different velocity profiles. 15
2.2 First-order long-wave models of different works. 19
2.3 Key-lecture and dimensionless numbers of different cited works. Re_0, Fr_0, We_0 indicate dimensionless scaling adopted here, namely expressions (2.17-2.18) and (2.21). In the work of Benney, Gjevik, Ruyer-Quil & Manneville, and Yih, the Weber is actually defined as We^{-1}. 26

3.1 Coefficients of the corrective term ${\tau_w}^{(c)}$ and the viscous term T, the conservative part of $\partial_x h$ being moved to the momentum flux of the shallow water equations. Summing lines one and two gives the third. 35
3.2 Coefficients of the momentum flux of (3.33b), the fulfillment of the Galilean invariance principle and the term P, the conservative part of $\partial_x h$ being moved to the momentum flux of the shallow water equations. Summing lines from one to three gives the forth. 36

7.1 Physical properties of fluids used for the validation tests of the single-layer model. 81
7.2 Values of kh_0 and corresponding wavelengths λ of performed numerical tests. 82
7.3 Fixed and mobile meshes used for the computational investigation of the Poiseuille flow, from the coarsest to the finest. 89
7.4 Errors on velocity profiles for the three mobile meshes considered in the ALE Poiseuille flow. 90
7.5 Physical properties of the air-water flow used for the two-layer validation test. 91

8.1 Values for kh for the horizontal confined channel test and the vertical large channel one. 96
8.2 Meshes used in this work, from the coarsest to the finest, and the one from Dietze & Ruyer-Quil's DNS. Note that, by construction, SWANS has only one vertical cell in the liquid layer. 98
8.3 Meshes used in this work, from the coarsest to the finest, and those used in Slosh by G. Blanchard. 103

Nomenclature

Δp	Pressure drop, Pa
$\mathcal{F}$	Shallow water flux
$\mathbf{D}$	Strain tensor, s^{-1}
$\mathbf{F}$	Body force, $Pa\ m^{-1}$
$\mathbf{g}$	Vector of gravity field, $m\ s^{-2}$
$\mathbf{n}$	Normal outward unit vector
$\mathbf{T^{(n)}}$	Viscous stress vector of normal $\mathbf{n}$, Pa
$\mathbf{T}$	Viscous stress tensor, Pa
$\mathbf{t}$	Tangent unit vector
$\mathbf{u}$	Vector of velocity field, $m\ s^{-1}$
a	Sound celerity, $m\ s^{-1}$
c	Complex wave speed, $m\ s^{-1}$
e	Characteristic velocity, $m\ s^{-1}$
f	Forcing frequency, Hz
G	Interfacial pressure gradient $-\partial_x p_i$, $Pa\ m^{-1}$
H	Channel height, m
h	Film thickness, m
i	Imaginary unit
k	Wavenumber, m^{-1}
L	Channel length, m

P	Pressure part of depth-integrated equations
p	Pressure field, Pa
p_i	Interfacial pressure, Pa
Q	Total flow rate, $m^2 s^{-1}$
q	Flow rate, $m^2\ s^{-1}$
T	Source term of depth-integrated equations
t	Time, s
U	Mean longitudinal velocity, $m\ s^{-1}$
u	Stream-wise velocity, $m\ s^{-1}$
V	Reference frame velocity, $m\ s^{-1}$
v	Cross-stream velocity, $m\ s^{-1}$
w	Span-wise velocity, $m\ s^{-1}$
x	Stream-wise direction coordinate, m
y	Cross-stream direction coordinate, m
z	Span-wise direction coordinate, m

Acronyms

ALE	Arbitrary Lagrangian-Eulerian
BL	Boundary-layer equations
CEDRE	Calcul d'Ecoulements (Diphasiques) (Réactifs) pour l'Energétique
CFD	Computational Fluid Dynamics
CFL	Courant-Friedrichs-Lewy condition
DNS	Direct Numerical Simulation
LS	Level Set
MATLAB	Matrix Laboratory
MUSCL	Monotonic Upstream-Centered Scheme for Conservation Laws
NACA	National Advisory Committee for Aeronautics
NS	Navier-Stokes equations
ONERA	Office National d'Etudes et de Recherches Aérospatiales
SW	Shallow water equations
SWANS	Shallow Water ALE Navier-Stokes
VOF	Volume of Fluid

WRIBL Weighted Residual Integral Boundary-Layer

Dimensionless group

Γ Shape factor

ε Shallow water parameter

ξ Cross-stream dimensionless coordinate

Fr Froude number (definition (3.12) for one layer and (4.13) for two layers)

Fr_{cr} Critical Froude number

M Mach number

m Dynamic viscosity ratio

r Density ratio

Re Reynolds number (definition (3.12) for one layer and (4.13) for two layers)

Re_{cr} Critical Reynolds number

We Weber number (definition (3.12) for one layer and (4.13) for two layers)

Greek Symbols

β Inclination angle, $^\circ$

δ Kronecker function

ϵ Amplitude of the perturbation

γ Surface tension, $N\ m^{-1}$

Λ equation (2.26) for falling films and (3.16) otherwise

λ Wavelength, m

μ Dynamic viscosity, $kg\ m^{-1}\ s^{-1}$

ν Kinematic viscosity, $m^2\ s^{-1}$

ω Complex angular velocity, $rad\ s^{-1}$

$\tau_w{}^{(c)}$ Wall shear stress correction, Pa

Π Pressure part of two-layer depth-integrated equations

Ψ Stream function

ρ Density, $kg\ m^{-3}$

Σ Stress tensor, Pa

τ_i Interfacial shear stress, Pa

τ_w Shear stress at the wall, Pa

ζ Bulk viscosity, $kg\ m^{-1}s^{-1}$

Numerical Symbols

Δt	Time step
Δx	Cell length
Δy	Cell height
γ_e	Stability parameter of the low-Mach scheme
∂K	Cell contour
$\pm$	Right and left side of the cell interface
σ	Capillary coefficient We^{-1}
φ	$h^{3/2}\sqrt{\sigma}$
$\hat{\mathbf{u}}$	ALE velocity
ϕ	Conserved variable vector of gas phase
$\mathbf{J}$	Jacobian matrix
$\mathbf{x}_K$	Coordinate of cell center
A	Cell surface in ij notations
B	Antisymmetric matrix
dh	Node displacement
E	Total energy
e	Subscript for edge
F	Thermodinamic free energy
f	Numerical flux
i	Cell index
j	Cell index
K	Cell index
m_e	Edge length
m_K	Cell surface
N	Cell number
n	Time level
p	Step of the Newton method
s	Source term vector
v	Conserved variable vector of film phase
w	$\sqrt{\sigma}\partial_x h/\sqrt{h}$ (section 6.2)

z	Entropy variable vector

Symbols

$[\cdot]$	Jump across the interface: $(\cdot)_2 - (\cdot)_1$
∇	Nabla operator
∇^2	Laplace operator, m^{-2}
$\otimes$	Outer product
∂_t	Time derivative, s^{-1}
∂_x	x-derivative, m^{-1}
∂_y	y-derivative, m^{-1}
$\tilde{}$	Dimensional variables

Superscripts

(0)	Order zero
(1)	Order one
$\prime$	Derivative with respect to h

Subscripts

0	Uniform flow
k	Phase index (1: liquid; 2: gas)
p	Perturbation of the equilibrium

1 Introduction

The dynamics of thin liquid films sheared by a laminar gas flow is applicable to many industrial processes. For example, heat pipes, distillation columns and cooling towers employ two-layer flows to perform heat and mass transfers. Particularly, the interaction between film and gas flows is often encountered in the aerospace domain, in configurations where the gas is mainly turbulent: pre-filming for injection systems, water ingestion within turboengines, de-icing of aircraft systems, deposition of alumina films over the walls of solid rocket motors. These aerospace configurations are a few examples of the applications investigated at ONERA. The interest of ONERA in these configurations derives from the effect that the development of wavy liquid films over the walls greatly modifies the transfers with the gas. For example, in the de-icing applications of aircraft wings, by a correct comprehension of the exchanges with the gas, one can predict the position where the film freezes, and thus prevent dangerous consequences.

The full understanding of all physical mechanisms of the interaction between the two phases is certainly an important vehicle to perform the computational analysis of such flows. Meanwhile, numerical simulations support the design of flow devices, such as coolers, injectors and pumps. Indeed, owing to the improvements in the fields of computer sciences and numerical techniques, Computational Fluid Dynamics (CFD) has known a vaste growth in the last years. However, the required computational cost represents still a great and crucial limitation, particularly when testing industrial configurations, such as those previously cited.

Hence, several studies have been conducted over the past decades, the main goal being to develop reduced models to study the dynamics of liquid films and try to reproduce well the experimental observation of interfacial waves. These waves are shown to be much larger than the film thickness, and as a consequence, the majority of such works focuses on long waves. With the earliest works on gravity-driven liquid films, a non-linear evolution equation for the film thickness has been developed for long-wave disturbances. However, it is well known that this equation fails when studying the behavior of an unstable film far from the instability threshold. Therefore, later works have mostly focused on integral models using the boundary-layer (BL) equations. Thanks to an appropriate correction of the wall shear stress term, these models allow to get the right critical Reynolds number, and thus the correct linear stability threshold in the long-wave limit.

Hence, the study of reduced models which correctly predict the entire dynamics and the stability threshold of gravity-driven thin liquid films has been deeply investigated so far. The corresponding computational analysis shows a good agreement in the comparison of spatio-temporal evolutions of the film thickness with the Direct Numerical Simulation (DNS) and the experiments. However, the development of reduced models applied to thin liquid films sheared by a laminar gas flow has not been fully established yet, one thinks for example of the aerospace configurations.
Similarly to the case of gravity-driven liquid films, the earliest works on modeling two-layer channel flows have provided a non-linear evolution equation describing the motion of the interface submitted to long waves. Yet, this model fails far from the instability threshold. More recently, a full long-wave model, which involves depth-integrated equations for both layers, has been developed for a strictly confined two-layer flow. The linear stability analysis of such a model matches with the Orr-Sommerfeld theory, and the corresponding numerical simulations of non-linear waves are in good agreement with the DNS. Nevertheless, the use of an integral model to analyze the gas phase has several constraints, particularly for the aerospace applications, such as those relevant to ONERA: the thickness of the gas flow is limited by the long-wave assumption; the gas phase is solved with integrated variables rather than velocity and pressure fields; the analysis is kept limited to a confined domain and is not extendible, for instance, to laminar boundary layers or turbulent flows over a wavy liquid film.

Hence, the lack of models permitting to study two-layer flows toward aerospace configurations justifies this Ph.D. work. It consists indeed in developing a reduced model in order to analyze and solve numerically the dynamics of liquid films sheared by a gas flow. Furthermore, since the aim of this work is to provide a coupling methodology, laminar gas flows are preferred to turbulent ones for simplicity and understanding.

This program has been fulfilled firstly by developing consistent depth-integrated equations for thin liquid films subject to given interfacial shear stress and pressure, and to the gravity force. The aim has been to start with a simplified model, involving the liquid phase only. To achieve this, the Navier-Stokes (NS) equations have been put in non-dimensional form, in order to underline the relative importance of each term of the equations. Subsequently, an integration over the film thickness has been performed. However, since the resulting system needs to be closed, an asymptotic expansion up to the first order of the non-dimensional Navier-Stokes equations has been developed. This is submitted to the choise of a small parameter ε characteristic of the film flow, which drives to the assumption of long waves. Finally, in order to validate the consistency of this integral model, the correction of the wall shear stress at order one has been compared with those avalaible in the literature in the simplified case of gravity-driven films (Chapter 3).

In a second step, the previous analysis has been extended to a two-layer flow in a confined channel. Similarly as before, an integral model has been derived accounting also for the effect of a laminar gas on the top of the film. Yet, a long-wave asymptotic expansion up to the first order in ε has provided velocity and stress fields, and has permitted to close the system of integrated equations. The total flow rate has been imposed, while the pressure gradient has been left free. This two-layer analysis has been merely used as validation of the numerical coupling methodology (Chapter 4).

Subsequently, a linear stability analysis has been performed for the above mentioned one- and two-layer integral models. By doing so, these reduced models have been validated and discussed: indeed, wave celerities and growth-rates have been compared to the Orr-Sommerfeld theory. Particularly, real and imaginary wave propagation velocities corresponding to the reduced models have been derived after linearization of the equations

around the equilibrium state. Seeking solutions in wavy form has then driven to the respective dispersion relations, whose resolution has provided the propagation wave velocities (Chapter 5).

As a further step, numerical methods have been developed with the aim to couple the shallow water (SW) equations of Chapter 3 to compressible Navier-Stokes equations, accounting for liquid and gas phases, respectively. A coupling methodology has been then provided, and consists in transferring interfacial stresses from the gas to the film, which in turn gives back interfacial velocities and the position of the interface. Particularly, the Arbitrary Lagrangian-Eulerian (ALE) method has been used to transfer it, by performing a vertical movement of the gas grid. The choice of developing such numerical methods is due to the need of ONERA to extend this coupling methodology to the CFD platform CEDRE, used for aerodynamics and combustion industrial problems. Indeed, CEDRE works with compressible Navier-Stokes equations and shallow water equations, and also admits moving grids. However, a coupling approach in studying interfacial waves is missing. Therefore, the objective here is to test this coupling methodology on a simpler code, in simulating well-documented channel flows. As a result, the code SWANS (Shallow Water ALE Navier-Stokes) has been developed in MATLAB. (Chapter 6).

Finally, the validation of such numerical methods, which give rise to the solver SWANS, has been provided. Firstly, the discretization of the integrated equations for the liquid phase has been validated by comparing wave propagation velocities of the linear regime with the theory of Chapter 5, as well as film thickness evolutions with experimental results given in the literature. On the other hand, the discretization technique of the Navier-Stokes equations has been validated in the simulation of test-cases whose solutions are known, such as the Poiseuille flow. In addition, the numerical coupling technique has been tested by comparing interfacial stresses with the asymptotic expressions of Chapter 4, described above (Chapter 7).

In a final step, the non-linear dynamics of films sheared by a gas flow has been studied with the code SWANS. Two scenarios have been discussed: two-layer flows developing in a horizontal strictly narrow channel and in a vertical large channel. In the former, thickness and interfacial stress space evolutions have been compared to the DNS and the full reduced model from the literature. In the latter, film thickness spatio-temporal evolutions have been compared to the DNS avalaible at ONERA through the code Slosh. (Chapter 8).

2 Review of long-wave modeling

This chapter gives an overview of previous works about thin liquid film modeling and linear stability analysis. A literature survey is firstly presented in order to provide a general summary of this subject and to describe motivations and progress achieved by the research during last decades. Then, low-dimensional models of selected works are shown for gravity-driven liquid films and two-layer flows, with the purpose to compare and validate the present work. Finally, the most relevant results in linear stability analysis of Navier-Stokes and shallow water equations are presented for falling and sheared liquid films.

2.1 Literature survey

The dynamics of thin liquid films has been studied for many years. Indeed, instabilities of thin films down inclined planes appear at low flow rates and manifest themselves with a wide range of wave evolution. This gives the opportunity to look at the development of long waves, from the inception to the transition to non-linear secondary structures, such as solitary waves.
Today, many aspects related to thin film dynamics have not been clarified yet. For example, interactions of solitary waves on falling films down an inclined plane, and the flooding phenomenon for sheared films are only a few illustrations. As a result, this subject still holds a great interest nowadays.

2.1.1 Gravity-driven liquid films

By the support of an experimental setup, Kapitza & Kapitza [41] were the first ones to focus on wave evolution on a falling liquid film. After them, important experimental wave observations were provided by Nosoko *et al.* [59], Alekseenko *et al.* [2], then by Liu & Gollub [47], and more recently by Dietze *et al.* [24, 23] for cylindrical configurations. Particularly, Liu *et al.* [48, 47, 49] have looked at waves arising on a liquid film falling down an inclined plane, with the advantage to deal with smaller velocity while keeping the same physics as the vertical case. Experiments have shown that the wave dynamics of thin liquid films is very peculiar. Indeed, Figure 2.1 shows experiments of Park & Nosoko [63], which describes well the typical behaviour of a vertical liquid film without forcing at the inlet. One can recognize three different long-wave regimes: up to 5 *cm* the film is flat, then 2-D waves develop at the interface, before turning into 3-D waves around 15 *cm* from the inlet.

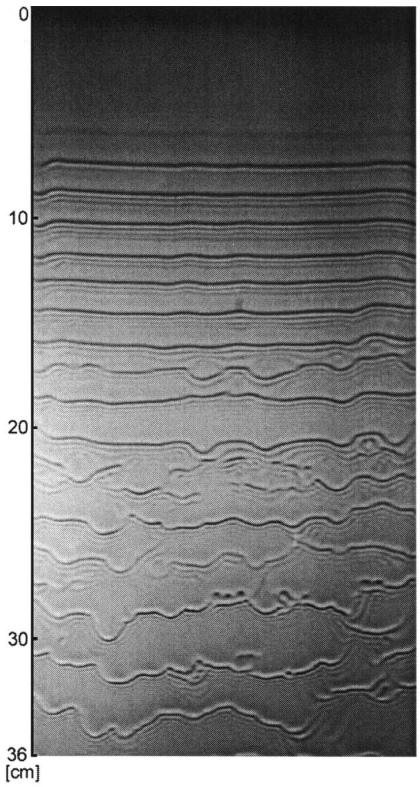

Figure 2.1: Development of waves on a vertical falling water film at $Re = 32.7$, without controlled perturbations at the inlet. Experiments of Park & Nosoko [63].

On the other hand, further experiments such as those of Nosoko & Miyara [58], have shown that by controlling the wave amplitude at the entrance, non-linear waves with different size and shape can develop along the film. For example, Figure 2.2 shows the wave pattern on vertical liquid films for two different inlet frequencies. One can notice the presence of *solitary waves*, i.e. waves composed by a main hump, which can be several film thickness high and host a recirculation zone, anticipated by capillary ripples. Hence, when a small amplitude perturbation is given at the inlet film, infinitesimal two-dimensional disturbances first develop; their amplitude then saturates to give rise to saturated waves. Subsequently, if the frequency is sufficiently low, 2-D and then 3-D solitary waves develop on the liquid film. If the frequency is high, saturated waves break directly into 3-D unsteady disturbances. This pattern has been well summarized by Chang [14].

All these experiments thus show that waves on the surface of a liquid film are strongly non-linear. In addition, for small Reynolds number, i.e. $Re < 300$, the wavelength of these non-linear waves is much larger than the thickness of the film. These two reasons have incited several works to generate simplified non-linear models able to reproduce experimental data, while getting the same stability threshold as the linearized Navier-Stokes equations.

In this direction, the first attempt was done by Nusselt [60], who has found a wavyless solution of the Navier-Stokes equations assuming a steady constant thickness film. Nusselt has derived a parabolic velocity profile of the falling film, where the gravity force is fully balanced by the wall shear stress. However, Nusselt's approach fails when unstable waves develop at the free surface of the liquid film.

Subsequent to this work, the linear stability analysis of falling liquid films in passive gas atmosphere has been widely investigated. First studies have been done by Benjamin and Yih. Benjamin [7] has proved that a vertical liquid film is always unstable to long waves. By a power-series approximations of the stream function of the Orr-Sommerfeld equation, Benjamin has evaluated wave propagation velocities of long and short waves at small Reynolds

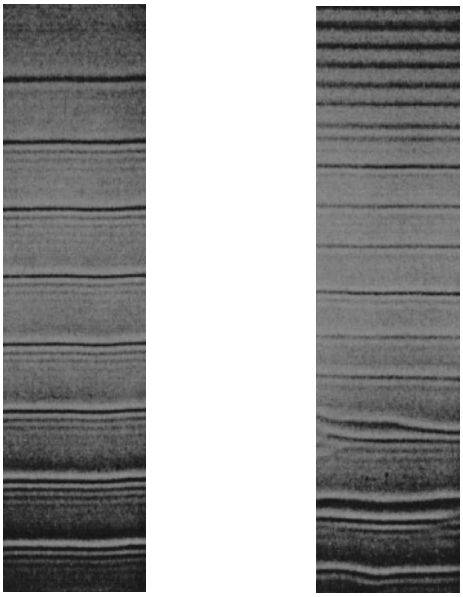

Figure 2.2: Waves on a vertical water film at $Re = 16.1$ for two different forcing frequencies: low frequency $f = 14.0\ Hz$ (left) and high frequency $f = 40.2\ Hz$ (right). Experiments of Nosoko & Miyara [58].

number. In a later work, Yih [95] has confirmed Benjamin's results of linear stability analysis and provided a simpler calculation method based on perturbation expansion of the Orr-Sommerfeld equation.
After them, Benney [9] has developed a non-linear evolution equation for the film thickness, which also predicts a correct stability threshold for the inception of long waves; his method is based on a gradient expansion of velocity and pressure fields by a small parameter $\varepsilon = h/\lambda$, measuring the littleness of the film thickness h compared to the wavelength λ of the waves. Benney's non-linear evolution equation was then modified by Gjevik [31] and Lin [46], who have shifted the surface tension to $\mathcal{O}(\varepsilon)$, by demonstrating its relevant role in the linear stability analysis. These approaches locate in the *lubrification theory*, for which the wave dynamics is studied by an evolution equation for the film thickness only. However, this theory is valid for small Reynolds number, being built by assuming small inertia effects. Indeed, Benney's evolution equation is demonstrated to produce finite-time blow-up for moderate Reynolds number, as pointed out by Pumir *et al.* [65] and Joo *et al.* [38].

For high Reynolds numbers, the use of boundary-layer equations obviates to restrictions of Benney's evolution equation. Shkadov [76] first has proposed an integral model based on the boundary-layer equations, for which the dynamics of thin films is enslaved to film thickness h and flow rate q. In details, the integration provided by Shkadov assumes a parabolic velocity profile, corresponding to the local Nusselt profile. Nevertheless, the limitation of Shkadov's model is the lack of consistency, yielding a disagreement of the dispersion relation with the Orr-Sommerfeld theory. Indeed, a linear stability analysis of Shkadov's integrated equations does not provide the correct critical Reynolds number, that is the threshold above which unstable long waves develop on the liquid film.
This shortcoming has been addressed by Ruyer-Quil & Manneville [69, 70], who have improved Shkadov's parabolic profile, by adding corrections of further orders in ε in form of polynomials, and integrated the boundary-layer equations by means of the weighted residual method. Therefore, the wall shear stress takes a correction of $\mathcal{O}(\varepsilon)$, which ensures the consistency of the model, that is, the linearized model provides the correct critical Reynolds number. Particularly, in the work of 1998, the authors have used a collocation method to

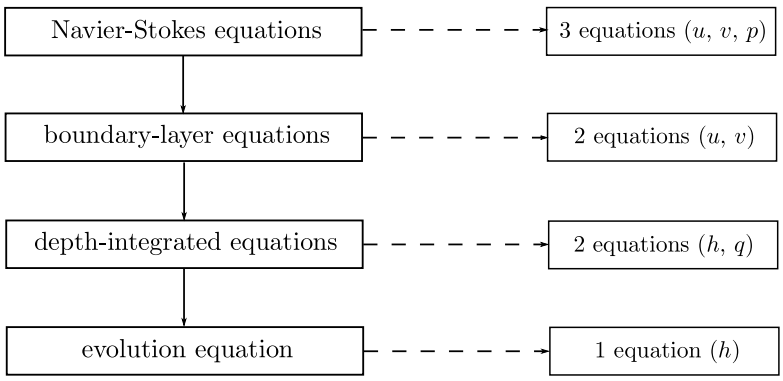

Figure 2.3: Levels of modeling approximation for falling liquid films.

get the integration process, while they have adopted the Galerkin method in the work of 2000. The latter, defined WRIBL (Weighted Residual Integral Boundary-Layer), has the advantage to converge already at order zero, thus preventing the long computations of the first-order profile. In line with this simplification, Luchini & Charru [50, 51] have then presented a way to avoid the computation of the first-order velocity field, based on the use of the kinetic-energy equation. Further details about accuracy and convergence of different models have been provided by Ruyer-Quil & Manneville [71] and Scheid *et al.* [74]. Shallow water modeling on arbitrary topography has been then studied by Boutounet *et al.* [12]. The scheme of Figure 2.3 summerizes the levels of approximations of different models.

The great advantage of disposing of reduced models is mainly valuable for numerical investigations. Indeed, depth-integrated equations allow to solve complex wave dynamics on falling liquid film by largely saving the computational cost compared to the full Navier-Stokes equations. However, several works about numerical investigations of falling liquid films by means of Navier-Stokes equations have been also provided. For example, Salamon *et al.* [72] have applied a finite-element method to describe vertical falling films and waves of finite amplitude. Then, Ramaswamy *et al.* [66] have coupled a finite-element approach with the ALE method to study temporal and spatial stability of non-linear waves. Another numerical study involving time-dependent Navier-Stokes equations applied to liquid films over inclined planes has been performed by Malamataris *et al.* [52]. Finally, in a recent work, Trifonov [89] has compared the Navier-Stokes solutions of non-linear waves to those of Shkadov's and Ruyer-Quil & Manneville's models.

2.1.2 Liquid films sheared by a gas flow

For what concerns two-layer flows, first experiments of Craik [21] and Cohen & Hanratty [19] have shown the presence of instabilities for confined configurations. Later, experiments by Henstock & Hanratty [36] and McCready & Hanratty [54] have proved that the occurrence of waves at the interface considerably amplifies the transfers between the liquid and the gas. Hence, in order to understand this mechanism, several studies have been conducted in the past. Consequently, in the same experimental work, Cohen & Hanratty [19], through the earlier studies of Miles and Benjamin [56, 8], and then Hanratty [34] have explained the physical process driving to the instability of two-layer flows: the disturbance in the velocity field in the gas produced by surface waves causes shear stress and pressure variations along the interface. More precisely, the component of pressure variations in phase with the wave slope and the component of shear stress variations in phase with the wave height, feed the liquid film instability. If the viscous dissipation in the liquid film is not larger than the energy transmitted by these mechanisms, surface-wave amplitude increases. This process finishes in turn by modifying the gas behavior and thus produces a coupled influence

between the two phases. Later, Kelly *et al.* [42] have given a description for the physical mechanism of the gravity-driven instability of long waves at the interface of a falling liquid film down an inclined plane. Instead, in case of imposed shear stress or imposed velocity, Smith [78] has provided an explaination for the gravity-driven instability. On the other hand, the mechanism of long-wave instability for two-layer Couette flows has been investigated by Barthelet *et al.* [5] and Charru & Hinch [18]. Furthermore, Boomkamp & Miesen [11] have given a wide discussion of the mechanisms responsible for different instabilities which can grow at the interface between two phases.

The analysis of linear stability of long waves between two layers has been the subject of several studies over the past decades. Yih [96] firstly has proved that the viscosity stratification between two layers of equal density and thickness causes the instability of long waves. Subsequently, Yiantsios & Higgins [94] have considered the effect of gravity force and density difference on the large-wavelength stability threshold. In another work, Charru & Fabre [17] have stated that Poiseuille flows are stable to long-wave disturbances only if the velocity of the primary flow is convex. Then, Tilley *et al.* [83] have studied the stability analysis of air-water and olive oil-water systems and have determined the influence of the channel thickness and the mean interfacial height on the stability of the flow. More recently, Healey [35] has studied the absolute instability of plane mixing layers, showing the effect of the confinement on the long-wave limit. Then, Valluri *et al.* [91] have provided a spatio-temporal analysis of a two-layer channel flow, investigating the transition from convective to absolute instability and proving the presence of a region absolutely unstable. In the same direction, Ò Naraigh *et al.* [61] have extended the work of Valluri *et al.* [91] to larger regions, of interest for oil and gas industries. Finally, Fuster *et al.* [30] have investigated convective and absolute instabilities of two-layer sheets in the primary atomization region, showing the dependence of the stability from liquid and gas velocities, as well as from the dynamic pressure ratio.

The development of reduced models to describe the dynamics of film flows and two-layer flows in general, arises from the need to decrease the computational cost, particularly expensive when analyzing the industrial configurations. However, there exists several works about direct numerical simulation of two-layer flows. Li *et al.* [45] have studied numerically two-layer Couette flows at low Reynolds number, showing the formation of fingers for periodic disturbances. Zhang *et al.* [97] have studied a Poiseuille flow by a front tracking numerical method. Then, Frank [27, 28] has analyzed liquid films sheared by laminar gas flows, and has compared long-wave solutions to gravity-capillary waves. In two recent works, Trifonov [87, 88] has performed direct numerical simulations of counter-current gas-liquid flows between flat and corrugated plates.

On the other hand, reduced models are mostly based on Benney's, Shkadov's and WRIBL approaches previously described for falling liquid films. Indeed, Tilley *et al.* [84] have derived a non-linear evolution equation describing the motion of the interface in the case of long waves. However, Tilley's model is based on a Benney's expansion applied to both phases, and thus it fails far from the threshold. Following Benney's method, Jurman & McCready [39] have instead developed a non-linear evolution equation for turbulent gas over liquid films. Later, Sisoev *et al.* [77] have developed a two-layer model based on the integral method of Shkadov. However, as mentioned above, this model does not permit to catch the right stability threshold. Subsequently, Matar *et al.* [53] have combined a long-wave theory and an integral model to derive a non-linear evolution equation for the interface. Yet, the use of a Benney's expansion to analyze the lower layer implies the shortcoming previously cited. Finally, Amaouche *et al.* [3] have applied the WRIBL method to gravity-driven two-layer channel flows. This work was subsequently extended by Alba *et al.* [1] to pressure-driven channel flows; however, they have assumed uniform density over the flow domain, and omitted the surface tension. In a recent work, Dietze & Ruyer-

Quil [25] have developed a fully reduced model for a confined two-layer flow, which makes use of the weighted residual method in the integration of the two-phase boundary-layer equations. The authors have studied gravity-driven and pressure-driven channel flows, and have validated the linear stability analysis by comparison with the Orr-Sommerfeld theory. They have also provided numerical analysis in good agreement with their DNS, performed by means of the flow solvers Gerris [64] and OpenFOAM. However, solving the gas phase by means of a low-dimensional model restricts the region of its application.
Meanwhile, the WRIBL approach has been employed by Tseluiko & Kalliadasis [90] to model liquid films sheared by a counter-current turbulent gas flow inside a channel. However, they have assumed the liquid-gas interface to be a no-slip wavy wall, thus reducing the possible applications. Subsequently, Vellingiri *et al.* [92] have used the same methodology to study co-current flows inside a channel. Finally, Samanta [73] has applied the WRIBL method to analyze the long-wave stability of shear-imposed falling films, and has extended the study of Smith [78] to higher Reynolds numbers.

Once the general summary of liquid films has been presented, some specific works are described in details.

2.2 The governing equations

The Navier-Stokes equations serve as instrument to model the flow of a compressible viscous fluid. These equations read

$$\begin{cases} \partial_t \tilde{\rho} + \nabla \cdot (\tilde{\rho}\tilde{\mathbf{u}}) = 0 \\ \partial_t(\tilde{\rho}\tilde{\mathbf{u}}) + \nabla \cdot (\tilde{\rho}\tilde{\mathbf{u}} \otimes \tilde{\mathbf{u}}) = -\nabla \tilde{p} + \tilde{\rho}\tilde{\mathbf{g}} + \nabla \cdot \tilde{\mathbf{T}} \end{cases} , \tag{2.1}$$

where ∇ is the nabla operator, accounting for the gradient and the divergence operators, and $\otimes$ defines the outer product. The velocity $\tilde{\mathbf{u}}$ has components ($\tilde{u}$,$\tilde{v}$,$\tilde{w}$) along stream-wise ($\tilde{x}$), cross-stream ($\tilde{y}$) and span-wise ($\tilde{z}$) directions, while ρ, p and $\mathbf{g}$ define density, pressure and gravity, respectively, and $\tilde{T}$ represents the viscous stress tensor (Anderson [4] and Batchelor [6]). The tilde identifies dimensional variables.
Most of problems considered in the present thesis will focus on two-dimensional thin liquid films falling down an inclined plane, and possibly affected either by given shear stress and pressure at the interface or by a laminar gas flowing on the top of the films. Furthermore, the flow conditions of the liquid and the reduced gas velocity permit to assume incompressible conditions. Therefore, for all problems treated here, such as a sheared thin liquid films as sketched in Figure 2.4, Navier-Stokes equations (2.1) reduce to

$$\begin{cases} \partial_x \tilde{u}_k + \partial_y \tilde{v}_k = 0 \\ \partial_t \tilde{u}_k + \tilde{u}_k \partial_x \tilde{u}_k + \tilde{v}_k \partial_y \tilde{u}_k = -\dfrac{1}{\rho_k}\partial_x \tilde{p}_k + g\sin\beta + \nu_k \nabla^2 \tilde{u}_k \\ \partial_t \tilde{v}_k + \tilde{u}_k \partial_x \tilde{v}_k + \tilde{v}_k \partial_y \tilde{v}_k = -\dfrac{1}{\rho_k}\partial_y \tilde{p}_k - g\cos\beta + \nu_k \nabla^2 \tilde{v}_k \end{cases} , \tag{2.2}$$

where β is the inclination of the plane and $\nu_k = \mu_k/\rho_k$ is the kinematic viscosity of the fluid. The subscript k identifies the phase, that is $k = 1$ for the liquid and $k = 2$ for the gas, while $\nabla^2 = \partial_{xx} + \partial_{yy}$ is the Laplacian operator. These equations must be completed with boundary conditions at the wall and at the interface, where $\tilde{y} = 0$ and $\tilde{y} = \tilde{h}$, respectively. The no-slip condition at the wall reads

$$\tilde{u}_1|_0 = 0 \ , \qquad \tilde{v}_1|_0 = 0 \ . \tag{2.3}$$

At the liquid-gas interface, boundary conditions state the continuity of velocities, and tangential and normal stresses. The continuity of velocities leads to

$$[\tilde{u}] = 0 \ , \qquad [\tilde{v}] = 0 \ , \tag{2.4}$$

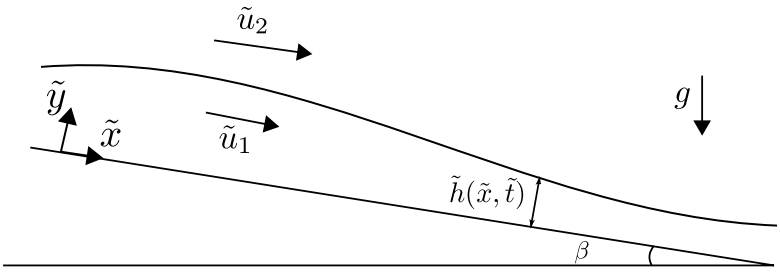

Figure 2.4: Sketch of a liquid film sheared by a gas flow and definition of the coordinate system. For falling films, $\tilde{u}_2 = 0$.

whereas

$$\partial_t \tilde{h} + \tilde{u}|_h \partial_x \tilde{h} = \tilde{v}|_h \tag{2.5}$$

is the kinematic condition. The continuity of stresses gives

$$[\tilde{\mathbf{n}} \cdot \tilde{\mathbf{T}}^{(\tilde{n})}] = \gamma \nabla \cdot \tilde{\mathbf{n}} \ , \tag{2.6}$$

$$[\tilde{\mathbf{t}} \cdot \tilde{\mathbf{T}}^{(\tilde{n})}] = 0 \ , \tag{2.7}$$

where $\mathbf{T}^{(\mathbf{n})} = \Sigma \cdot \mathbf{n}$ is the stress vector at the interface with normal $\mathbf{n}$, while Σ is the stress tensor and γ the surface tension. Tangent and normal unit vectors to the interface are defined as

$$\tilde{\mathbf{n}} = \frac{1}{\sqrt{1+\partial_x^2 \tilde{h}}} \begin{Bmatrix} -\partial_x \tilde{h} \\ 1 \end{Bmatrix} \ , \tag{2.8a}$$

$$\tilde{\mathbf{t}} = \frac{1}{\sqrt{1+\partial_x^2 \tilde{h}}} \begin{Bmatrix} 1 \\ \partial_x \tilde{h} \end{Bmatrix} \ . \tag{2.8b}$$

The symbol $[\cdot]$ replaces the jump $(\cdot)_2 - (\cdot)_1$ across the interface. Finally, top boundary conditions to apply to the gas flow will be performed later for precise geometry and flow conditions.

Hence, the system of equations (2.2) with the boundary conditions (2.3-2.8) describes the dynamics of a falling film down an inclined plane, and possibly driven by a laminar gas flow.

2.3 Modeling of gravity-driven thin liquid films

Previous models of gravity-driven films flowing down an inclined plane, see Figure 2.4 with $\tilde{u}_2 = 0$, will be presented in this section. Since the presence of the gas phase reduces to a constant pressure, the subscript 1 in the liquid will be omitted for the descriptions of these models. Table 2.2 at the end of this section resumes all works detailed here and their main differences.

2.3.1 Nusselt's solution

A uniform and steady solution of the system of equations (2.2-2.8) has been found by Nusselt, in the case of a falling film in a passive gas atmosphere. In his work of 1916 [60], Nusselt has studied the film condensation by neglecting inertia effects into the liquid. He has thus treated a wavyless problem, based on the assumption that the film thickness is steady and uniform, so that both the derivatives with respect to x and t, and the cross-stream velocity $\tilde{v}$ vanish in (2.2-2.8). As a consequence, velocity and pressure fields turn

to be

$$\tilde{u}_0(\tilde{y}) = \frac{1}{2\nu} g \sin\beta (2\tilde{h}_0 - \tilde{y})\tilde{y} \ , \tag{2.9}$$

$$\tilde{p}_0(\tilde{y}) = \rho g \cos\beta (\tilde{h}_0 - \tilde{y}) \ , \tag{2.10}$$

where $\tilde{h}_0$ is the wavyless film thickness, and subscript 0 specifies the uniform parallel flow. The velocity profile has a parabolic shape, given by the balance of the gravity force and the wall shear stress. The corresponding flow rate is obtained by the definition

$$\tilde{q}_0 = \int_0^{\tilde{h}_0} \tilde{u}_0(\tilde{y}) \, d\tilde{y} \ , \tag{2.11}$$

and thus provides

$$\tilde{q}_0 = \frac{g \sin\beta \tilde{h}_0^3}{3\nu} \ , \tag{2.12}$$

which is constant. Instead, the mean longitudinal film velocity $\tilde{U}_0 = \tilde{q}_0/\tilde{h}_0$ leads to

$$\tilde{U}_0 = \frac{g \sin\beta \tilde{h}_0^2}{3\nu} \ . \tag{2.13}$$

Although Nusselt's achievement was very remarkable, his approach does not contemplate waves at the free surface of the film, because of its construction. Therefore, several studies follow this one with the attempt to describe linear and non-linear waves on thin liquid films.

2.3.2 The long-wave theory

Experiments on thin liquid films at small Reynolds number show that the height of wave crests is always small compared to the wavelength of the waves. For example, on a liquid film about 1 *mm* thick falling down an inclined plane, waves can be more than 1 *cm* long. Yet, in the experiments of Liu and Gollub [47], the ratio between film thickness and wavelength never exceeds 0.1. This behaviour justifies then the introduction of a *shallow water parameter* ε, measuring the smallness of Nusselt's film thickness to a characteristic length along the stream-wise direction. Meanwhile, parameter ε also expresses the littleness of stream-wise and time derivatives ∂_x, ∂_t with respect to cross-stream derivatives ∂_y: there is then a separation of scales, consequence of slow changes of the interface of the liquid film along space and time. In the linear regime, ε can be expressed as function of the wavelength of the perturbation λ, i.e. $\varepsilon = \tilde{h}_0/\lambda = k\tilde{h}_0/2\pi$, where k defines the wavenumber; in the non-linear regime, $\varepsilon \sim \partial_{x,t}$, that is the smallness of the interfacial slope and its variation in time.

The assumption of long waves drives to the so-called long-wave theory, and allows to simplify the Navier-Stokes equations (2.2-2.8). One can thus work with dimensionless parameters, in order to highlight the most important terms of the equations. Therefore, dimensionless variables can be obtained as

$$x = \frac{\tilde{x}}{\tilde{h}_0} \ , \qquad y = \frac{\tilde{y}}{\tilde{h}_0} \ , \qquad t = \frac{\tilde{t}}{\tilde{T}} \ , \tag{2.14a}$$

$$u = \frac{\tilde{u}}{\tilde{U}_0} \ , \qquad v = \frac{\tilde{v}}{\tilde{U}_0} \ , \qquad p = \frac{\tilde{p}}{\rho \tilde{U}_0^2} \ . \tag{2.14b}$$

where $\tilde{h}_0$ and $\tilde{U}_0$ are characteristic length and velocity of the film flow, for instance the Nusselt uniform flow previously described. Scaling (2.14) allows to write system (2.2-2.8) in dimensionless form. The procedure used in this work consists on the transformations

$$\tilde{\partial_{x,t}} \longrightarrow \varepsilon \partial_{x,t} \ , \qquad \tilde{\partial_{xx}} \longrightarrow \varepsilon^2 \partial_{xx} \ , \tag{2.15}$$

where the symbol tilde on top of derivatives refers to dimensional variables. With these transformations, the continuity equation of (2.2) becomes $\varepsilon\partial_x u + \partial_y v = 0$. Therefore, this relation forces v to be smaller than u, namely $v = \mathcal{O}(\varepsilon)$, which is in line with the incompressible state. As a consequence, in addition to transformations (2.15) one can also use $\tilde{v} \longrightarrow \varepsilon v$. Finally, system (2.2) reads

$$\begin{cases} \partial_x u + \partial_y v = 0 \\ \varepsilon(\partial_t u + u\partial_x u + v\partial_y u) = -\varepsilon\partial_x p + \dfrac{1}{Fr}\sin\beta + \dfrac{1}{Re}(\varepsilon^2\partial_{xx}u + \partial_{yy}u) \\ \varepsilon^2(\partial_t v + u\partial_x v + v\partial_y v) = -\Big(\partial_y p + \dfrac{1}{Fr}\cos\beta\Big) + \dfrac{\varepsilon}{Re}(\varepsilon^2\partial_{xx}v + \partial_{yy}v) \end{cases} . \tag{2.16}$$

Two dimensionless numbers occur in the dimensionless equations (2.16). The Reynolds number Re is defined as

$$Re = \frac{\tilde{U}_0\tilde{h}_0}{\nu} , \tag{2.17}$$

and can be interpretated as the ratio of inertial to viscous forces. Therefore, for low Reynolds number the film is governed by viscous stresses. The Froude number Fr is defined as

$$Fr = \frac{\tilde{U}_0^2}{g\tilde{h}_0} , \tag{2.18}$$

and can be read as the Mach number, since gives the ratio of film velocity to gravitational wave speed. If the Froude number is smaller than unity, then the flow is said *subcritical* and informations can travel upstream. If the Froude number is bigger than unity, then the flow is *supercritical* and informations travel downstream only. If the Froude number is equals to unity, the flow is denoted as *critical*.
The dimensionless wall boundary condition (2.3) is given by

$$u|_0 = 0 , \qquad v|_0 = 0 , \tag{2.19}$$

while the corresponding continuities (2.5-2.7) at the free surface, where $y = h = \tilde{h}/\tilde{h}_0$, read

$$\partial_t h + u|_h\partial_x h = v|_h , \tag{2.20a}$$

$$\begin{aligned} &Re(1+\varepsilon^2\partial_x^2 h)p|_h + 2\varepsilon(1-\varepsilon^2\partial_x^2 h)\partial_x u|_h \\ &+ 2\varepsilon\partial_x h(\partial_y u|_h + \varepsilon^2\partial_x v|_h) = -\frac{Re}{We}\frac{\varepsilon^2\partial_{xx}h}{\sqrt{1+\varepsilon^2\partial_x^2 h}} , \end{aligned} \tag{2.20b}$$

$$-4\varepsilon^2\partial_x h\partial_x u|_h + (1-\varepsilon^2\partial_x^2 h)(\partial_y u|_h + \varepsilon^2\partial_x v|_h) = 0 . \tag{2.20c}$$

The Weber number We appearing in the boundary condition of normal stresses is given by

$$We = \frac{\rho\tilde{h}_0\tilde{U}_0^2}{\gamma} , \tag{2.21}$$

and is a measure of the ratio of inertial forces to surface tension.
All terms $\mathcal{O}(\varepsilon^2)$ and smaller will be neglected in the present work, and thus only models accurate to order one in the parameter ε, i.e. $\mathcal{O}(\varepsilon)$, will be considered. Furthermore, if one supposes that $Re = \mathcal{O}(1)$, $Fr = \mathcal{O}(1)$ and $We = \mathcal{O}(\varepsilon^2)$, to be justified in Chapter 3, then equations (2.16) can be reduced to two equations. Indeed, by integrating the y-momentum equation with the help of the boundary condition (2.20b), one gets

$$p(x,y,t) = -\frac{\varepsilon^2}{We}\partial_{xx}h + \frac{1}{Fr}\cos\beta(h-y) . \tag{2.22}$$

Then, by replacing the pressure derivative $\partial_x p$ in the x-momentum equation leads to

$$\begin{cases} \partial_x u + \partial_y v = 0 \\ \varepsilon(\partial_t u + u\partial_x u + v\partial_y u) = -\varepsilon\dfrac{\cos\beta}{Fr}\ \partial_x h + \dfrac{\sin\beta}{Fr} + \dfrac{1}{Re}\partial_{yy} u + \dfrac{\varepsilon^3}{We}\partial_{3x} h \end{cases} . \tag{2.23}$$

From now onwards, all expressions will be written without the parameter ε, taking into account the transformations $\varepsilon\partial_{x,t} \longrightarrow \partial_{x,t}$, $\varepsilon^2\partial_{xx} \longrightarrow \partial_{xx}$ and $v \longrightarrow \varepsilon v$.
It should be noted that the presence of a constant interfacial pressure p_i into the boundary condition (2.20b) does not affect the x-momentum equation, due to the derivative $\partial_x p$.

2.3.3 Benney's non-linear equation

In his work of 1966 [9], Benney has studied long waves on the steady flow of thin liquid films down an inclined plane. By a systematic expansion procedure in the small parameter ε, Benney has developed a non-linear evolution equation for the film thickness. Unlike a linearized long-wave development, Benney's approach takes into account long waves of arbitrary amplitude, while only the stream-wise variations of the film thickness are limited. When ε is small, one can expand the velocity field as

$$u = u^{(0)} + u^{(1)} + \dots \tag{2.24a}$$

$$v = v^{(0)} + v^{(1)} + \dots\ , \tag{2.24b}$$

where first-order variables are $\mathcal{O}(\varepsilon)$. By replacing these into the equations (2.23), the leading-order velocity profiles provided by Benney's method lead to

$$u^{(0)}(x,y,t) = \Lambda y(hy - \frac{y^2}{2})\ , \qquad v^{(0)}(x,y,t) = 0\ , \tag{2.25}$$

where

$$\Lambda = \frac{Re}{Fr}\sin\beta\ . \tag{2.26}$$

For uniform flow, the stream-wise zeroth-order velocity coincides with Nusselt's solution (2.9). This shows that the order zero of Benney's development corresponds to local equilibrium. At order one, velocity profiles can be recovered from Benney's work. Here, the non-linear evolution equation is provided only, which is obtained by the continuity equation, after replacement of the appropriate dimensionless flow rate $q(x,t) = q^{(0)} + q^{(1)}$, defined as

$$q = \int_0^h u\, dy\ . \tag{2.27}$$

Benney's evolution equation reads

$$\partial_t h + \Lambda h^2 \partial_x h + \partial_x\Big[\Big(\frac{2}{15}Re\Lambda^2 h^6 - \frac{1}{3}\frac{Re}{Fr}\cos\beta h^3\Big)\partial_x h\Big] = 0\ . \tag{2.28}$$

As special case, Benney has studied the weakly non-linear stability problem for the liquid film falling down an inclined plane and has derived the Landau equation. Otherwise, linearizing his result (2.28), Benney has found the critical Reynolds number $Re_{cr} = 5/6\cot\beta$, which coincides with the linear stability result of Yih and Benjamin of falling liquid films (see section 2.5).

Nusselt's and Benney's approaches fall in the *lubrification theory*, because all variables are enslaved to the film thickness only. However, because of this behaviour, evolution equations of the form (2.28) work well only close to the stability threshold.

Table 2.1: Leading-order closure models for three different velocity profiles.

shape	$u(y)$	$h\Gamma$	τ_w
uniform	U_0	$\frac{q^2}{h}$	0
linear	$\frac{2U_0}{h}y$	$\frac{4}{3}\frac{q^2}{h}$	$2\frac{q}{h^2}$
semi-parabolic	$\frac{3U_0}{2}\frac{y}{h}\Big(2-\frac{y}{h}\Big)$	$\frac{6}{5}\frac{q^2}{h}$	$3\frac{q}{h^2}$

In later works, Lin [46] and Gjevik [31] have added surface tension to the non-linear equations of Benney (2.28). Indeed, Benney has considered surface tension only at higher order of accuracy, while Lin and Gjevik have shown that the We number is usually $\mathcal{O}(\varepsilon^{-2})$, and thus surface tension has to be taken into account for the calculation of the wave velocity. Particularly, in his work, Lin has used an expansion in the small amplitude of the waves based on the theory of Reynolds and Potter [68]. On the other hand, Gjevik has applied Benney's asymptotic method with the corrections of the surface tension and has found the non-linear equation

$$\partial_t h + \Lambda h^2 \partial_x h + \partial_x \Big[\Big(\frac{2}{15} Re \Lambda^2 h^6 - \frac{1}{3}\frac{Re}{Fr}\cos\beta h^3 \Big)\partial_x h + \frac{1}{3}h^3 \frac{Re}{We}\partial_{3x} h \Big] = 0 \ , \tag{2.29}$$

which differs from (2.28) only in the capillary term.

2.3.4 Shkadov's model

In his work of 1967 [76], Shkadov has derived a new method to solve the non-linear waves on a vertical liquid film, in order to get closer to the experimental data. The main contribution to be assigned to Shkadov's work is the approach based on the integration of the boundary-layer equations, which causes that all variables are enslaved to film thickness and flow rate. Indeed, by integrating the equations (2.23), one gets*

$$\begin{cases} \partial_t h + \partial_x q = 0 \\ \partial_t q + \partial_x (h\Gamma) + \dfrac{\cos\beta}{Fr} h \partial_x h = \dfrac{1}{Re}\Big(\Lambda h - \tau_w\Big) + \dfrac{1}{We} h \partial_{3x} h \end{cases} , \tag{2.30}$$

where $u_y|_0 = \tau_w$ is the shear stress at the wall, q is the dimensionless volumetric flow rate per unit width and Γ is a *shape factor*, defined by Hanratty [34] as

$$\Gamma = \frac{1}{h}\int_0^h u^2 \, dy \ . \tag{2.31}$$

Note that all terms of the equations (2.30) are expressed as function of unknowns h and $q = Uh$, thickness and flow rate of the film, respectively. Only two terms do not fulfill this feature, such as the momentum transport and the wall shear stress. This issue suggests the need to develop closure models. Closure models consist in assuming a proper shape for the velocity profile, in order to enslave all terms of the equation to h and q only. For example, Table 2.1 shows three different velocity profiles, namely the uniform, linear and semi-parabolic, and their closure.

*A more detailed integration procedure will be treated in Chapter 3 for a complex case, as part of this work.

Following his procedure, Shkadov has assumed Kapitza's self-similar parabolic velocity profile to close the integrated equations, that is

$$u(x,y,t) = 3U(x,t)\frac{1}{2}\xi(2-\xi) \ , \tag{2.32}$$

where $\xi = y/h$. Hence, Shkadov's model leads to[†]

$$\begin{cases} \partial_t h + \partial_x q = 0 \\ \partial_t q + \partial_x\Big(\frac{6}{5}\frac{q^2}{h}\Big) + \frac{\cos\beta}{Fr}h\partial_x h = \frac{1}{Re}\Big(\Lambda h - 3\frac{q}{h^2}\Big) + \frac{1}{We}h\partial_{3x}h \end{cases} . \tag{2.33}$$

In order to compare Shkadov's integrated model to Benney's non-linear evolution equation, one can achieve a Benney's asymptotic expansion for the flow rate $q = q^{(0)} + q^{(1)} + \ldots$, where $q^{(0)} = \Lambda\ h^3/3$ is the local equilibrium flow rate, in line with Benney's leading order. Hence, by appropriate replacement of time derivatives by means of the integrated continuity equation $\partial_t h + \partial_x q = 0$ and by substituting the order-zero flow rate, an analysis of the second of (2.33) provides $q^{(1)}$, namely

$$q^{(1)} = \frac{1}{3}h^3 Re\Big[\frac{1}{3}\Lambda^2 h^3\partial_x h - \frac{\cos\beta}{Fr}\partial_x h + \frac{1}{We}\partial_{3x}h\Big] \ . \tag{2.34}$$

When adopting the flow rate $q = q^{(0)} + q^{(1)}$ in the integrated continuity equation, one obtains

$$\partial_t h + \Lambda h^2\partial_x h + \partial_x\Big[\Big(\frac{1}{9}Re\Lambda^2 h^6 - \frac{1}{3}\frac{Re}{Fr}\cos\beta h^3\Big)\partial_x h + \frac{1}{3}h^3\frac{Re}{We}\partial_{3x}h\Big] = 0 \ , \tag{2.35}$$

which disagrees with Benney's equation (2.28), or more precisely Gjevik's equation (2.29), because of the coefficient of h^6. This manifests that Shkadov's integrated model does not provide the right stability threshold. Indeed, by performing a stability analysis, as will be shown later, one gets $Re_{cr} = \cot\beta$, which is in contrast with the long-wave stability result (Orr-Sommerfeld equation). This happens because Shkadov's model lacks the correction of the wall shear stress accurate at order one.

2.3.5 Ruyer-Quil & Manneville's model

In a work of 1998 [69], Ruyer-Quil & Manneville have extended Shkadov's approach and provided a consistent integral model, in order to capture the correct stability threshold. Specifically, their model is based on the weighted residual method: solution of the governing equations (2.23) is sought in the form

$$u(x,y,t) = \sum_{j=0}^{N} b_j(x,t)f_j(\xi) \ , \tag{2.36}$$

where f_j are chosen test functions and $\xi = y/h$; subsequently, the resulting equation is projected on the basis of the test functions, and the imposition of zero residuals leads to a linear system for the coefficients b_j. Such residuals are obtained by means of chosen weighted functions w_j. However, expansion coefficients b_j must vary slowly with respect to x and t, as h does. Detailed informations about the weighted residual method and its application to falling liquid films can be found in Kalliadasis *et al.* [40]. Ruyer-Quil & Manneville have thus proposed further accuracy to Shkadov's parabolic velocity profile (2.32), namely

$$u(x,y,t) = b_0(x,t)f^{(0)}(\xi) + b_1(x,t)f^{(1)}(\xi) \ , \tag{2.37}$$

[†]As a matter of fact, Shkadov has treated the problem of a vertical falling film, for which $\sin\beta = 1$ and $\cos\beta = 0$. Here, a certain inclination β of the plane is assumed with the intent to compare different methods.

where test functions $f^{(0)}(\xi) = -\xi^2/2 + \xi$ and $f^{(1)}(\xi) = (\xi^4/4 - \xi^3 + \xi^2)/6$ are combinations of zeroth- and first-order velocity profiles given by the Benney's asymptotic expansion. Particularly, $f^{(0)}(\xi)$ is proportional to the leading order velocity profile (2.25), while the polynomial $f^{(1)}(\xi)$ is chosen by fulfillment of two conditions on the derivatives at $\xi = 0$ and $\xi = 1$.
One of the most important results of their work consists in showing that an appropriate correction of the wall shear stress permits to get rid of Shkadov's inconsistency. Hence, by expressing the wall shear stress as $\tau_w = 3q/h^2 + {\tau_w}^{(c)}$ and by the definition of the flow rate (2.27), unknowns b_0 and b_1 can be expressed as function of q and ${\tau_w}^{(c)}$, namely $b_0 = 3q/h^2 + h{\tau_w}^{(c)}$ and $b_1 = -15h{\tau_w}^{(c)}$.‡
By replacing the velocity profile (2.37) and the wall shear stress τ_w into the integrated equations (2.30), ${\tau_w}^{(c)}$ is still unknown. The additional equation can be obtained by imposing further conditions at $y = 0$. By differentiating the equation (2.23) with respect to y and evaluating the resulting expression at $y = 0$, one gets $\partial_t(\partial_y u|_0) - \partial_{3y} u|_0$. By replacing the velocity profile (2.37) into this expression and by observing that ${\tau_w}^{(c)}$ is first-order accurate, the missing condition reads

$$ {\tau_w}^{(c)} = \frac{Re}{15} h^2 \partial_t\Big(\frac{3q}{h^2}\Big) \ . \tag{2.38} $$

Finally, expression (2.38) can be written as ${\tau_w}^{(c)} = Re(\partial_t q + 2q/h\partial_x q)/5$ with the help of the continuity equation. Therefore, from the integrated equations (2.30), Ruyer-Quil & Manneville's integral model reads

$$ \begin{cases} \partial_t h + \partial_x q = 0 \\ \partial_t q + \partial_x\Big(\dfrac{q^2}{h}\Big) + \dfrac{1}{3}\dfrac{q}{h}\partial_x q + \dfrac{5}{6}\dfrac{\cos\beta}{Fr} h\partial_x h = \dfrac{5}{6Re}\Big(\Lambda h - 3\dfrac{q}{h^2}\Big) + \dfrac{5}{6We} h\partial_{3x} h \end{cases} . \tag{2.39} $$

The definition (2.38) confirms that ${\tau_w}^{(c)}$ is first-order accurate, because of the derivative with respect to time is $\mathcal{O}(\varepsilon)$. Therefore, in order to explicit it as a function of space derivatives of h, only the zeroth-order flow rate has to be used, leading to

$$ {\tau_w}^{(c)} = -\frac{Re}{15}\Lambda^2 h^4 \partial_x h \ , \tag{2.40} $$

where mass conservation equation and definition of the flow rate have been used here.
Yet, in order to compare this model to Benney's evolution equation (2.28), by performing an asymptotic expansion of the flow rate $q = q^{(0)} + q^{(1)} + \ldots$, one gets, as shown before in the case of Shkadov's equations,

$$ q^{(1)} = \frac{1}{3} h^3 Re\Big[\frac{2}{5}\Lambda^2 h^3 \partial_x h - \frac{\cos\beta}{Fr}\partial_x h + \frac{1}{We}\partial_{3x} h\Big] \ . \tag{2.41} $$

Replacing the flow rate $q = q^{(0)} + q^{(1)}$ in the integrated continuity equation, leads to Benney's (or Gjevik's) non-linear evolution equation (2.28), indicating that Ruyer-Quil & Manneville's integrated model provides the correct stability threshold.
In a similar way, the analysis of such a model at second order of accuracy is based on the definition of four coefficients for the velocity profile, from b_2 to b_5, and suited boundary conditions to reduce the final system of equations to three unknowns, h, q and ${\tau_w}^{(c)}$.

In a further work [70], the same authors have improved this model with the aim to find it in a simpler and more efficient way. Rather than the collocation method, for which the weighted functions are Dirac delta, the weighted residual approach is based on the Galerkin method, where weighted functions coincide with test functions. The benefit given by the Galerkin method consists in the closure of the integral model already at order zero. The

‡Note that if $q = q^{(0)}$ (i.e. $q^{(1)} = 0$), then ${\tau_w}^{(c)} = {\tau_w}^{(1)}$.

fulfillment of the boundary conditions at the wall and at the free surface enables to express the polynomials f_j as

$$f_j(\xi) = \xi^{j+1} - \frac{j+1}{j+2}\xi^{j+2} \ . \tag{2.42}$$

Indeed, the first-order residual reads

$$\int_0^h f_j(\xi)\Big(\partial_t u + u\partial_x u + v\partial_y u - \frac{1}{Re}\partial_{yy}u\Big)\,dy \ = \frac{2h}{(j+2)(j+3)}\Big(-\frac{\cos\beta}{Fr}\,\partial_x h + \frac{\sin\beta}{Fr} + \frac{1}{We}\partial_{3x}h\Big), \tag{2.43}$$

where the coefficients of the r.h.s depending on j derives by the integral of the weighted functions (2.42). Considering the zeroth-order residual from (2.43), only the dissipative term $\int_0^h f_0(\xi)\partial_{yy}u\,dy$ requires the correction of order one. However, a double integration by parts permits to express this integral term as $-q/h^2$, and thus the evolution equation for a_0 becomes already the integral equation of the model, which reads

$$\begin{cases} \partial_t h + \partial_x q = 0 \\ \partial_t q + \partial_x\Big(\frac{9}{7}\frac{q^2}{h}\Big) - \frac{1}{7}\frac{q}{h}\partial_x q + \frac{5}{6}\frac{\cos\beta}{Fr}h\partial_x h = \frac{5}{6Re}\Big(\Lambda h - 3\frac{q}{h^2}\Big) + \frac{5}{6We}h\partial_{3x}h \end{cases} . \tag{2.44}$$

By comparing this equation to the previously found from the same authors (2.39), one can realize that some coefficients are different. However, an asymptotic expansion of the flow rate, gives Benney's equation (2.28). This means that both models are consistent. Indeed, it is possible to obtain one from the other by simple manipulation of the expression of q as function of h. In a certain way, this suggests that plenty of consistent models can be found, with different properties, by appropriate manipulation of the coefficients.

2.3.6 Luchini & Charru's model

In a recent work [50, 51], Luchini & Charru have used energy balance considerations to provide a consistent model of shallow water equations. With their approach, the authors avoid long computations of the first order velocity $u^{(1)}$. However, their method can be recovered by the Galerkin weighted residual approach (2.43) of Ruyer-Quil & Manneville, as will be shown at the end of this paragraph. The difference with the method of Luchini & Charru is the physical interpretation of the approach.

One can consider a Benney-like asymptotic expansion of the velocity field, for which $u^{(1)}$ satisfies the gauge condition

$$\frac{1}{h}\int_0^h u^{(1)}\,dy = 0 \ . \tag{2.45}$$

At first order, the integrated kinetic-energy equation can be obtained by multiplying the momentum equation (2.23) by $u^{(0)}$ and then by integrating over the film thickness, which leads to

$$\partial_t\Big(\int_0^h \frac{(u^{(0)})^2}{2}\,dy\Big) + \partial_x\Big(\int_0^h \frac{(u^{(0)})^3}{2}\,dy\Big) + hU\partial_x P = -f = -\frac{2}{Re}\int_0^h \partial_y u^{(0)}\partial_y u^{(1)}\,dy \ , \tag{2.46}$$

where f is the dissipation (sum of the order zero and order one), and P the modified pression, embracing both the thermodynamic pressure and the gravitational potential. In the case of falling films down an inclined plane, $\partial_x P = 1/Fr(\sin\beta - \partial_x h\cos\beta)$ is known. By using integral by parts and equation (2.45), the first-order correction $f^{(1)}$ turns to be identically zero. In details,

$$\begin{aligned} \frac{Re}{2}f^{(1)} &= \int_0^h \partial_y u^{(0)}\partial_y u^{(1)}\,dy = (\partial_y u^{(0)}u^{(1)})|_0^h - \int_0^h \partial_{yy}u^{(0)}u^{(1)}\,dy \\ &= \partial_y u^{(0)}|_h u^{(1)}|_h - \partial_y u^{(0)}|_0 u^{(1)}|_0 + \frac{3U}{h^2}\int_0^h u^{(1)}\,dy = 0 \ . \end{aligned} \tag{2.47}$$

Table 2.2: First-order long-wave models of different works.

source	$u^{(1)}$	equations	surface tension	consistent
Benney	asymptotic	1	$\mathcal{O}(\varepsilon^3)$	yes
Gjevik	asymptotic	1	$\mathcal{O}(\varepsilon)$	yes
Shkadov	—	2	$\mathcal{O}(\varepsilon)$	no
Ruyer-Quil & Manneville (1998)	collocation	2	$\mathcal{O}(\varepsilon)$	yes
Ruyer-Quil & Manneville (2000)	Galerkin	2	$\mathcal{O}(\varepsilon)$	yes
Luchini & Charru	energy eq.	3	—	yes
this work	asymptotic	2	$\mathcal{O}(\varepsilon)$	yes

As a result, one can consider the integral system of x-momentum and kinetic energy equations

$$\partial_t q + \frac{6}{5}\partial_x(\frac{q^2}{h}) + h\partial_x P = -\frac{\tau_w}{Re} \ , \tag{2.48a}$$

$$\frac{6}{5}\partial_t \frac{q}{h} + \frac{54}{35}\frac{q}{h}\partial_x \frac{q}{h} - \frac{6}{35}\frac{q}{h^2}\partial_t h + \partial_x P = -\frac{3}{Re}\frac{q}{h^3} \ . \tag{2.48b}$$

With the addition of the continuity equation $\partial_t h + \partial_x q = 0$, equations (2.48) become a system of consistent shallow water equations accurate at order one. If the first-order pressure gradient $\partial_x P^{(1)}$ is unknown, as could be for flows in a slowly varying duct, equation (2.48b) allows to express it without computing $u^{(1)}$. Then, the momentum equation enables to find the correction of the wall shear stress at first order. Otherwise, if $\partial_x P^{(1)}$ is known, as for falling liquid films on a flat wall, by replacing (2.48b) into (2.48a) one directly finds $\tau_w^{(1)}$. Indeed it reads

$$\tau_w^{(1)} = -Re\Big(-\frac{1}{5}\partial_t q + \frac{6}{7}\frac{q}{h}\partial_x q + \frac{12}{35}\frac{q^2}{h^2}\partial_x h + \frac{48}{35}\frac{q}{h}\partial_t h\Big) \ . \tag{2.49}$$

Then, by using the continuity equation and by replacing the leading order flow rate $q = \Lambda h^3/3$, the wall shear stress at order one reduces to

$$\tau_w^{(1)} = -\frac{Re}{15}\Lambda^2 h^4 \partial_x h \ , \tag{2.50}$$

which coincides with the correction found by Ruyer-Quil & Manneville, equation (2.40). Hence, by an asymptotic expansion of the flow rate q, one can recover Benney's equation (2.28) after use of the continuity equation. This means that the model of Luchini & Charru is also consistent at order one.

Finally, it is worthwhile to show that the kinetic-energy equation (2.46), obtained by multiplying the momentum equation by $u^{(0)}$, coincides with the Galerkin weighted residual equation (2.43), because in the Galerkin method test functions are exactly the weighted functions, i.e. $w_0 = f_0 = u^{(0)}$. This proves that for falling liquid films the two methods drive to the same conclusions.

2.4 Modeling of two-layer channel flows

In this section, the system of two immiscible, viscous fluids flowing in an inclined channel is considered, and two different integral models are presented. Geometry and notations are

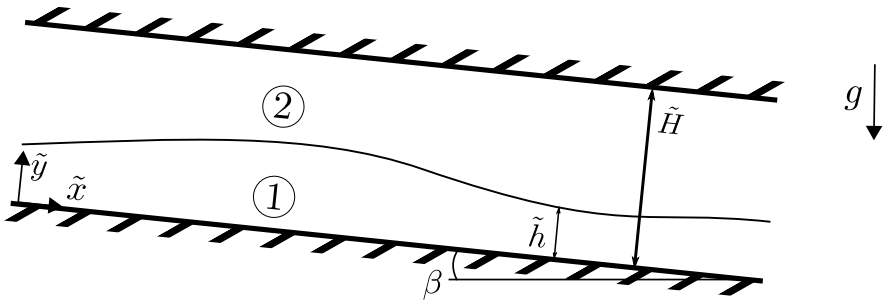

Figure 2.5: Definition of the geometry of a liquid film (index $k = 1$) sheared by a gas flow (index $k = 2$) in an inclined channel.

sketched in Figure 2.5.

2.4.1 Long-wave theory

Similarly to films driven by gravity, waves encountered in confined channels for two-layer flows are much larger than film and gas thicknesses. This suggests that the assumption of long waves can be made also for two-layer flows in confined domains. As before, one can thus introduce a small parameter ε measuring the littleness of space and time derivatives $\partial_{x,t}$. In the linear regime, it is reasonable to define $\varepsilon = \tilde{H}/\lambda = k\tilde{H}/2\pi$, where λ is the wavelength of perturbed waves developing at the liquid-gas interface. In the non-linear regime, $\varepsilon \sim \partial_{x,t}$, giving the idea that the interface is slowly modified in space and time.

Thanks to the long-wave assumption, equations (2.2) simplify. In order to express these equations in dimensionless form, one can define dimensionless variables as

$$x = \frac{\tilde{x}}{\tilde{H}} , \qquad y = \frac{\tilde{y}}{\tilde{H}} , \qquad t = \frac{\tilde{t}}{\tilde{T}} , \tag{2.51a}$$

$$u = \frac{\tilde{u}}{\tilde{Q}/\tilde{H}} , \qquad v = \frac{\tilde{v}}{\tilde{Q}/\tilde{H}} , \qquad p = \frac{\tilde{p}}{\rho_1 \tilde{Q}^2/\tilde{H}^2} . \tag{2.51b}$$

The scaling is based on channel height $\tilde{H} = \tilde{h}_1 + \tilde{h}_2$, which is fixed, and total flow rate $\tilde{Q} = \tilde{q}_1 + \tilde{q}_2$, chosen for instance at $t = 0$. Particularly, from the integral continuity equation, $\tilde{Q}$ is uniform, to be seen later.
As for the falling film configuration, by using the transformations (2.15) plus $v \longrightarrow \varepsilon v$, equations (2.2) take the form

$$\begin{cases} \partial_x u_k + \partial_y v_k = 0 \\ \varepsilon(\partial_t u_k + u_k \partial_x u_k + v_k \partial_y u_k) = -\varepsilon \partial_x p_k + \dfrac{1}{Fr}\sin\beta + \dfrac{1}{Re}\dfrac{m_k}{r_k}(\varepsilon^2 \partial_{xx} u_k + \partial_{yy} u_k) \\ \varepsilon^2(\partial_t v_k + u \partial_x v_k + v_k \partial_y v_k) = -\Big(\partial_y p_k + \dfrac{1}{Fr}\cos\beta\Big) + \dfrac{\varepsilon}{Re}\dfrac{m_k}{r_k}(\varepsilon^2 \partial_{xx} v_k + \partial_{yy} v_k) \end{cases} , \tag{2.52}$$

where Re and Fr, as well as the Weber number appearing in the following boundary conditions, are defined by means of the uniform film thickness and the total flow rate $\tilde{Q}$, as detailed in Chapter 4. Parameters m_k and r_k are defined as

$$m_k = \begin{cases} 1 , & k = 1 \\ \mu_2/\mu_1 , & k = 2 \end{cases} , \qquad r_k = \begin{cases} 1 , & k = 1 \\ \rho_2/\rho_1 , & k = 2 \end{cases} . \tag{2.53}$$

Since also at the top of the domain there are fixed walls, corresponding boundary conditions read

$$u_k = 0 , \qquad v_k = 0 , \tag{2.54}$$

whereas at the interface between the two layers one gets from (2.4-2.7)

$$[u] = 0 \ , \qquad [v] = 0 \ , \tag{2.55a}$$

$$Re(1+\varepsilon^2\partial_x^2 h)[p|_h] + 2(1-\varepsilon^2\partial_x^2 h)\varepsilon[m\partial_x u|_h] + 2\varepsilon\partial_x h[m(\partial_y u|_h + \varepsilon^2\partial_x v|_h)] = \frac{1}{We}\frac{\varepsilon^2\partial_{xx}h}{\sqrt{1+\varepsilon^2\partial_x^2 h}} \ , \tag{2.55b}$$

$$-4\varepsilon^2\partial_x h[m\partial_x u|_h] + (1-\varepsilon^2\partial_x^2 h)[m(\partial_y u|_h + \varepsilon^2\partial_x v|_h)] = 0 \ , \tag{2.55c}$$

$$\partial_t h + u_1|_h\partial_x h = v_1|_h \ . \tag{2.55d}$$

System (2.52-2.55) describes the coupled dynamics of a two-layer flow in a channel.

2.4.2 Tilley's non-linear equation

The analysis of Tilley *et al.* [84] follows Benney's approach, see section 2.3.3, and applies for the case of two-layer shallow flows. Indeed, with the aim to find a criterion for the flooding phenomenon, the authors have developed a non-linear evolution equation describing the motion of the liquid-gas interface. As for Benney's single-layer approach, this evolution equation is valid for small slopes, i.e. $\partial_x h = \mathcal{O}(\varepsilon)$. Starting from boundary-layer equations (2.52) accurate at $\mathcal{O}(\varepsilon)$, one can replace the Benney's gradient expansion (2.24) and subsequently develop the order zero and the order one. Particularly, the degree of freedom used in their procedure states that the total flow rate, given by the sum of liquid and gas flow rates, is constant in space and time and is entirely provided by zeroth-order velocities, according to

$$\int_0^H u^{(0)}\, dy = Q \ . \tag{2.56}$$

Specifically, condition (2.56) replaces the interfacial continuity of normal velocity. Once the first order film velocity has been obtained as function of h, Q and physical properties, one can find the non-linear evolution equation by means of the integral continuity equation of the film, namely

$$\partial_t h + \partial_x \int_0^h u\, dy = 0 \ , \tag{2.57}$$

where $u = u^{(0)} + u^{(1)}$ contains both leading and first-order contributions. Finally, the evolution equation for the liquid-gas interface takes the form

$$\partial_t h + A_1\partial_x h + \partial_x[(A_2+A_3)\partial_x h + A_4\partial_{3x}h] = 0 \ , \tag{2.58}$$

where coefficients A_1 and A_2 account for inertial effects, A_3 represents hydrostatic pressure and A_4 surface tension effects. Coefficients are not explicited here, and can be found in their paper.
By neglecting all terms related to the second phase, one recovers Benney's equation (2.28).

2.4.3 Dietze & Ruyer-Quil's modeling

Based on the film model of Ruyer-Quil & Manneville [70] described in section 2.3.5, Dietze & Ruyer-Quil [25] have provided a full reduced model to study wavy liquid films in interaction with a confined laminar gas flow. Two-phase boundary-layer equations (2.52) can be expressed up to $\mathcal{O}(\varepsilon^2)$; the authors have then neglected inertial terms of order $\mathcal{O}(\varepsilon^2)$, keeping only dissipative terms of this order of accuracy. This procedure is the generalized *simplified second-order model* for single phase developed by Ruyer-Quil & Manneville [70], who have shown as second-order dissipative terms allow to capture well non-linearities of

traveling waves.
Yet, by adopting the weighted residual approach, one can write

$$\int_0^h w_1(y) BL_1 \, dy + r \int_h^H w_2(y) BL_2 \, dy = 0 \ , \tag{2.59}$$

where w_k are weighted functions and BL_k the boundary layer equations (2.52) of each phase, simplified as described above. With a Benney's gradient expansion of the velocity field and further substitution into the residuals (2.59), all variables are enslaved to flow rates q_k and film thickness h. However, integrals $\int_0^h w_1(y)\partial_{yy}u_1 \, dy$ and $\int_h^H w_2(y)\partial_{yy}u_2 \, dy$ still contain first-order velocity corrections, which are unknown. Therefore, weighted functions w_k can be chosen in a way that these integrals vanish, with the help of gauge conditions

$$\int_0^h {u_1}^{(1)} \, dy = 0 \ , \qquad \int_h^H {u_2}^{(1)} \, dy = 0 \ . \tag{2.60}$$

This procedure can be seen as the extension to two phases of the Galerkin approach used by Ruyer-Quil & Manneville [70] for falling liquid films.

By using this full low-dimensional model, Dietze & Ruyer-Quil have analyzed two configurations: a horizontal pressure-driven two-layer flow and a gravity-driven liquid film in interaction with co- and counter-corrent gas flows. The authors have firstly shown how this full reduced model can capture the long-wave linear stability threshold, as well as celerity and growth rate of linear waves, in comparison with the two-phase Orr-Sommerfeld theory. In addition, in order to validate non-linear interfacial wave evolutions, they have performed DNS analysis by means of flow solvers Gerris (Popinet [64]) and OpenFOAM. Dietze & Ruyer-Quil have thus compared model calculations of film thickness, velocity and streamline patterns with those of DNS, showing a good agreement.
Further details of model equations, stability theory and comparison with DNS can be found in their paper.

2.5 Review of long-wave linear stability analysis

The present section describes the main results in long-wave linear stability analysis of thin liquid films, to be used in next chapters for comparison. Stability analysis of the linearized Navier-Stokes equations will be firstly presented. Then, a brief description of the stability analysis applied to integral models will be shown.
The linear stability analysis is built by performing an infinitesimal perturbation to the film thickness (and possibly the velocity field, or yet the average flow rate), such as

$$h = h_0 + \hat{h} e^{ik(x-ct)} \ , \tag{2.61}$$

where h_0 is the equilibrium thickness, i.e. Nusselt's for gravity-driven liquid films, and $\hat{h}$ the amplitude of the perturbation and $c = c_r + ic_i$ the wave speed. A more detailed description of linear stability analysis will be performed in Chapter 5 as part of this work.

2.5.1 Stability analysis of gravity-driven liquid films

One of the first results in linear stability analysis is due to Benjamin [7], who has studied the stability of a liquid film subject to gravity and flowing down an inclined plane at low Reynolds number, in the presence of surface tension. His work of 1957 was motivated by the existance of numerous experiments showing the absence of waves for vertical liquid films at very low Reynolds numbers (Grimley [33] and Binnie [10], mainly). On the contrary, Benjamin has proved that a vertical liquid film is always unstable to large wavelength

disturbances for all finite Reynolds numbers, either in presence or in absence of surface tension.
By linearization of the single-layer Navier-Stokes equations (2.2), one can find the Orr-Sommerfeld differential equation (Orr [62], Sommerfeld [80])

$$\Psi^{IV} - 2k^2\Psi^{II} + k^4\Psi = ikRe[(U_0 - c)(\Psi^{II} - k^2\Psi) - U_0^{II}\Psi] \ , \tag{2.62}$$

where Ψ is the stream function, and derivatives have to be seen with respect to y. Further details about the Orr-Sommerfeld equation with application to liquid films can be found in Charru [16] and Kalliadasis *et al.* [40].
The method proposed by Benjamin consists in looking for a power-series approximation of the stream function Ψ. This series is demonstrated to converge fast for small Reynolds numbers and allows to find the general expression of the wave speed as function of the wavenumber k and the Reynolds number Re. For long waves, i.e. $k << 1$, this expression can be simplified, and leads to

$$c_r = 3 \ , \tag{2.63a}$$

$$c_i = \Big(\frac{6}{5}Re - k^2\frac{Re}{We} - \cot\beta\Big)k \ . \tag{2.63b}$$

The instability of long waves is governed by $c_i > 0$; for very long waves, i.e. $k \to 0$ the condition becomes

$$Re > \frac{5}{6}\cot\beta \ . \tag{2.64}$$

This relation governing the instability of long waves for falling liquid films states that a vertical liquid film is always unstable for all finite Reynolds numbers, and surface tension does not play an important role to the threshold. When the liquid film flows down an inclined plane, the stability threshold depends on the inclination β of the plane only.

In a later work, Yih [95] has reviewed the stability of falling liquid films down an inclined plane. Particularly, Yih has treated the stability problem related to small wavenumbers, small Reynolds numbers and large wavenumbers. In the case of small wavenumbers, that is the situation of interest hereby, Yih has demonstrated that $k = 0$ is a correct approximation of large wavelengths. Indeed, by setting $k = 0$ in the Orr-Sommerfeld equation and simply solving $\Psi^{IV} = 0$ with corresponding boundary conditions, wave propagation c_r exactly coincides with the one provided by Benjamin, see (2.63a). Furthermore, if the wavenumber k departs from zero, stability threshold (2.64) can be easily found by an approximation of the Orr-Sommerfeld equation in first power of k. Hence, Yih's stability analysis for long waves provides the same results as Benjamin's, and uses a simpler procedure.

2.5.2 Stability analysis of gravity-driven films with constant shear stress

One can consider a liquid film falling down an inclined plane and sheared by a constant interfacial stress τ_i. For this configuration, firstly Smith & Davis [79] have provided the stability analysis of such a flow. Then, Smith [78] has given an explaination for the instability mechanism and provided a critical value of the Reynolds number, above which long waves amplify. Particularly, by applying a regular perturbation expansion for $k \to 0$, firstly introduced by Yih [95] for falling liquid films, Smith has calculated propagation velocities in presence of a non-zero interfacial stress, namely

$$c_r = 3(1 + \tau_i) \ , \tag{2.65}$$

$$c_i = \Big(\frac{2}{5}Re\ c_r - \cot\beta\Big)k \ . \tag{2.66}$$

From these, one can recover the critical Reynolds number by imposing $c_i = 0$, which reads

$$Re_{cr} = \frac{5\cot\beta}{6(1+\tau_i)} \ . \tag{2.67}$$

It is immediate to verify that for zero shear stress the critical Reynolds leads to the previously cited results of Benjamin and Yih, see (2.64).
However, it is worthwhile to mention that Smith's dimensionless velocity, with appropriate scaling, coincides with Nusselt's profile (2.9), and does not contain the shear stress. This is important to be pointed out for further comparisons throughout this work (see section 5.3.2).
With the same scaling as Smith, Samanta [73] has studied the stability of sheared-imposed liquid films by means of a low-dimensional model (based on the WRIBL method previously described, see section 2.3.5). Samanta has extended the work of Smith up to moderate Reynolds numbers. However, the critical Reynolds number coincides with the expression (2.67).

2.5.3 Stability analysis of two-layer flows

The earliest work on stability of long waves at the interface of a two-layer flow is due to Yih. In his work of 1967 [96], Yih has studied the instability of two superposed layers, with the aim to show that viscosity stratification can drive to the instability of the interface. Yih has demonstrated that the instability of plane Couette-Poiseuille flows is obtained for any Reynolds number in presence of viscosity difference between the two fluids.
By using the above-mentioned regular perturbation expansion of his stability work for falling liquid films, Yih has derived wave-propagation speeds in the case of moving and steady upper boundaries. Here, only the case of steady boundary will be shown, with the intention to compare this result with those of the present work. In order to highlight the effect due to the viscosity stratification, one can consider a plane Poiseuille whose fluids have same thickness and density. At the first approximation, i.e. imposing $k = 0$ in the Orr-Sommerfeld differential equation (2.62) for both fluids, one obtains

$$c_r = \frac{3 + 10m + 3m^2}{m^2 + 14m + 1} \ . \tag{2.68}$$

On the other hand, by studying the second approximation, i.e. $\mathcal{O}(k)$ for small wavenumbers, but different from zero, the imaginary part of the wave speed reads

$$c_i = \frac{kRe}{1680}\frac{(m+1)(m-1)^2(7m^6 - 226m^5 + 4169m^4 + 6436m^3 + 4169m^2 - 226m + 7)}{(1 + 14m + m^2)^3 m^2} \ . \tag{2.69}$$

Finally, by showing the evolution of c_i with respect to m, one can state the plane Poiseuille flow is always unstable to large wavelengths when thickness and density are the same for both fluids.

2.5.4 Stability analysis of the integral models for gravity-driven films

As already mentioned, the stability analysis applied to depth-integrated equations has been initiated by Benney [9] in his work of 1966. Starting from the evolution equation for the film thickness (2.28), Benney has linearized the problem by imposing infinitesimal perturbations to the equilibrium film thickness, according to $h = h_0 + h_p$, where subscript p refers to the perturbation. By doing so, Benney has found the complex wave speed $c_r + ic_i$ in agreement with the results of Benjamin and Yih, expressions (2.63).

However, a detailed stability analysis of integral models has been performed by Ruyer-Quil & Manneville [69] in their paper of 1998. The authors have linearized the system (2.39) of averaged equations around Nusselt's solution. By performing then an asymptotic expansion of the wave speed c in the limit $k << 1$, i.e. large wavelengths, the authors have obtained

$$c = 3 + 3i\Big(\frac{2}{5}Re - \frac{1}{3}\cot\beta\Big)k + 3\Big(\frac{22}{45}\cot\beta Re - \frac{44}{75}Re^2\Big)k^2 + O(k^3)\ . \tag{2.70}$$

This expression derives from the model (2.39) accurate at order one, it is thus exact up to $O(k)$. In order to quantify the error at $O(k^2)$, the authors have compared wave speed (2.70) with the exact asymptotic expansion of the Orr-Sommerfeld equation, namely

$$c = 3 + 3i\Big(\frac{2}{5}Re - \frac{1}{3}\cot\beta\Big)k + 3\Big(-1 + \frac{10}{21}\cot\beta Re - \frac{4}{7}Re^2\Big)k^2 + O(k^3)\ . \tag{2.71}$$

Finally, Ruyer-Quil & Manneville have shown that the wave speed corresponding to their model accurate at order two (not discussed here, being beyond the purpose of this work) coincides with the equation (2.71) up to $O(k^3)$.

In conclusion, Table 2.3 shows dimensionless numbers of mentioned works and the comparison with the definitions of this work.
In the end, a review of the most relevant works about thin liquid film modeling and stability analysis has been presented in this chapter. In the following, these works will be referred to for comparisons and validations.
Next chapter deals with the development of a low-dimensional model for the dynamics of thin liquid films subject to given shear stress and pressure as function of space and time, and possibly the gravity force.

Table 2.3: Key-lecture and dimensionless numbers of different cited works. Re_0, Fr_0, We_0 indicate dimensionless scaling adopted here, namely expressions (2.17-2.18) and (2.21). In the work of Benney, Gjevik, Ruyer-Quil & Manneville, and Yih, the Weber is actually defined as We^{-1}.

source	$\tilde{U}/\tilde{U}_0$	Re/Re_0	Fr/Fr_0	We/We_0
Benney	3/2	3/2	not defined	Fr_0^{-1}
Gjevik	3/2	3/2	not defined	$Fr_0^{-1}\sin\beta$
Shkadov	1	3	1	1
Ruyer-Quil & Manneville (98-00)	$(\nu g\sin\beta)^{1/3}\tilde{U}_0^{-1}$	$\nu^2(g\sin\beta)^{-1}$	not defined	$\tilde{h}_0/9(\nu^{-2}g\sin\beta)^{5/3}$
Luchini & Charru	1	1	$(Fr_0\cos\beta)^{-1/2}$	—
Benjamin	3/2	1	9/4	9/4
Yih (1963)	1	1	Fr_0^{-1}	1
Smith	3	3	not defined	$Fr_0^{-1}\sin\beta$
this work	1	1	1	1

3 Development of consistent shallow water equations for thin liquid films

In this chapter, depth-integrated equations are developed with the aim to model the dynamics of thin liquid films driven by gravity, and by pressure and shear stress given at the surface as function of space and time. Therefore, the main difference with the gravity-driven film models presented in the previous chapter is the insertion of interfacial pressure and shear stress. As already mentioned, the great advantage of low-dimensional models compared to the full Navier-Stokes equations is the computational cost required by the simulations, and represents in this work one of the main motivations for developing integrated models of thin liquid films.
Hence, depth-integrated equations can be obtained by integration of the Navier-Stokes equations over the film thickness. However, thanks to the thinness of the liquid film, the cross-stream velocity is much smaller than the stream-wise velocity, and a long-wave assumption can be performed after the integration. As a matter of fact, this assumption drives to the boundary-layer equations, which are a simpler set of equations than the full Navier-Stokes. Therefore, the shallow water equations can be alternatively obtained by directly integrating the boundary-layer equations.
Nevertheless, these integrated equations need closure laws, and those are guaranteed by an asymptotic expansion of the boundary-layer equations up to the first order in respect of the shallow water parameter ε, which represents the ratio of the film thickness to the characteristic length of the stream-wise direction. This scale is usually chosen as the wavelength of the waves at the surface of the film. The methodology used in this chapter in deriving the above mentioned shallow water equations is sketched in the scheme of the Figure 3.1.

3.1 The governing equations

With reference to Figure 3.2, a liquid film flowing down an inclined plane and subject to given pressure and shear stress is considered. Pressure and shear stress are given at the interface and are general functions of space and time, namely $\tilde{p}_i(\tilde{x},\tilde{t})$ and $\tilde{\tau}_i(\tilde{x},\tilde{t})$. These can express, for instance, the action of a gas flow over the liquid film. For such a flow, the

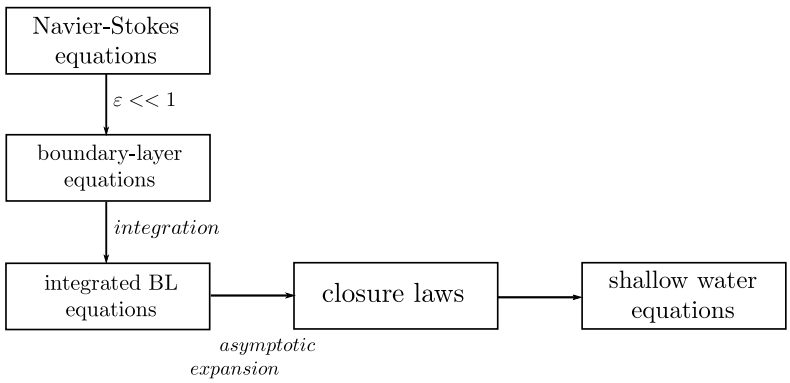

Figure 3.1: Road map of Chapter 3.

2D incompressible Navier-Stokes equations read

$$\begin{cases} \partial_x \tilde{u} + \partial_y \tilde{v} = 0 \\ \partial_t \tilde{u} + \tilde{u}\partial_x \tilde{u} + \tilde{v}\partial_y \tilde{u} = -\dfrac{1}{\rho}\partial_x \tilde{p} + g\sin\beta + \nu\nabla^2 \tilde{u} \\ \partial_t \tilde{v} + \tilde{u}\partial_x \tilde{v} + \tilde{v}\partial_y \tilde{v} = -\dfrac{1}{\rho}\partial_y \tilde{p} - g\cos\beta + \nu\nabla^2 \tilde{v} \end{cases} , \tag{3.1}$$

where the tilde designates dimensional variables. Then, $\tilde{u}$ and $\tilde{v}$ are the streamwise ($\tilde{x}$) and cross-stream ($\tilde{y}$) velocity components, $\tilde{p}$ the pressure, g the gravity force, and $\nu = \mu/\rho$ the kinematic viscosity of the liquid.
These equations must be completed with boundary conditions at the wall and at the surface. At the bottom, where $\tilde{y} = 0$, the no-slip condition reads

$$\tilde{u} = 0 \ , \qquad \tilde{v} = 0 \ . \tag{3.2}$$

At the interface instead, where $\tilde{y} = \tilde{h}$, boundary conditions state the continuity of tangential and normal stresses, namely

$$\tilde{\mathbf{t}} \cdot \tilde{\mathbf{T}}^{(\tilde{n})} = \tilde{\tau}_i(\tilde{x}, \tilde{t}) \ , \tag{3.3}$$

$$\tilde{\mathbf{n}} \cdot \tilde{\mathbf{T}}^{(\tilde{n})} = \tilde{p}_i(\tilde{x}, \tilde{t}) + \gamma\nabla \cdot \tilde{\mathbf{n}} \ , \tag{3.4}$$

where $\tilde{\mathbf{T}}^{(\tilde{n})} = \tilde{\Sigma} \cdot \tilde{\mathbf{n}}$ is the stress vector at the interface with normal $\tilde{\mathbf{n}}$, while $\tilde{\Sigma}$ is the stress tensor, and γ the surface tension. Yet, the interfacial shear stress $\tilde{\tau}_i(\tilde{x}, \tilde{t})$ and the interfacial pressure $\tilde{p}_i(\tilde{x}, \tilde{t})$ are given functions of space and time. As in Chapter 2, tangent and normal unit vectors to the interface are defined as

$$\tilde{\mathbf{n}} = \frac{1}{\sqrt{1 + \partial_x^2 \tilde{h}}} \begin{Bmatrix} -\partial_x \tilde{h} \\ 1 \end{Bmatrix} \ , \tag{3.5a}$$

$$\tilde{\mathbf{t}} = \frac{1}{\sqrt{1 + \partial_x^2 \tilde{h}}} \begin{Bmatrix} 1 \\ \partial_x \tilde{h} \end{Bmatrix} \ . \tag{3.5b}$$

The conditions at the interface are completed by the kinematic condition, which imposes the interface to be a material line, and reads

$$\partial_t \tilde{h} + \tilde{u}|_h \partial_x \tilde{h} = \tilde{v}|_h \ . \tag{3.6}$$

The system of equations (3.1) with the corresponding boundary conditions (3.2-3.6) entirely describes the dynamics of the liquid film of Figure 3.2.

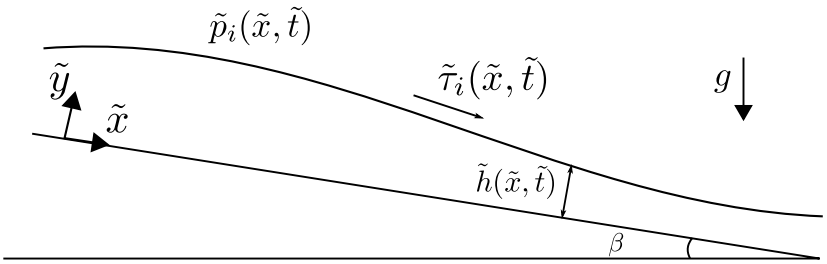

Figure 3.2: Sketch of a liquid film subject to interfacial shear stress and pressure, and the gravity.

3.1.1 The dimensionless equations

As detailed before in section 2.3.2, waves that develop on the surface of a liquid film at moderate Re can be considered long compared to the film thickness. This suggests the introduction of the parameter $\varepsilon = k\tilde{h}_0/2\pi$, where $\tilde{h}_0$ is the uniform dimensional thickness, which measures the smallness of the film thickness with reference to the wavelength of the perturbation. In the non-linear regime, where the linear theory loses its meaning, ε scales space and time derivatives $\partial_{x,t}$. Therefore, the long-wave theory applied to thin liquid films imposes small, i.e. $\mathcal{O}(\varepsilon)$, space-time thickness variations, without any assumptions about the amplitude of the thickness itself.

In order to identify the dominant terms of the system (3.1), one can work with dimensionless equations by means of dimensionless variables representative of the liquid flow, such as

$$x = \frac{\tilde{x}}{\tilde{h}_0} \ , \qquad y = \frac{\tilde{y}}{\tilde{h}_0} \ , \qquad t = \frac{\tilde{t}}{\tilde{T}} \ , \tag{3.7a}$$

$$u = \frac{\tilde{u}}{\tilde{U}_0} \ , \qquad v = \frac{\tilde{v}}{\tilde{U}_0} \ , \qquad p = \frac{\tilde{p}}{\rho\tilde{U}_0^2} \ , \qquad \tau_i = \frac{\tilde{\tau}_i}{\tilde{U}_0\mu/\tilde{h}_0} \ . \tag{3.7b}$$

Here, $\tilde{h}_0$, $\tilde{U}_0$ and $\tilde{T} = \tilde{h}_0/\tilde{U}_0$ still refer to the uniform flow (alternatively, other quantities might be chosen as characteristic scales).
In line with the scaling, dimensionless equations can be found by considering the trasformations

$$\partial_{x,t} \longrightarrow \varepsilon\partial_{x,t} \ , \qquad \partial_{xx} \longrightarrow \varepsilon^2\partial_{xx} \ , \qquad v \longrightarrow \varepsilon v \ , \tag{3.8}$$

where the smallness of the cross-stream velocity v derives by the continuity equation $\varepsilon\partial_x u + \partial_y v = 0$, as explained in section 2.3.2. Indeed, the procedure drives exactly to the dimensionless equations (2.16). However, the assumption of long waves on thin liquid films can be also seen as the boundary-layer approximations, i.e. boundary layer smaller than the scale of the body, which brings to the boundary-layer equations, that are a simpler system of equations in comparison with the full Navier-Stokes (Anderson [4]). As a matter of fact, for $\varepsilon << 1$ the equations (2.16) up to order one can be seen as the boundary-layer equations. Therefore, these read

$$\begin{cases} \partial_x u + \partial_y v = 0 \\ \partial_t u + u\partial_x u + v\partial_y u = -\partial_x p + \dfrac{1}{Fr}\sin\beta + \dfrac{1}{Re}\partial_{yy} u \\ 0 = -\dfrac{1}{Fr}\cos\beta - \partial_y p \end{cases} \ , \tag{3.9}$$

where the parameter ε has been omitted. By doing so, one assumes that $\partial_{x,t} \sim \varepsilon$. The corresponding boundary conditions at the wall, where $y = 0$, are

$$u = 0 \ , \qquad v = 0 \ . \tag{3.10}$$

At the interface, where $y = h$, the continuity of tangential and normal stresses, as well as the kinematic condition, read respectively

$$p|_h = p_i(x,t) - \frac{1}{We}\partial_{xx}h \ , \tag{3.11a}$$

$$\partial_y u|_h = \tau_i(x,t) \ , \tag{3.11b}$$

$$\partial_t h + u|_h \partial_x h = v|_h \ . \tag{3.11c}$$

Boundary conditions (3.11a) and (3.11b) derive from the gravity-driven ones (2.20b) and (2.20c) with the addition of the interfacial pressure $p_i(x,t)$ (by means of the transformation $p|_h \longrightarrow p|_h - p_i$) and the shear stress $\tau_i(x,t)$, respectively. The dimensionless numbers Reynolds, Froude and Weber are defined as section 2.3.2, namely

$$Re = \frac{\tilde{U}_0 \tilde{h}_0}{\nu} \ , \qquad Fr = \frac{\tilde{U}_0^2}{g\tilde{h}_0} \ , \qquad We = \frac{\rho \tilde{U}_0^2 \tilde{h}_0}{\gamma} \ . \tag{3.12}$$

The system of equations (3.9) completed by boundary conditions (3.10) and (3.11) represents the full dimensionless boundary-layer system of the problem of Figure 3.2.

3.2 Integration over the film thickness

The importance of integrating the equations allows to reduce the degrees of freedom of the system and to pass from unknowns u, v and p to *averaged* ones h and q. However, before integrating the boundary-layer equations (3.9), it is suitable to replace the y-momentum equation into the x-momentum through the pressure p. This can be achieved by integrating the third of the (3.9) with the boundary condition (3.11a), which leads to the pressure field

$$p(x,y,t) = -\int_0^x G(x)\,dx - \frac{1}{We}\partial_{xx}h + \frac{1}{Fr}\cos\beta(h-y) \ . \tag{3.13}$$

With reference to the equation (3.11a), $-G(x)$ is the interfacial pressure space-derivative $\partial_x p_i$ (alternatively, one can choose the pressure gradient at the bottom). Thus, boundary-layer equations (3.9) reduce to a system of two equations, which reads

$$\begin{cases} \partial_x u + \partial_y v = 0 \\ \partial_t u + u\partial_x u + v\partial_y u = G - \dfrac{\cos\beta}{Fr}\,\partial_x h + \dfrac{\sin\beta}{Fr} + \dfrac{1}{Re}\partial_{yy}u + \dfrac{1}{We}\partial_{3x}h \end{cases} . \tag{3.14}$$

As shown in the Appendix A, by the help of the Leibniz's integration rule and the boundary condition (3.11c), one finds

$$\partial_t h + \partial_x q = 0 \ , \tag{3.15a}$$

$$\partial_t q + \partial_x\Big(\int_0^h u^2\,dy\Big) + \frac{\cos\beta}{Fr}h\partial_x h = \frac{1}{Re}\Big(\Lambda h + \tau_i - \partial_y u|_0\Big) + \frac{1}{We}h\partial_{3x}h \ , \tag{3.15b}$$

where $\tau_w = \partial_y u|_0$ is the wall shear stress, whereas

$$\Lambda = \frac{Re}{Fr}\sin\beta + Re\ G(x) \tag{3.16}$$

takes into account the stream-wise component of gravity and the pressure gradient, which both contribute to destabilize the liquid film.

These equations are enslaved to film thickness h and y-averaged flow rate q (alternatively, y-averaged stream-wise velocity), with the exception of the integral of squared velocity and the wall shear stress. Hence, integrated boundary-layer equations (3.15) need

closure models. In order to close these equations, one can provide an asymptotic expansion of the boundary-layer equations (3.14) with respect to the small parameter ε, and thus obtain velocity and stress fields. The replacement of the velocity profile into the integral and the wall shear stress thus permits to close the equations. Nevertheless, in Chapter 2 a description of different closure models has been already presented. In particular, a parabolic velocity profile does not assure to capture the correct stability threshold, as demonstrated for Shkadov's model (2.33) on gravity-driven films. The velocity profile must then contain the correction at order one. However, an analysis of the order of magnitude in the equations (3.14) shows that inertial, i.e. the left-hand side, and surface tension terms, as well as the term $\partial_x h$, are smaller than the others. This can be achieved from the consideration that $\partial_{x,t} \sim \varepsilon$. This can be also seen in the integral equations (3.15), where all terms multiplying $1/Re$ are greater than the others. Indeed, greater terms satisfy the equilibrium condition, for which inertia is neglected. As a consequence, when considering the integral equation (3.15b) at order one, it appears that only the wall shear stress requires a closure of the first order. On the other hand, the integral of the squared velocity, being already $\mathcal{O}(\varepsilon)$, simply needs the leading order, since a correction of order one in ε would provide terms of order two, namely

$$\varepsilon\partial_x\Big(\int_0^h u^2\,dy\Big) \longrightarrow \varepsilon\partial_x\Big(\int_0^h {u^{(0)}}^2\,dy\Big) + \mathcal{O}(\varepsilon^2)\ , \tag{3.17a}$$

$$\frac{1}{Re}\partial_y u|_0 \longrightarrow \frac{1}{Re}\partial_y\Big[u^{(0)} + \varepsilon u^{(1)}\Big]\Big|_0 + \mathcal{O}(\varepsilon^2)\ . \tag{3.17b}$$

3.3 The asymptotic expansion

The asymptotic expansion allows to explicit the velocity field, to be subsequently used as closure of the integrated equations (3.15). In order to perform the asymptotic expansion of the boundary-layer equations (3.14), the velocity field has to be expanded as Benney's (2.24), namely

$$u(x,y,t) = u^{(0)}(x,y,t) + u^{(1)}(x,y,t) + \dots\ , \tag{3.18a}$$

$$v(x,y,t) = v^{(1)}(x,y,t) + v^{(2)}(x,y,t)\dots\ , \tag{3.18b}$$

where the superscript (1) denotes smaller quantities (order ε) than (0)'s. Yet, $v^{(0)} = 0$ because of the continuity equation of the system (3.14), as the boundary-layer theory states. Furthermore, it is ordinary for thin liquid films to suppose $Re = \mathcal{O}(1)$, $Fr = \mathcal{O}(1)$ and $We = \mathcal{O}(\varepsilon^2)$. Particularly, conditions $Re = \mathcal{O}(1)$ and $Fr = \mathcal{O}(1)$ are assumed with the aim to simplify the derivation of the dimensionless equations. Indeed it can be relaxed: looking back at the x-momentum Navier-Stokes equation (2.16) accurate at order one, namely

$$\varepsilon Re(\partial_t u + u\partial_x u + v\partial_y u) = -\varepsilon Re\partial_x p + \frac{Re}{Fr}\sin\beta + \partial_{yy} u\ , \tag{3.19}$$

it is noteworthy that the real conditions to be respected are $\varepsilon Re << 1$ and $Fr \sim Re$.

3.3.1 Expansion at order zero

At the leading order, following the expansion (3.18), the system of equations (3.14) becomes

$$\begin{cases} \partial_x u^{(0)} + \partial_y v^{(1)} = 0 \\ \dfrac{1}{Re}\Lambda + \dfrac{1}{Re}\partial_{yy} u^{(0)} = 0 \end{cases}\ . \tag{3.20}$$

The boundary conditions at the wall read

$$u^{(0)}|_0 = 0 \ , \qquad v^{(1)}|_0 = 0 \ , \tag{3.21}$$

whereas at the interface

$$\partial_y u^{(0)}|_h = \tau_i \ . \tag{3.22}$$

Upon integrating twice the second of (3.20), and by imposing the conditions (3.22) and subsequently the (3.21), one obtains the leading order velocity profile

$$u^{(0)}(x,y,t) = \tau_i y + \Lambda(hy - \frac{y^2}{2}) \ , \tag{3.23}$$

typical of a Poiseuille-Couette flow. The corresponding flow rate reads

$$q^{(0)} = \frac{1}{3}\Lambda h^3 + \frac{1}{2}\tau_i h^2 \ . \tag{3.24}$$

The order zero can be seen as the local equilibrium of the flow. Indeed, for uniform flow, the leading order coincides with the solution of the system (3.9). The wall shear stress instead is

$$\tau_w^{(0)} = 3\frac{q^{(0)}}{h^2} - \frac{1}{2}\tau_i \ . \tag{3.25}$$

In addition, the cross-stream velocity component is given by the continuity equation, as

$$v^{(1)} = Re \ \partial_x G \frac{y^3}{6} - (\partial_x \tau_i + \Lambda \partial_x h + Re \ \partial_x G \ h)\frac{y^2}{2} \ . \tag{3.26}$$

3.3.2 Expansion at order one

At the first order in ε, the system of equations (3.14) reads

$$\begin{cases} \partial_x u^{(1)} + \partial_y v^{(2)} = 0 \\ \partial_t u^{(0)} + u^{(0)}\partial_x u^{(0)} + v^{(1)}\partial_y u^{(0)} = \dfrac{1}{We}\partial_{3x} h - \dfrac{\cos\beta}{Fr}\partial_x h + \dfrac{1}{Re}\partial_{yy} u^{(1)} \end{cases} . \tag{3.27}$$

Given to the quasi-static nature of the problem and the magnitude of the We number, this system exhibits inertial and capillary terms compared to the leading order (3.20). This can be also recovered by analysing the order of each term in (3.19). The first-order boundary conditions at the wall read

$$u^{(1)}|_0 = 0 \ , \qquad v^{(2)}|_0 = 0 \ , \tag{3.28}$$

whereas at the interface

$$\partial_y u^{(1)}|_h = 0 \ . \tag{3.29a}$$

The first-order velocity profile of the liquid film can be obtained similarly to the order zero, to give

$$\begin{aligned} u_1^{(1)} = {} & \frac{Re}{24}(2h-y)(-y^2+2hy+4h^2)y\left[(\Lambda h + \tau_i)\Lambda \ \partial_x h - Re \ \partial_t G\right] \\ & + \frac{Re^2}{360}\left[\Lambda(y^5+24h^5+15h^2y^3-6hy^4-20h^3y^2) + 3\tau_i(-10h^4+5hy^3-2y^4)\right] y \ \partial_x G \\ & + \frac{Re}{24}\left[(4h^3-y^3)\tau_i + (2h^3+y^3-2hy^2)\Lambda h\right] y \ \partial_x \tau_i - \frac{Re}{6}(3h^2-y^2)y \ \partial_t \tau_i \\ & + \frac{Re}{2}\Big(\frac{1}{We}\partial_{3x} h - \frac{\cos\beta}{Fr}\partial_x h\Big)(2h-y)y \ . \end{aligned} \tag{3.30}$$

The corresponding flow rate is

$$\begin{aligned} q^{(1)} = {} & \frac{2}{15}(\Lambda h + \tau_i)\Lambda h^5 Re\ \partial_x h + \frac{Re}{3}h^3\Big(\frac{1}{We}\partial_{3x}h - \frac{\cos\beta}{Fr}\partial_x h\Big) \\ & + \frac{Re^2}{2520}h^6(64\Lambda h - 91\tau_i)\partial_x G + \frac{1}{240}(7\Lambda h - 18\tau_i)h^5 Re\ \partial_x \tau_i \\ & - \frac{2}{15}h^5 Re^2\ \partial_t G - \frac{5}{24}Re\ h^4\ \partial_t \tau_i\ . \end{aligned} \tag{3.31}$$

The first-order wall shear stress ${\tau_w}^{(1)} = \partial_y u^{(1)}|_0$ instead reads

$$\begin{aligned} {\tau_w}^{(1)} = {} & \frac{1}{3}\Lambda h^3 Re(\Lambda h + \tau_i)\ \partial_x h + \frac{1}{60}Re^2\ h^4(4\Lambda h - 5\tau_i)\ \partial_x G \\ & + \frac{1}{12}Re\ h^3(\Lambda h - 2\tau_i)\ \partial_x \tau_i - \frac{1}{3}Re^2 h^3 \partial_t G - \frac{1}{2}Re\ h^2 \partial_t \tau_i\ . \end{aligned} \tag{3.32}$$

As expected, the first-order velocity, flow rate and wall shear stress depend on the spatio-temporal derivatives of the interfacial shear stress and pressure gradient, as well as the thickness h, and thus their magnitude is of order ε.

3.4 Closure of the integrated equations

Once velocity and stress fields have been fully computed, system (3.15) of integrated boundary-layer equations can be finally closed. The closure procedure follows expressions (3.17), for which only the wall shear stress term needs a closure law at order one, whereas the integral of squared velocity requires simply the order zero. Therefore, by using velocity profiles (3.23) and (3.30), the closure of the equations (3.15) leads to

$$\partial_t h + \partial_x q = 0\ , \tag{3.33a}$$

$$\begin{aligned} \partial_t q + \partial_x\Big[\frac{6}{5}\frac{q^2}{h} + \frac{1}{60}h^3\tau_i(\Lambda h + 2\tau_i)\Big] + \frac{\cos\beta}{Fr}h\partial_x h \\ = \frac{1}{Re}\Big[\Lambda h + \tau_i - \tau_w\Big] + \frac{1}{We}h\ \partial_{3x}h\ , \end{aligned} \tag{3.33b}$$

where $\tau_w = {\tau_w}^{(0)} + {\tau_w}^{(1)}$, previously found. One can notice that the closure of the integral of squared velocity (3.17a) follows the gravity-driven film modeling (see for example Shkadov equations (2.33) or Luchini & Charru's (2.48a)), according to which $\int_0^h u^2\,dy = 6/5q^2h^{-1}$. However, in the current analysis on sheared liquid films, the presence of the shear stress τ_i involves an additional term when expressing (3.17a) by means of the flow rate (3.24). Furthermore, since the leading-order wall shear stress is expressed as function of $q^{(0)}$ and τ_i, see (3.25), following Ruyer-Quil & Manneville [69] one can represent the full wall shear stress τ_w as a dependency of $[q^{(0)} + q^{(1)}]$ and τ_i, namely

$$\tau_w = \frac{3q}{h^2} - \frac{\tau_i}{2} + {\tau_w}^{(c)}\ , \tag{3.34}$$

where ${\tau_w}^{(c)}$ represents the correction to the wall shear stress due to the first-order analysis. This reads

$$\begin{aligned} {\tau_w}^{(c)} = {} & {\tau_w}^{(1)} - \frac{3q^{(1)}}{h^2} \\ = {} & -\frac{1}{15}\Lambda h^3 Re(\Lambda h + \tau_i)\ \partial_x h - \frac{1}{840}Re^2 h^4(8\Lambda h - 21\tau_i)\ \partial_x G \\ & - \frac{1}{240}h^3 Re(\Lambda h - 14\tau_i)\ \partial_x \tau_i + \frac{1}{15}Re^2 h^3\ \partial_t G + \frac{1}{8}h^2 Re\ \partial_t \tau_i\ . \end{aligned} \tag{3.35}$$

Finally, (3.33-3.35) are a closed set of equations describing, with a precision $\mathcal{O}(\varepsilon)$, the dynamics of a liquid film subject to given interfacial pressure and shear stress, and possibly to the gravity force. This system thus represents the integrated model accurate at first order with unknowns h and q.

3.5 Further considerations on shallow water equations

This section deals with further considerations about the first-order model of integrated equations (3.33-3.35). Firstly, in the limit of falling liquid films in a passive atmosphere, i.e. $G = \tau_i = 0$ and thus $\Lambda = Re/Fr \sin\beta$, gradient expansion and closure method performed here can be validated by comparison with previous works cited in Chapter 2. In this configuration, the first-order flow rate (3.31) becomes

$$q^{(1)} = \frac{1}{3}h^3\Big[\frac{2}{5}\Lambda^2 h^3\partial_x h - \frac{\cos\beta}{Fr}\partial_x h + \frac{1}{We}\partial_{3x}h\Big] \ , \tag{3.36}$$

which agrees with the one provided by Ruyer-Quil & Manneville [69], equation (2.41). Then, by developing $\partial_t h + \partial_x[q^{(0)} + q^{(1)}] = 0$, one finds exactly Benney's evolution equation (2.28), which is also the same result obtained by Ruyer-Quil & Manneville. As explained in section 2.3.3, Benney has found that this evolution equation correctly predicts stability threshold on long waves. Therefore, this is a first validation of the consistency of the model (3.33-3.35).
In a second step, it is possible to validate the correction of the wall shear stress (3.35). In the limit of falling liquid films, this turns into

$${\tau_w}^{(c)} = -\frac{Re}{15}\Lambda^2 h^4\partial_x h \ , \tag{3.37}$$

which coincides with those provided by Ruyer-Quil & Manneville (2.40) and by Luchini & Charru (2.50). Furthermore, correction (3.37) depends on $\partial_x h$: in the case of sinusoidal perturbations, this quantity is in quadrature with the free surface h. This implies that between the zeroth- and the first-order wall shear stresses there exists a phase lead, as pointed out by Luchini & Charru [51] for a perturbed bottom.

As further consideration on depth-integrated equations (3.33-3.35), it is worthwhile to recall that this model will be implemented in a finite-volume numerical code, i.e. the code SWANS, to be shown in Chapter 6. From a computational point of view, it is preferable to gather all terms in $\partial_x h$ and write them in conservative form, with the purpose to handle them with an approximate Riemann solver.

The wall shear stress correction ${\tau_w}^{(c)}$, equation (3.35), contains spatio-temporal derivatives which are given functions of space and time, with the exception of the thickness space-derivative $\partial_x h$. Therefore, it is preferable to transfer it to the left-hand side of the (3.33b), after expressing its conservative form, namely

$$\begin{aligned} &-\frac{1}{15}\Lambda h^3 Re(\Lambda h + \tau_i)\ \partial_x h = -\partial_x\Big(\frac{1}{75}Re\Lambda^2 h^5 - \frac{1}{60}Re\Lambda\tau_i h^4\Big) \\ &+\frac{2}{75}Re^2\Lambda h^5\partial_x G + \frac{1}{60}Re^2\tau_i h^4\partial_x G + \frac{1}{60}Re\Lambda h^4\partial_x\tau_i \end{aligned} \tag{3.38}$$

It is clear that since the shear stress and pressure gradient depend on x and t, this conservative form provides other terms to be kept in ${\tau_w}^{(c)}$. Table 3.1 shows how coefficients of ${\tau_w}^{(c)}$ are modified after extracting the conservative form of $\partial_x h$, to create a new term T, to be written later. The sum of each row gives the results in the last line.

Furthermore, in the applications investigated at ONERA there are often shifted and rotating walls, such as the rotating components of the turbomachinery. In this and similar configurations, it is suitable to dispose of a long-wave model which satisfies the Galilean invariance principle.

Table 3.1: Coefficients of the corrective term ${\tau_w}^{(c)}$ and the viscous term T, the conservative part of $\partial_x h$ being moved to the momentum flux of the shallow water equations. Summing lines one and two gives the third.

	$\partial_x h$		$\partial_x G$		$\partial_x \tau_i$		$\partial_t G$	$\partial_t \tau_i$
	G	τ_i	G	τ_i	G	τ_i		
${\tau_w}^{(c)}$	$-1/15$	$-1/15$	$-1/105$	$1/40$	$-1/240$	$14/240$	$1/15$	$1/8$
eq. (3.38)	$1/15$	$1/15$	$2/75$	$1/60$	$1/60$	0	0	0
T	0	0	$3/175$	$1/24$	$1/80$	$14/240$	$1/15$	$1/8$

3.5.1 The Galilean invariance principle

The Galilean invariance principle states that the Navier-Stokes equations are unaltered in all inertial frames, but not the boundary conditions. For example, one can consider a fix reference frame and a moving one with a constant velocity V. Since the shallow water equations are derived from the Navier-Stokes equations, it is convenient for several industrial applications to provide the condition to extend the Galilean invariant principle also to the shallow water equations. By doing this, the left-hand side of the equations (3.33b) can be written as

$$\partial_t(hU) + \partial_x(\mathcal{F}(h, U, x, t)) \ , \tag{3.39}$$

where U is the y-averaged film velocity and $\mathcal{F}(h, U, x, t) = \alpha h U^2 + P(h, x, t)$ designates the momentum flux of the shallow water equations, α being constant. By applying the Galilean-coordinate transformation (only in this paragraph the prime denotes variables in the moving reference frame)

$$U' = U - V \ , \qquad t' = t \ , \tag{3.40a}$$

$$x' = x - Vt \ , \qquad h' = h \ , \tag{3.40b}$$

to the shallow water left-hand side (3.39), one obtains

$$\begin{aligned} \partial_t q + \partial_x(\mathcal{F}(h, U, x, t)) &= \partial_{t'}(h'(U' + V)) - V\partial_{x'}(h'(U' + V)) + \partial_{x'}(\mathcal{F}(h', U' + V, x', t')) \\ &= \partial_{t'} q' + V\partial_{t'} h' - V\partial_{x'} q' - V^2 \partial_{x'} h' + \partial_{x'}(\mathcal{F}(h', U' + V, x', t')) \\ &= \partial_{t'} q' + \partial_{x'}\Big((\mathcal{F}(h', U' + V, x', t')) - 2Vh'U' - V^2 h'\Big) \ . \end{aligned} \tag{3.41}$$

Here the continuity equation (3.33a) has been also used. Finally, one can find out that by expressing the momentum flux as $\mathcal{F}(h, U, x, t) = \alpha h U^2 + P(h, x, t)$, the shallow water equations turn to be Galilean invariant if $\alpha = 1$. This means that in the momentum equation (3.33b), the coefficient of q^2/h has to be equal to one. Therefore, $q^2/(5h)$ can be converted in three terms function of h only by replacing the leading-order flow rate (3.24), namely

$$\frac{1}{5}\frac{q^2}{h} = \frac{1}{45}\Lambda^2 h^5 + \frac{1}{15}\Lambda\tau_i h^4 + \frac{1}{20}\tau_i^2 h^3 \ . \tag{3.42}$$

Table 3.2 shows how coefficients of the momentum flux change by satisfying the Galilean invariance principle. Yet, as for Table 3.1, the sum of each row provides the coefficients of the bottom line, and the coefficients of P, to be defined in next section.

3.5.2 The final system of shallow water equations

Once the closure technique and the Galilean invariance principle have been described, one can write the final form of shallow water equations, which will be mostly used in this work,

Table 3.2: Coefficients of the momentum flux of (3.33b), the fulfillment of the Galilean invariance principle and the term P, the conservative part of $\partial_x h$ being moved to the momentum flux of the shallow water equations. Summing lines from one to three gives the forth.

	q^2/h	h^5	h^4	h^3	h^2
flux of (3.33b)	6/5	0	1/60	1/30	1/2
eq. (3.38)	0	−1/75	−1/60	0	0
Galilean invariance	−1/5	1/45	1/15	1/20	0
P	1	2/225	1/15	1/12	1/2

namely

$$\partial_t h + \partial_x q = 0 \ , \tag{3.43a}$$

$$\partial_t q + \partial_x\Big(\frac{q^2}{h} + P\Big) = \frac{1}{Re}\Big[\Lambda h - \frac{3q}{h^2} + \frac{3}{2}\tau_i - T\Big] + \frac{1}{We} h\ \partial_{3x} h \ , \tag{3.43b}$$

where P is the "pressure" part (in analogy with the Navier-Stokes equations) of the shallow water momentum flux and T derives from ${\tau_w}^{(c)}$, see (3.35), without the conservative part of the term $\partial_x h$, being transferred to P:

$$P = \frac{2}{225}\Lambda^2 h^5 + \frac{1}{15}\Lambda\tau_i h^4 + \frac{1}{12}{\tau_i}^2 h^3 + \frac{1}{2}\frac{h^2}{Fr}\cos\beta \ , \tag{3.44}$$

$$\begin{aligned} T =& \frac{1}{240} h^3 Re(3\Lambda h + 14\tau_i)\ \partial_x \tau_i \\ &+ Re^2 h^4\Big(\frac{3}{175}\Lambda h + \frac{1}{24}\tau_i\Big)\ \partial_x G \\ &+ \frac{1}{15} Re^2 h^3\ \partial_t G + \frac{1}{8} h^2 Re\ \partial_t \tau_i \ , \end{aligned} \tag{3.45}$$

which resume all steps previously described. Equations (3.43) completed with the definitions of P and T are depth-averaged equations and have the same properties of consistency as the system (3.33-3.35). Indeed, as shown for both models of Ruyer-Quil & Manneville, equations (2.39) and (2.44), by appropriate manipulation of several terms of the shallow water equations, different consistent model can be obtained, which differ for other properties.

In conclusion, a set of shallow water equations has been found in this chapter, with the aim to describe the dynamics of thin liquid films subject to pressure and shear stress given at the interface, and possibly to the gravity force. The closure technique has been validated by comparing the correction of the wall shear stress with the one avalaible in literature in the case of falling films driven by gravity.
The natural extension of this chapter consists in considering a gas flow over the liquid film, in a way that interfacial shear stress and pressure are not arbitrary anymore, since those represent the action of a gas flow. Therefore, a set of shallow water equations will be derived in the next chapter for a confined film-gas interacting system.

4 Development of consistent shallow water equations for confined two-layer flows

A set of depth-integrated equations capturing the dynamics of thin liquid films sheared by a confined laminar gas flow is derived in this chapter. Unlike the previous analysis, the liquid film interacts with a gas flow, and interfacial shear stress and pressure exerted on the film are those provided by the coupled interaction. The purpose of such a development consists in supplying a validation support for the performed computational investigations, to be presented in Chapter 6.
In similarity with the single-layer model described in Chapter 3, two-layer shallow water equations can be obtained by integration of the Navier-Stokes equations over each layers. Since the waves observed in such a two-layer flow are much longer than the channel height, and thus much longer than film and gas thicknesses, one can assume the validity of the long-wave theory. However, as pointed out in Chapter 3, long-wave theory drives to the boundary-layer equations. As a consequence, shallow water equations are obtained by direct integration of the boundary-layer equations. However, after integration, depth-averaged equations require closure laws. Therefore, a Benney's asymptotic expansion of the boundary-layer equations allows providing velocity and stress fields and closing the system. Indeed, unlike the previous chapter, the asymptotic expansion also provides the interfacial stress fields. The small parameter ε on which the expansion is based represents the ratio between the channel height and the wavelength of the perturbation. Given that the flow is strongly confined, the assumption of small ε is widely justified. The methodology in deriving the two-layer shallow water equations is sketched in the scheme of Figure 4.1 and follows the steps of Chapter 3, to which it will be made reference hereby.

4.1 The governing equations

A laminar gas in interaction with a wavy liquid film flowing into a confined horizontal channel is considered, as sketched in Figure 4.2. There are two different ways to study such a problem. One consists in fixing the volumetric flow rate of each fluids and leave the pressure gradient free, and find it by the solution (Tilley *et al.* [84]). The second is to fix the pressure drop of the channel and one flow rate, the other being obtained by the solution (Alba *et al.* [1]). Here the total flow rate is imposed while the pressure gradient is left free, in line with the work of Tilley *et al.* [84] described in Chapter 2. Navier-Stokes equations

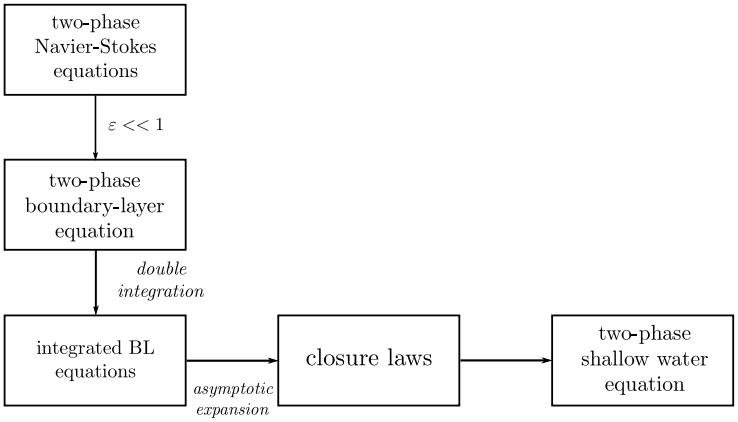

Figure 4.1: Road map of Chapter 4.

of such a problem are the same as system (2.2) with $\beta = 0$, namely

$$\begin{cases} \partial_x \tilde{u}_k + \partial_y \tilde{v}_k = 0 \\ \partial_t \tilde{u}_k + \tilde{u}_k \partial_x \tilde{u}_k + \tilde{v}_k \partial_y \tilde{u}_k = -\dfrac{1}{\rho_k} \partial_x \tilde{p}_k + \nu_k \partial_{yy} \tilde{u}_k \\ \partial_t \tilde{v}_k + \tilde{u}_k \partial_x \tilde{v}_k + \tilde{v}_k \partial_y \tilde{v}_k = -\dfrac{1}{\rho_k} \partial_y \tilde{p}_k - g + \nu_k \partial_{yy} \tilde{v}_k \end{cases} , \tag{4.1}$$

where the subscript k is the index identifying the phase, $k = 1$ for the liquid and $k = 2$ for the gas. Velocities must satisfy no-slip boundary conditions at bottom and top walls, where $\tilde{y} = 0$ and $\tilde{y} = \tilde{H}$, respectively, namely

$$\tilde{u}_k = 0 \ , \qquad \tilde{v}_k = 0 \ . \tag{4.2}$$

On the other hand, velocities match at the film-gas interface $\tilde{y} = \tilde{h}$, to give

$$[\tilde{u}] = 0 \ , \qquad [\tilde{v}] = 0 \ , \tag{4.3}$$

where $[\cdot] = (\cdot)_2 - (\cdot)_1$ identifies the jump across the interface. The continuity of stresses provides instead

$$[\tilde{\mathbf{t}} \cdot \tilde{\mathbf{T}}^{(\tilde{n})}] = 0 \ , \tag{4.4}$$

$$[\tilde{\mathbf{n}} \cdot \tilde{\mathbf{T}}^{(\tilde{n})}] = \gamma \nabla \cdot \tilde{\mathbf{n}} \ , \tag{4.5}$$

whose definitions have been given in Chapter 3, see (3.4) and (3.5). Finally, the kinematic condition at the interface reads

$$\partial_t \tilde{h} + \tilde{u}_1|_h \partial_x \tilde{h} = \tilde{v}_1|_h \ . \tag{4.6}$$

System of equations (4.1) completed by boundary conditions (4.2-4.6) represents the fundamental tool to study the dynamics of the film-gas interacting system of Figure 4.2.

4.1.1 The dimensionless equations

Working with dimensionless equations permits to underline the dominant terms and remove those that are negligible. Denoting the channel height with $\tilde{H}$, dimensionless variables are defined as

$$x = \frac{\tilde{x}}{\tilde{H}} \ , \qquad y = \frac{\tilde{y}}{\tilde{H}} \ , \qquad t = \frac{\tilde{t}}{\tilde{T}} \ , \tag{4.7a}$$

$$u = \frac{\tilde{u}}{\tilde{Q}/\tilde{H}} \ , \qquad v = \frac{\tilde{v}}{\tilde{Q}/\tilde{H}} \ , \qquad p = \frac{\tilde{p}}{\rho_1 \tilde{Q}^2/\tilde{H}^2} \ , \tag{4.7b}$$

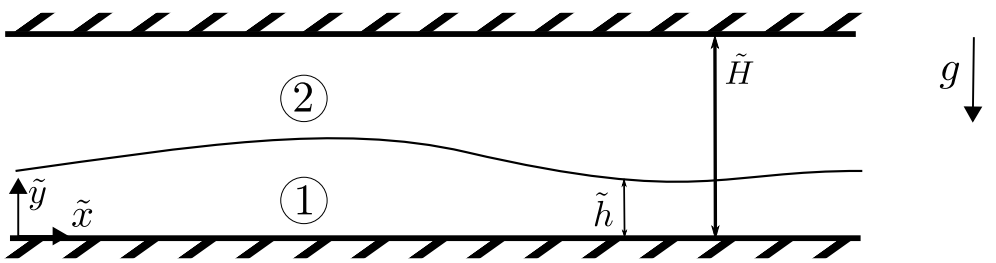

Figure 4.2: Two-layer pressure-driven flow in a strongly confined channel: indices 1 and 2 identify liquid and gas phases, respectively.

provided that the total flow rate $\tilde{Q}$ is kept unaltered. In addition to the ratio of dynamic viscosities $m = \mu_2/\mu_1$, another fundamental parameter of the problem is the ratio of densities $r = \rho_2/\rho_1$.

In order to derive the dimensionless equations, one can use transformations (3.8) and follow the same procedure as the single-layer configuration. Yet, waves encountered in confined channels are much longer than the total height. This justifies a long-wave approach, based on the introduction of the small parameter $\varepsilon = k\tilde{H}/2\pi$, measuring the smallness of space and time derivatives. Indeed, in the non-linear regime $\varepsilon \sim \partial_{x,t}$. The long-wave theory simplifies the Navier-Stokes equations, leading to the boundary-layer equations, which in turn coincide with the equations accurate at order one in ε, namely

$$\begin{cases} \partial_x u_k + \partial_y v_k = 0 \\ \partial_t u_k + u_k \partial_x u_k + v_k \partial_y u_k = -\dfrac{1}{r_k}\partial_x p_k + \dfrac{1}{Re}\dfrac{m_k}{r_k}\partial_{yy} u_k \\ 0 = -\dfrac{1}{Fr} - \dfrac{1}{r_k}\partial_y p_k \end{cases} . \tag{4.8}$$

where m_k and r_k are defined as

$$m_k = \begin{cases} 1 , & k = 1 \\ m , & k = 2 \end{cases} , \qquad r_k = \begin{cases} 1 , & k = 1 \\ r , & k = 2 \end{cases} . \tag{4.9}$$

No-slip boundary conditions at bottom ($y = 0$) and top ($y = H$) walls read

$$u_k = 0 , \qquad v_k = 0 . \tag{4.10}$$

At the interface, where $y = h$, velocities match as

$$[u] = 0 , \qquad [v] = 0 , \tag{4.11}$$

while the continuity of tangential and normal stresses, as well as the kinematic condition read

$$[p|_h] = \frac{1}{We}\partial_{xx} h , \tag{4.12a}$$

$$[m\partial_y u|_h] = 0 , \tag{4.12b}$$

$$\partial_t h + u_1|_h \partial_x h = v_1|_h . \tag{4.12c}$$

Reynolds, Froude and Weber numbers are defined respectively as

$$Re = \frac{\tilde{Q}}{\nu_1} , \qquad Fr = \frac{\tilde{Q}^2}{g\tilde{h}_0^3} , \qquad We = \frac{\rho_1 \tilde{Q}^2}{\gamma \tilde{h}_0} , \tag{4.13}$$

where $\tilde{h}_0$ is the uniform film thickness. System (4.8) with corresponding boundary conditions (4.10-4.12) can be seen as the problem to which perform the asymptotic expansion.

4.2 Integration over the film-gas thickness

Similarly to the procedure of Chapter 3, system of boundary-layer equations (4.8) can be reduced to two equations through the replacement of the pressure p_k into the x-momentum equations of each phase. Hence, by integrating the y-momentum equations for each phase, and by using the boundary condition (4.12a) one obtains

$$p_1(x,y,t) = -\int_0^x G(x)\,dx - \frac{1}{We}\partial_{xx}h + \frac{1}{Fr}(h-y)\ , \tag{4.14}$$

$$p_2(x,y,t) = -\int_0^x G(x)\,dx + \frac{r}{Fr}(h-y)\ , \tag{4.15}$$

where $-G(x)$ is the local space-derivative of the pressure exerted by the gas at the interface, to be written later. Finally, boundary-layer equations (4.8) reduce to

$$\begin{cases} \partial_x u_k + \partial_y v_k = 0 \\ \partial_t u_k + u_k\partial_x u_k + v_k\partial_y u_k = \dfrac{G}{r_k} - \dfrac{1}{Fr}\partial_x h + \dfrac{\delta_k}{r_k}\dfrac{1}{We}\partial_{3x}h + \dfrac{1}{Re}\dfrac{m_k}{r_k}\partial_{yy}u_k \end{cases}\ , \tag{4.16}$$

where δ_k is the Kronecker function, namely

$$\delta_k = \begin{cases} 1\ , & k=1 \\ 0\ , & k=2 \end{cases}\ . \tag{4.17}$$

By employing the Leibniz's integration rule and by following the steps of the Appendix A for a single-phase system, the integration of the boundary-layer equations (4.16) over each respective thickness leads to

$$\partial_t h + \partial_x q_1 = 0\ , \tag{4.18a}$$

$$\partial_t q_1 + \partial_x\Big(\int_0^h u_1^2\,dy\Big) + \frac{1}{Fr}h\partial_x h = Gh + \frac{1}{Re}\Big(\tau_i - \partial_y u_1|_0\Big) + \frac{1}{We}h\partial_{3x}h\ , \tag{4.18b}$$

$$\partial_t h - \partial_x q_2 = 0\ , \tag{4.18c}$$

$$\partial_t q_2 + \partial_x\Big(\int_h^H u_2^2\,dy\Big) + \frac{1}{Fr}h\partial_x h = \frac{G}{r}h + \frac{1}{Re}\frac{1}{r}\Big(\partial_y u_2|_H - \tau_i\Big)\ , \tag{4.18d}$$

where $\tau_{w1} = \partial_y u_1|_0$ is the wall shear stress exerted by the liquid at the bottom and $\tau_{w2} = m\partial_y u_2|_0$ is the wall shear stress exerted by the gas at the top wall of the channel. Furthermore, τ_i is the interfacial shear stress exerted by the gas on the film flow. The total flow rate Q is conserved into the domain because the flow is incompressible and the walls are rigid, thus Q depends on time only. Indeed, the sum of continuity equations (4.18a) and (4.18c) provides $\partial_x Q = 0$.

Thanks to the integration over each thickness, these equations are enslaved to film thickness h and y-averaged flow rates q_1 and q_2 (alternatively, y-averaged stream-wise velocities). However, similarly to the single-layer model of Chapter 3, integrals of squared velocity and wall shear stresses need closure models. Therefore, a Benney's gradient expansion at $\mathcal{O}(\varepsilon)$ can be performed. However, an analysis of the expressions (3.17), still valid here for the two-layer system, shows that only wall shear stresses require a closure of the first order, whereas integrals of the squared velocity simply needs the leading order closure.

4.3 The asymptotic expansion

The asymptotic expansion of the system of equations (4.16) provides velocity and stress fields at order zero and one, to be adopted to close the system (4.18) of integrated equations.

Furthermore, stress and pressure gradient fields obtained by the asymptotic expansion will be used as validation for the numerical technique adopted in this work, to see in Chapter 6. Following Benney [9], velocity, stress and pressure gradient fields are expanded as

$$u_k(x,y,t) = u_k^{(0)}(x,y,t) + u_k^{(1)}(x,y,t) + \dots \ , \tag{4.19a}$$

$$v_k(x,y,t) = v_k^{(1)}(x,y,t) + v_k^{(2)}(x,y,t) + \dots \ , \tag{4.19b}$$

$$\tau_i(x,t) = \tau_i^{(0)}(x,t) + \tau_i^{(1)}(x,t) + \dots \ , \tag{4.19c}$$

$$G(x,t) = G^{(0)}(x,t) + G^{(1)}(x,t) + \dots \ , \tag{4.19d}$$

where the order (0) defines quantities $\mathcal{O}(1)$, while the order (1) is $\mathcal{O}(\varepsilon)$, and so on. Although the pressure gradient is defined by means of the x-derivative, i.e. $G = -\partial_x p_i$, the presence of the order-zero pressure gradient in (4.19d) points out that the pressure gradient is the cause of the movement of the flow and is supplied by the choice of $\rho_1 U^2$ as pressure unit, see (4.7). Indeed, this approach is justified given that in a classical single-layer Poiseuille flow the pressure gradient is the only quantity changing along the stream-wise direction. With reference to Chapter 3, the omission of the zero-th order y-velocity in (4.19b) derives from the analysis of the continuity equation $\partial_x u_k + \partial_y v_k = 0$. Furthermore, the assumption that

$$Re = \mathcal{O}(1) \ , \qquad We = \mathcal{O}(\varepsilon^{-2}) \ , \qquad Fr = \mathcal{O}(1) \ , \tag{4.20}$$

can be relaxed to $\varepsilon Re << 1$ and $Fr \sim Re$.

4.3.1 Expansion at order zero

At the leading order, system (4.16) becomes

$$\begin{cases} \partial_x {u_k}^{(0)} + \partial_y {v_k}^{(1)} = 0 \\ \dfrac{G^{(0)}}{r_k} + \dfrac{1}{Re}\dfrac{m_k}{r_k}\partial_{yy} {u_k}^{(0)} = 0 \end{cases} , \tag{4.21}$$

completed by no-slip boundary conditions at bottom and top walls, namely

$${u_k}^{(0)} = 0 \ , \qquad {v_k}^{(1)} = 0 \ , \tag{4.22}$$

and continuity of velocities and stresses at the interface, as

$$[u^{(0)}] = 0 \ , \tag{4.23a}$$

$$[v^{(1)}] = 0 \ , \tag{4.23b}$$

$$[m\partial_y u^{(0)}|_h] = 0 \ . \tag{4.23c}$$

By using the boundary condition (4.23c), the integration of the second of (4.21) over each layer gives

$$u_{k,y}^{(0)} = \frac{\tau_i^{(0)}}{m_k} + \frac{Re}{m_k} G^{(0)}(h-y) \ . \tag{4.24}$$

A further integration of (4.24), with the conditions in the left of (4.22) provides the Couette-Poiseuille velocity profiles of liquid and gas phases. The former is given by

$$u_1^{(0)}(x,y,t) = \tau_i^{(0)} y + Re \ G^{(0)}(h - \frac{y}{2})y \ . \tag{4.25}$$

The latter, instead, reads

$$u_2^{(0)}(x,y,t) = -\frac{\tau_i^{(0)}}{m}(H-y) - \frac{Re}{m} G^{(0)}\Big(h(H-y) - \frac{1}{2}(H^2 - y^2)\Big) \ . \tag{4.26}$$

Corresponding wall shear stresses read

$$\tau_{1w}^{(0)} = u_{1,y}^{(0)}|_0 = \frac{3q_1^{(0)}}{h^2} - \frac{1}{2}\tau_i^{(0)} \ , \tag{4.27}$$

and

$$\tau_{2w}^{(0)} = m u_{2,y}^{(0)}|_1 = -\frac{3q_2^{(0)} m}{(H-h)^2} - \frac{1}{2}\tau_i^{(0)} \ . \tag{4.28}$$

However, the quantities $\tau_i^{(0)}$ and $G^{(0)}$ are still unknown. The leading order interfacial shear stress can be obtained by imposing the condition (4.23a), which leads to

$$\tau_i^{(0)} = -\frac{Re\ G^{(0)}}{2}\frac{mh^2 - (H-h)^2}{mh + (H-h)} \ , \tag{4.29}$$

where $H-h$ is the thickness of the gas layer. This expression is function of the film thickness h and the height of the channel H, the ratio of viscosities m, as well as the zeroth-order pressure gradient $G^{(0)}$, which is still unknown. It can be determined by using the boundary condition of cross-stream velocities (4.23b). However, due to the continuity equation of (4.21), this leads to a differential equation for the pressure gradient, whose resolution is suitable to be avoided.
Therefore, in line with the work of Tilley *et al.* [84] one can express the pressure gradient as function of h and Q only, without going through the above-mentioned differential equation. Without loss of generality one can impose

$$q_1^{(1)} + q_2^{(1)} = \int_0^h u_1^{(1)}\, dy + \int_h^H u_2^{(1)}\, dy = 0 \ , \tag{4.30}$$

that is, the flow rate is entirely provided by zeroth-order velocities, and both the first-order flow rates vanish. As described above, the total flow rate is hereby assumed constant into the channel, namely

$$Q = q_1^{(0)}(x,t) + q_2^{(0)}(x,t) = const. \ , \tag{4.31}$$

with

$$q_1^{(0)} = \int_0^h u_1^{(0)}\, dy \ , \qquad\qquad q_2^{(0)} = \int_h^H u_2^{(0)}\, dy \ . \tag{4.32}$$

The expression of the flow rates for both phases leads to

$$q_1^{(0)}(x,t) = \tau_i^{(0)}\frac{h^2}{2} + Re\ G^{(0)}\frac{h^3}{3} \ , \tag{4.33}$$

$$q_2^{(0)}(x,t) = -\tau_i^{(0)}\frac{(H-h)^2}{2m} + Re\ G^{(0)}\frac{(H-h)^3}{3m} \ . \tag{4.34}$$

Finally, the pressure gradient $G^{(0)}$ can be determined through the condition (4.31), once the interfacial shear stress (4.29) is replaced into (4.33) and (4.34). One obtains

$$G^{(0)} = \frac{12Q}{Re}\frac{m(mh + H - h)}{H^4 + (m-1)^2h^4 + 2h(m-1)(2h^2H - 3hH^2 + 2H^3)} \ . \tag{4.35}$$

When replacing this expression into the (4.29), the interfacial shear stress exerted by the gas over the film flow reads

$$\tau_i^{(0)} = -\frac{6Qm[-H^2 + (m-1)h^2 + 2hH]}{H^4 + (m-1)^2h^4 + 2h(m-1)(2h^2H - 3hH^2 + 2H^3)} \ , \tag{4.36}$$

and depends on Q, h, H and m only. At this stage, the liquid velocity profile can be written as

$$u_1^{(0)}(x,y,t) = \frac{6Qmy\big[(m-1)h^2 - y(m-1)h + H(H-y)\big]}{1+(m-1)^2h^4 + 2h(m-1)(2h^2-3h+2)} \ , \tag{4.37}$$

whereas the gas velocity profile as

$$u_2^{(0)}(x,y,t) = \frac{6Q(y-H)\big[(m-1)h^2 - (y+H)(m-1)h - yH\big]}{1+(m-1)^2h^4 + 2h(m-1)(2h^2-3h+2)} \ . \tag{4.38}$$

Yet, order zero of the gradient expansion coincides with the local equilibrium of the two-layer flow. Noteworthy is that the expansion at order zero would be the same also if the total flow rate Q were not constant. In this case, it suffices to replace Q with $Q(t)$ into the fields (4.35-4.38), and $\tilde{Q}$ with $\tilde{Q}(t=0)$ into the scaling (4.7) and the dimensionless numbers (4.13).

4.3.2 Expansion at order one

At order one, the system of equations (4.16) turns into

$$\begin{cases} \partial_x {u_k}^{(1)} + \partial_y {v_k}^{(2)} = 0 \\ \partial_t {u_k}^{(0)} + {u_k}^{(0)}\partial_x {u_k}^{(0)} + {v_k}^{(1)}\partial_y {u_k}^{(0)} = \dfrac{G^{(1)}}{r_k} - \dfrac{\partial_x h}{Fr} + \dfrac{\delta_k}{r_k}\dfrac{\partial_{3x}h}{We} + \dfrac{m_k}{r_k}\dfrac{\partial_{yy}{u_k}^{(1)}}{Re} \end{cases} \ , \tag{4.39}$$

As for single-layer first-order development of Chapter 3, at $\mathcal{O}(\varepsilon)$ inertial and capillarity terms appear, due to the quasi-static nature of the problem and the magnitude of the We number (4.20). Indeed, in the equation (4.16) terms in G and $\partial_{yy}u_k$ are bigger than the others and give the equilibrium. Corresponding boundary conditions at both walls read

$${u_k}^{(1)} = 0 \ , \qquad\qquad {v_k}^{(2)} = 0 \ , \tag{4.40}$$

whereas at the film-gas interface

$$[u^{(1)}] = 0 \ , \tag{4.41a}$$

$$[v^{(2)}] = 0 \ , \tag{4.41b}$$

$$[m\partial_y u^{(1)}|_h] = 0 \ . \tag{4.41c}$$

Upon integrating twice the x-momentum equation of (4.39) through the boundary conditions (4.41c) and the left of (4.40), one obtains the first-order velocity profiles of both phases, still functions of the unknowns ${\tau_i}^{(1)}$ and $G^{(1)}$. Similarly as the order zero, the first-order interfacial shear stress can be determined by means of the boundary condition (4.41a) of continuity of velocity across the interface. On the other hand, first-order pressure gradient can be found by imposing the condition (4.30), stating that first-order flow rates vanish. Velocity, interfacial and wall stress, and pressure gradient fields are given in the Appendix B as function of the thickness h and the height of the channel H, as well as the ratio of viscosities m.

4.4 Closure of the two-layer integrated equations

Once those fields have been entirely expressed, integrated equations (4.18) can be finally closed. Yet, integrals of squared velocity are closed simply using leading-order velocity profiles (4.25) and (4.26). On the other hand, being greater than other terms, wall shear

stresses $\partial_y u_1|_0$ and $m\partial_y u_2|_0$ require also first-order velocity profiles. Therefore, the closure technique leads to

$$\partial_t h + \partial_x q_1 = 0 \ , \tag{4.42a}$$

$$\partial_t q_1 + \partial_x \Big[\frac{6}{5}\frac{q_1^2}{h} + \Pi_1\Big] = Gh + \frac{1}{Re}\Big(\tau_i - \tau_{w1}\Big) + \frac{1}{We}h\partial_{3x}h \ , \tag{4.42b}$$

$$\partial_t h - \partial_x q_2 = 0 \ , \tag{4.42c}$$

$$\partial_t q_2 + \partial_x \Big[\frac{6}{5}\frac{q_2^2}{H-h} + \Pi_2\Big] = \frac{G}{r}h + \frac{1}{Re}\frac{1}{r}\Big(\tau_{w2} - \tau_i\Big) \ , \tag{4.42d}$$

where $q_k = q_k^{(0)}$ for $k = 1, 2$ (since $q_k^{(1)} = 0$), and the "pressure" contributions Π_1 and Π_2 of the momentum flux derive by the integral of each velocity profile and are defined as

$$\Pi_1 = \frac{1}{30}{\tau_i^{(0)}}^2 h^3 + \frac{1}{60}Re(G^{(0)}\tau_i^{(0)}h^4) + \frac{h^2}{2}\frac{1}{Fr} \ , \tag{4.43a}$$

$$\Pi_2 = -\frac{1}{60m^2}\tau_i^{(0)}\Big(Re\ G^{(0)}(H-h)^4 - 2\tau_i^{(0)}(H-h)^3\Big) + \frac{h^2}{2}\frac{1}{Fr} \ . \tag{4.43b}$$

As described in Chapter 3, the closure of the integral of squared velocity makes use of the flow rate definitions (4.33-4.34), in analogy with the gravity-driven film modeling, according to which $\int_0^h u^2\, dy = 6/5 q^2 h^{-1}$.
Furthermore, since the total flow rate Q is given, only one between the momentum equations (4.42b) and (4.42d) is independent. Therefore, system (4.42a-4.42c) and (4.43a), or alternatively the system (4.42a,4.42c,4.42d) plus (4.43b), represents the consistent two-layer model of depth-integrated equations accurate at order one, for confined channel when the total flow rate Q is constant. The coupling between the two phases is guaranteed by the longitudinal pressure gradient $-G$ and the interfacial stress τ_i, defined in (4.35), (B.5), (4.36) and (B.3), respectively for the orders zero and one. These are the effects provided by the gas on the liquid. The wall shear stresses τ_{wk} are defined in (4.27) and (4.28) at order zero and in the Appendix B at order one, equations (B.6) and (B.7).

4.5 Discussions

The form of equations (4.42) is the same as the single-layer integrated equations (3.33) of Chapter 3. In this scenario, the gas flowing above the film manifests itself with the presence of an interfacial shear stress and pressure which depend on geometrical and physical properties of the problem, instead of being simple given functions of space and time. The equations and the asymptotic expansion at order one result also more complicated and longer than the single-layer analysis. In line with Luchini & Charru [50], who have shown that for gravity-driven and pressure-driven films the kinetic-energy equation allows to get rid of the computation at $\mathcal{O}(\varepsilon)$, one can thus attempt to extend their work to film-gas systems. On the contrary, the presence of the interfacial shear stress τ_i prevents to use kinetic-energy equations of both phases to avoid the asymptotic expansion of order one.

As further consideration, in analogy with Chapter 3, one can express the wall shear stresses τ_{wk} as function of the flow rates q_k and the interfacial shear stress τ_i. This can be achieved with the aim to be consistent with the expansion at order zero (see equations (4.27) and (4.28)). As a consequence, a correction for both the wall shear stresses has to be considered in line with the expression (3.35) of Chapter 3. Since here ${q_k}^{(1)} = 0$, these corrections are given by

$${\tau_{wk}}^{(c)} = {\tau_{wk}}^{(1)} + \frac{{\tau_i}^{(1)}}{2} \ . \tag{4.44}$$

In addition, one recalls the Galilean invariance principle already described in section 3.5.1 for the single-layer long-wave model: it has been demonstrated that the coefficient of $\partial_x(q^2h^{-1})$ into the integrated momentum equation must be 1 in order to get the invariance. By applying these two items, equations (4.42b) and (4.42d) turn into

$$\partial_t q_1 + \partial_x\Big[\frac{q_1^2}{h} + \hat{\Pi}_1\Big] = Gh + \frac{1}{Re}\Big(\frac{3}{2}\tau_i - 3\frac{q_1}{h^2} - {\tau_{w1}}^{(c)}\Big) + \frac{1}{We}h\partial_{3x}h \ , \tag{4.45a}$$

$$\partial_t q_2 + \partial_x\Big[\frac{q_2^2}{H-h} + \hat{\Pi}_2\Big] = \frac{G}{r}h + \frac{1}{Re}\frac{1}{r}\Big({\tau_{w2}}^{(c)} + 3\frac{q_2}{(H-h)^2} - \frac{3}{2}\tau_i\Big) \ , \tag{4.45b}$$

where $\hat{\Pi}_1 = \Pi_1 + 1/5q_1^2h^{-1}$ and $\hat{\Pi}_2 = \Pi_2 + 1/5q_2^2(H-h)^{-1}$, keeping in mind that ${q_k}^{(1)} = 0$ so that q_1 and q_2 are taken from (4.33-4.34).
Finally, equations (4.44,4.45a), or alternatively (4.44,4.45b), in addition to the continuity equations (4.42a) and (4.42c), are a set of closed depth-integrated equations accurate at order one in the description of two-layer channel flows, and which fulfill the Galilean invariance principle. Pressure gradient $-G$, shear stress τ_i and wall shear stresses τ_{wk} are defined as above.

In conclusion, a set of two-layer shallow water equations has been derived in the present chapter, in order to describe the coupled dynamics of film-gas systems flowing in a confined domain. The asymptotic expansion is necessary to close these equations and follows the work of Tilley et al. [84], being based on a costant total flow rate, rather than imposed pressure gradient. The performed asymptotic expansion and the resulting stress fields will be used in Chapter 7 to validate the developed numerical methods and the coupling approach. Furthermore, the closure technique is demonstrated to be in line with the validated methodology of the Chapter 3.
Finally, next chapter deals with an analysis of linear stability applied to both the single-layer and two-layer shallow water equations. This will allow for validating these low-dimensional models in the linear regime and then the performed numerical methods.

5 Linear stability analysis of one- and two-layer shallow water equations

In the present chapter, the linear stability analysis of the previously developed one- and two-layer shallow water equations is provided. The linear stability analysis serves as validation of those reduced models, since it allows to compare the dispersion relations and the resulting wave velocities with those available in the literature and presented in Chapter 2. In addition, it gives the threshold condition which drives the transition from stable to unstable regimes. As further motivation, the wave velocities found by means of the stability analysis will be used in Chapter 7 to validate the linear regime of the shallow water numerical discretization.
In this chapter it is also discussed the role of the interfacial shear stress in the stability of thin liquid films. Particularly, in the simplified configuration of a constant shear stress applied on the surface of a falling film, it will be investigated whether it behaves as stabilizing or destabilizing factor.
As sketched in the scheme of Figure 5.1, the dispersion relation can be found from the linearized form of the shallow water equations. Thickness and flow rate have to be decomposed in equilibrium and perturbed states, where the latter is a sinusoidal perturbation of small amplitude, and replaced into these linearized equations. Finally, solutions of the dispersion relation provide the wave velocities. The analysis starts with the study of the long-wave model derived in Chapter 3 and then moves to the two-layer model developed in Chapter 4.

5.1 The base state

In order to perform the stability analysis of the one- and two-layer long-wave models develop in the previous chapters, the base state is described for each configuration. The base states are presented in dimensional units, keeping in mind that the stability analysis is studied with dimensionless variables.

5.1.1 Film subject to interfacial pressure and shear stress

Given the Navier-Stokes equations (3.1) and the corresponding boundary conditions, a base state solution can be found when derivatives $\partial_{x,t}$ vanish. The base state thus represents the equilibrium condition of the film, i.e. the state when the interface is flat and y is the only independent variable, see Figure 5.2. The equilibrium state is relevant because it stands

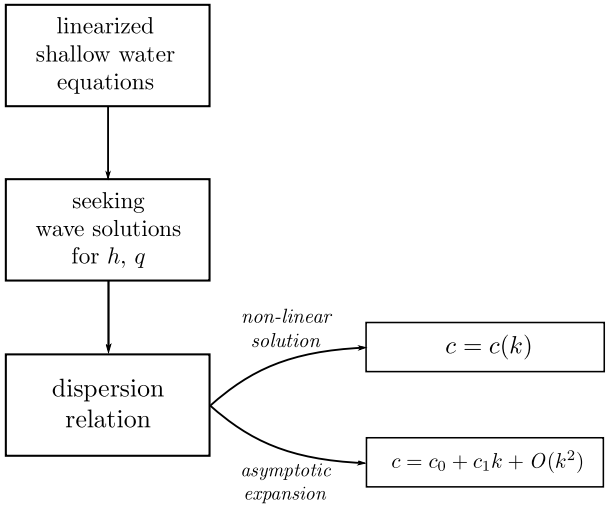

Figure 5.1: Road map of Chapter 5.

for the base state to perturb in the following linear stability analysis. Hence, velocity and pressure fields read

$$\tilde{u}_0(\tilde{y}) = \frac{1}{2\nu}(g\sin\beta - \rho^{-1}\partial_x\tilde{p}_i)(2\tilde{h}_0 - \tilde{y})\tilde{y} + \frac{\tilde{\tau}_i}{\mu}\tilde{y} \ , \qquad \tilde{v}_0 = 0 \ , \tag{5.1}$$

$$\tilde{p}_0(\tilde{y}) = \tilde{p}_i + \rho g\cos\beta(\tilde{h}_0 - \tilde{y}) \ , \tag{5.2}$$

where the subscript 0 refers to uniform flow conditions. The velocity profile $\tilde{u}_0$ has been found by performing a double integration of the x-momentum equation of the system (3.1), and by the definition $\tilde{\tau}_i = \mu\partial_y\tilde{u}|_h$. It has to be noted that, although given functions of space and time, interfacial shear stress and pressure gradient are considered to vary slowly. The corresponding flow rate is given by the integral of $\tilde{u}_0$ across the flat thickness of the film, and leads to

$$\tilde{q}_0 = \frac{g\sin\beta - \rho^{-1}\partial_x\tilde{p}_i}{3\nu}\tilde{h}_0^3 + \frac{\tilde{\tau}_i}{2\mu}\tilde{h}_0^2 \ , \tag{5.3}$$

The mean longitudinal film velocity $\tilde{U}_0 = \tilde{q}_0/\tilde{h}_0$ reads instead

$$\tilde{U}_0 = \frac{g\sin\beta - \rho^{-1}\partial_x\tilde{p}_i}{3\nu}\tilde{h}_0^2 + \frac{\tilde{\tau}_i}{2\mu}\tilde{h}_0 \ . \tag{5.4}$$

The presence of the pressure derivative $\partial_x\tilde{p}_i$ into the velocity profile is due to the fact that the variation along x of the interfacial pressure cannot be neglected a priori. For example, if one considers a water film developing on a NACA12 wing at 4° incidence and chord 0.6 m, at speed corresponding to a Mach number $M = 0.4$, the pressure gradient $\partial_x\tilde{p}_i = -7.8\cdot 10^3\ Pa\ m^{-1}$ halfway the stagnation point and the trailing edge. These flight conditions are typical of a plane in a holding pattern before landing. In rainy configurations, one finds a 10 μm film thick when neglecting the influence of the wing slope and the gravity. The effect that $\rho^{-1}\partial_x\tilde{p}_i$ plays a similar role as the gravity force in the development of the film justifies the choice made here to keep the pressure gradient as the same order as the gravity.

It is worthwhile to mention that this equilibrium state coincides with Nusselt's (2.9-2.13) when shear stress and interfacial pressure vanish.

5.1.2 Two-layer pressure-driven flow

When the liquid-gas interface is flat, all derivatives $\partial_{x,t}$ of equations (4.1) vanish and one can recover the equilibrium condition of the pressure-driven two-layer flow. With reference

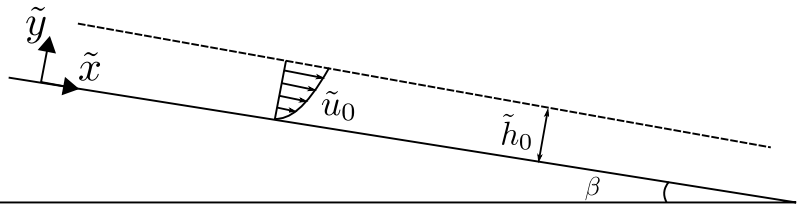

Figure 5.2: Uniform flow of a gravity-driven liquid film down an inclined plane.

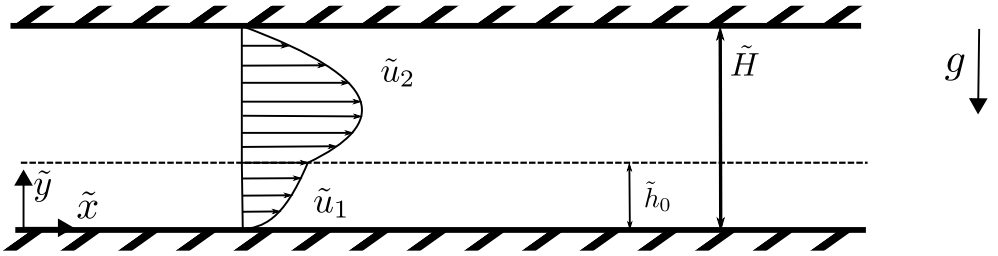

Figure 5.3: Uniform flow of a two-layer in an horizontal channel.

to Figure 5.3, one can consider a liquid-gas system of imposed total flow rate $\tilde{Q}$. When the interface is wavyless, the total pressure gradient $\Delta\tilde{p}/\tilde{L}$ is constant, where $\Delta\tilde{p}$ is the inlet-outlet pressure drop along $\tilde{L}$. A double integration of the x-momentum equation of system (4.1) leads to film and gas equilibrium velocity profiles, namely

$$\tilde{u}_{1,0}(\tilde{y}) = \frac{\Delta\tilde{p}}{\tilde{L}\mu_1}\frac{\tilde{y}}{2}(\tilde{y} - 2\tilde{h}_0) + \frac{\tilde{\tau}_i\tilde{y}}{\mu_1} \ , \tag{5.5}$$

$$\tilde{u}_{1,0}(\tilde{y}) = \frac{\Delta\tilde{p}}{\tilde{L}\mu_2}\frac{\tilde{H} - \tilde{y}}{2}(2\tilde{h}_0 - \tilde{H} + \tilde{y}) - \frac{\tilde{\tau}_i(\tilde{H} - \tilde{y})}{\mu_2} \ , \tag{5.6}$$

where $\tilde{h}_0$ is the uniform thickness of the film. However, shear stress $\tilde{\tau}_i$ and pressure gradient $\Delta\tilde{p}/\tilde{L}$ are still unknown. The former can be computed through the boundary condition (4.3) applied to longitudinal velocities. This drives to

$$\tilde{\tau}_i = -\frac{1}{2}\frac{\Delta\tilde{p}}{\tilde{L}}\ \frac{-\tilde{h}_0^2 m + (\tilde{H} - \tilde{h}_0)^2}{\tilde{h}_0 m + \tilde{H} - \tilde{h}_0} \ , \tag{5.7}$$

where $m = \mu_2/\mu_1$ gives the ratio of gas viscosity to liquid viscosity. The pressure gradient is given instead by imposing the condition $\tilde{q}_1 + \tilde{q}_2 = \tilde{Q}$ and leads to

$$\frac{\Delta\tilde{p}}{\tilde{L}} = -\frac{12\tilde{Q}(\tilde{h}_0 m + \tilde{H} - \tilde{h}_0)\mu_2}{\tilde{h}_0^4 m^2 + (\tilde{H} - \tilde{h}_0)^4 + 2\tilde{h}_0(\tilde{H} - \tilde{h}_0)(2\tilde{H}^2 + \tilde{h}_0^2 - \tilde{h}_0\tilde{H})} \tag{5.8}$$

For example, Figure 5.4 shows a typical equilibrium velocity profile of a confined two-layer flow over a wavelength of 26 mm, when film thickness is 0.13 mm and gas thickness 0.26 mm (numerical test to be reproduced in Chapter 8).

5.2 Linearization around the equilibrium state

With reference to Figures 5.2 and 5.3, one can consider infinitesimal perturbations around the equilibrium state of the form

$$h = h_0 + h_p \ , \tag{5.9a}$$

$$q = q_0 + q_p \ . \tag{5.9b}$$

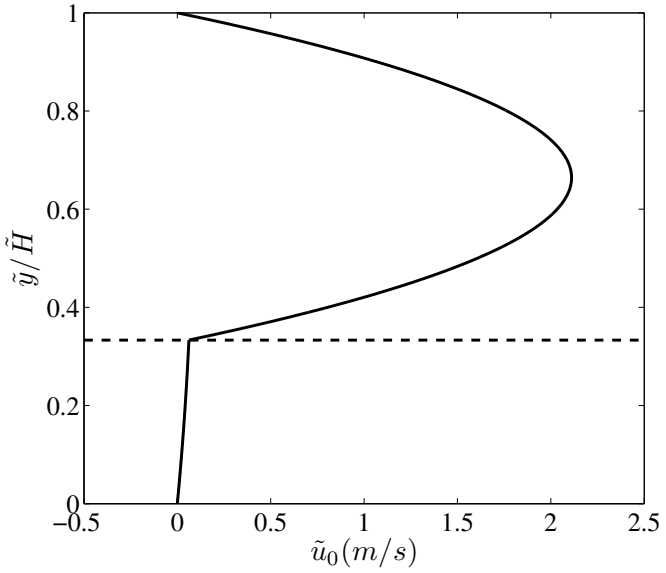

Figure 5.4: Uniform velocity profile of an air-water flow in a channel: $\tilde{Q} = 4.06 \cdot 10^{-4}\ m^2 s^{-1}$, $\tilde{L} = 26\ mm$, $\tilde{H} = 0.39\ mm$, $r = 0.001$ and $m = 0.01$. Dashed line is the flat interface.

where subscripts 0 and p refer to the base state previously derived and the perturbation, respectively. Since the amplitude of the perturbations is much smaller than the magnitudes of film thickness and flow rate at the equilibrium state, the shallow water equations can be linearized. The general form of the linearized equations read

$$\partial_t \mathbf{Q}_p + \mathbf{A}\partial_x \mathbf{Q}_p = \mathbf{B}\mathbf{Q}_p + \mathbf{S}\partial_{3x}\mathbf{Q}_p \ , \tag{5.10}$$

where $\mathbf{Q} = \binom{h}{q}$ is the conserved variable vector of the shallow water equations. Matrices $\mathbf{A}$, $\mathbf{B}$, $\mathbf{S}$ read

$$\mathbf{A} = \begin{bmatrix} 0 & 1 \\ a_{21} & a_{22} \end{bmatrix} \ , \qquad \mathbf{B} = \begin{bmatrix} 0 & 0 \\ b_{21} & b_{22} \end{bmatrix} \ , \qquad \mathbf{S} = \begin{bmatrix} 0 & 0 \\ s_{21} & 0 \end{bmatrix} \ , \tag{5.11}$$

whose coefficients will be expressed later for both the single- and two-layer problems. Hence, solutions to the linearized problem can be sought in the form

$$\mathbf{Q}_p = \hat{\mathbf{Q}} \exp[i(kx - \omega t)] \ , \tag{5.12}$$

where $i^2 = -1$ is the imaginary unit, ω the angular velocity and $k = 2\pi/\lambda$ the wavenumber, with λ wavelength of the sinusoidal perturbation. Furthermore, $\hat{\mathbf{Q}}$ defines the amplitude of the perturbation around the equilibrium position. Specifically, (5.12) is

$$h_p = \hat{h} \exp[i(kx - \omega t)] \ , \tag{5.13a}$$

$$q_p = \hat{q} \exp[i(kx - \omega t)] \ . \tag{5.13b}$$

The wavenumber k is assumed to be real, whereas the angular velocity ω can take complex values, and as a consequence, so does the wave velocity $c = \omega/k$, namely

$$\omega = \omega_r + i\omega_i = kc_r + ikc_i \ . \tag{5.14}$$

The real part c_r identifies the propagation velocity of the waves, whereas kc_i defines the growth rate. Therefore, the sign of the growth rate kc_i provides the evolution of the interface: when kc_i is negative the liquid film is stable to large wavelength disturbances;

inversely, when kc_i is positive large waves on the interface amplifies; on the other hand, $kc_i = 0$ represents the transition between stable and unstable conditions. Particularly, for $kc_i = 0$ one can define the neutral stability curve, which sets the transition stable-unstable in the plane $k-Re$ (alternatively, in the plane $f-Re$), to be shown later in the configuration of the experiments of Liu & Gollub [47].
When replacing the wavy solutions (5.12) into the linearized problem (5.10), one obtains

$$(-ikc\mathbf{I} + ik\mathbf{A} - \mathbf{B} + ik^3\mathbf{S})\hat{\mathbf{Q}}\exp[ik(x-ct)] = 0 \ , \tag{5.15}$$

where $\mathbf{I}$ is the unit matrix. Solving this expression leads to the dispersion relation, which connects k and c. If the matrix $(-ikc\mathbf{I} + ik\mathbf{A} - \mathbf{B} + ik^3\mathbf{S})$ is invertible, the solution of the system (5.15) provides $\hat{\mathbf{Q}} = 0$. Otherwise, seeking non-zero solutions of $\hat{\mathbf{Q}}$, one must impose that the matrix $(-ikc\mathbf{I}+ik\mathbf{A}-\mathbf{B}+ik^3\mathbf{S})$ is not invertible. Therefore, the dispersion relation can be found by imposing

$$det(-ikc\mathbf{I} + ik\mathbf{A} - \mathbf{B} + ik^3\mathbf{S}) = 0 \ . \tag{5.16}$$

The solution of the dispersion relation permits then to express the complex wave velocity c as function of the wavenumber k. However, first-order models are exact, by construction, up to the first order in ε. One can thus anticipate that only zeroth- and first-order wave velocity c are entirely captured by first-order long-wave models. Therefore, as sketched in the scheme of Figure 5.1, it seems more appropriate to obtain the wave velocity by an asymptotic expansion of ω in powers of the wavenumber k (thus, in the limit $k << 1$, which corresponds to large wavelength disturbances, in line with the assumptions made so far). Hence, the corresponding expression of c related to first-order models can be written as

$$c = c_0 + c_1 k + O(k^2) \ , \tag{5.17}$$

where, in the limit $k << 1$, c_0 and c_1 can be seen as the leading contributions to c_r and c_i, respectively. By comparing this expression to the asymptotic expansion of the Orr-Sommerfeld theory, one can better underline that first-order models are able to catch the correct c_0 and c_1, but manifest errors on further orders of accuracy. This will be shown in detail later.
Once the general methodology in deriving the dispersion relation of long-wave models has been described, its application to the models derived in Chapter 3 and Chapter 4 will be developed.

5.3 Thin liquid film stability analysis

In order to study the linear stability of thin liquid films subject to gravity and given interfacial shear stress and pressure (see Chapter 3), one can refer to the system of equations (3.43)-(3.45). As described above, the dispersion relation can be obtained by replacing the wavy solutions (5.13a), (5.13b) into the linearized form of these equations, and by subsequent imposition of the condition (5.16). Coefficients of matrices $\mathbf{A}$, $\mathbf{B}$ and $\mathbf{S}$ of (5.11) read, respectively,

$$a_{21} = -\frac{q_0^2}{h_0^2} + e^2 \ , \qquad a_{22} = 2\frac{q_0}{h_0} \ , \tag{5.18a}$$

$$b_{21} = \frac{1}{Re}\Big(\Lambda + \frac{dT}{dh}\Big|_0 + 6\frac{q_0}{h_0^3}\Big) \ , \qquad b_{22} = -\frac{3}{Re}\frac{1}{h_0^2} \ , \tag{5.18b}$$

$$s_{21} = \frac{h_0}{We} \ , \tag{5.18c}$$

where T comes from the (3.45), and Λ is defined in (3.16). More precisely, a_{21} and a_{22} are the coefficients of $\partial_x h$ and $\partial_x q$, respectively, when performing $\partial_x(q^2/h + P)$. The variable e in the coefficient a_{21} is the *characteristic velocity**, which is defined as

$$e^2 = \frac{dP}{dh} \ , \tag{5.19}$$

where P is the "pressure" term (3.44). Indeed, $q_0/h_0 \pm e$ are the eigenvalues corresponding to the matrix $\mathbf{A}$. Hence, the corresponding dispersion relation yields

$$\begin{aligned} &k^2c^2 + \Big(3\frac{ik}{Reh_0^2} - 2\frac{q_0}{h_0}k\Big)kc \\ &- \frac{h_0}{We}k^4 - \Big(-\frac{q_0^2}{h_0^2} + \frac{2}{45}\Lambda^2 h_0^4 + \frac{4}{15}\Lambda\tau_i h_0^3 + \frac{1}{4}\tau_i^2 h_0^2 + \frac{\cos\beta}{Fr}h_0\Big)k^2 \\ &- \Big(\frac{\Lambda}{Re} + \frac{6q_0}{Reh_0^3} + \frac{1}{20}\Lambda h_0^3\partial_x\tau_i + \frac{7}{40}\tau_i h_0^2\partial_x\tau_i + \frac{3}{35}\Lambda Reh_0^4\partial_x G \\ &+ \frac{1}{6}Reh_0^3\tau_i\partial_x G + \frac{1}{5}Reh_0^2\partial_t G + \frac{1}{4}h_0\partial_t\tau_i\Big)ik = 0 \ , \end{aligned} \tag{5.20}$$

where $\partial_x G = \partial_x \Lambda$ (see definition (3.16)). Equilibrium thickness h_0 can be taken equal to unity without loss of generality. This choice is in agreement with the scaling rule (3.7). Yet, interfacial shear stress τ_i and pressure gradient $-G$, as well as their derivatives are given functions of time and stream-wise component of space.
As already stated in the previous section, the complex wave velocity c can be obtained by solving the dispersion relation (5.20). Starting from this relation, one can analyze simpler configurations, such as those of a falling liquid film and a constant sheared liquid film.

5.3.1 Falling film in a passive gas atmosphere

The simplest interesting case is when only gravity drives the liquid layer, such as a falling film flowing down an inclined plane. In this configuration, the dispersion relation (5.20) gets a shorter form, given that shear stress, pressure gradient and the respective spatio-temporal derivatives vanish. Also Λ simplifies and becomes constant, according to $\Lambda = Re\ Fr^{-1}\sin\beta$ (see defintion (2.26), or (3.16) with $G(x) = 0$). Furthermore, from the equilibrium condition, one gets

$$U_0 = \frac{\tilde{h}_0^2 g\sin\beta}{3\nu\tilde{U}_0} = \frac{Re\sin\beta}{3Fr} \ , \tag{5.21}$$

and, as a consequence, $q_0 = Re\ Fr^{-1}\sin\beta/3$. Finally, dispersion relation (5.20) reads

$$k^2c^2 + \Big(3\frac{i}{Re} - \frac{2}{3}\frac{Re\sin\beta}{Fr}\Big)k^2c - \frac{k^4}{We} + \Big(\frac{1}{15}\frac{Re^2\sin^2\beta}{Fr^2} - \frac{\cos\beta}{Fr}\Big)k^2 - 3\frac{\sin\beta}{Fr}ik = 0 \ . \tag{5.22}$$

Dispersion relation (5.22) can be solved in MATLAB in order to provide real and imaginary wave speed c: Figure 5.5 shows celerity and growth rate with respect to wavenumbers for a water-glycerin falling film at $Re = 8.5$. Furthermore, the surface tension exhibits a clear trend in stabilizing the short waves, i.e. large wavenumbers, as appear by comparing the curves with and without surface tension.
However, wave speed c can be alternatively recovered by replacing the asymptotic expansion $c_0 + c_1 k + O(k^2)$ into the dispersion relation (5.22). Indeed, keeping only the terms at order

*The characteristic velocity has implications in the definitions of system properties: for example, when $e > 0$ the system is hyperbolic. More details can be found in Whitham [93].

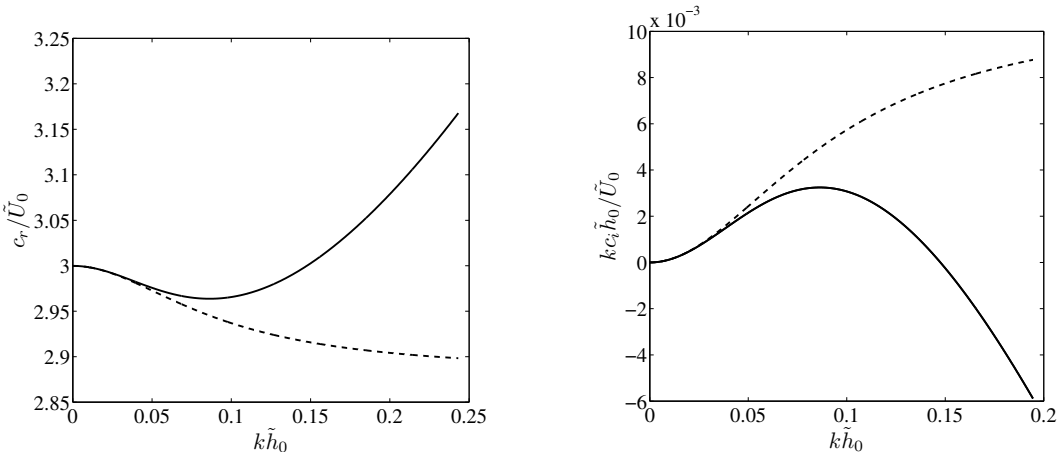

(a) *Dimensionless wave celerity.* (b) *Dimensionless growth rate.*

Figure 5.5: Dispersion curves from (5.22) for a water-glycerin gravity-driven film down an inclined plane of $\beta = 6.4°$. Dimensionless numbers: $Re = 8.5$, $Fr = 0.316$, $We = 0.048$. Case with surface tension (solid line) and without surface tension (dashed line).

zero one obtains c_0, while at order one this provides c_1. Finally, this procedure leads to the wave velocity

$$c = 3 + \Big(\frac{6}{5}Re - \cot\beta\Big)ik + O(k^2) \ , \tag{5.23}$$

after appropriate substitution of $\Lambda = Re\ Fr^{-1}\sin\beta = 3$, which comes directly from the definition (3.12) of the dimensionless numbers. Yet, c_0 and c_1 can be read, in the limit $k << 1$, as the real and imaginary wave speed c_r and c_i. The effect that $c_r = 3$, which can be also recovered from Figure 5.5 for $k = 0$, means that the waves move three times faster than the averaged film. On the other hand, from the expression (5.23), $kc_i = 0$ imposes the stability threshold, which can be expressed in terms of either a critical Reynolds number or a critical Froude number. Specifically, one obtains

$$Re_{cr} = \frac{5}{6}\cot\beta \ , \qquad\qquad Fr_{cr} = \frac{5}{18} \ . \tag{5.24}$$

Both the real and imaginary wave velocities and the threshold conditions for Re and Fr coincide with those provided by the analysis of Benjamin [7] and Yih [95], presented in Chapter 2, expressions (2.63) and (2.64).

Stability conditions (5.24) state that when $Re < Re_{cr}$, or equivalently $Fr < Fr_{cr}$, the film is stable to large wavelength disturbances: the amplitude of an infinitesimal initial disturbance will decrease in time. On the contrary, the film is unstable to large wavelength disturbance if $Re > Re_{cr}$, or equivalently $Fr > Fr_{cr}$: the amplitude of the sinusoidal initial perturbation will increase and saturate in non-linear waves, as highlighted by numerous experiments, as in Figure 2.2 of Chapter 2. From these critical numbers one can also recover that a horizontal film is always stable, whereas a vertical film is always unstable. Indeed, the destabilizing action of the longitudinal component of gravity vanishes for the horizontal case, and thus wave crests are pressed down; for vertical liquid films, this coincides with g and wave crests are pushed forward with an asymmetric motion, which brings to the so-called Kapitza instability. Particularly, this asymmetry is governed by non-linear effects, because wave crests move faster given that the velocity is proportional to the thickness. Therefore, waves tend to assume the typical shape of *saw teeth*, which is visible for example with solitary waves.

As further validation, wave velocity (5.23) can be compared to the exact asymptotic expansion (2.71) of the Orr-Sommerfeld equation. As stated before, first-order models

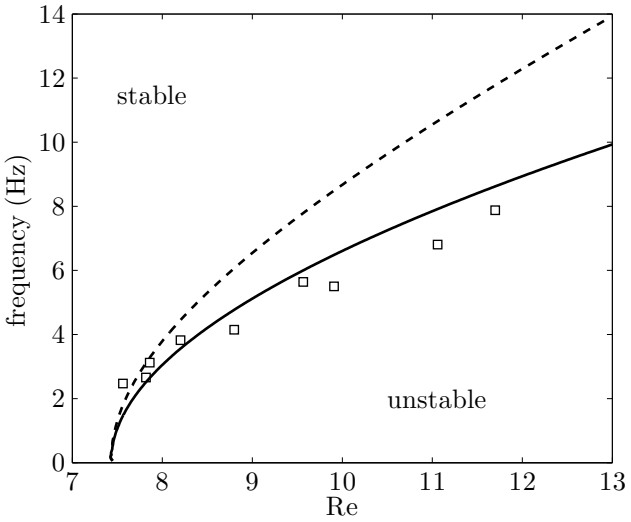

Figure 5.6: Neutral stability curve for gravity-driven water-glycerin films down a 6.4° inclined plane. Solid line: Orr-Sommerfeld theory; dashed line: first-order long-wave model of Chapter 3, subject to gravity only; squares: experiments of Liu, Paul and Gollub [48, 47].

provide correct wave propagation velocity and stability threshold, i.e. c_0 and c_1. However, in order to quantify the error of the second-order wave velocity c_2 one can develop the second order, meaning that $c_0 + c_1 k + c_2 k^2 + O(k^3)$ must be replaced into the dispersion relation (5.22). Looking at the order two, wave velocity (5.23) can be augmented to

$$c = 3 + \Big(\frac{6}{5}Re - \cot\beta\Big)ik + 3\Big(\frac{4}{9}\cot\beta Re - \frac{8}{15}Re^2\Big)k^2 + O(k^3)\ . \tag{5.25}$$

Comparing this to the exact asympotic expansion (2.71) of the Orr-Sommerfeld equation, as well as to the wave speed provided by the first-order model of Ruyer-Quil & Manneville [69] presented in section 2.3.5, expression (2.70), coefficients are the same up to the order one, and this is valid for all consistent models accurate at $\mathcal{O}(\varepsilon)$. For example, Figure 5.6 shows the neutral stability curve associated to the single-layer model developed in Chapter 3, in the case of simple falling film, and the exact curve provided by the O-S theory. Differences are due to discrepancies between equations (5.25) and (2.71) from the second order onwards. Furthermore, Figure 5.6 presents also results from the experiments of Liu & Gollub [47].

5.3.2 Falling film with constant shear stress

As further step, one can consider the case of a liquid film driven by gravity and constant shear stress. In this configuration, the equilibrium flow rate (5.3) becomes

$$\tilde{q}_0 = \rho g \sin\beta \frac{\tilde{h}_0^3}{3\mu} + \frac{\tilde{\tau}_i}{2\mu}\tilde{h}_0^2\ . \tag{5.26}$$

Furthermore, according to the dimensionless scaling (3.7), the dimensionless averaged velocity yields

$$U_0 = \frac{1}{3}\frac{Re}{Fr}\sin\beta + \frac{\tau_i}{2}\ , \tag{5.27}$$

meaning that there is an additional term depending on τ_i compared to the previous case, see expression (5.21). Therefore, recalling that $h_0 = 1$, the dimensionless equilibrium flow rate leads to $q_0 = Re\ Fr^{-1}\sin\beta/3 + \tau_i/2$. Finally, by replacing those into the dispersion

relation (5.20) of the general case, and by removing all spatio-temporal derivatives, as well as the pressure gradient, one obtains

$$\begin{aligned} &k^2c^2 + \Big(3\frac{i}{Re} - \frac{2}{3}\frac{Re\sin\beta}{Fr} - \tau_i\Big)k^2c - \frac{k^4}{We} \\ &+ \Big(\frac{1}{15}\frac{Re^2\sin^2\beta}{Fr^2} + \frac{1}{15}\frac{Re\sin\beta}{Fr}\tau_i - \frac{\cos\beta}{Fr}\Big)k^2 - 3\Big(\frac{\sin\beta}{Fr} + \frac{\tau_i}{Re}\Big)ik = 0 \ , \end{aligned} \tag{5.28}$$

where Λ has been replaced through the definition (2.26). With an analogous procedure as before, by replacing the asymptotic expansion $c_0 + c_1k + O(k^2)$ into the dispersion relation (5.28), the solution at different orders leads to the wave velocity

$$c = \frac{Re}{Fr}\sin\beta + \tau_i + \frac{Re}{3}i\Big(-\frac{2}{5}\frac{Re^2}{Fr^2}(\sin\beta)^2 - \frac{2}{5}\tau_i\frac{Re}{Fr}\sin\beta + \frac{\cos\beta}{Fr}\Big)k + O(k^2) \ . \tag{5.29}$$

With appropriate replacement of $Re\ Fr^{-1}\sin\beta = 3 - 3\tau_i/2$, which derives by considering $U_0 = 1$ into the equilibrium (5.27), in line with the previous analysis the wave velocity (5.29) changes both in the real and imaginary part, compared to the previous case. Indeed, one obtains $c_r = 3 - 1/2\tau_i$. Hence, the dimensionless propagation velocity of interfacial waves is smaller with respect to the falling film configuration, i.e. $c_r = 3$, and this happens because the shear stress increases the film velocity more than the wave speed.
By imposing the condition $kc_i = 0$, the stability threshold in terms of Re and Fr numbers reads

$$Re_{cr} = \frac{5/6\cot\beta}{1 - \tau_i/6} \ , \qquad Fr_{cr} = \frac{5/18}{(1 - \tau_i/2)(1 - \tau_i/6)} \ . \tag{5.30}$$

For zero shear stress, the stability threshold coincides with the case of falling film (5.24). On the other hand, the value of Re_{cr}, as for Fr_{cr}, increases when a constant shear stress is applied in the direction of the film flow. Its effect is thus to stabilize the film to large wavelength disturbances. Indeed, when the Reynolds number is kept unchanged (hence, the flow rate unaltered) the increase of the shear stress provides an increase of Re_{cr}. In other words, if a liquid film is unstable to large waves, by keeping the same Re number can become stable if a greater shear stress is applied at the surface.
However, when increasing the shear stress applied at the surface of the film, the increment of the Re_{cr} is bounded. Precisely, for fixed flow rate, i.e. fixed Reynolds number, the equilibrium condition (5.26) governs the relation between the equilibrium thickness $\tilde{h}_0$ and the shear stress $\tilde{\tau}_i$ applied at the surface of the liquid film: the trend is sketched in Figure 5.7 for an inclination of $\beta = 6°$ and different Reynolds numbers. The effect that the base-state film $\tilde{h}_0$ becomes thinner when increasing the shear stress is in accordance with the idea that a wind stress in the direction of a liquid flow drives the film faster. Therefore, if the liquid flow rate $\tilde{q}_0$ is kept unaltered, the thickness consequently decreases at the equilibrium. Indeed, by developing the dimensionless expression of τ_i (3.7b), one obtains

$$\tau_i = \frac{\tilde{\tau}_i}{\mu\tilde{q}_0/\tilde{h}_0^2} = \frac{\Big(\tilde{q}_0 - \rho g\sin\beta\frac{\tilde{h}_0^3}{3\mu}\Big)\frac{2\mu}{\tilde{h}_0^2}}{\mu\frac{\tilde{q}_0}{\tilde{h}_0^2}} = 2 - \frac{2}{3}\frac{\rho g\sin\beta\tilde{h}_0^3}{\mu\tilde{q}_0} \ . \tag{5.31}$$

By considering that $\tilde{h}_0$ decreases when increasing $\tilde{\tau}_i$, the value of the dimensionless shear stress τ_i is thus confined in the range $(0, 2)$. This makes the critical Reynolds lying in the range $(5/6\cot\beta, 5/4\cot\beta)$, as sketched in Figure 5.8: the bottom value coincides with zero shear stress configuration, the top one is the maximum, for high $\tilde{\tau}_i$. Alternatively, expression (5.31) can be rewritten as

$$\tau_i = \frac{\tilde{\tau}_i}{\rho g\sin\beta\frac{\tilde{h}_0}{3} + \frac{\tilde{\tau}_i}{2}} = \frac{1}{\rho g\sin\beta\frac{\tilde{h}_0}{3\tilde{\tau}_i} + \frac{1}{2}} \ , \tag{5.32}$$

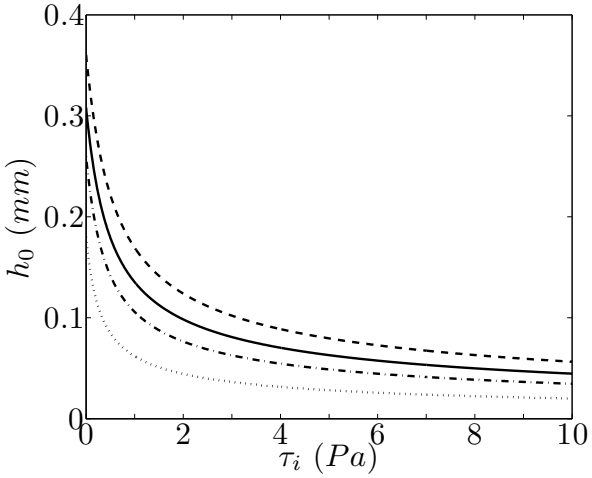

Figure 5.7: Equilibrium thickness versus shear stress from (5.26), for a water film down a $\beta = 4^\circ$ inclined plane, and for several Reynolds numbers: $Re = 2$ dotted line, $Re = 6$ dash-dot line, $Re = 10$ solid line, $Re = 16$ dashed line.

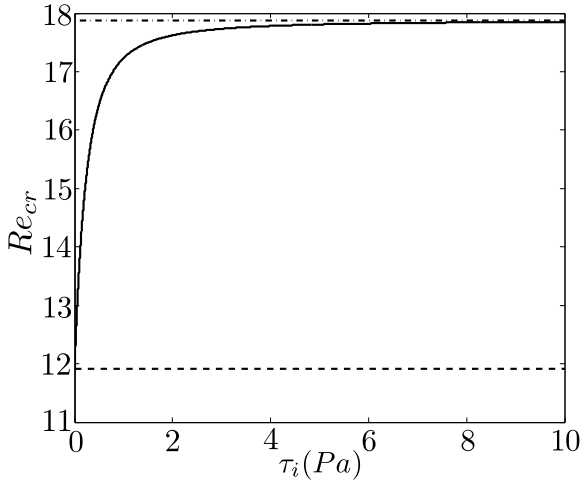

Figure 5.8: Critical Reynolds number versus shear stress from (5.30) and (5.31), for a water film down a $\beta = 6^\circ$ inclined plane. Dashed line is the limit of gravity-driven films, i.e. $\tau_i = 0$; dash-dotted line is the limit of an infinite τ_i.

from which one can recover the trend of τ_i when increasing $\tilde{\tau}_i$, keeping in mind the evolution shown in Figure 5.7.

For example, one can consider an experience in which a water film flows down a 6° inclined plane at $Re = 10$. In this condition, stability threshold (5.24) provides $Re_{cr} = 7.9$, the film is thus unstable to large-wavelength disturbances and, if the plane is long enough, interfacial waves will grow above the film. Nusselt's equilibrium condition yields a water thickness of 308 μm. In addition, one can equip the inclined plane with a device which provides a constant shear stress, i.e. a channel of constant section. With an established air flow, one can produce for example a shear stress of 0.35 Pa exerted on the liquid film. By keeping the same liquid flow rate (thus, same Reynolds number), equilibrium condition (5.26) states that the thickness of the water becomes shorter and reaches 200 μm. Hence, the dimensionless shear stress is 1.3 (see (5.31)), which leads to a critical Reynolds of 10.2, from the stability threshold (5.30). Since the Reynolds number of the water film is smaller than the critical value, the film keeps stable and interfacial waves of large wavelength reduce their amplitude.

By comparing the expression of the critical Reynolds with the one provided by Smith [78]

and then Samanta [73] (see section 2.5), the effect of the shear stress goes in the opposite direction. Indeed, in Smith's (or Samanta's) work the shear stress has the tendency to destabilize the liquid film; furthermore, the wave celerity c_r increases with respect to the zero interfacial stress configuration. This difference is due to the definition of the Reynolds number. In the present analysis this depends on the averaged velocity of the film and thus includes also the wind stress, namely

$$Re = \frac{\rho g \sin\beta}{3\mu\nu}\tilde{h}_0^3 + \frac{\tilde{\tau}_i}{2\mu\nu}\tilde{h}_0^2 \ . \tag{5.33}$$

Smith's result differs from this one in the definition of the Reynolds number. In his work, in fact, it depends on the average velocity of a film subject to gravity only, and thus is not function of the shear stress, according to $Re = \rho g \sin\beta \tilde{h}_0^3 \nu^{-2}$.
Unlike Smith's, the advantage of the present analysis is based on practical considerations: experiences at fixed Re do not imply fixed equilibrium thickness $\tilde{h}_0$; modifications of the shear stress induces changes of the equilibrium condition; experiences are easy to be reproduced.
However, it is worthwhile to mention that by using Smith's scaling the analysis of the wave velocity (5.29) drives to his stability threshold (2.67).

5.4 Two-layer flow stability analysis

After the linear stability of thin liquid films subject to gravity and given interfacial shear stress and pressure, one can perform the stability analysis for the two-layer model of a liquid-gas flow in a confined channel (continuity equations in (4.42) with momentum equation (4.45a)). Unlike the previous analysis, where shear stress and pressure gradient are given functions of space and time, in the film-gas system of Chapter 4 the shear stress exerted by the gas at the interface and the correspnding pressure gradient are provided by the asymptotic expansion and are functions of thickness h, channel height H, viscosity ratio m and total flow rate Q.

In order to find the dispersion relation of such a system of equations, one can develop the condition (5.16), where coefficients of matrices $\mathbf{A}$, $\mathbf{B}$ and $\mathbf{S}$ in (5.11) read, respectively,

$$a_{21} = -\frac{q_0^2}{h_0^2} + e^2 \ , \qquad a_{22} = 2\frac{q_0}{h_0} \ , \tag{5.34a}$$

$$b_{21} = \frac{d}{dh}\Big|_0\Big(G^{(0)}h + \frac{3}{2}\frac{{\tau_i}^{(0)}}{Re}\Big) + 6\frac{q_0}{Re\ h_0^3} \ , \qquad b_{22} = -\frac{3}{Re}\frac{1}{h_0^2} \ , \tag{5.34b}$$

$$s_{21} = \frac{h_0}{We} \ . \tag{5.34c}$$

Leading-order pressure gradient $-G^{(0)}$ and shear stress ${\tau_i}^{(0)}$ are defined in (4.35) and (4.36), respectively. On the other hand, the characteristic velocity e gathers all coefficients of the integrated model depending on $\partial_x h$, namely

$$e^2 = \frac{d}{dh}\Big|_0\Big(\frac{1}{5}\frac{q_1^2}{h} + \Pi_1\Big) - G^{(1)}h + \frac{1}{Re}\Big(\frac{3}{2}\tau_i - 3\frac{q_1}{h^2} - {\tau_{w1}}^{(c)}\Big) \ , \tag{5.35}$$

where q_1, Π_1, $G^{(1)}$, ${\tau_i}^{(1)}$, ${\tau_{w1}}^{(c)}$ are specified in (4.33), (4.43a), (B.5), (B.3) and (4.44), respectively. Hence, the dispersion relation derived from the condition (5.16) yields

$$-k^2c^2 - \Big(3\frac{ik}{Reh_0^2} - 2\frac{q_0}{h_0}k^2\Big)kc + \frac{h_0}{We}k^4 + D_1k^2 + D_2ik = 0 \ , \tag{5.36}$$

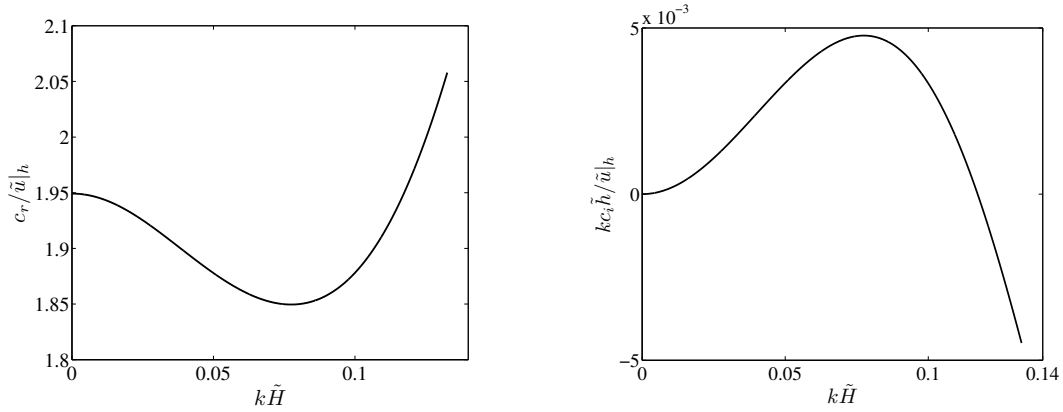

(a) *Dimensionless wave celerity.* (b) *Dimensionless growth rate.*

Figure 5.9: Dispersion curves from (5.36) for an air-water system flowing in a confined channel neglecting the gravity: $\tilde{H} = 0.39\ mm$, $\tilde{h}_0 = 0.13\ mm$, $\tilde{u}|_h = 0.06\ m\ s^{-1}$. Dimensionless numbers: $Re_1 = 4.48$, $Re_2 = 36.8$, $Fr = 0.93$, $We = 0.002$.

where coefficients D_1 and D_2 are expressed in Appendix C. As already described in the previous section, the solution of the dispersion relation provides the complex wave velocity c. For example, after solving with MATLAB the equation (5.36), Figure 5.9 shows real and imaginary parts of c for an air-water flows in a confined channel. Yet, the real part represents the wave celerity, whereas the imaginary part the growth rate. A first-order integrated model provides the right values of c_r and c_i only for small wavenumbers, which corresponds to large wavelengths, where the model is valid.

Nevertheless, one can also perform an asymptotic expansion of the relation (5.36) for $k << 1$, which leads to an expression of the form (5.17). Alternatively, c_0 and c_1 can be obtained from zeroth- and first-order flow rates $q^{(0)}$ and $q^{(1)}$, defined in (4.33) and (B.4), respectively. This procedure allows for avoiding long computations and will be thus applied to this configuration, being more complicated than the previous one. Indeed, one can express $q^{(0)} = f_1(h)$ and $q^{(1)} = f_2(h)\partial_x h + f_3(h)\partial_{3x} h$: by replacing those into the continuity equation $\partial_t h + \partial_x[q^{(0)} + q^{(1)}] = 0$, one obtains

$$\partial_t h + f_1'\partial_x h + f_2\partial_{xx} h + f_2'\partial_x^2 h + f_3\partial_{4x} h + f_3'\partial_x h\partial_{3x} h = 0\ , \tag{5.37}$$

where primes denote derivatives with respect to h. Finally, by neglecting non-linear terms $\partial_x^2 h$ and $\partial_x h\partial_{3x} h$ in (5.37) and seeking wavy solutions of the form (5.13a), leads to

$$c = f_1'(h_0) + i[f_2(h_0)k - f_3(h_0)k^3]\ , \tag{5.38}$$

whose coefficients correspond to leading and first-order wave velocity c.

Finally, results of the stability analysis can be compared with those derived in literature, particularly from Yih [96].

5.4.1 Comparison with Yih's results

As already mentioned in section 2.5, Yih has studied the stability of two immiscibile layers with same density and thickness shown in Figure 5.10. Neglecting the surface tension, Yih has proved that the instability is due to the viscosity contrast between the two layers. Zeroth- and first-order wave velocities provided by Yih are expressed in (2.68) and (2.69). The purpose of this section is to validate the wave velocity obtained through the expression (5.38), by comparison with Yih's results. Applying Yih's assumption to the solution

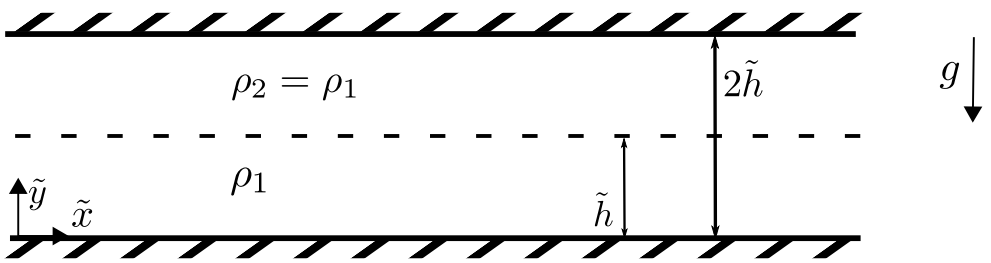

Figure 5.10: Yih's two-layer configuration.

of the (5.38), leading-order wave celerity c_0 reads

$$c_0 = \frac{24Qm(3 + 10m + 3m^2)}{(1 + 14m + m^2)^2} \ , \tag{5.39}$$

while first-order c_1 is

$$c_1 = \frac{3Q^2kRe}{35} \frac{(m+1)(m-1)^2(7m^6 - 226m^5 + 4169m^4 + 6436m^3 + 4169m^2 - 226m + 7)}{(1 + 14m + m^2)^5} \ . \tag{5.40}$$

When choosing the same scaling as Yih, namely $Q = (1 + 14m + m^2)/24m$, coefficients turn to be the same between the two analysis, keeping in mind that k and Re are double with the present scaling. This represents thus a validation for the asymptotic model and the two-layer shallow water equations derived in Chapter 4.

Further validations, which have not been computed here, are the comparison with the work of Yiantsios & Higgins [94], who have extended the work of Yih to general configurations of any thickness and density of the two layers, and the check of the symmetry properties determined by Charru & Fabre [17], such as those with respect to the vertical and the horizontal planes.

In conclusion, the linear stability analysis of both the models developed in the previous chapters has been performed. The main goal of this analysis has been to discuss the wave celerity and the growth rate provided by the models in the linear regime with those available in the literature. Furthemore, in the case of falling liquid films subject to a constant interfacial stress, the stability threshold has provided a different result compared to Smith, explained by the scaling difference. A more detailed analysis has also revealed that the critical Reynolds number is bounded and cannot always increase by intensifying the shear stress.

The next step to accomplish is the numerical discretization of the averaged-equations of Chapter 3 and compressible Navier-Stokes equations, accounting for liquid and gas phases, respectively. The coupling technique will be also presented in next chapter. As already mentioned, the hypothesis of thin gas is very restrictive for the aerospace applications investigated at ONERA. This justifies the choice to couple a reduced model of films to a Navier-Stokes code for the gas. This will bring to the development of the code SWANS.

6 Development of numerical schemes in coupling shallow water and Navier-Stokes equations: the SWANS model

This chapter deals with the development of numerical methods with the purpose to couple the long-wave first-order model of sheared liquid films (Chapter 3) to the Navier-Stokes equations in the gas phase. Based on such numerical methods, the code SWANS is then developed in MATLAB and used to describe the non-linear dynamics of two-layer flows in a channel, as sketched in Figure 6.1. On one side, a code based on discrete shallow water equations is developed in order to model the liquid film (from now onwards, it will be called *film code*). On the other hand, compressible Navier-Stokes equations are discretized to study a laminar gas flow on the top of the liquid film (called *gas code* from now onwards). Finally, a physical and numerical method permitting to couple film and gas codes is developed. This coupling method takes place at the interface between the two phases and employes the ALE technique.

Besides to be a stimulating computational subject in itself, this numerical approach is motivated by the need to dispose of a liquid-gas coupling methodology to be applied to industrial codes, such as the CEDRE platform developed at ONERA for aerodynamics and combustion problems. Indeed, CEDRE platform is able to solve gas flows by means of compressible Navier-Stokes equations, possibly on moving grids, and thin liquid layers with depth-integrated equations. However, a coupling methodology permitting to study non-linear dynamics of liquid films sheared by a gas flow is missing. Therefore, this work becomes a fundamental study to be subsequently extended to complex industrial codes.

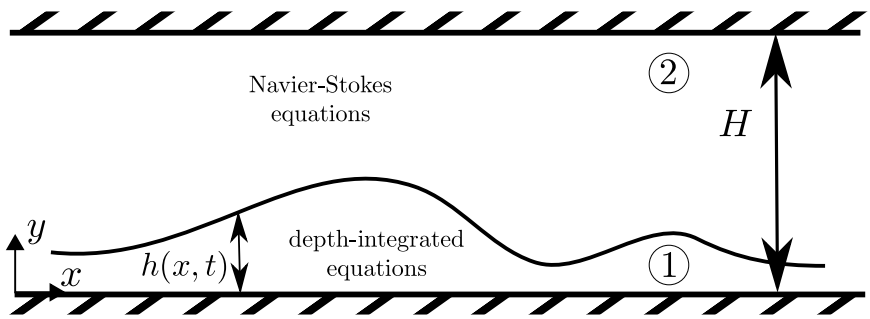

Figure 6.1: Sketch of the performed computational investigation. Indices 1 and 2 refer to liquid and gas phases, respectively.

6.1 The general architecture

With reference to Figure 6.1, the aim of the performed computational analysis consists in coupling section-averaged equations with compressible Navier-Stokes equations. This technique thus allows to investigate two-layer flows and represents a compromise between the two-layer Direct Numerical Simulation and the full averaged model, given by the use of depth-integrated equations for both phases. The former has been strongly developed in last decades: methods as Volume of Fluid (VOF) and Level-Set (LS), as well as hybrid techniques, have been highly improved in computational cost and precision. For example, recent developments in the application to the atomization problem are due, among the others, to Fuster *et al.* [29] and Tomar *et al.* [85] for VOF, Desjardins *et al.* [22] and Zuzio *et al.* [98] for LS, Sussman *et al.* [82] and Menard *et al.* [55] for coupled LS/VOF.
However, the thinness of the liquid film shown by several experiments, as already discussed in Chapter 2, suggests that shallow water equations rather than Navier-Stokes equations can be used to model the liquid film when performing computational analysis. This permits to greatly reduce the computational cost compared to the complete DNS, which requires, for example, several cells within the thickness to describe well the physics of the liquid layer, against the single cell demanded by the shallow water discretization.
On the other hand, a two-layer long-wave model, given by the application of averaged equations to both phases, as developed by Dietze & Ruyer-Quil [25], is able to describe only the physics of strictly confined flows. Indeed, the long-wave theory typical of such approaches imposes the gas thickness to be small compared to the wavelength of developing waves. More precisely, the condition to be verified is $(H - h) << \lambda/Re_2$, which is even more restrictive given the high speed of the gas flow. Noteworthy is that such an approach cannot be adopted for most of aerospace and automobile applications.

Therefore, the computational technique developed in this work, i.e. coupling shallow water and Navier-Stokes equations, allows to get rid of the above mentioned shortcomings.

6.1.1 Case study

The scenario analyzed hereby consists of a two-dimensional channel, with a liquid film flowing at the bottom and a laminar gas on the top of it, as in Figure 6.1. The liquid film is assumed to be thin compared to the wavelength of the interfacial waves. On the contrary, any limitations of gas thickness has to be taken into account, given to the Navier-Stokes resolution, as mentioned above. The only restriction left for the gas flow is the Reynolds number, which must be smaller than 2000 in order to be consistent with the assumption of laminar conditions.*
Given this configuration, two main tests will be discussed and numerically investigated in Chapter 8: a strictly confined flow, for which the discretization through two-layer averaged equations is still valid; a large channel, where the assumption of thin gas layer is not verified. Typical applications of the former are microchannels, coolers and heat exchangers, while the latter can be applied to aerospace motor flows and oil duct cleaning.

6.1.2 Two-layer flow and boundary conditions

The two-layer problem of Figure 6.1 is thus studied by coupling depth-integrated equations and compressible Navier-Stokes equations accounting for liquid and gas phases, respectively. The shallow water equations have been already developed in Chapter 3, and are rewritten here in dimensional form to highlight the coupling with the gas. Hence, for the liquid, the

*For a gas flowing in a channel, experiments show that when $Re > 2000$ the flow starts to be turbulent.

dimensional form of equations (3.43) reads

$$\partial_t \tilde{h} + \partial_x \tilde{q}_1 = 0 \ , \tag{6.1a}$$

$$\partial_t \tilde{q}_1 + \partial_x \Big(\frac{\tilde{q}_1^2}{\tilde{h}} + \tilde{P} \Big) = \tilde{\Lambda} \tilde{h} - \frac{1}{\rho_1} \Big[\mu_1 \frac{3\tilde{q}_1}{\tilde{h}^2} + \frac{3}{2} \tilde{\tau}_i - \tilde{T} \Big] + \frac{\gamma}{\rho_1} \tilde{h} \ \partial_{3x} \tilde{h} \ , \tag{6.1b}$$

where $\tilde{\Lambda} = g \sin\beta + \tilde{G} \rho_1^{-1}$, while $\tilde{P}$ and $\tilde{T}$ can be recovered from the respective dimensionless expressions (3.44) and (3.45) by means of the transformations

$$\Lambda \longrightarrow \frac{\tilde{\Lambda}}{\nu_1} \ , \qquad \tau_i \longrightarrow \frac{\tilde{\tau}_i}{\mu_1} \ , \qquad T \longrightarrow \mu_1 \tilde{T} \ , \qquad Fr^{-1} \longrightarrow g \qquad Re \longrightarrow \nu_1^{-1} \ . \tag{6.2}$$

Particularly, $\tilde{P} = \tilde{P}(\tilde{\tau}_i, \tilde{\Lambda})$ and $\tilde{T} = \tilde{T}(\tilde{\tau}_i, \tilde{\Lambda}, \partial_{x,t} \tilde{\tau}_i, \partial_{x,t} \tilde{G})$. The domain of resolution of the equations (6.1) is $\Omega_1 = \{0 \leq x \leq L\}$. On the other hand, for the gas, compressible Navier-Stokes equations read

$$\begin{cases} \partial_t \tilde{\rho}_2 + \nabla \cdot (\tilde{\rho}_2 \tilde{\mathbf{u}}_2) = 0 \\ \partial_t (\tilde{\rho}_2 \tilde{\mathbf{u}}_2) + \nabla \cdot (\tilde{\rho}_2 \tilde{\mathbf{u}}_2 \otimes \tilde{\mathbf{u}}_2) = -\nabla \tilde{p}_2 + \tilde{\mathbf{F}}_2 + \nabla \cdot \tilde{\mathbf{T}}_2 \end{cases} , \tag{6.3}$$

where ∇ is the nabla operator, $\tilde{\mathbf{T}}_2$ the viscous stress tensor and $\tilde{\mathbf{F}}_2$ a body force, also inclusive of the gravity force. The domain of resolution of such equations is instead $\Omega_2(t) = \{0 \leq x \leq L; \ h(x,t) \leq y \leq H\}$.

The coupling between the two phases takes place at the interface. The gas exerts interfacial shear stress $\tilde{\tau}_i$ and pressure gradient $-\tilde{G}$ over the film, which are defined as

$$\tilde{\tau}_i = \mu_2 \partial_y \tilde{u}_2|_{\tilde{h}} \ , \tag{6.4a}$$

$$\tilde{G} = -\partial_x \tilde{p}_2|_{\tilde{h}} \ . \tag{6.4b}$$

For what concerns the gas, the top wall is rigid and fixed, in a way that the boundary conditions yield

$$\tilde{u}_2(\tilde{y} = \tilde{H}) = 0 \ , \qquad \tilde{v}_2(\tilde{y} = \tilde{H}) = 0 \ . \tag{6.5}$$

Otherwise, the liquid film transfers to the gas the velocity and the position of the interface: Navier-Stokes equations (6.3) are thus solved by means of the continuity of velocities and compatibility condition, namely

$$\tilde{u}_2|_{\tilde{h}} = \tilde{u}_1|_{\tilde{h}} \ , \tag{6.6a}$$

$$\tilde{v}_2|_{\tilde{h}} = \tilde{v}_1|_{\tilde{h}} \ , \tag{6.6b}$$

$$\partial_t \tilde{h} + \tilde{u}|_h \partial_x \tilde{h} = \tilde{v}|_h \ , \tag{6.6c}$$

where the latter is valid for both the liquid and the gas, due to the equivalence of velocities at the interface. The system is closed by the derivation of $\tilde{u}_1|_{\tilde{h}}$ through the leading-order velocity profile (3.23) derived in Chapter 3. At $\tilde{y} = \tilde{h}$, expression (3.23) leads to

$$\tilde{u}_1|_{\tilde{h}} = \frac{3}{2} \frac{\tilde{q}_1}{\tilde{h}} + \frac{1}{4} \tilde{\tau}_i \tilde{h} \ , \tag{6.7}$$

while $\tilde{v}_1|_{\tilde{h}}$ is directly obtained by the compatibility equation (6.6c). This coupling methodology has been then developed into MATLAB, after discretization and implementation of the depth-integrated equations (film code) and the compressible Navier-Stokes equations (gas code). The final result is the solver SWANS to be described in next sections.

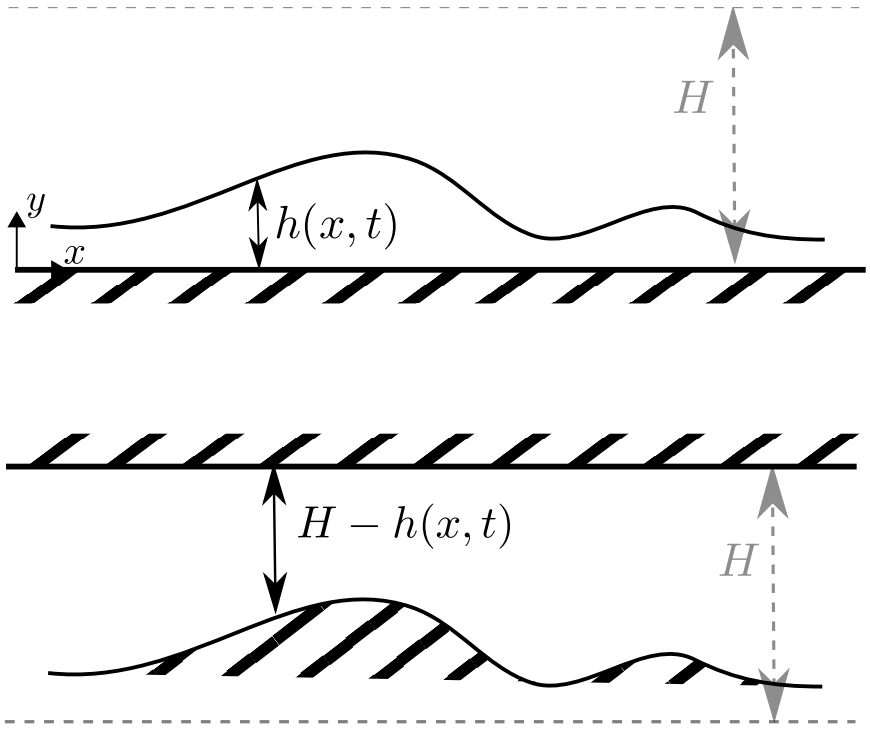

Figure 6.2: Sketch of film (top) and gas (bottom) code geometries. In the background, dashed lines indicate the base configuration, i.e. Figure 6.1.

6.1.3 Computational technique

From a computational point of view, the two-layer channel flow of Figure 6.1 is treated with periodic boundary conditions on left and right sides, while top and bottom sides are rigid walls. Periodic boundary conditions assure that the flow going out of the domain is reinjected at the entrance, verifying the conditions of a *closed flow*. On the other hand, initial conditions correspond to the perturbed equilibrium state.
The general structure of both codes is sketched in Figure 6.2: the channel geometry of Figure 6.1 is divided into two frameworks, one for each code. In the first configuration, see top of Figure 6.2, the film code allows for studying a sheared liquid film flowing on a flat and rigid wall. This would represent the bottom wall of the considered problem of Figure 6.1. Indeed, the film code deals with the liquid phase only and cannot see the top wall of the channel. On the contrary, the bottom of Figure 6.2 shows that the gas code analyzes the dynamics of a laminar gas bounded on the top by a rigid and fixed wall, and on the bottom by a liquid film, which is modeled as a wavy wall with a certain motion. Indeed, the gas code does not interact with the flat down wall of the channel, being treated by the film code only. As detailed later, the two codes exchange informations at the interface. Particularly, following the previous section, the choice is made here to provide interfacial shear stress and pressure gradient from the gas code to the film, while the film code returns shape and velocity of the interface to the gas. This data exchange permits to model the interface and all mutual effects between the liquid and the gas. This choice of coupling methodology is in natural accordance with the use of the ALE technique in the gas code. However, other choices of liquid-gas coupling are possible.

Another interesting feature of such a coupling methodology concerns the surface tension discretization. Indeed, since in the performed coupling methodology the film code transfers to the gas the velocity and the position of the interface, the surface tension has not to be implemented into the gas code. The gas can see the effects of the surface tension by the deformation of the interface, which is computed at each time step by the film code taking

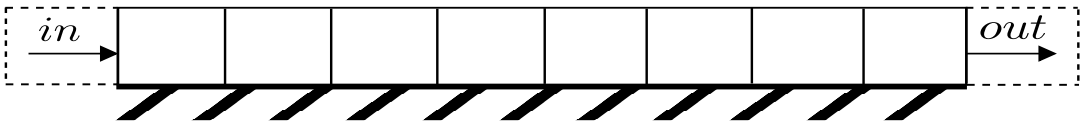

Figure 6.3: Sketch of the film mesh and definitions of periodic boundary conditions.

into account the capillary effects, in accordance with the hydrostatic pressure (3.13).
And last, if the capillary characteristic time is the smallest, the absence of the surface tension into the gas code allows for getting greater time steps in the computational investigations, compared to the classical full DNS.

6.2 Discrete one-layer depth-integrated equations

Film code geometry (top of Figure 6.2) is built by discretization of the depth-integrated equations of Chapter 3. Since the long-wave model is based on integrated variables, in the numerical approach one single cell in the vertical direction is sufficient to compute the film. Figure 6.3 shows the mesh used for the film code, with attention to periodic boundary conditions. Yet, periodic boundary conditions impose that all flow at the exit is reinjected at the entrance, i.e. $(\cdot)_{in} = (\cdot)_{out}$. Indeed, these conditions are numerically satisfied by imposing that *ghost cells* on the right side have the same flow conditions as the inlet and vice versa.

Discrete shallow water equations used in the film code are taken from the integral model (3.43) of Chapter 3, rewritten here for convenience:

$$\partial_t h + \partial_x q = 0 \ ,$$
$$\partial_t q + \partial_x\Big(\frac{q^2}{h} + P\Big) = \frac{1}{Re}\Big[\Lambda h - \frac{3q}{h^2} + \frac{3}{2}\tau_i - T\Big] + \frac{1}{We} h \ \partial_{3x} h \ .$$

The "pressure" term P is function of h, Λ and τ_i and is defined in (3.44). The term T is instead defined in (3.45). The description of the discretization of the shallow water equations will be discussed under dimensionless form, keeping in mind that the analysis of the dimensional form (6.1) leads to identical conclusions.

System (6.1) allows to find the thickness h and the averaged liquid flow rate q, once the shear stress τ_i and the pressure gradient $-G$ are given. Figure 6.4 shows input and output data of the film code: in every single cell of the mesh, thickness h and averaged liquid flow rate q are computed, from which the velocity field at the interface is computed and sent to the gas code, to be detailed later.

Following the work of Noble & Vila [57] formulated for the Euler-Korteweg system, depth-integrated equations (3.43) have been discretized through an *augmented* system. This method consists in reducing the order of the shallow water system by adding one evolution equation for the surface tension, as shown below. This need arises from the discretization of the surface tension which involves third derivatives, i.e. $\partial_{3x} h$.
Indeed, Noble & Vila [57] have derived the Von Neumann stability of several difference approximations of the Euler-Korteweg system, which has a similar form as the shallow water equations (3.43), and have demonstrated that when the dispersive term is discretized with classical centered difference approximations, then upwind schemes, such as the Godunov scheme, are always unstable. Otherwise, centered schemes, such as Lax-Friedrichs and Rusanov, are stable under an appropriate Courant, Friedrichs, Lewy (CFL) condition. Furthermore, Noble & Vila have recalled that a centered approximations of the dispersive terms does not assure that the schemes used for the Euler-Korteweg system are *entropy stable*, in the sense that corresponding difference approximations dissipate the energy. This

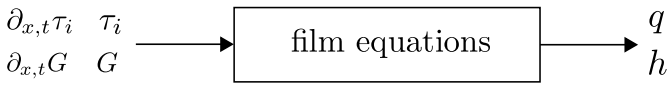

Figure 6.4: Input and output of the film code.

has driven the authors to propose a discretization method of the surface tension based on an *augmented* system, and to apply it in the simulation of Liu & Gollub experiments [47] of falling liquid films down an inclined plane. Therefore, their approach has been taken in this work, and extended and applied to the system of shallow water equations (3.43), describing liquid films driven by shear stress and pressure gradient.

If one introduces the quantity $w = \sqrt{\sigma}\partial_x h/\sqrt{h}$, where $\sigma = We^{-1}$ is the capillary coefficient of the integrated equations, system (3.43) recalled at the previous page takes the form

$$\partial_t h + \partial_x(hU) = 0 \ , \tag{6.8}$$

$$\partial_t(hU) + \partial_x(hU^2 + P) = \frac{1}{Re}\Big[\Lambda h - \frac{3U}{h} + \frac{3}{2}\tau_i - T\Big] + \partial_x(\varphi(h)\partial_x w) \ , \tag{6.9}$$

$$\partial_t(hw) + \partial_x(hUw) = -\partial_x(\varphi(h)\partial_x U) \ , \tag{6.10}$$

where $U = q/h$ and $\varphi(h) = h^{3/2}\sqrt{\sigma}$. Equation (6.10) has been obtained after multiplication of the continuity equation by $\sqrt{h\sigma}$ and subsequent derivation with respect to x. It is worthwhile to mention that developing the term $\partial_x(\varphi(h)\partial_x w)$ into the equation (6.9), one exactly gets the surface tension term of system (3.43). As a matter of fact, discrete shallow water equations have been expressed by reducing the order of the system with an evolution equation for w. It thus contains only second derivatives in x. This additional equation can be seen as an internal energy equation.
Following Noble & Vila [57], system (6.8-6.10) can be written in the conservative form

$$\partial_t v + \partial_x f(v) = s(v) + \partial_x(B(h)\partial_x z) \ , \tag{6.11}$$

where $v = (h, hU, hw)^T$ is the conserved variable vector of shallow water equations and $f(v) = (hU, hU^2 + P, hUw)^T$ the corresponding flux. Vector $s(v)$ and matrix $B(h)$ are defined as

$$s(v) = \begin{Bmatrix} 0 \\ \frac{1}{Re}\Big[\Lambda h - \frac{3U}{h} + \frac{3}{2}\tau_i - T\Big] \\ 0 \end{Bmatrix} \ , \qquad B(h) = \begin{pmatrix} 0 & 0 & 0 \\ 0 & 0 & \varphi \\ 0 & -\varphi & 0 \end{pmatrix} \ , \tag{6.12}$$

and the matrix $B(h)$ is antisymmetric. On the other hand, one can designate the total energy of the system as sum of kinetic and thermodynamic free energies, namely $E = h(U^2/2 + w^2/2) + F(h)$. By expressing it as function of conserved variables v, then $z = \nabla_v E(v)$ represents the "entropy variable" vector, that is $z = ((U^2/2 + w^2/2) + F', U, w)$. Note that function $F(h)$ does not enter in the equation (6.11) given that the first column of $B(h)$ contains all zeros, namely[†]

$$B(h)\partial_x z = \begin{Bmatrix} 0 \\ \varphi\partial_x w \\ -\varphi\partial_x U \end{Bmatrix} \ . \tag{6.13}$$

[†]As a matter of fact, if one wants to express the function $F(h)$, this follows from the relation $hF' - F = P$, where the prime denotes the derivative with respect to h, and P is given in (3.44). Therefore, $F(h)$ takes the form

$$F(h) = h\int_0^h P(r)r^{-2}\,dr \ .$$

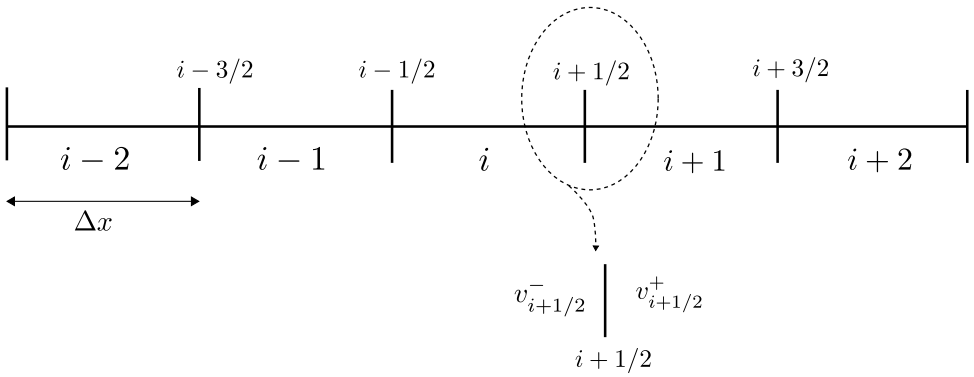

Figure 6.5: Sketch of the stencil of the film mesh, and definitions of variables at the interface.

Only a few numerical schemes applied to equations (6.8-6.10) are found to be entropy stable, see [57] for further details. Among those, Rusanov scheme has been adopted here to discretize system (6.8-6.10).

6.2.1 Spatio-temporal discretization schemes

Discrete equations of the film code have been obtained by means of a second-order accurate space discretization, and the Rusanov flux for the approximate Riemann solver. Time discretization is computed through the Heun's method, which can be seen as an improved Euler's method or a two-step Runge-Kutta method. Before showing the time discretization technique, it is appropriate to present the space discretization under the simpler case of Forward Euler time discretization. Only then, a detailed procedure of Heun's method will be analyzed.

With reference to Figure 6.5, by integrating equations (6.11) over the cell i and the time interval $(n, n+1)$, one obtains

$$v_i^{n+1} = v_i^n - \frac{\Delta t}{\Delta x}(f^n_{i+1/2} - f^n_{i-1/2}) + \Delta t s_i^n + \frac{\Delta t}{\Delta x^2}[B^n_{i+1/2}(z^n_{i+1} - z^n_i) - B^n_{i-1/2}(z^n_i - z^n_{i-1})] \,, \quad (6.14)$$

where indices i, $i+1$, $i-1$ refer to central, right and left cells respectively, while $i+1/2$ and $i-1/2$ specify interface values. This is an *explicit* scheme, in the sense that discrete equations (6.14) contain only one unknown at time level $n+1$. In line with the finite volume technique, the integration of equations (6.11) produces cell averaged quantities. Therefore, one can define v_i^n as the mean value within the cell i of v at time n, namely

$$v_i^n = \frac{1}{\Delta x}\int_{x_{i-1/2}}^{x_{i+1/2}} v^n(x)\, dx \,. \quad (6.15)$$

Similarly, the integration of the source term $s(v)$ leads to

$$\int_{t^n}^{t^{n+1}} \int_{x_{i-1/2}}^{x_{i+1/2}} s(x,t)\, dt dx \simeq \Delta x \Delta t \; s_i^n \,, \quad (6.16)$$

where the approximation arises because s_i^n represents the averaged value in space of s at time n, rather than averaged value in space and time, as it should be. Recalling the momentum equation (6.9) of the augmented system of shallow water equations, the source term contains space and time derivatives of interfacial shear stress τ_i and pressure gradient $-G$ provided by the gas to the liquid film, through the term T defined in (3.45). Space derivatives have been discretized by means of central difference approximations, namely

$$(\partial_x \tau_i)_i^n = \frac{(\tau_i)^n_{i+1} - (\tau_i)^n_{i-1}}{2\Delta x} \,, \qquad (\partial_x G)_i^n = \frac{G^n_{i+1} - G^n_{i-1}}{2\Delta x} \,, \quad (6.17)$$

while respective time derivatives have been approximated with a backward discretization, that is

$$(\partial_t \tau_i)_i^n = \frac{(\tau_i)_i^n - (\tau_i)_i^{n-1}}{\Delta t} \ , \qquad (\partial_t G)_i^n = \frac{G_i^n - G_i^{n-1}}{\Delta t} \ . \tag{6.18}$$

On the contrary, flux f and matrix B, as well as derivatives $\partial_x z$, must be evaluated at the interface separating two adjacent cells, and are defined as

$$f_{i+1/2}^n \simeq \frac{1}{\Delta t} \int_{t^n}^{t^{n+1}} f_{i+1/2}(t)\, dt \ , \tag{6.19}$$

$$B_{i+1/2}^n \partial_x z^n \simeq \frac{1}{\Delta t} \int_{t^n}^{t^{n+1}} [B_{i+1/2}(t) \partial_x z(t)]\, dt \ . \tag{6.20}$$

Yet, given that superscript n specifies evaluation at time n rather than time averaged quantities, time integrations are not exact. Furthermore, $(z_{i+1}^n - z_i^n)/\Delta x$ approximates $\partial_x z^n$ at the interface $i + 1/2$, where z_i^n is the "entropy variable" vector within the cell i at time n. In order to write the matrix B at the interface, one can express $\varphi_{i+1/2} = \sqrt{\sigma}((h_{i+1} + h_i)/2)^{3/2}$ from the definition of φ previously provided. The formulation of fluxes at the interface is obtained by considering that the discontinuity between left and right averaged sides produces a *Riemann problem*. Therefore, this discontinuity is solved with the Rusanov scheme, which is demontrated to be entropy stable for the Euler-Korteweg equation, see [57]. Omitting the superscript n, Rusanov flux yields (Toro [86])

$$f_{i+1/2} = \frac{f(v_{i+1/2}^+) + f(v_{i+1/2}^-)}{2} - \max_{i+1/2^\pm} [U + e] \frac{v_{i+1/2}^+ - v_{i+1/2}^-}{2} \ , \tag{6.21}$$

where the characteristic velocity e^2 has been defined in (5.19) and $U = v(2)/v(1)$. Quantities $v_{i+1/2}^+$ and $v_{i+1/2}^-$ are the right and left states across the interface in $i+1/2$, respectively, as sketched in Figure 6.5. These can be found through a MUSCL space discretization, which leads to

$$v_{i+1/2}^- = v_i + \frac{v_{i+1} - v_{i-1}}{4} \ , \tag{6.22a}$$

$$v_{i+1/2}^+ = v_{i+1} - \frac{v_{i+2} - v_i}{4} \ . \tag{6.22b}$$

The use of the MUSCL approximation, i.e. second-order space discretization, can be recovered from the stencil of Figure 6.5: in order to compute left and right interface states, one needs to know averaged values within two cells backward and forward, namely $i - 2$ and $i + 2$, respectively. On the contrary, for a first-order space discretization, one needs only values in the center of adjacent cells.
Specifically, in the equation (6.21) the characteristic velocity $e^2 = dP/dh$, where P is the "pressure" term defined in (3.44), reads

$$e^2 = \frac{2}{45}\Lambda^2 h^4 + \frac{4}{15}\Lambda \tau_i h^3 + \frac{1}{4}\tau_i^2 h^2 + \frac{h}{Fr}\cos\beta \ . \tag{6.23}$$

This velocity e^2 must be positive in order to deal with hyperbolic equations (Whitham [93]). Particularly, all terms of (6.23) are positive, with the exception of the term in $\Lambda\tau_i$: as a consequence, the sign of e^2 has to be always verified a posteriori. For example, Figure 6.6 shows the time evolution of minimum normalized e^2 corresponding to the test to be analyzed in detail in Chapter 8: an air-water system flowing in a confined channel with $Re_1 = 4.48$ and $Re_2 = 36.8$. It is shown that in this configuration e^2 is always positive and the corresponding equations are thus hyperbolic.

As mentioned before, the Heun's method has been adopted here as time discretization technique. Since this method is an improved Euler's method or a two-step Runge-Kutta

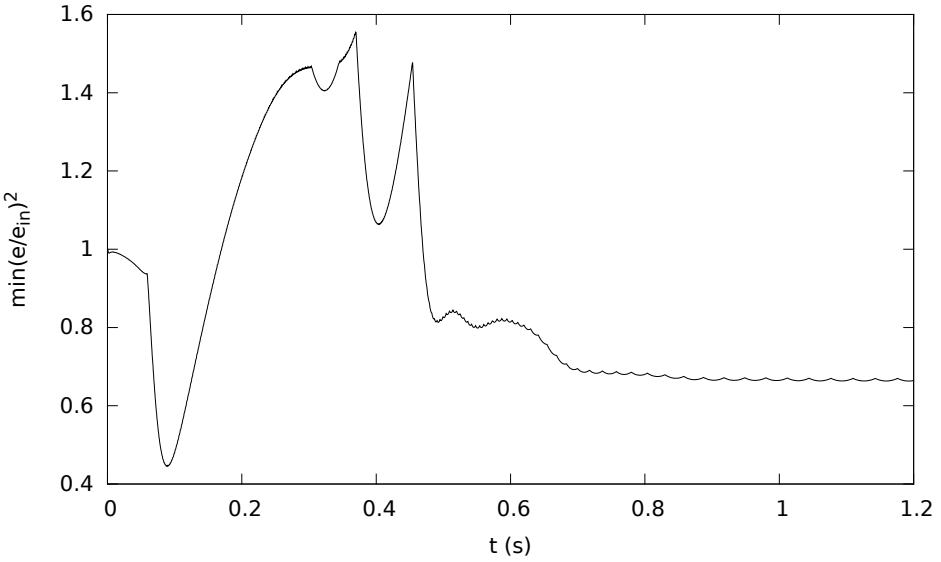

Figure 6.6: Time evolution of the minimum characteristic velocity e^2 normalized with the initial value $e_{in} = 2.5 \cdot 10^{-4}\ m^2 s^{-2}$. Two-layer flow with dimensionless numbers: $Re_1 = 4.48$, $Re_2 = 36.8$, $Fr = 0.93$, $We = 0.002$, and geometry given by $\tilde{H} = 0.39\ mm$ and $\lambda = 26\ mm$. After $0.7\ s$ periodic waves appear.

method, the solution at time $n+1$ is obtained by two levels of approximation rather than one. Indeed, the first level of time approximation has the same form as the Forward Euler (6.14), and the solution can be defined as $v_i^{n+1/2}$, namely

$$v_i^{n+1/2} = v_i^n - \frac{\Delta t}{\Delta x}(f_{i+1/2}^n - f_{i-1/2}^n) + \Delta t s_i^n + \frac{\Delta t}{\Delta x^2}[B_{i+1/2}^n(z_{i+1}^n - z_i^n) - B_{i-1/2}^n(z_i^n - z_{i-1}^n)] \ , \tag{6.24}$$

Then, the solution at time $n+1$ reads

$$\begin{aligned} v_i^{n+1} = & \frac{v_i^n + v_i^{n+1/2}}{2} - \frac{\Delta t}{\Delta x}\frac{f_{i+1/2}^{n+1/2} - f_{i-1/2}^{n+1/2}}{2} \\ & + \frac{\Delta t}{2}\left[s_i^{n+1/2} + \frac{1}{\Delta x^2}\Big(B_{i+1/2}^{n+1/2}(z_{i+1}^{n+1/2} - z_i^{n+1/2}) - B_{i-1/2}^{n+1/2}(z_i^{n+1/2} - z_{i-1}^{n+1/2}) \Big) \right] , \end{aligned} \tag{6.25}$$

where superscript $n+1/2$ refers to quantities evaluated at the first step of Heun's method.

6.2.2 The CFL condition for the augmented system of shallow water equations

The CFL condition is a necessary condition for the stability of numerical schemes. Indeed it imposes that the computational domain is contained into the physical domain. This condition drives to a relation between space and time discretization to be satisfied in every cell and at each time step. Without surface tension, this condition reads $\Delta t \leq \Delta x/|U+e|$ for the classical finite volume schemes. Instead, for the augmented system of shallow water equations (6.8-6.10) it is given by (Noble & Vila [57])

$$\Delta t \leq \frac{7^{7/6}\sqrt{3}}{24}\left(\frac{\sqrt{U+e}}{\sigma}\right)^{2/3} \Delta x^{7/3} + \mathcal{O}(\Delta x^{10/3}) \ , \tag{6.26}$$

for sufficiently small Δx and using a MUSCL space discretization with the Riemann solver of Rusanov. In addition, although expression (6.26) has been found by Noble & Vila for

the Euler-Korteweg system, i.e. by neglecting source terms in (6.9), it is used here as CFL condition for the film code.

At this stage, the film code has been entirely described. This code has been subsequently coupled to compressible Navier-Stokes equations by means of the ALE technique. As further step, the description of the gas code will be shown, as well as the coupling methodology.

6.3 Discrete compressible Navier-Stokes equations

For a two-dimensional problem, such as the problem considered here, see bottom of Figure 6.2, compressible Navier-Stokes equations (6.3) take the form

$$\begin{cases} \partial_t \rho + \partial_x(\rho u) + \partial_y(\rho v) = 0 \\ \partial_t(\rho u) + \partial_x(\rho u^2) + \partial_y(\rho uv) = -\partial_x p + F_x + \mu(2\partial_{xx}u + \partial_{yy}u + \partial_{xy}v) \\ \partial_t(\rho v) + \partial_x(\rho uv) + \partial_y(\rho v^2) = -\partial_y p + F_y + \mu(2\partial_{yy}v + \partial_{xx}v + \partial_{xy}u) \end{cases} , \tag{6.27}$$

where the tilde will be omitted from now onwards to simplify all notations.[‡] This system of equations has been discretized with a first-order space-time discretization by using a low-Mach scheme in addition to the ALE technique. The low-Mach scheme, based on the work of Grenier *et al.* [32], allows for solving compressible flows at low speeds, where classical approximate Riemann solvers are very dissipative, given that the flow velocity is much smaller than the sound celerity. The main reason for solving flows at low Mach number with compressible schemes is due to the fact that this approach can be then extended to industrial codes, such as CEDRE platform [67] developed at ONERA.
On the other hand, the ALE technique is used in coupling the low-Mach scheme with shallow water equations for the liquid phase, and must be considered when developing the discrete compressible Navier-Stokes equations. Particularly, the ALE moving mesh allows for transferring the interface position from the liquid to the gas and will be detailed later.

Before showing the analysis of the discrete equations and the low-Mach scheme, one checks how the Navier-Stokes equations are modified by the node motion of the grid. Recalling the equations (6.3), this system can be written as (neglecting the tilde and the subscript)

$$L_{\mathbf{u}} = -\nabla \cdot \mathbf{\Sigma}^E + \nabla \cdot \mathbf{T} + \mathbf{F} , \tag{6.28}$$

where $L_{\mathbf{u}} = \partial_t \phi + \nabla \cdot (\phi \otimes \mathbf{u})$. The vector $\phi = (\rho, \rho u, \rho v)^T$ is the conserved variable vector, while $\mathbf{\Sigma}^E$ is the "pressure contribution" of the stress tensor $\mathbf{\Sigma} = -\mathbf{\Sigma}^E + \mathbf{T}$. These are defined as

$$\mathbf{\Sigma}_x^E = \begin{Bmatrix} 0 \\ p \\ 0 \end{Bmatrix} , \qquad \mathbf{\Sigma}_y^E = \begin{Bmatrix} 0 \\ 0 \\ p \end{Bmatrix} , \qquad \mathbf{T}_x = \begin{Bmatrix} 0 \\ T_{xx} \\ T_{xy} \end{Bmatrix} , \qquad \mathbf{T}_y = \begin{Bmatrix} 0 \\ T_{xy} \\ T_{yy} \end{Bmatrix} . \tag{6.29}$$

When the grid moves, a mesh velocity has to be involved into the Navier-Stokes equations. For the moment, one can define a generic mesh velocity $\hat{\mathbf{u}}$ for each edge, to be defined later, corresponding to the node motion. Therefore, the effect of the arbitrary motion of the computational mesh leads to rewrite equations (6.28) as

$$L_{\hat{\mathbf{u}}} = -\nabla \cdot [\mathbf{\Sigma}^E + \phi \otimes (\mathbf{u} - \hat{\mathbf{u}})] + \nabla \cdot \mathbf{T} + \mathbf{F} , \tag{6.30}$$

[‡]For convenience, the analysis of the film code has been described in dimensionless variables, while the gas code will be shown via a dimensional approach.

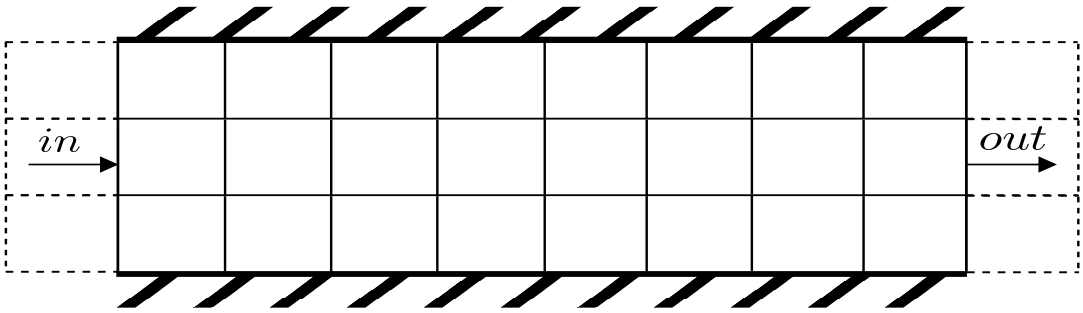

Figure 6.7: Sketch of the gas mesh and definitions of periodic boundary conditions.

where $L_{\hat{\mathbf{u}}} = \partial_t \phi + \nabla \cdot (\phi \otimes \hat{\mathbf{u}})$. Finally, the motion of the grid modifies only the inviscid side of the equations.

6.3.1 Low-Mach scheme description

In developing the above mentioned low-Mach scheme, it is appropriate to treat separately inviscid and viscous contributions of (6.30), since spatial discretization of viscous terms requires specific attention. Therefore, equations (6.30) without both the viscous terms and body force read

$$\begin{cases} L_{\hat{\mathbf{u}}}(\rho) + \nabla \cdot [\rho(\mathbf{u} - \hat{\mathbf{u}})] = 0 \\ L_{\hat{\mathbf{u}}}(\rho \mathbf{u}) + \nabla \cdot [(\rho \mathbf{u} \otimes (\mathbf{u} - \hat{\mathbf{u}})] + \nabla p = 0 \end{cases} . \tag{6.31}$$

The geometry considered for the gas code is shown in the bottom of Figure 6.2. The code is thus two-dimensional and an example of cell grid is sketched in Figure 6.7. However, thanks to the ALE technique, all nodes can move into the domain causing that initial rectangular cells modify the shape. Details about the ALE development will be treated later for the coupling strategy. Figure 6.8 shows two different notations used in the following for the development of discrete equations: on the left, K designates the cell, Ke its neighborhood cells and $\mathbf{n}_{e,K}$ the outward normal corresponding to the edge e; on the right, classical ij notations are presented, and these turn useful because the code is developed on a structured grid. Therefore, equations (6.31) are discretized as

$$\rho_K^{n+1} = \frac{m_K^n}{m_K^{n+1}} \rho_K^n - \frac{\Delta t}{m_K^{n+1}} \sum_{e \in \partial K} \left(l^- \rho_{Ke}^{n+1} + l^+ \rho_K^{n+1} \right) m_e^{n+1} , \tag{6.32}$$

$$\rho_K^{n+1} \mathbf{u}_K^{n+1} = \frac{m_K^n}{m_K^{n+1}} \rho_K^n \mathbf{u}_K^n + \frac{\Delta t}{m_K^{n+1}} \sum_{e \in \partial K} \left(l^- \rho_{Ke}^{n+1} \mathbf{u}_{Ke}^n + l^+ \rho_K^{n+1} \mathbf{u}_K^n + p_e^{n+1} \mathbf{n}_{e,K} \right) m_e^{n+1} , \tag{6.33}$$

where ∂K is the cell contour, m_K the cell surface and m_e the length of the edges. By definition (Grenier *et al.* [32]),

$$l^- = \min[\mathbf{w}_e^n \cdot \mathbf{n}_{e,K}, 0] - \gamma_e \max[p_{Ke}^{n+1} - p_K^{n+1}, 0] , \tag{6.34a}$$

$$l^+ = \max[\mathbf{w}_e^n \cdot \mathbf{n}_{e,K}, 0] - \gamma_e \min[p_{Ke}^{n+1} - p_K^{n+1}, 0] , \tag{6.34b}$$

$$\mathbf{w}_e^n = \frac{1}{2}(\mathbf{u}_K^n + \mathbf{u}_{Ke}^n) - \hat{\mathbf{u}}_e^n , \tag{6.34c}$$

$$p_e^{n+1} = \frac{1}{2}(p_K^{n+1} + p_{Ke}^{n+1}) . \tag{6.34d}$$

The superscript n refers to the time step, while the parameter γ_e is instead a positive coefficient to be adjusted later for scheme stability. The velocity $\mathbf{w}_e^n$ defined on the edge e at time n takes into account also the ALE velocity $\hat{\mathbf{u}}_e^n$, to be defined later.

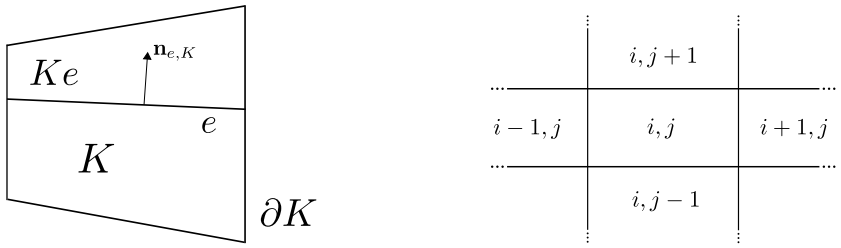

(a) *Notations for cell K.* (b) *Notations for cell i, j.*

Figure 6.8: Two different cell notations for the low-Mach scheme used in this work.

Furthermore, linearizing the equation of state around the base state, the pressure p can be written as $p = p^\star + a^2(\rho - \rho^\star)$, $p^\star$ and $\rho^\star$ being reference pressure and density and a the sound celerity. Discrete equation (6.32) is implicit, meaning that there are several unknowns at level $n+1$. On the other hand, equation (6.33) is explicit and thus the whole velocity field can be directly found when the density is known.
The implicit mass conservation equation (6.32) can be put in the form $\Phi(\underline{\rho}) = 0$, where $\underline{\rho} = (\rho_{ij}^{n+1}, \rho_{i+1,j}^{n+1}, \rho_{i,j+1}^{n+1}, \rho_{i-1,j}^{n+1}, \rho_{i,j-1}^{n+1})^T$ contains all unknowns for the cell i, j at time step $n+1$. These unknowns are five because every cell has four neighborhood cells, as shown in Figure 6.8b. Function $\Phi(\underline{\rho})$ is expressed in the Appendix D, equation (D.1).
Non-linear system $\Phi(\underline{\rho}) = 0$ can be solved by means of the Newton method, for which it takes the form

$$\Phi(\underline{\rho}^p) + \mathbf{J}(\underline{\rho}^p)\ [\underline{\rho}^{p+1} - \underline{\rho}^p] = 0\ , \tag{6.35}$$

where the superscript p identifies the Newton step, and $\mathbf{J}$ the Jacobian matrix of derivatives of Φ with respect to ρ, say Φ_ρ. The explicit form of linear system (6.35), as well as derivatives Φ_ρ, are given in the Appendix D. The procedure to create the Jacobian matrix and solve the linear system (6.35) consists in:

1. evaluating the function Φ. At the initial Newton step ($p = 0$) quantities $\underline{\rho}^p$ are known, either as initial condition at $t = 0$ or as the state at time n;

2. expressing the derivatives Φ_ρ (see Appendix D, equation (D.3));

3. creating the matrix $\mathbf{J}(\underline{\rho}^p)$. It is worthwhile to mention that every row of $\mathbf{J}$ has five coefficients, corresponding to densities into the central cell plus one for each neighborhood cells, whereas all other coefficients are zero;

4. solving the linear system (6.35) and finding the unknowns at step $p+1$;

5. verifying the convergence of the Newton method, imposing

$$\max_{ij} \left[\frac{\underline{\rho}^{p+1} - \underline{\rho}^p}{\underline{\rho}^p} \right] < \epsilon\ , \tag{6.36}$$

   where ϵ is a small arbitrary quantity;

6. when the condition (6.36) is satisfied, progressing in time by imposing $\underline{\rho}^{n+1} = \underline{\rho}^{p+1}$.

Knowing all densities at the time step $n+1$ for each cell, it is possible to solve explicitely momentum balance equations (6.33), whose discrete form is expressed in (D.5) for the first component of the velocity field.

6.3.2 Viscous stress discretization

Once the discretization of the inviscid part of the Navier-Stokes equations (6.3) has been described, viscous terms can be developed in discrete form. The viscous stress tensor $\mathbf{T}$ is given by

$$\mathbf{T} = 2\mu\mathbf{D} + \zeta\nabla\cdot\mathbf{u}\mathbf{I} \simeq 2\mu\mathbf{D} \ , \tag{6.37}$$

where μ and ζ are dynamic and bulk viscosity coefficients, respectively. The matrix $\mathbf{D} = (\nabla\mathbf{u} + \nabla\mathbf{u}^T)/2$ is the strain tensor, whereas $\mathbf{I}$ is the identity matrix. The approximation sign in the definition (6.37) arises by considering that the numerical method presented here is applied to laminar flows in duct at low speeds: the flow is thus assumed to be incompressible, namely $\nabla\cdot\mathbf{u} = 0$. Furthermore, when applying the divergence operator to the strain tensor $\mathbf{D}$, it is appropriate to recall the definition

$$\nabla\cdot\nabla\mathbf{u}^T = \nabla(\nabla\cdot\mathbf{u}) \ . \tag{6.38}$$

Therefore, the above mentioned incompressibility condition leads to $\nabla\cdot\mathbf{T} \simeq \nabla\cdot(\mu\nabla\mathbf{u})$. Finally, the viscous tensor discretization resolves into the discretization of the velocity gradient only. With the help of the Gauss theorem, the divergence of the velocity gradient consists in the evaluation of the gradient of velocity on every edge. The goal is thus to reconstruct the velocity gradient on the edge starting from the averaged velocity in the center of each cell. By doing so, one can write for each cell K

$$\begin{aligned}\nabla\cdot\mathbf{T}_K &= \mu\sum_{e\in\partial K}(\nabla\mathbf{u})_e\cdot\mathbf{n}_{e,K}\ m_e \\ &= \mu\sum_{e\in\partial K}\frac{\mathbf{u}_{Ke}-\mathbf{u}_K}{\|\mathbf{x}_{Ke}-\mathbf{x}_K\|^2}(\mathbf{x}_{Ke}-\mathbf{x}_K)\cdot\mathbf{n}_{e,K}\ m_e \ ,\end{aligned} \tag{6.39}$$

where the vector $(\mathbf{x}_{Ke} - \mathbf{x}_K)$ is the distance between the centers of the cell K and its neighborhood cells Ke. Expression (6.39) is valid on orthogonal cells, where the vector $(\mathbf{x}_{Ke}-\mathbf{x}_K)$ is perpendicular to the edge and parallel to its normal $\mathbf{n}_{e,K}$. For non-orthogonal cells, the previous expression is not consistent and one must improve it by considering the projection of the center vector on the normal to the edge. For example, Coudière *et al.* [20] have proposed the diamond technique based on the adoption of a diamond cell in order to recover the velocity gradient on the edge. In the present work, expression (6.39) has been employed also for non-orthogonal meshes, rather than the extension to the diamond technique. This leads to a certain error in quantifying the viscous stress and suggests an improvement for the present method. However, in the application considered here this error is minimal and can be neglected. As further justification of this approximation, two validation tests will be described in next chapter: the ALE Poiseuille flow, and a two-layer flow in a confined channel showing good agreement between the computed shear stress and the asymptotic evolution provided in Chapter 4, which is valid due to the narrow geometry.

6.3.3 Boundary conditions

With reference to Figure 6.2, the bottom wall of the gas domain coincides with the interface of the liquid film: it is a moving wall which follows both the film velocity and the position of the interface, as it will be detailed later. The top wall is instead fixed and rigid, in a way that both the velocity field and the displacement of the wall are zero. Furthermore, the density corresponding to top and bottom ghost cells has been taken equal to the density into the cell K. In other words, the density satisfies symmetry boundary conditions at top and bottom walls.

On the contrary, periodic boundary conditions are employed at right and left sides of the domain, imposing closed flow conditions, i.e. the amount of gas quitting from the

right corresponds to what enters from the left. Therefore, ghost cells at the left boundary behaves as the first ones, and vice versa.
For example, one fills the matrix $\mathbf{J}$ by respecting these conditions. If the rectangular domain has N_x and N_y cells in x- and y-directions, respectively, when solving the Newton method (6.35) the number of unknowns is then $N_x \cdot N_y$, and the size of the vector $\underline{\delta\rho}^p = [\underline{\rho}^{p+1} - \underline{\rho}^p]$ is $(N_x \cdot N_y, 1)$, as well as the vector $\Phi(\underline{\rho}^p)$. Size of the matrix $\mathbf{J}(\underline{\rho}^p)$ is instead $(N_x \cdot N_y, N_x \cdot N_y)$. Hence, the row of the matrix corresponding to the boundary cell $(1, N_y)$ reads

$$\mathbf{J}(\kappa,\kappa) = \Phi_{\rho_{i,j}}(\underline{\delta\rho}^p) + \Phi_{\rho_{i,j+1}}(\underline{\delta\rho}^p) \ , \tag{6.40a}$$

$$\mathbf{J}(\kappa,\kappa + N_x - 1) = \Phi_{\rho_{i-1,j}}(\underline{\delta\rho}^p) \ , \tag{6.40b}$$

$$\mathbf{J}(\kappa,\kappa + 1) = \Phi_{\rho_{i+1,j}}(\underline{\delta\rho}^p) \ , \tag{6.40c}$$

$$\mathbf{J}(\kappa,\kappa - N_x) = \Phi_{\rho_{i,j-1}}(\underline{\delta\rho}^p) \ , \tag{6.40d}$$

where $\kappa = i + N_x(j-1)$ is the single index connected to the matrix, lying in the range $[1, N_x \cdot N_y]$. The element $\mathbf{J}(\kappa,\kappa)$ has a double contribution due to the symmetry condition on the density field, while the left periodic boundary condition occur for the element $\mathbf{J}(\kappa,\kappa + N_x - 1)$.

6.3.4 The stability criterion

Similarly to the film code, in order to check the stability of the above described low-Mach scheme, one can impose the entropy of the system being time decreasing. This leads to two stability conditions to be verified, one limiting the time step and the other the parameter γ_e, namely (Grenier *et al.* [32])

$$\Delta t \leq \frac{m_K}{2 l_K m_{\partial K}} \ , \tag{6.41}$$

$$\gamma_e \geq \Delta t \max\left[\frac{m_{\partial K}}{2\rho_K^{n+1} m_K}, \frac{m_{\partial Ke}}{2\rho_{Ke}^{n+1} m_{Ke}}\right] \ , \tag{6.42}$$

where $m_{\partial K}$ is the cell perimeter and l_K is defined as

$$l_K = \frac{1}{\rho_K^{n+1} m_K} \sum_{e \in \partial K} |l^-| \rho_{Ke}^{n+1} m_e \ . \tag{6.43}$$

Condition (6.41) can be seen as a CFL condition for the low-Mach scheme. Indeed, $m_K/m_{\partial K}$ is nothing but a characteristic length of the mesh, such as Δx or Δy. Furthermore, this stability condition does not contain the sound celerity, thanks to the implicit form of the mass conservation (6.32). This represents a great advantage for flows at low speed, since the velocity is much smaller than the sound celerity.
Although the above described low-Mach scheme takes into account also the ALE technique, conditions (6.41) and (6.42) have been adopted in the present work.

6.4 Coupling approach development

After the description of film and gas codes, physical and numerical coupling between the two can be finally discussed. Figure 6.9 resumes all steps of the coupling process in the range $(n, n+1)$:

1. the film code computes film thickness h and averaged velocity U at time level $n+1$. By doing so, equation (6.9) shows that interfacial shear stress τ_i and pressure gradient

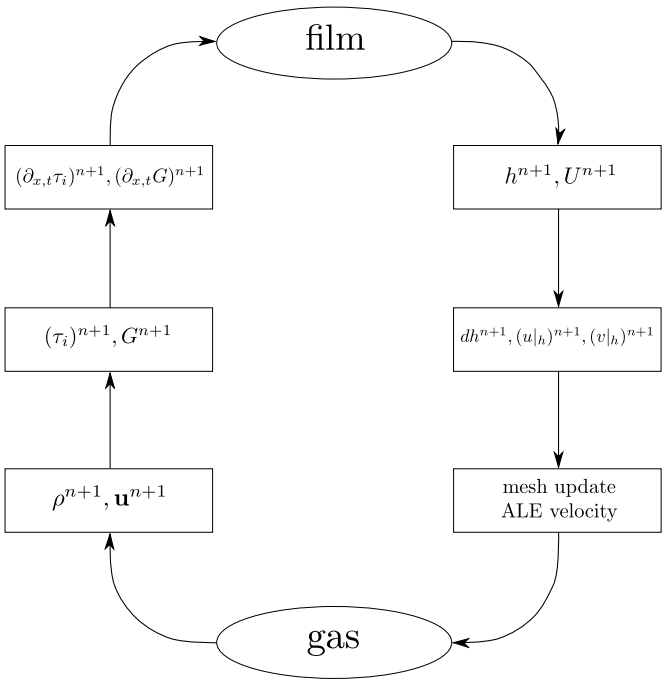

Figure 6.9: Sketch of the coupling methodology and time progress $n \longrightarrow n+1$.

$-G$, as well as their respective spatio-temporal derivatives must be known. These are given either from the previous computation at time n or from the initial condition at time $t = 0$, where perturbed equilibrium conditions are imposed;

2. film thickness h^{n+1} and averaged velocity U^{n+1} can be then used to evaluate the velocity field at the interface, namely $(u|_h)^{n+1}$ and $(v|_h)^{n+1}$, and the displacement of the interface with respect to the previous time step;

3. subsequently, the position of the interface at time $n+1$ can be manipulated to update the mesh of the gas code. The bottom cell of the grid moves exactly as the interface, while the motion of all other nodes is submitted to a mesh-update law, to be discussed later;

4. the displacement of every single node allows for evaluating the ALE velocity $\hat{\mathbf{u}}$ corresponding to each edge;

5. the gas code takes interfacial velocities and updated mesh and velocity as input to compute density and velocity fields at time step $n + 1$, in line with the low-Mach scheme previously discussed;

6. finally, interfacial shear stress τ_i^{n+1} and pressure gradient $-G^{n+1}$ can be computed, as well as their respective spatio-temporal derivatives by means of central difference and backward discretization.

This coupling methodology applies a first-order time discretization and is explicit, in a way that the gas code adopts at time level n the output provided by the film evaluated at the step $n + 1$. As a consequence, the time step is imposed by the minimum between the two codes. In certain configurations, the viscous time step $t_v \simeq \Delta y^2/\nu_g$ represents the lower limit, since the discrete viscous term (6.39) is treated explicitely. Otherwise, the time step is imposed by the film stability (6.26). Yet, the implicit mass conservation equation used in the developed low-Mach scheme allows to dispose of a weak stability criterion (6.41).

6.4.1 Film to gas coupling

As already stated, the film code takes interfacial shear stress τ_i and pressure gradient $-G$ as input for the computation of film thickness h and averaged velocity U, following the numerical scheme (6.11). Nevertheless, the gas code requires velocities evaluated at the interface, as well as the displacement of the interface at each time step.
From the averaged velocity U, one can obtain the interfacial longitudinal velocity $u|_h$ by means of the asymptotic expansion discussed in Chapter 3. Particularly, the leading-order velocity profile (3.23) is used to evaluate the interfacial longitudinal velocity $u|_h$ at order zero, to be justified at the end of this paragraph. Indeed, this can be written directly as function of the averaged film velocity U as

$$(u|_h)_i^{n+1} = \frac{3}{2}U_i^{n+1} + \frac{1}{4}(\tau_i)_i^n \ , \tag{6.44}$$

where the use of the shear stress at time n is due to the explicit coupling methodology which causes a *delay* of the evaluation process. For what concerns the transversal interfacial velocity, the kinematic boundary condition yields

$$(v|_h)_i^{n+1} = (\partial_t h)_i^{n+1} + (u|_h)_i^{n+1}(\partial_x h)_i^{n+1} \ , \tag{6.45}$$

after appropriate discretization of $\partial_{x,t}h$ with central difference and backward approximations, namely

$$(\partial_x h)_i^{n+1} = \frac{h_{i+1}^{n+1} - h_{i-1}^{n+1}}{2\Delta x} \ , \qquad (\partial_t h)_i^{n+1} = \frac{h_i^{n+1} - h_i^n}{\Delta t} \ . \tag{6.46}$$

The interfacial velocity (6.44) is obtained at order zero and transfered to the gas. As a consequence, the gas receives the position of the interface and the interfacial transversal velocity both consistent with the order one, while the interfacial longitudinal velocity at order zero. This does not imply great errors on the coupling approach and is justified by two issues: firstly, first-order fields greatly modify the interface shape, but remain very small compared to leading-order's. This will be shown in Chapter 7 when comparing zeroth- and first order stress fields. Secondly, film thickness h is correct at the order one because derived from consistent equations (6.8-6.10) and is well sent to the gas. Therefore, the effect of transferring leading-order interfacial velocity from the film to the gas is a good estimate, given that the interface is computed at order one and moved to the gas.

6.4.2 ALE method development

In this section, the development of the ALE technique is discussed. This technique is a combination of Eulerian and Lagrangian approaches, since the nodes of the grid can move arbitrarily, and has the advantage to handle high mesh distortion avoiding fine resolutions. Indeed, it solves the main shortcomings of Eulerian and Lagrangian descriptions.
During last decades, the ALE technique has been applied for the resolution of free-surface flows, such as the works of Hirt *et al.* [37] on finite difference mesh and Soulaïmani *et al.* [81] for finite element discretization. Particularly, Ramaswamy *et al.* [66] have applied the ALE technique on finite element mesh to describe thin liquid film instabilities by means of Navier-Stokes equations, by validating their approach with comparison to the experiments of Liu & Gollub [47]. Donea *et al.* [26] have instead applied the ALE method in the context of fluid-structure interactions. On the contrary, the combination of the ALE technique and the low-Mach scheme, as developed in this work, and its application to thin liquid films modeled through shallow water equations represents a novelty from computational and modeling points of view.

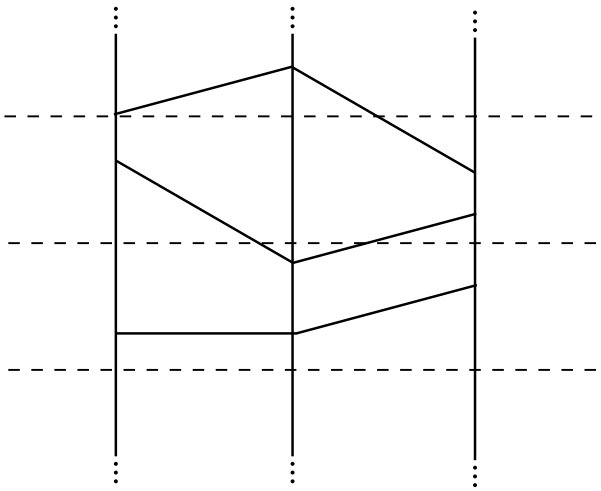

Figure 6.10: Sketch of cell displacement through the ALE technique. Dashed lines indicate the starting orthogonal configuration.

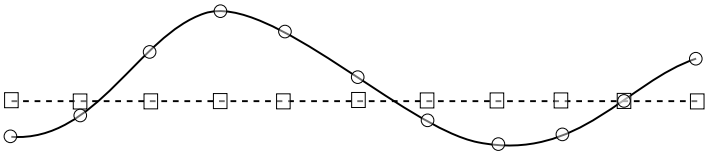

Figure 6.11: Node displacements through the ALE technique at the interface liquid-gas. The dashed line indicates the uniform flow.

In the developed low-Mach computational scheme, it has been chosen that grid nodes can move along the vertical direction only. Therefore, the initial rectangular shape of cells turn possibly into trapezoid, because left and right edges remain always parallel to each other, as sketched in Figure 6.10. Given the position of the interface at the time step $n+1$ and in the center of each film cell, say h_i^{n+1}, one can recover the position of each corresponding node relative to the equilibrium state h_0 (equal for every cell), namely

$$\delta_{i+1/2}^{n+1} = \frac{h_{i+1}^{n+1} + h_i^{n+1}}{2} - h_0 \ . \tag{6.47}$$

More precisely, since the domain of resolution of Navier-Stokes equations does not contain the liquid film, see Figure 6.2, the equilibrium film thickness h_0 must be subtracted from h at each time step. Furthermore, since the ALE technique demands node displacements rather than cell displacements, node position $\delta_{i+1/2}^{n+1}$ is sent to the gas to update each bottom node of the grid through the relation $dh_{i+1/2}^{n+1} = \delta_{i+1/2}^{n+1} - \delta_{i+1/2}^{n}$, which is the relative motion of the interface during time. Yet, $dh_{i+1/2}^{n+1}$ is the displacement of the gas mesh for all nodes in the bottom, at time $n+1$, as sketched in Figure 6.11. However, the ALE technique requires a mesh-update methodology which generates the new mesh at each time step. In the present work, with the aim to avoid strong mesh distortions, the grid is kept as regular as possible. Hence, an algebraic law is used in order to transfer the interface displacement $dh_{i+1/2}^{n+1}$ to all other nodes in the vertical direction. This law reads

$$dh_{i+1/2,\chi}^{n+1} = \frac{dh_{i+1/2}^{n+1}}{N_y}(N_y - \chi), \tag{6.48}$$

where $\chi = j + 1/2$ with $j = 1, \ldots, N_y - 2$. In order to avoid wall effects, top cells are fixed, namely $dh_{i+1/2,N_y-1/2}^{n+1} = 0$.

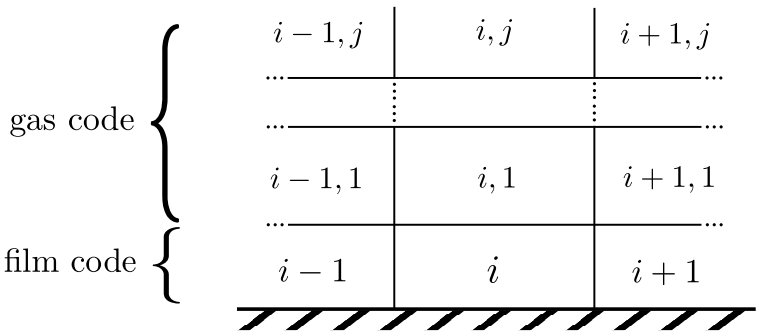

Figure 6.12: Film and gas mesh: coupling between the two codes and notations.

Another relevant feature of the ALE technique is the velocity assigned to each node. In this work, since the grid moves only in the y-direction, the longitudinal component $\hat{u}$ of the ALE velocity vanishes, namely $\hat{\mathbf{u}} = \left(\begin{smallmatrix} 0 \\ \hat{v} \end{smallmatrix}\right)$. The y-velocity component $\hat{v}$ is defined for every edge, based on the displacement of the nodes at both sides of the edge. It reads

$$\hat{v}_e = \frac{1}{dt}(dh_{N_1} + dh_{N_2}) \ , \tag{6.49}$$

where subscripts N_1 and N_2 refer to the two nodes of the edge e.

6.4.3 Gas to film coupling

The last step of the coupling methodology consists in the resolution of the gas flow and in the subsequent transfer of interfacial shear stress and pressure gradient to the film. Shear stress is computed on the bottom edges of the grid: in line with the expression (6.39), the interfacial shear stress provided by the gas code reads

$$(\tau_i)_K = \mu \frac{\mathbf{u}_S - \mathbf{u}_K}{\|\mathbf{x}_S - \mathbf{x}_K\|^2}(\mathbf{x}_S - \mathbf{x}_K) \cdot \mathbf{n}_{S,K} \ , \tag{6.50}$$

where the subscript S refers to the *South* cell of the generic cell K (or, alternatively the generic cell $(i, 1)$ in the bottom of the gas mesh), see Figure 6.12. However, the position of cell centers has to be determined at each time step in order to evaluate the discrete viscous shear stress. This can be achieved by means of the definition of the center of a trapezoid: it lies along the median of the two bases and is $h(2a + b)/3(a + b)$ distant from the longer base b (while a is the length of the shorter base and h the height of the trapezoid, that coincides with Δx in this configuration).

The pressure gradient is instead given by the x-momentum balance equation (6.33) completed by the viscous contribution (6.39) and possibly by a body force. Indeed, the pressure gradient in each cell is directly provided by

$$G_K^{n+1} = -\frac{1}{m_K^{n+1}} \sum_{e \in \partial K} p_e^{n+1} \mathbf{n}_{e,K} m_e^{n+1} \ . \tag{6.51}$$

This quantity is then transfered to the film code. Precisely, the liquid film needs the pressure gradient at the interface, rather than in the center of the first cell. As a matter of fact, it will be demonstrated in the next chapter that the pressure gradient (6.51) approximates well the one given by the asymptotic expansion described in Chapter 4.

Finally, spatio-temporal derivatives of interfacial shear stress and pressure gradient are computed as already shown in (6.17) and (6.18).

6.5 Additional remarks

Two-layer scenarios analyzed in this work are mainly focused on flows driven by pressure gradient, given by a pressure drop between the exit and the entry of the channel. However, the numerical schemes developed in this chapter are built with periodic boundary conditions at left and right sides. This is thus not consistent with a prescribed pressure drop, because periodic boundary conditions do not contemplate any difference between the flow quitting the domain and the flow entering from the left.
This shortcoming has been solved by replacing the pressure difference Δp with an acceleration applied into the domain $F_x = \Delta p/\rho L$. This acceleration depends on the density of each fluid and then assumes different values for liquid and gas (particularly, it is one thousand bigger in the gas flow). However, after appropriate substraction of F_x, the pressure gradient (6.51) keeps unaltered because its evolution is spatially periodic, since so does the film thickness h and all related quantities.

As additional remark, some spurious oscillations of the pressure field have been found when highly refining the mesh, particularly in the x-direction. Perhaps, these oscillations are given by the numerical coupling between the two codes. Indeed, this shortcoming has been solved in a first attempt by applying a filter to the pressure gradient transferred from the gas to the film. However, this problem does not affect all results presented here because there is no need to refine the mesh until spurious oscillations arise.

6.6 Conclusions

This chapter has presented the numerical methods used to describe the non-linear dynamics of a liquid film flowing in the bottom of a channel and sheared by a laminar gas flow. The liquid is thin compared to the wavelength of developing waves and has been thus simulated by means of the first-order long-wave model presented in Chapter 3. On the contrary, the gas flow has been treated with compressible Navier-Stokes equations, discretized with a low-Mach scheme, which works well at low speeds. The coupling methodology is based on an explicit transfer between the two phases, as well as by the transfer of the interface position thanks to the ALE technique. This numerical approach has been then implemented in MATLAB and the code SWANS has been developed.

Next chapter is dedicated to the validation of such a computational approach through appropriate test-cases, to be compared either to experiments or exact analytical solutions.

7 Validation of the SWANS numerical schemes by analytical solutions and experiments

This chapter has the purpose to show a few test-cases analyzed in this work to validate the code SWANS. Since SWANS is built by the coupling of film and gas codes, described in the previous chapter, the description of test-cases will start by presenting the validation of the film code. Subsequently, the validation of the gas code and the ALE technique will be shown, to conclude with the test of the coupling technique, which makes use of the asympotic expansions provided in Chapter 4.

7.1 Shallow water code's validation

This section aims to show the validity of the shallow water discretization previously described. Two main tests are presented here: the linear regime of a gravity-driven liquid film with the purpose to compare wave celerities and growth rates to the stability theory; the non-linear wave dynamics of falling films to be compared to the experiments available in the literature. Particularly, the linear regime is validated precisely, thanks to the reference solution found in Chapter 5. For what concerns the non-linear regime instead, the comparison with the experiments is performed on a qualitative level, as detailed later.

7.1.1 Linear stability of gravity-driven films

In order to validate the linear regime, one considers a liquid film falling down an inclined plane in a passive gas atmosphere. As in the experiments of Liu & Gollub [47], the liquid is a mixture of water-glycerin of 54% by weight, whose physical properties are shown in Table 7.1. The plane has an inclination of 6.4° with respect to the horizontal and the film flows down it at $Re = 8.5$: these two parameters are sufficient to fully describe the dynamics of such a flow. Nevertheless, following the definitions of Froude and Weber numbers, see

Table 7.1: Physical properties of fluids used for the validation tests of the single-layer model.

fluid	$\rho(kg\ m^{-3})$	$\nu(10^{-5}m^2s^{-1})$	$\gamma(10^{-3}N\ m^{-1})$
water-glycerin	1070	62.8	67
air	1.23	1.5	—

Table 7.2: Values of kh_0 and corresponding wavelengths λ of performed numerical tests.

kh_0	λ (mm)
0.0305	200
0.0406	150
0.0609	100
0.0871	70
0.1051	58
0.1172	52
0.1325	46
0.1524	40
0.1793	34

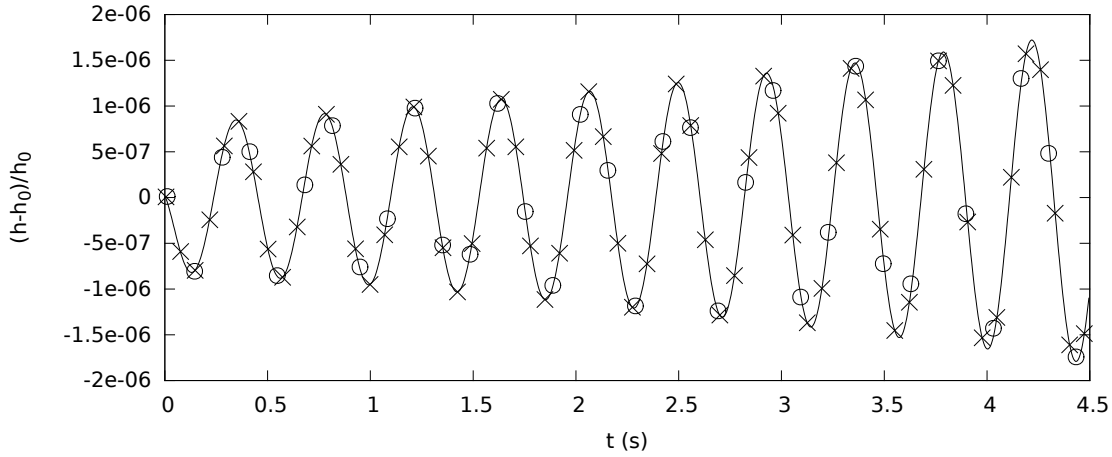

Figure 7.1: Temporal evolution of the dimensionless film thickness at imposed wavelength $\lambda = 70\ mm$, and convergence of three mesh sizes: 40 (circles), 80 (cross) and 160 (solid line) cells in the domain. Dimensionless numbers: $Re = 8.5$, $We = 0.048$, $Fr = 0.31$.

expressions (3.12), one obtains $Fr = 0.31$ and $We = 0.048$, while $\tilde{U}_0$ is the Nusselt's profile defined in (2.13). As already mentioned, owing to periodic boundary conditions at right and left sides of the computational domain, the wavelength λ has to be imposed. Hence, in order to study the linear regime of such a flow, several tests are performed changing the imposed wavelength from 34 mm to 200 mm, see Table 7.2.

As initial condition, film thickness and flow rate are perturbed with a sinusoidal law, namely

$$h = h_0\Big[1 + \epsilon \sin\Big(2\pi\frac{x}{\lambda}\Big)\Big]\ , \tag{7.1a}$$

$$q = q_0\Big[1 + \epsilon \sin\Big(2\pi\frac{x}{\lambda}\Big)\Big]\ , \tag{7.1b}$$

where $h_0 = 0.97\ mm$ and $q_0 = 5.3 \cdot 10^{-5}\ m^2 s^{-1}$ are Nusselt's uniform thickness and flow rate, respectively, and $\epsilon = 10^{-6}$ is sufficiently small to remain in the linear regime. Therefore, sinusoidal waves develop on the free surface of the film with decreasing or increasing amplitude.

Figure 7.1 shows the time evolution of the film thickness at imposed wavelength $\lambda = 70\ mm$, and highligths the convergence of three mesh sizes (see caption). Such convergence is also sketched in Figure 7.2, which shows for the same test the time evolution of the maximum thickness in the domain.

Finally, the corresponding numerical wave celerity c_r and growth rate kc_i are compared

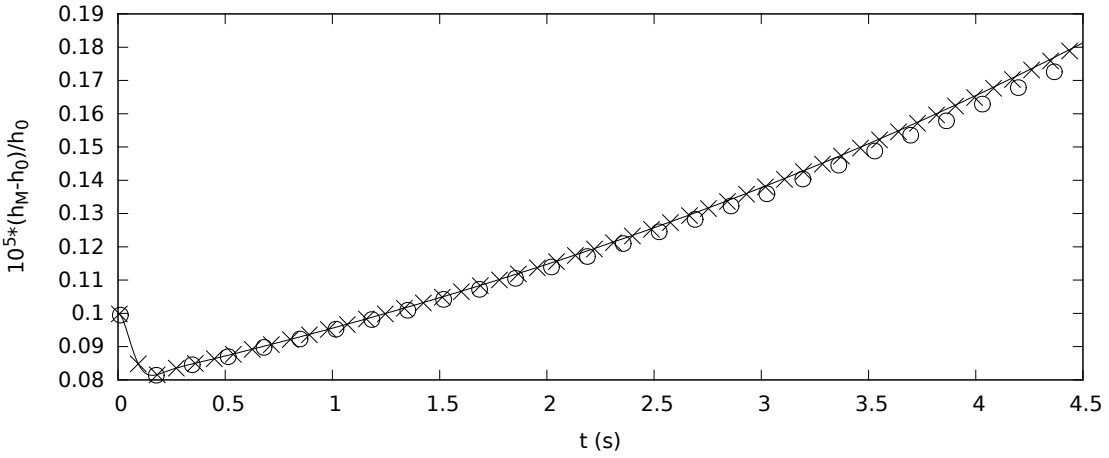

Figure 7.2: Temporal evolution of the dimensionless maximum film thickness h_M in the domain at imposed wavelength $\lambda = 70\ mm$, and convergence of three mesh sizes: 40 (circles), 80 (cross) and 160 (solid line) cells in the domain. Dimensionless numbers: $Re = 8.5$, $We = 0.048$, $Fr = 0.31$.

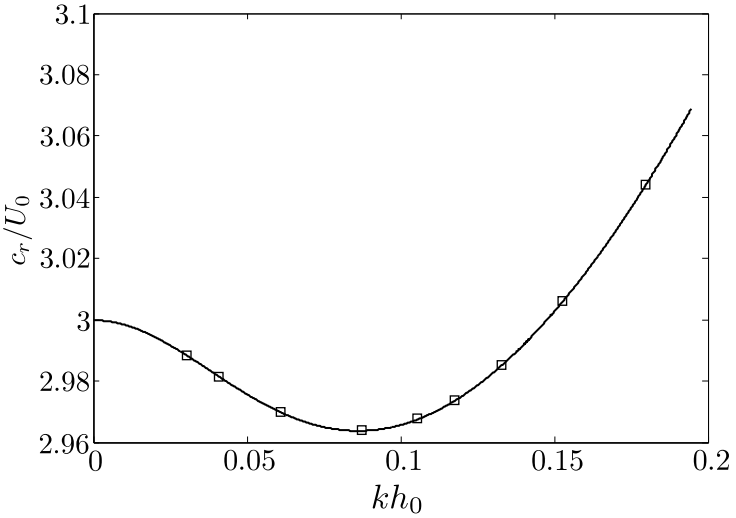

Figure 7.3: Wave celerity of a gravity-driven film of water-glycerin down a 6.4° inclined plane. Dimensionless numbers: $Re = 8.5$, $We = 0.048$, $Fr = 0.31$. Solid line: solution of the long-wave dispersion relation (5.22); squares: code SWANS.

to those provided by the long-wave linear stability theory derived in Chapter 5. Indeed, the theoretical complex wave velocity c is taken from the resolution of the dispersion relation (5.22), valid for gravity-driven liquid films. The comparisons on wave celerity c_r and growth rate c_i between the performed numerical analysis and the long-wave linear stability theory are sketched in Figures 7.3 and 7.4, which show a good agreement. Such a comparison allows validating the augmented system (6.8-6.10) and the consequent discretization of the surface tension.
Further linear regime validations have been computed in an analogous way in the case of oscillating shear stress and pressure gradient, and are not shown here.

7.1.2 Comparison with Liu & Gollub's experiments

Once the linear stability of the film code has been validated, the non-linear regime can be analyzed by comparing the numerical solution to the experiments of Liu & Gollub [47]. As already stated, experiments by Liu & Gollub have been performed with films flowing down an inclined plane, permitting to observe complex wave dynamics at much lower speed

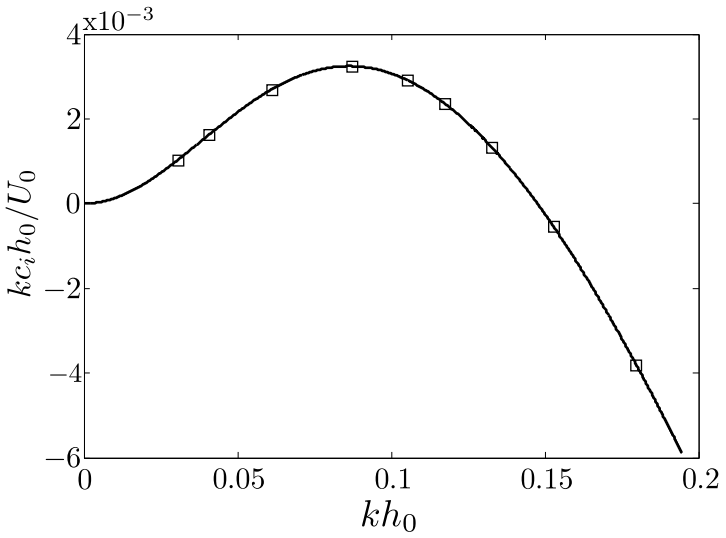

Figure 7.4: Linear growth rate of a gravity-driven film of water-glycerin down a 6.4° inclined plane. Dimensionless numbers: $Re = 8.5$, $We = 0.048$, $Fr = 0.31$. Solid line: solution of the long-wave dispersion relation (5.22); squares: computational analysis.

than vertical falling films. Particularly, the authors have shown that by modifying the forcing frequency, saturated waves change drastically: at low frequencies, one can observe stationary solitary waves, while at high forcing frequencies capillary ripples disappear and saturated waves become more regular and their peaks are lower.
Hence, the aim of the comparison of the numerical solution to the experiments of Liu & Gollub consists in showing that the non-linear wave dynamics provided by the film code is in accordance with the physics of liquid films on a qualitative level. Indeed, it is well known that first-order integrated equations (3.43) considered in this work, are not able to catch the correct amplitude of peaks because of the omission of dissipative terms appearing at second-order with respect to the small parameter ε. Particularly, the effect of second-order terms manifests itself at Reynolds numbers far from the critical one, as the experiments considered here do. More precisely, the experiments of Liu & Gollub to be compared to the numerical solution have been performed at $Re = 19.3$ with two forcing frequencies of $f = 4.5\ Hz$ and $f = 7\ Hz$, thus much distant from the threshold $Re_{cr} = 7.5$. For example, recalling Figure 5.6 of Chapter 5, one can notice the divergence of first-order models from the Orr-Sommerfeld theory when increasing the Reynolds number.

In order to compare the numerical solution to the experiments, it is worthwhile mentioning again that the film code works with periodic boundary conditions, as shown in Figure 6.3, meaning that in the performed computational analysis the wavelength, rather than the frequency, must be imposed. The wavelength can be visually recovered by the experiments, and corresponds to $\lambda = 5\ cm$ and $\lambda = 3\ cm$ for the two tests considered here. Since saturated waves are periodic waves which travel at constant speed, space and time are interchangeable. However, the exactitude of the imposed conditions can be verified a posteriori by measuring the period T of the periodic waves of the numerical solution and computing the frequency according to $f = 1/T$.

The liquid film flows down a 6.4° inclined plane at $Re = 19.3$; the fluid is a 54% by weight mixture of water and glycerin, see Table 7.1 for physical properties. The flow is then perturbed with sinusoidal waves, following the expressions (7.1), with an amplitude of $\epsilon = 10^{-3}$. Figure 7.5 shows the temporal evolution of the dimensionless film thickness with a prescribed wavelength $\lambda = 5\ cm$, which corresponds to the experiment of Liu & Gollub at $f = 4.5\ Hz$, sketched in Figure 7.7 for comparison. Yet, the effect that these waves are spatially periodic allows for matching time evolution of the numerical

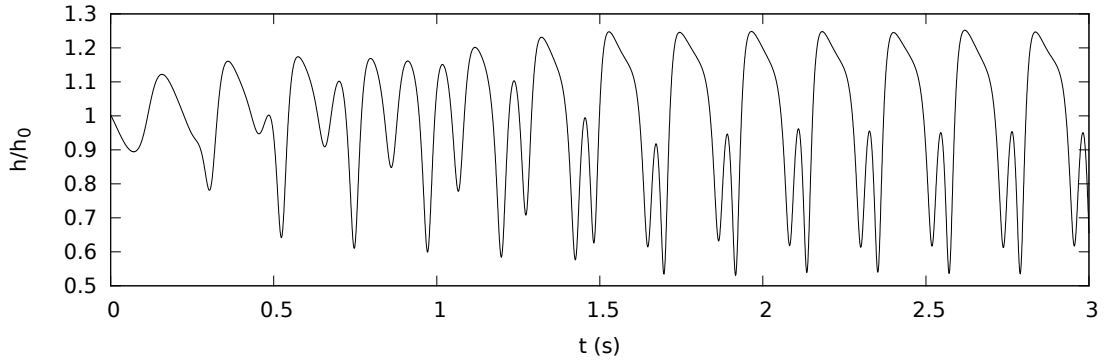

Figure 7.5: Temporal wave dynamics and saturated waves, spatially periodic, of a falling water-glycerin film down a 6.4° inclined plane. Data correspond to Liu & Gollub experiments: $Re = 19.3$, $We = 35$, $f = 4.5\ Hz$ ($\lambda = 5\ cm$ in the performed computational analysis).

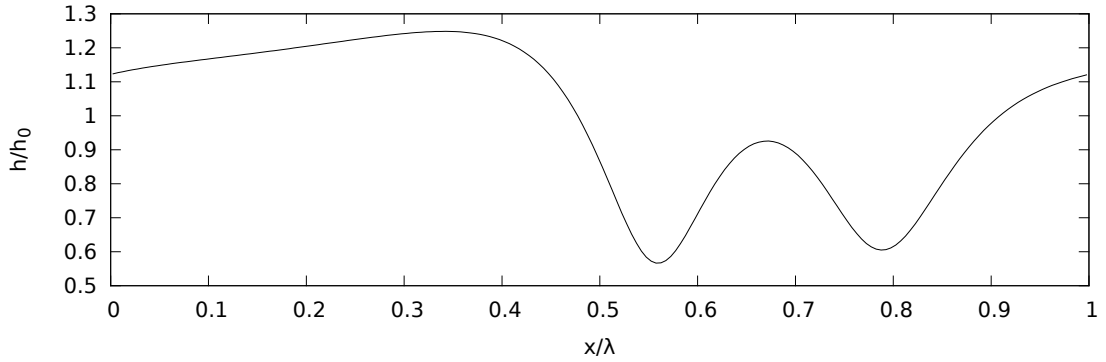

Figure 7.6: Shape of saturated waves of a falling water-glycerin film down a 6.4° inclined plane, at $t = 1.6\ s$. Data correspond to Liu & Gollub experiments: $Re = 19.3$, $We = 35$, $f = 4.5\ Hz$ ($\lambda = 5\ cm$ in the performed computational analysis).

analysis to space evolution of the experiments. The main hump of saturated waves is anticipated by a small depression. This phenomenology is better observable in Figure 7.6, where the computational solution of the dimensionless film thickness is shown in function of the normalized wavelength.

When the forcing frequency increases to $f = 7\ Hz$, i.e. the imposed wavelength in the performed computational analysis decreases to $\lambda = 3\ cm$, the small secondary peak disappears and saturated waves have only a main peak. Figure 7.8 shows the time evolution of the dimensionless film thickness obtained by means of the film code under periodic boundary conditions. This evolution can be compared to the experiments of Liu & Gollub sketched in the right of Figure 7.7. Furthermore, Figure 7.9 shows the space evolution of periodic waves computed by the film code at $t = 1.6\ s$.

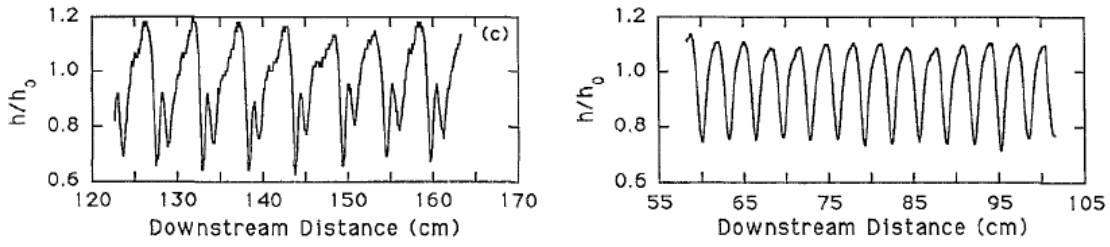

Figure 7.7: Experiments of Liu & Gollub [47] for a falling water-glycerin film down a 6.4° inclined plane, at $Re = 19.3$ and $We = 35$. On the left, forcing frequency $f = 4.5\ Hz$, on the right $f = 7\ Hz$.

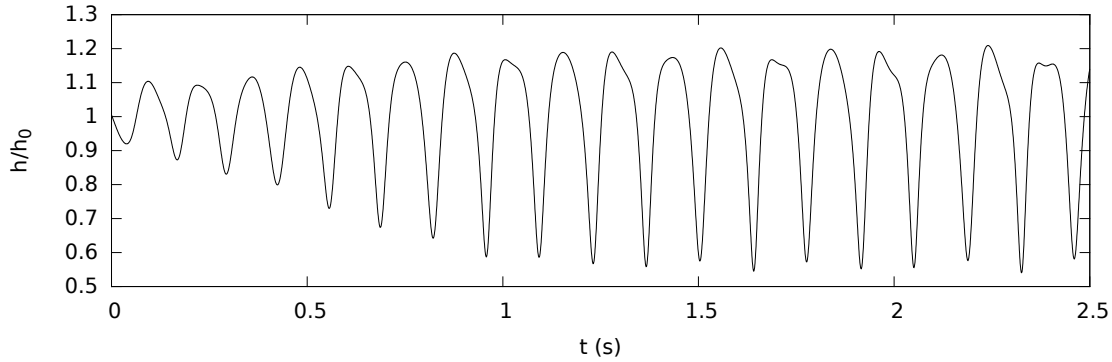

Figure 7.8: Temporal wave dynamics and saturated waves, spatially periodic, of a falling water-glycerin film down a 6.4° inclined plane. Data correspond to Liu & Gollub experiments: $Re = 19.3$, $We = 35$, $f = 7\ Hz$ ($\lambda = 3\ cm$ in the performed computational analysis).

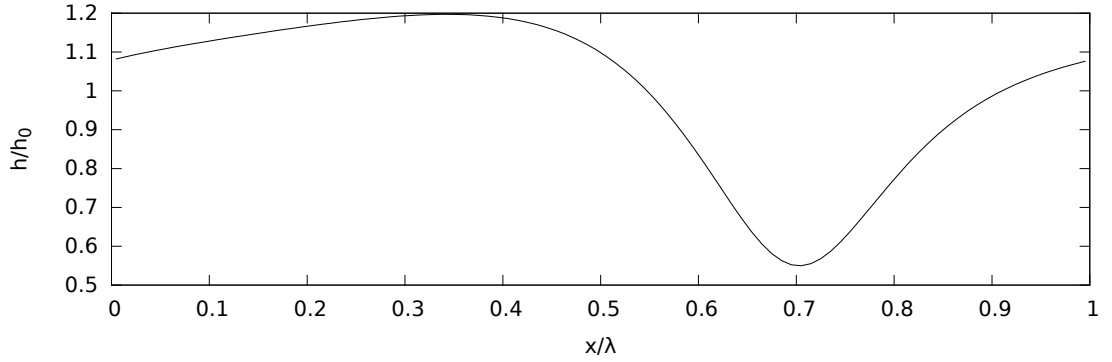

Figure 7.9: Shape of saturated waves of falling water-glycerin film down a 6.4° inclined plane, at $t = 1.6\ s$. Data correspond to Liu & Gollub experiments: $Re = 19.3$, $We = 35$, $f = 7\ Hz$ ($\lambda = 3\ cm$ in the performed computational analysis).

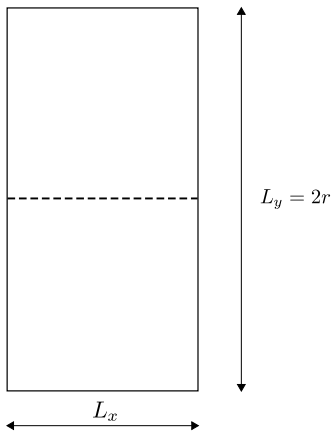

Figure 7.10: Geometry of the plane Poiseuille flow. Channel length is $L_x = 1\ mm$ and the height is $L_y = 2r = 2\ mm$.

As mentioned above, comparisons between numerical and experimental results must be analyzed at a qualitative level. Indeed, the aim of such comparisons is to demonstrate that the numerical scheme (6.11) of discrete shallow water equations captures well the regimes of non-linear waves for falling liquid films. Hence, Figures 7.5 and 7.8 shows agreement of the numerical solutions with the experiments in non-linear wave regimes. However, the amplitude of saturated waves is almost 10% higher in the numerical solution: this is due to the approximation of the first-order model, which misses second-order dissipative terms. Precisely, it has been demonstrated that these terms plays an important role on the amplitude and phase of capillary ripples, rather than the main hump, see Kalliadasis et al. [40] for details. However, the difference shown in the amplitude between numerical investigation and experiments can be also explained by the use of periodic boundary conditions for the simulations. For example, the inverse period T^{-1} returns $f = 4.34\ Hz$ for the first test and $f = 7.69\ Hz$ for the second, and both differ of $4\% \div 10\%$ from forcing frequencies used by Liu & Gollub in their experiments, meaning that the wavelengths used in the numerical investigation are not exact, being evaluated from their paper from visual observation.

7.2 Navier-Stokes code's validation

This section shows the test-case of a Poiseuille flow with the aim to validate the compressible Navier-Stokes code and the ALE technique. A plane Poiseuille flow is firstly computed on a fixed and uniform mesh and then on a moving grid. The resulting velocity profiles are compared to the exact solution, and the corresponding deviations are quantified. An analysis of convergence is also performed.
As matter of fact, other validation test-cases involving the developed Navier-Stokes code, such as the shock-tube on fixed and moving mesh have been performed, although these are not shown here.

7.2.1 The ALE Poiseuille flow

The Poiseuille flow is an essential test to validate the discretization of the shear stress. Furthermore, in the second test performed here the grid has a certain motion permitting to inspect also the ALE technique.
The geometry is sketched in Figure 7.10. An air stream, whose physical properties are listed in Table 7.1, flows into the channel at $Re = 200$. Imposing that the Reynolds number is based on the maximum air velocity U_M and that the characteristic scale is the vertical size of the channel, one obtains $U_M = \nu Re/L_y = 1.5\ m\ s^{-1}$ as the maximum velocity into the

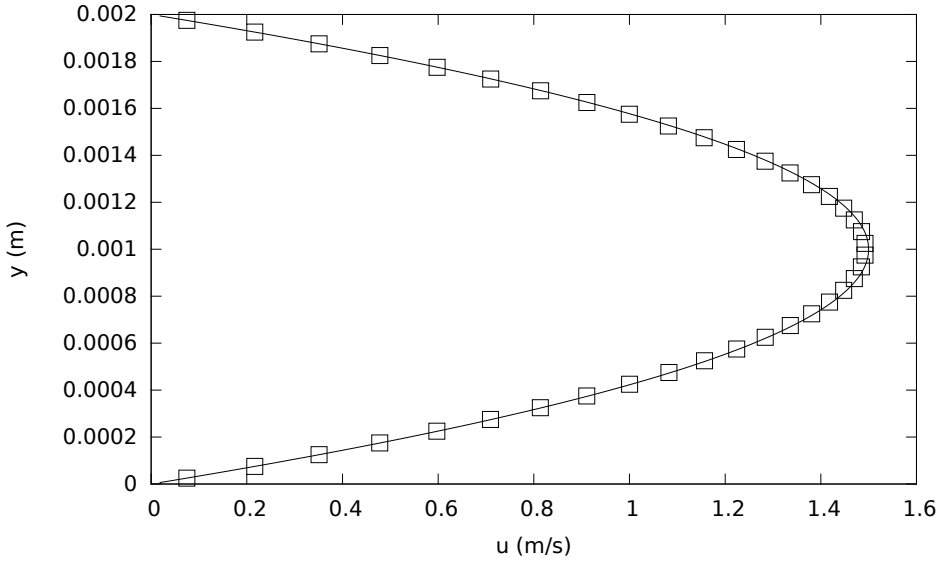

Figure 7.11: Poiseuille velocity profile at $t = 0.4\ s$ on a fixed grid and comparison with the exact solution. Squares: mesh 10x40; solid line: exact profile.

domain. Steady Poiseuille flow is known to have a parabolic profile, given by the equation $\partial_{yy} u = -F/\nu$, where F is the external force (alternatively, the pressure gradient resulting from the pressure drop between entry and exit sides). Upon double integration under no-slip boundary conditions at both walls, in addition to $u(y = r) = U_M$ along the axis, one gets the velocity profile and the value of the external force. The former reads

$$u(y) = -\frac{1}{2}\frac{F}{\nu} y(y - r) + U_M \frac{y}{r} \ , \tag{7.2}$$

while the latter yields

$$F = \frac{2U_M \nu}{r^2} = 44.1\ m\ s^{-2} \ . \tag{7.3}$$

It is worthwhile to recall that the gas code works with periodic boundary conditions at left and right sides. Therefore, the pressure gradient of the plane Poiseuille flow is replaced by a longitudinal force ρF.

The physical time necessary to reach steady conditions can be read as the time required by the viscosity to diffuse from the walls to the center, namely $t = r^2/\nu \simeq 0.07s$. Therefore, all the performed simulations have been stopped reasonably *far* after the achievement of steady conditions.

The initial condition used for the Poiseuille flow is an uniform velocity, which corresponds to the averaged value $\bar{u} = 1\ m\ s^{-1}$.

In the first test, the grid is fixed and uniform, and details about the mesh size are listed in Table 7.3. Figure 7.11 compares the resulting velocity profile with the exact one, given by the expression (7.2): the two velocity profiles overlap.

In the second test, the line corresponding to the axis of the channel moves with a sinusoidal motion governed by

$$dh = \epsilon \frac{r}{10} \sin\left(2\pi \frac{x}{L_x}\right) \ , \tag{7.4}$$

and a sketch of the moving mesh is shown in Figure 7.12. Parameter ϵ lies in the interval $(-1, 1)$ and oscillates at each time step in order to have several oscillations during the

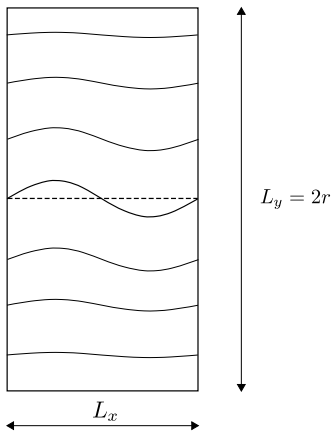

Figure 7.12: Sketch of the grid motion in the ALE plane Poiseuille flow, at the maximum amplitude.

Table 7.3: Fixed and mobile meshes used for the computational investigation of the Poiseuille flow, from the coarsest to the finest.

mesh	$\Delta x(\mu m)$	$\Delta y(\mu m)$	grid
10x10	100	200	fixed
10x20	100	100	fixed
10x40	100	50	fixed
10x40	100	50	mobile
20x80	50	25	mobile
40x160	25	12.5	mobile

computation. Hence, the maximum deviation of the mesh corresponds to 10% of the radius. Since the displacement dh is imposed on the axis, then an algebraic law propagates this central deviation until the walls in a symmetric way on both sides, from dh to zero, in line with the expression (6.48). More precisely, expression (6.48) is valid in the case of a moving bottom wall which models the liquid film. In the ALE Poiseuille flow performed here, top and bottom walls are rigid and flat, otherwise no analytical solution would exist.

In order to study the convergence rate of the numerical scheme, different meshes have been used for the Poiseuille flow on moving grid, and those are listed in Table 7.3. Velocity profiles are shown in Figure 7.13. The coarsest mesh, the same used for the fixed grid, does not provide a matching profile with the exact one, unlike the previous case. Hence, this deviation is due to the grid motion (7.4) and in particular to its amplitude, which reaches one tenth of the half channel when $\epsilon = \pm 1$. The difference between the solution of fixed and moving mesh can be also explained by the omission of correction of the velocity gradient for non-orthogonal mesh, as detailed in section 6.3.2. However, the finer the mesh, the smaller is the deviation between numerical and analytical velocity profiles. In addition, errors given by the three different grids have been quantified with the infinity norm and the 1-norm, which read

$$L_\infty = \max_j \frac{|u_{ex,j} - u_j|}{u_{ex,j}} \ , \tag{7.5}$$

$$L_1 = \frac{1}{N_y} \sum_j \frac{|u_{ex} - u|}{u_{ex}} \ , \tag{7.6}$$

where N_y corresponds to the number of cells in the y-direction, and u_{ex} to the exact velocity

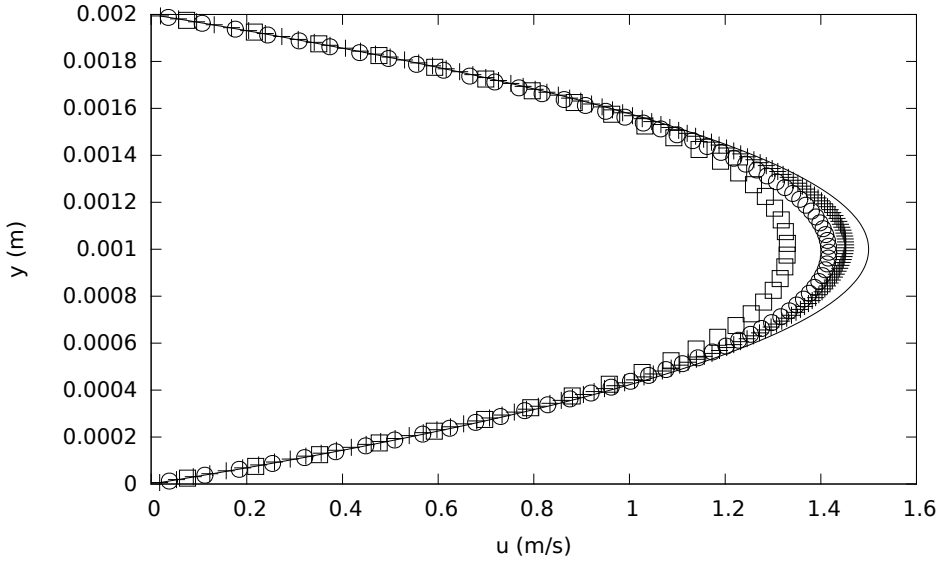

Figure 7.13: Velocity profiles at $t = 0.4\ s$ for three different moving grids and comparison with the exact solution. Squares: mesh 10x40; circles: mesh 20x80; cross: mesh 40x160; solid line: exact profile.

Table 7.4: Errors on velocity profiles for the three mobile meshes considered in the ALE Poiseuille flow.

mesh	grid	L_∞	L_1	r_∞	r_1	n_{osc}
10x10	fixed	—	0.0471	—	—	—
10x20	fixed	—	0.0206	—	1.19	—
10x40	fixed	—	0.0086	—	1.26	—
10x40	mobile	0.1130	0.0645	—	—	21
20x80	mobile	0.0681	0.0365	0.73	0.82	22
40x160	mobile	0.0412	0.0195	0.73	0.91	23

profile. Those have been also used to evaluate the convergence rate, namely

$$r_\infty = \frac{ln(L_\infty)|_{coarser} - ln(L_\infty)|_{finer}}{ln(2)} \ , \tag{7.7}$$

$$r_1 = \frac{ln(L_1)|_{coarser} - ln(L_1)|_{finer}}{ln(2)} \ . \tag{7.8}$$

The convergence rate is demonstrated to be almost 1 for numerical schemes with a first-order space discretization, such as the low-Mach scheme developed in this work. Table 7.4 shows the errors and the convergence rate applied to all meshes considered here. For the fixed grid, where the matching with the exact solution is explicit (see Figure 7.11), only the 1-norm has been computed. A further column of this table gives the number of oscillation n_{osc} of the mesh, to prove that the law (7.4) applied to the grid motion provides almost the same number of oscillations during the whole computation.

7.3 Validation of the coupling technique

This section aims to validate the coupling methodology of the code SWANS, described in Chapter 6. The performed test-case concerns a liquid-gas system flowing in a strictly confined channel, in order to examine interfacial shear stress and pressure gradient provided by

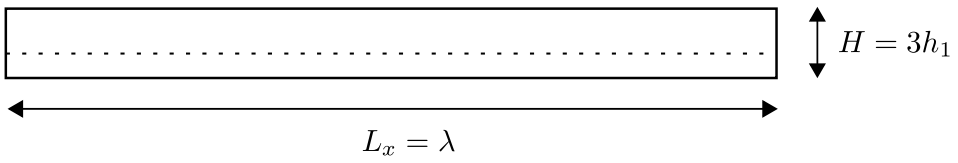

Figure 7.14: Geometry of the horizontal channel, which is 13 mm long and 0.39 mm high. Scaling is 8 : 1 for the x-direction and 24 : 1 for the y-direction. Dotted line expresses the uniform flow.

Table 7.5: Physical properties of the air-water flow used for the two-layer validation test.

fluid	$\rho(kg\ m^{-3})$	$\nu(10^{-5}m^2s^{-1})$	$\gamma(10^{-3}N\ m^{-1})$	r	m
water	1000	0.1	76.9	0.001	0.01
air	1	1			

the gas. Indeed, those are compared with the corresponding fields given by the asymptotic expansion of Chapter 4, which are valid because of the narrow channel.

7.3.1 Shear stress and pressure gradient validation

A liquid-gas flow is solved numerically by means of SWANS. The validity of the spatio-temporal evolution of the interface is not hereby investigated, because it will be the subject of the next chapter. In this section, the coupling methodology is tested by comparing interfacial shear stress and pressure gradient provided by the gas to those given by the asymptotic expansion of the Chapter 4, for a given shape of the interface. Of course, in order to use such an asymptotic expansion as validation, the channel must be strictly confined, meaning that the thickness of both layers is small compared to the wavelength. The geometry is sketched in Figure 7.14 and represents a two-dimensional channel. The uniform film thickness is half of the gas thickness, in a way that $kh_2 = 0.125$ and $kh_1 = 0.062$, and both are much smaller than the unity.

Recalling the results of the asymptotic expansion of Chapter 4, zeroth- and first-order interfacial shear stress and pressure gradient depend on the shape of the interface $h(x,t)$ and its space derivative $\partial_x h$, as well as by the channel height H, total flow rate Q and physical properties of both fluids, which are listed in Table 7.5. This means that given the shape of the interface in space and time, the asymptotic field give the correct stress fields. Particularly, shear stress asymptotic field is expressed in (4.36) and (B.3), while asymptotic pressure gradient field in (4.35) and (B.5). However, these fields are based on the assumption $Q = const.$, and are thus correct in the situations where a total flow rate Q is imposed in the channel and the pressure gradient is left free. On the contrary, in the numerical analysis investigated in this work, a pressure drop is imposed between the entry and the exit of the channel, leaving the total flow rate free. As a consequence, the total flow rate is not constant during the simulation.* For this reason, the comparison of the interfacial shear stress and pressure gradient between the numerical solution and the asymptotic fields has to be meant on a qualitative level.

The liquid film flows in the bottom of the channel, while the gas flow is on the top of it. Such an air-water flow is driven by a pressure drop between the two sides of the channel. Physical parameters and mesh size are given in the caption of Figure 7.15. After imposing an initial sinusoidal perturbation of film thickness and flow rate, according to the definition (7.1) with $\epsilon = 0.05$, the simulation has not been kept for long, in a way that the total flow rate Q has not much changed from the initial value, i.e. less than 5% with respect to the initial value $Q_{in} = 7.2 \cdot 10^{-4}m^2s^{-1}$. Film thickness is sketched in

*The total flow rate is uniform thanks to the continuity equations $\partial_t h + \partial_x q_1 = 0$ and $\partial_t h - \partial_x q_2 = 0$.

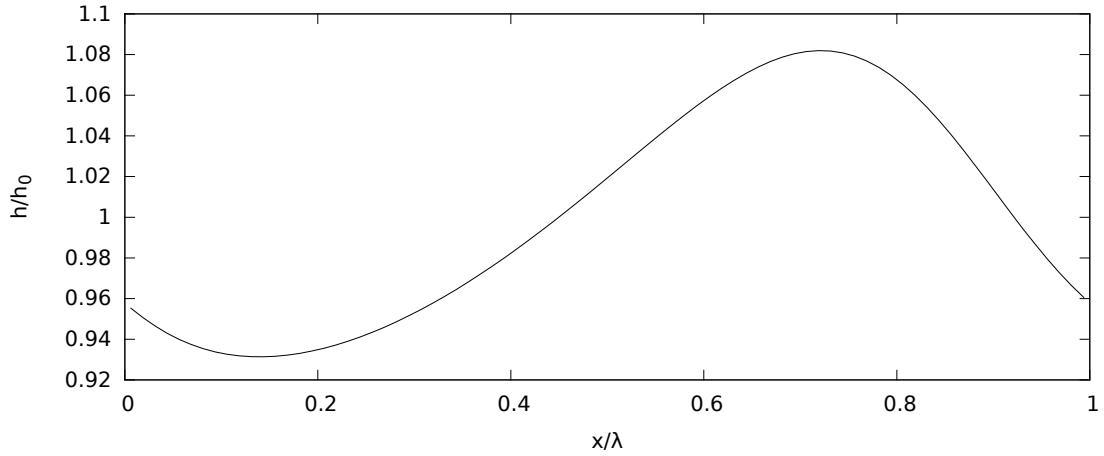

Figure 7.15: Film thickness at $t = 0.03\ s$ from SWANS. Dimensionless numbers: $Re_1 = 8.7$, $Re_2 = 71.3$. Pressure drop: $\Delta p = 62\ Pa$. Mesh size: $\Delta_x = 81.2\ \mu m$, $\Delta_y = 10.8\ \mu m$.

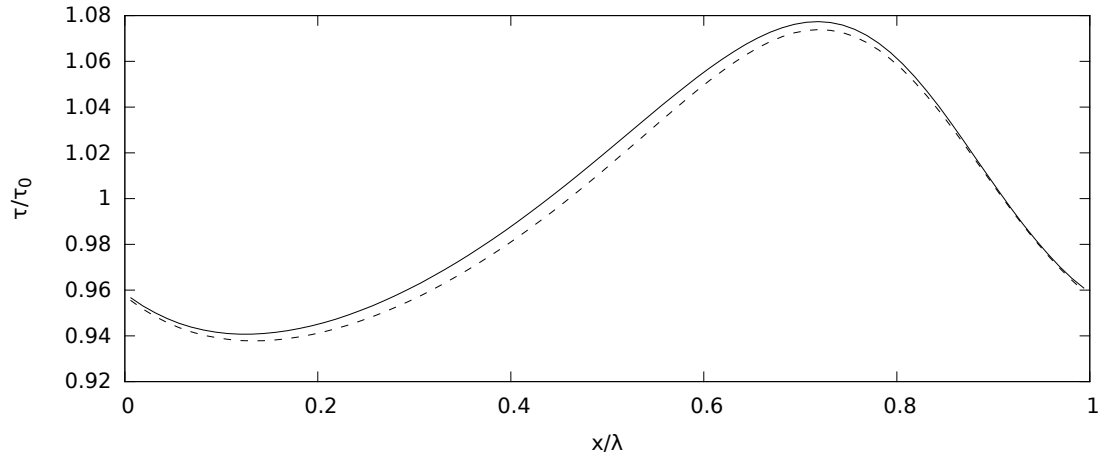

Figure 7.16: Interfacial shear stress normalized with the uniform value $\tau_0 = 0.61\ Pa$, corresponding to film thickness of Figure 7.15. Solid line: asymptotic expansion; dashed line: code SWANS. Physical and numerical parameters in the caption of Figure 7.15.

Figure 7.15. Yet, the purpose of such a numerical test does not consist in validating the film thickness evolution. Here, the aim is to compare asymptotic and numerical interfacial shear stress and pressure gradient when the shape of the interface is given. Finally, Figures 7.16 and 7.17 show the comparison between the asymptotic expansion and the code SWANS. The evolution agrees on a qualitative level. Particularly, the numerical interfacial shear stress matches well with the asymptotic field. Larger differences are instead found between the numerical and asymptotic interfacial pressure gradient. However, as explained above, no further investigations can be made in order to quantify and explain the differences, owing to the uncertainty on the asymptotic fields. It is worthwhile to mention that one can perform further validation tests by reducing kh_1 and kh_2, i.e. by considering longer and more narrow channels, in order to reduce the aforementioned error of the asymptotic expansion.

7.4 Conclusions

Once the validation of the code SWANS has been presented, the non-linear dynamics of two-layer flows in a channel can be finally achieved. Comparison with the DNS will be

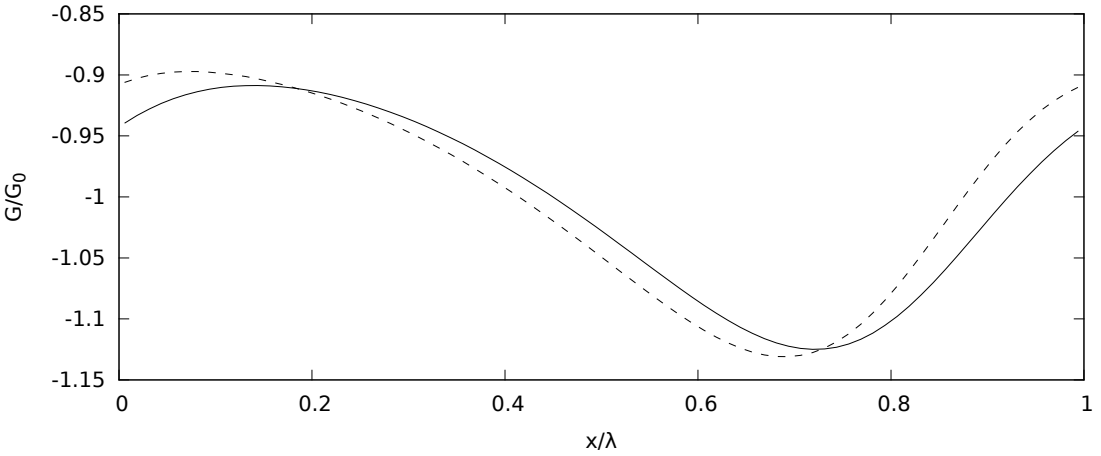

Figure 7.17: Space evolution of the interfacial pressure gradient normalized with the uniform value $G_0 = 4769\ Pa\ m^{-1}$, corresponding to film thickness of Figure 7.15. Solid line: asymptotic expansion; dashed line: code SWANS. Physical and numerical parameters in the caption of Figure 7.15.

shown in two different configurations: a strictly confined channel, where the hypothesis of thin gas is still valid, and a large channel in which only the liquid film is thin compared to the wavelength.

8 Non-linear dynamics of two-layer flows: SWANS results and comparison with DNS analysis

This chapter aims to investigate the SWANS model in simulating non-linear waves occurring in two-layer co-current flows. For this purpose, two tests have been performed. The first is taken from the work by Dietze & Ruyer-Quil [25] and consists in a strongly confined film-gas system driven by pressure gradient in a horizontal channel. The performed computational analysis provides spatio-temporal evolutions of the film thickness, as well as interfacial shear stress and pressure gradient fields. These are then compared to the results provided by DNS simulations of Dietze & Ruyer-Quil by means of OpenFOAM, as well as to their full reduced model, which consists in using depth-integrated equations in both layers.
The second test, instead, is a vertical two-layer system driven by gravity and flowing in a large channel, meaning that the liquid film is thin compared to the wavelength of traveling waves while the gas layer is not. Therefore, a full reduced model cannot be applied in this configuration, while the SWANS model allows for studying also this liquid-gas flow. This is one of the main point of SWANS. The spatio-temporal evolution of the film thickness of the performed analysis is compared to the DNS provided by G. Blanchard at ONERA, by means of the code Slosh (Chanteperdrix *et al.* [15], Schied *et al.* [75]).

8.1 Description of the horizontal test

As stated above, the test is taken from Dietze & Ruyer-Quil [25], which in turns has been suggested by the work of Frank [28]. A liquid film flows in a horizontal channel sheared by a confined laminar gas. Such a two-layer flow is pressure-driven and develops in a strictly narrow channel, whose geometry is sketched in Figure 8.1. The uniform film thickness is 1/3 of the channel height, meaning that the gas flow in the uniform condition is twice

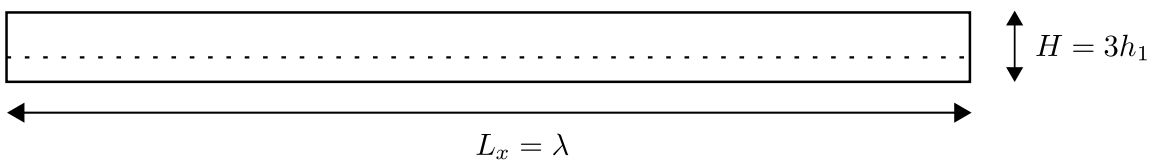

Figure 8.1: Geometry of the horizontal test from Dietze & Ruyer-Quil [25], with $L_x = 26\ mm$ and $H = 0.39\ mm$. Scaling is $5:1$ for the x-direction and $24:1$ for the y-direction. Dotted line expresses the equilibrium film thickness.

Table 8.1: Values for kh for the horizontal confined channel test and the vertical large channel one.

test	channel	$kh_1(\cdot 10^{-2})$	$kh_2(\cdot 10^{-2})$
horizontal	narrow	3.14	6.28
vertical	large	20.5	748.7

thicker than the film.
This test has been used by Dietze & Ruyer-Quil with the purpose to validate their full reduced long-wave model, based on the use of depth-integrated equations for both the liquid and gas phases. Meanwhile, this strongly confined flow has wide applications in coolers and distillation columns, where heat and mass transfers are relevant phenomena. Following Frank [28], gravity is not considered as may happen for film flowing under micro-gravity conditions. Finally, Table 8.1 shows the values of kh for the liquid and the gas: the long-wave theory can be applied to both layers.

8.1.1 Initial flow conditions

The initial conditions coincide with the perturbed uniform flow: in order to compare the non-linear regime with the one provided by Dietze & Ruyer-Quil, the perturbation has a sinusoidal shape of amplitude $\epsilon = 0.25$, namely

$$h = h_0\Big[1 + \epsilon \sin\Big(2\pi\frac{x}{\lambda}\Big)\Big] \ , \tag{8.1a}$$

$$q = q_0\Big[1 + \epsilon \sin\Big(2\pi\frac{x}{\lambda}\Big)\Big] \ . \tag{8.1b}$$

A pressure jump of $\Delta p = 64\ Pa$ is imposed between the entry and exit sides of the channel, and the velocity profiles are parabolic and match at the interface for $u|_h = 0.0621\ m\ s^{-1}$, in the uniform flow. Figure 5.4 of Chapter 5 shows, for example, the uniform velocity profiles of this system. Interacting fluids are water and air, whose physical properties are listed in Table 7.5 of the previous chapter. All other physical parameters of this test are described in the caption of Figure 8.2.

8.1.2 Non-linear dynamics

Figure 8.2 shows the time evolution of the film thickness consequence of the perturbed equilibrium (8.1). At the beginning, interfacial waves develop before the achievement of periodic conditions, characterized by periodic waves composed by a main hump anticipated by capillary ripples. More precisely, in the periodic regime the waves move at constant velocity and an observer would see the same wave passing within his window at a constant rate. This distinguishes the behavior of *traveling waves*, since these waves can be studied in the reference system $x - ct$ where c is the wave celerity.

On the other hand, Figures 8.3 and 8.4 show the tendency and the convergence of the film thickness when refining Δx and Δy, respectively. Details about all meshes used here are listed in Table 8.2, with comparison with Dietze & Ruyer-Quil's DNS grid. Worthy is that refining the mesh, peaks of the traveling wave are higher, while capillary ripples manifest higher amplitude and shorter wavelength. In addition, one can notice that the convergence in the y-direction, from Figure 8.4, works well. On the contrary, to get a proper convergence in the x-direction, see Figure 8.3, one should refine more, although a clear tendency is already established.

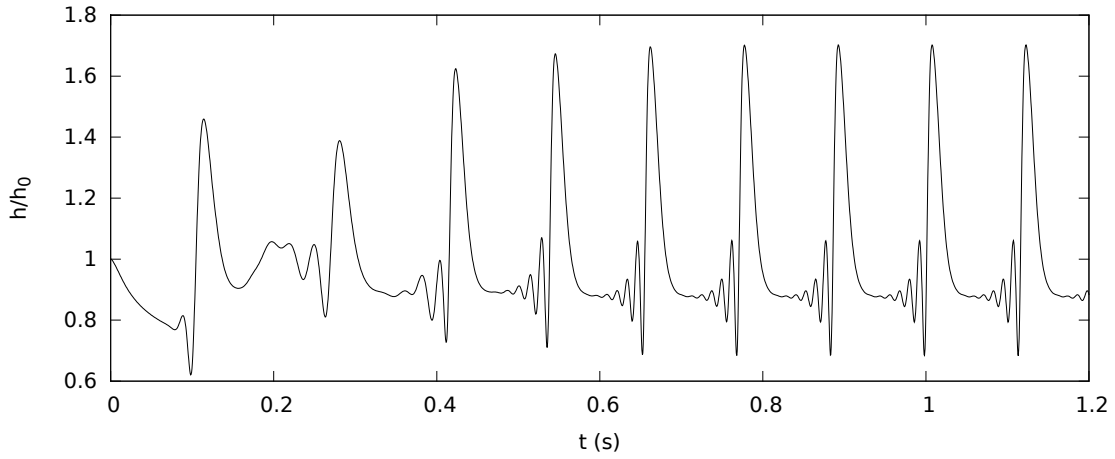

Figure 8.2: Time evolution of the film thickness normalized with the uniform flow. Dimensionless numbers: $Re_1 = 4.48$, $Re_2 = 36.8$, $Fr = 0.93$, $We = 2 \cdot 10^{-3}$. Uniform pressure gradient and shear stress: $G_0 = -\Delta p/L = 2461.5\ Pa\ m^{-1}$, $\tau_{i0} = 0.32\ Pa$.

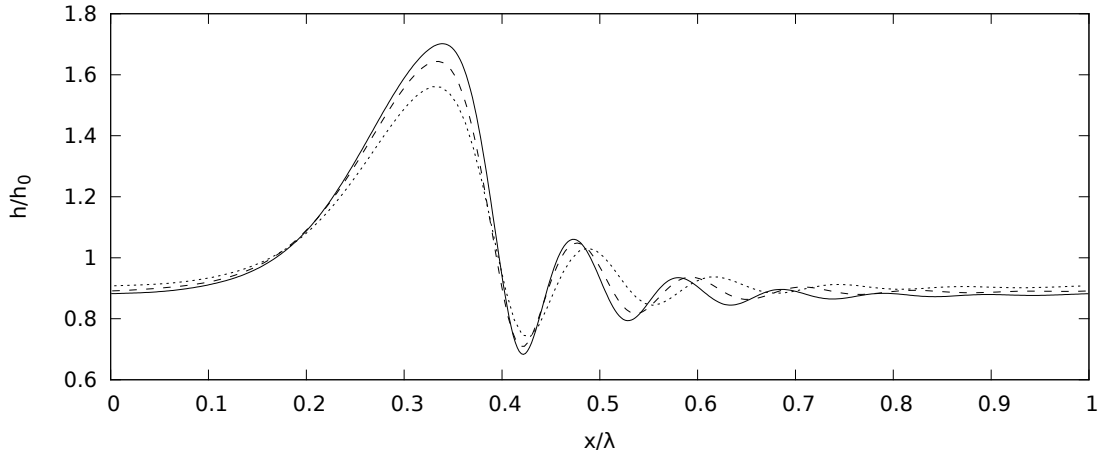

Figure 8.3: Film thickness at $t = 0.75\ s$ normalized to the flat equilibrium value versus stream-wise direction normalized with the wavelength. Convergence in the x-direction for three different meshes. Solid line: mesh 4 in Table 8.2; dashed line: mesh 2; dotted line: mesh 1. Physical parameters are detailed in the caption of Figure 8.2.

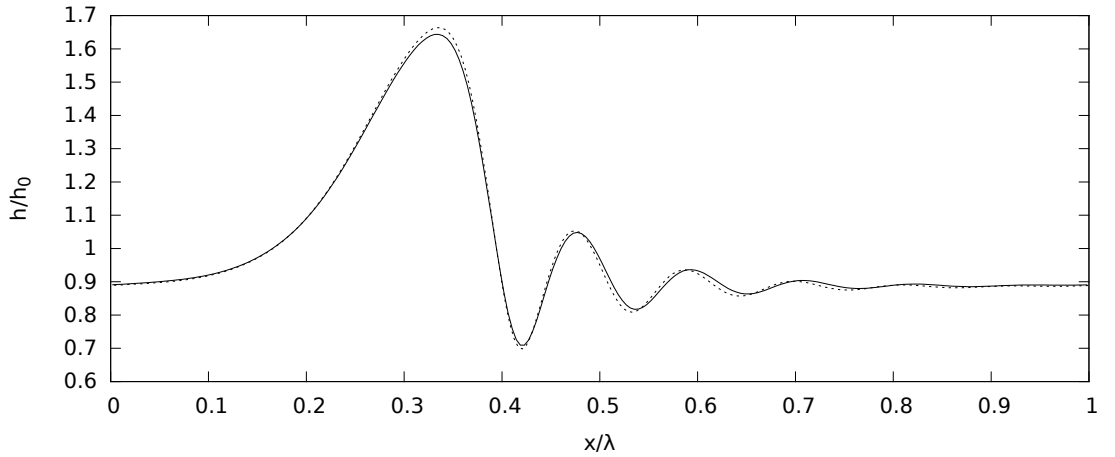

Figure 8.4: Film thickness at $t = 0.75\ s$ normalized to the flat value versus stream-wise direction normalized with the wavelength. Convergence in the y-direction for two different meshes. Solid line: mesh 3 in Table 8.2; dotted line: mesh 2. Physical parameters are detailed in the caption of Figure 8.2.

Table 8.2: Meshes used in this work, from the coarsest to the finest, and the one from Dietze & Ruyer-Quil's DNS. Note that, by construction, SWANS has only one vertical cell in the liquid layer.

mesh	$\Delta x(\mu m)$	$\Delta y(\mu m)$	$\Delta x/\Delta y$	cell number $(\cdot 10^3)$
1	216.7	10.83	20	3
2	108.3	10.83	10	6
3	108.3	8.12	13	7.9
4	54.16	10.83	5	12
Diet. & RQ. (DNS)	11.25	7.5	1.5	120

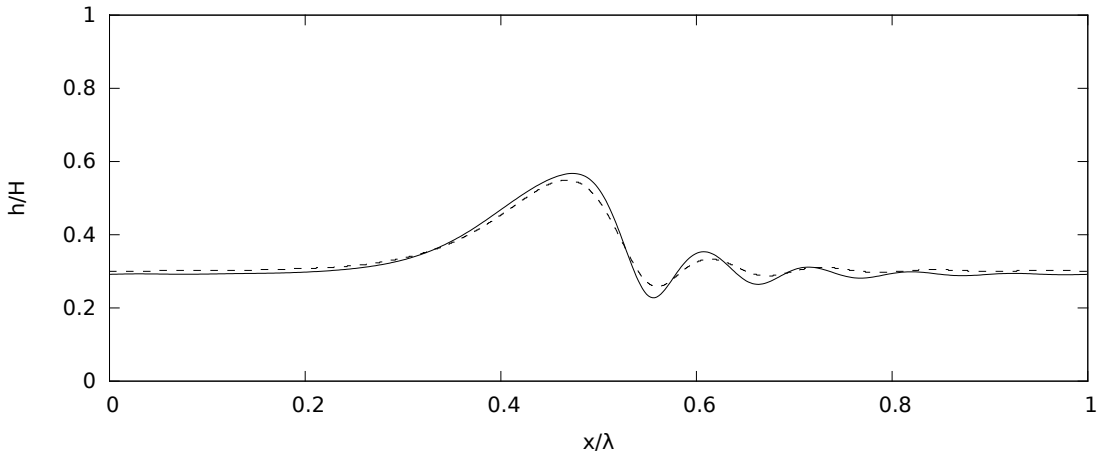

Figure 8.5: Traveling wave in the channel, and comparison between DNS of Dietze & Ruyer-Quil (dashed line), Figure 7(a) of [25], and SWANS (solid line). Physical parameters are detailed in the caption of Figure 8.2. DNS data courtesy of G. Dietze.

8.1.3 The SWANS model versus DNS analysis

In order to validate the SWANS model, the space evolution of the film thickness has been compared with the one provided by the DNS from Dietze & Ruyer-Quil. As a matter of fact, Dietze & Ruyer-Quil have adopted periodic boundary conditions to reproduce such a test. However, the authors have used the OpenFOAM flow solver which allows to handle periodic boundary conditions on the velocity field while non-periodic pressure conditions. Figure 8.5 compares the film thickness of the traveling wave normalized with the channel height H. Firstly, one can notice that traveling waves reach large levels of amplitude, by occupying more than half of the entire channel. Secondly, the comparison between SWANS and DNS shows good agreement: the deviation at the peak level is almost 5%. A larger difference between the two arises at capillary ripples. However, it has been already cited in this work that first-order long-wave models miss second-order stream-wise diffusion and this manifests itself mostly on amplitude and phase of capillary ripples (Kalliadasis *et al.* [40]).

8.1.4 The SWANS model versus the two-layer long-wave model

As already mentioned, the test shown above is composed by a liquid film and a confined laminar gas flow. For both layers, the thickness is very small compared to the wavelength of traveling waves, in such a way that the long-wave theory can be used for both. Indeed, this approach has driven to the previously cited work of Dietze & Ruyer-Quil.

Figure 8.6 shows the space evolution of the film thickness and the comparison between the SWANS model and the two-layer long-wave model developed by Dietze & Ruyer-Quil. The film thickness evolution, normalized with the uniform flow, shows that the amplitude of

the periodic waves reaches almost 70% of the equilibrium thickness. Furthermore, interfacial shear stress and pressure gradient found by means of the SWANS model have been also compared to the full reduced model of Dietze & Ruyer-Quil. Figures 8.7 and 8.8 shows good agreement, although one notices a larger difference in the amplitude of the main peak, as well as a small discrepancy in the "horizontal" sector.
The instability mechanism can be investigated by means of the pressure distribution on the wave: given to the presence of the wave and the resulting reduction of the cross-section, the gas velocity upstream (before the wave) is smaller, while it is larger downstream (after the wave). For example, this is shown in Figure 8.9: on the left the gas velocity profile is taken at $x/\lambda = 0.35$ of Figure 8.6, downstream of the wave, while on the right at $x/\lambda = 0.55$ of Figure 8.6, just upstream of the wave and in the capillary region. One can notice that the effect of the wave peak in the confined gas is strong. Therefore, the pressure gradient, which is negative because the flow is pressure-driven, gives an asymmetric motion to the wave leading to the instability. In addition, one can notice that the interfacial shear stress and pressure gradient are in phase with the wave shape.

These comparisons demonstrate that using the ALE technique to transfer the interface position is a satisfying instrument for the non-linear description of two-layer flows. Furthermore, the low-Mach scheme used to model gas flows at very low speeds respond very well, as well as the strategy to replace the initial pressure gradient with a longitudinal acceleration.

A further investigation consists in solving this test by means of the two-layer long-wave model developed in Chapter 4. As already mentioned, the performed asymptotic expansion of Chapter 4 is based on constant total flow rate Q. On the contrary, this test is computed by imposing a constant pressure gradient while the total flow rate varies in time. As a matter of fact, time derivatives of the total flow rate have been obviously not considered. This model is thus not compatible with the present test because those terms are not considered at order one. However, Figure 8.10 shows the time evolution of the normalized film thickness obtained with the two-layer long-wave model of Chapter 4: by comparing this evolution with the Figure 8.2, one can notice that the amplitude of traveling waves is smaller than the one from DNS and SWANS, but the main physics is captured anyway. Although the discrepancies in amplitude and speed of the traveling waves, it is worthwhile to highlight that the computational cost is greatly reduced because of the presence of two cells in the vertical direction (one for each layer), feature of the low-dimensional model. In addition, the convergence is obtained earlier, namely already for $\Delta x = 325\mu m$ with respect to $20\mu m \div 50\mu m$ required by SWANS and by the DNS. Therefore, the time necessary for the two-layer long-wave model of Chapter 4 to compute this test is almost 5 minutes, against the 12 days required by SWANS with the finest mesh of Table 8.2.

8.1.5 Analysis of compressibility effects

One recalls that the low-Mach scheme used to discretize the compressible Navier-Stokes equations in the gas phase allows solving flows at very low speed, such as the two-layer horizontal flow described above. However, given the use of compressible equations, some compressibility effects can arise due to the extremely confined configuration. With the aim to check whether the solution is modified by the presence of compressibility effects, Figure 8.11 shows the Mach number and the density (or pressure) distribution into the channel. One firstly observes that the Mach number is very low, as expected, due to the moderate gas speed. Noteworthy is that the analysis of the density field shows piece-wise variations along the stream-wise direction of the channel. This explains that the presence of the wave, although of great amplitude, does not modify the density field in the cross-stream

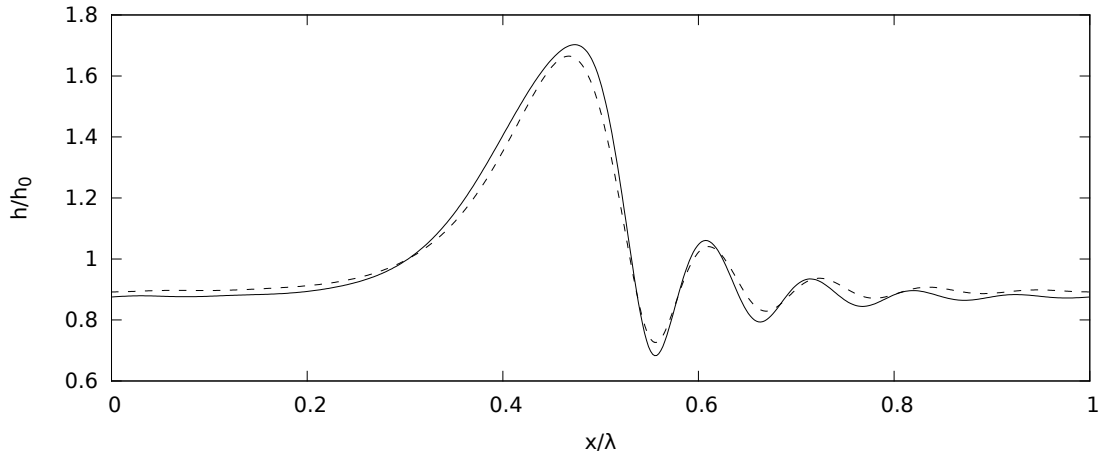

Figure 8.6: Space evolution of film thickness normalized to the flat value. Comparison between the two-layer long-wave model of Dietze & Ruyer-Quil (dashed line) and SWANS (solid line). Physical parameters are detailed in the caption of Figure 8.2. Data of the two-layer long-wave model courtesy of G. Dietze.

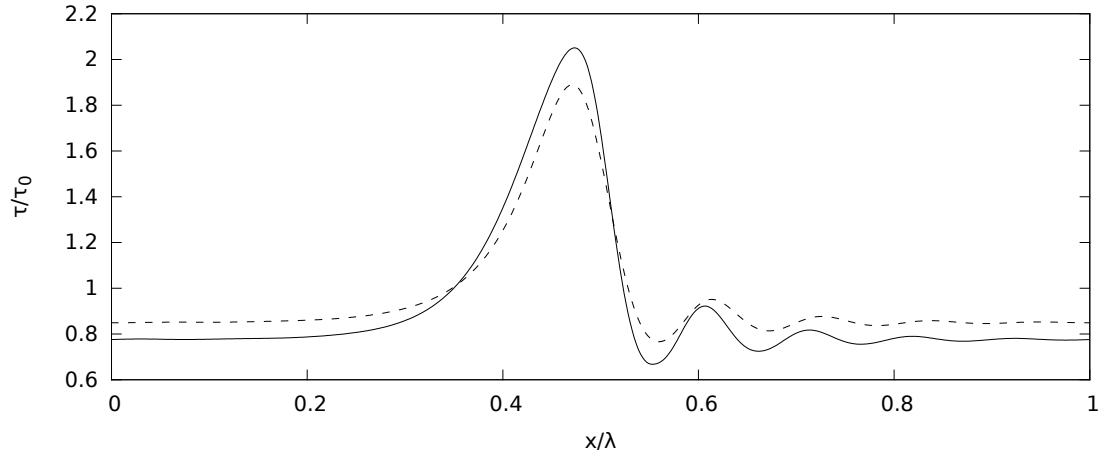

Figure 8.7: Space evolution of interfacial shear stress normalized to the uniform condition. Comparison between the two-layer long-wave model of Dietze & Ruyer-Quil (dashed line), Figure 8(c) of [25] after appropriate scaling, and SWANS (solid line). Physical parameters are detailed in the caption of Figure 8.2. Data of the two-layer long-wave model courtesy of G. Dietze.

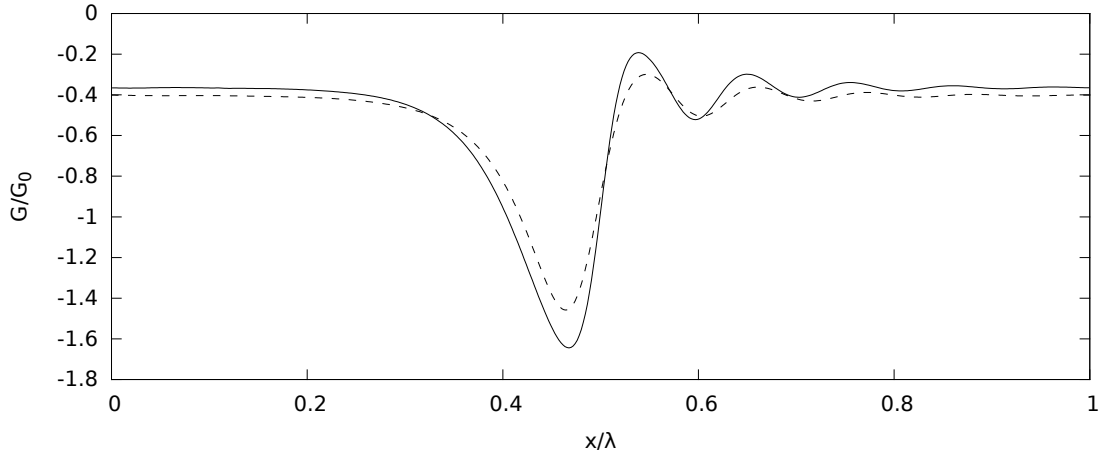

Figure 8.8: Space evolution of interfacial pressure gradient normalized to the uniform condition. Comparison between the two-layer long-wave model of Dietze & Ruyer-Quil (dashed line), Figure 8(b) of [25] after appropriate scaling, and SWANS (solid line). Physical parameters are detailed in the caption of Figure 8.2. Data of the two-layer long-wave model courtesy of G. Dietze.

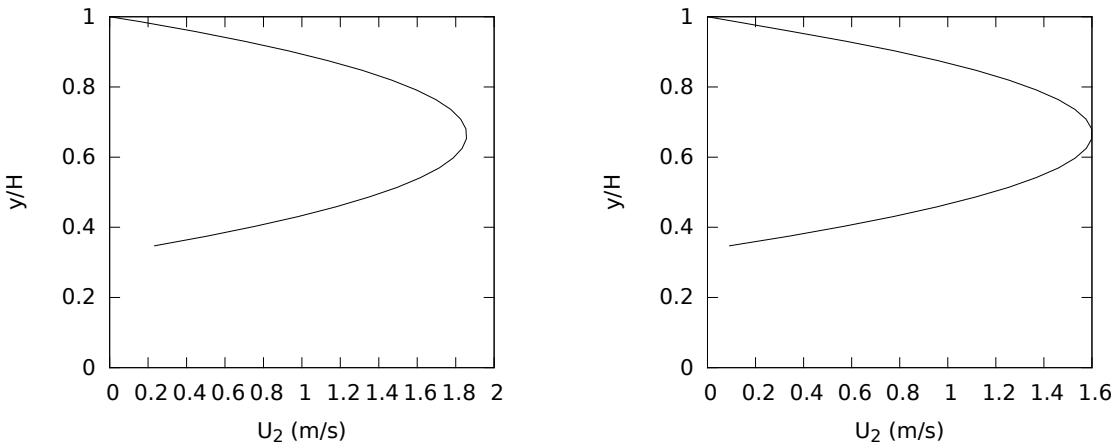

(a) *Gas velocity profile at* $x/\lambda = 0.35$ *of Figure 8.6.* (b) *Gas velocity profile at* $x/\lambda = 0.55$ *of Figure 8.6.*

Figure 8.9: Gas velocity profiles (normalized at the uniform flow: interface locates at $y/H = 1/3$).

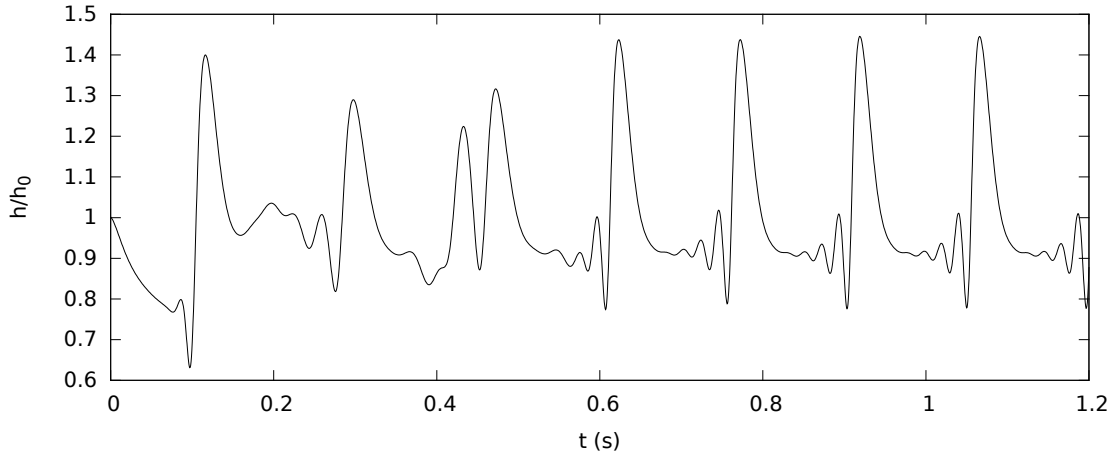

Figure 8.10: Time evolution of the film thickness normalized with the equilibrium film state obtained by means of the two-layer depth-integrated equations of Chapter 4. Physical parameters are detailed in the caption of Figure 8.2.

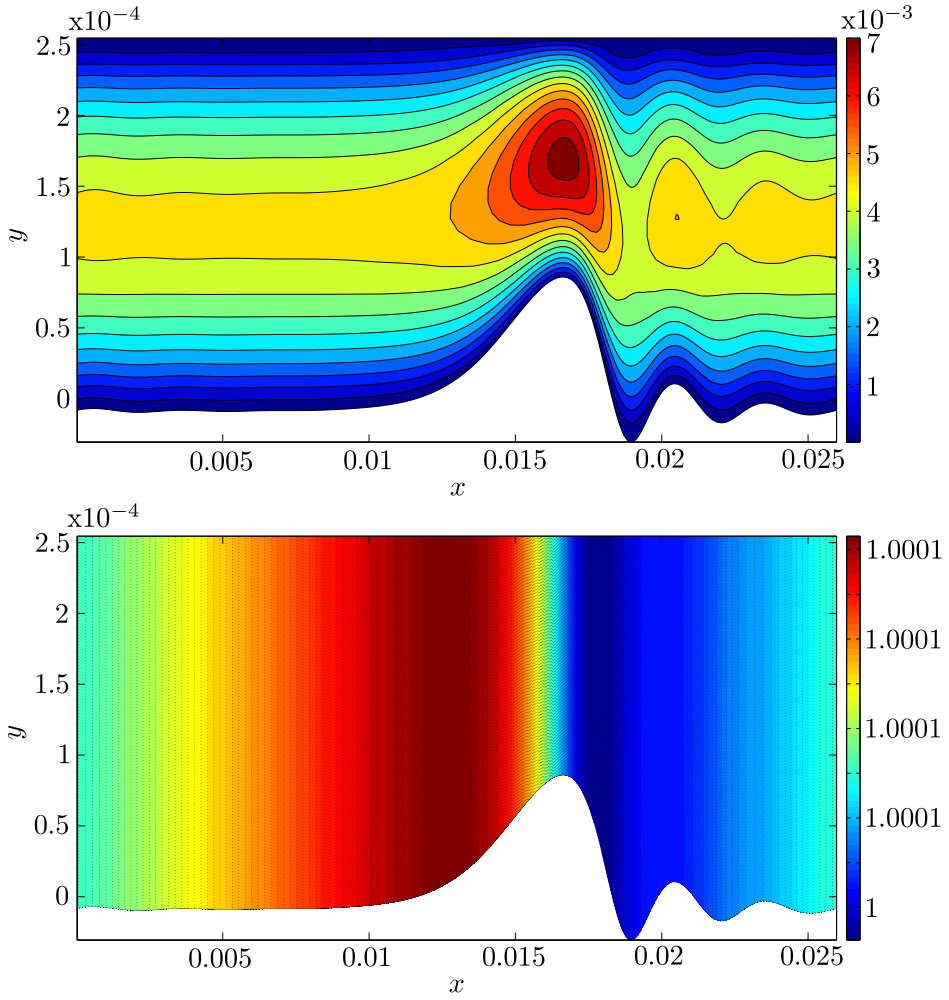

Figure 8.11: (top) Mach number contour in the gas phase. (bottom) Density contour ($kg\ m^{-3}$), or pressure contour, in the gas phase. The liquid film is white.

direction, suggesting that no compressibility effects appear.
Meanwhile, one can notice that the pressure (or the density) does not increase in the capillary region just after the main hump, although there exists a widening of the effective gas section: this shows that in addition to the inviscid contribution, i.e. Bernoulli velocity and pressure distributions, also the shear stress plays an important role in such a test.

8.2 Vertical two-layer flow

In this section, an air-water system flowing in a vertical large channel is considered. In such a configuration, the long-wave theory can be applied to the liquid film only, because the gas thickness is of the same order as the imposed wavelength, see Table 8.1 for the respective kh. Unlike the two-layer long-wave model, the SWANS approach allows for resolving such configurations given the compressible Navier-Stokes equations used in the description of the gas flow.
The channel geometry is sketched in Figure 8.12: the wavelength is $\lambda = 5.2\ mm$, whereas the height of the channel is $H = 6.37\ mm$. The uniform film thickness is instead $h_1 = 0.17\ mm$. The uniform flow is disturbed according to $h = h_0[1 + \epsilon \sin(2\pi x/\lambda)]$ (and same for the flow rate q), where $\epsilon = 0.25$.
Physical parameters are described in the caption of Figure 8.13. The total flow rate is almost entirely given by the gas, being the ratio of flow rates very high, namely $q_2/q_1 = 1194$.

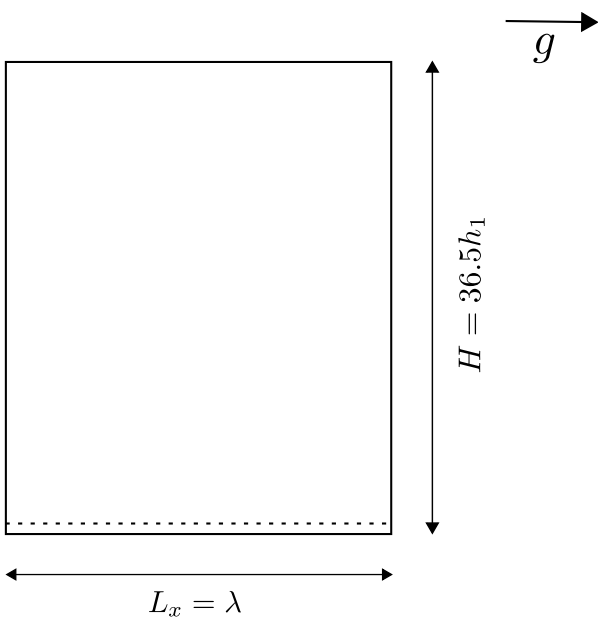

Figure 8.12: Geometry sketch (with a 10 : 1 scaling) of the vertical test, where $L_x = 5.2\ mm$ and $H = 6.37\ mm$. Dotted line expresses the equilibrium film thickness.

Table 8.3: Meshes used in this work, from the coarsest to the finest, and those used in Slosh by G. Blanchard.

mesh	$\Delta x(\mu m)$	$\Delta y(\mu m)$	$\Delta x/\Delta y$	cell number $(\cdot 10^3)$
5	130	124	1.05	2
6	65	31	2.1	16
7	130	15.5	8.39	16
Slosh coarse (DNS)	65	15.5	4.2	16
Slosh fine (DNS)	30	8	3.75	140

Figure 8.13 shows the time evolution of the normalized film thickness. One can notice that saturated non-linear waves are monochromatic and are not anticipated neither by capillary ripples nor by smaller peaks. This behavior recalls the experiments of Liu & Gollub [47] for gravity-driven falling liquid films discussed in Chapter 7, according to which, when increasing the forcing frequency, i.e. reducing the wavelength, amplitude of saturated waves decreases and capillary ripples disappear.
Indeed, an analysis of the magnitude of shear stress and gravity terms shows that the dominant effect in this scenario is the gravity force, given that the flow is vertical. For example, by considering the dimensional integrated film equation (6.1b) of Chapter 6 in the uniform flow conditions, one recovers $3/2\tilde{\tau}_i\rho_1^{-1}/(\tilde{\Lambda}\tilde{h}_0) \simeq 0.03$. This elucidates that the mechanism responsible for the instability of this flow is mainly the inertia.

The convergence of different grids, listed in Table 8.3, has also been investigated. Figure 8.14 shows the space evolution of the saturated waves for two different meshes: the convergence on the film thickness is clear. However, convergence on the gas velocity profiles is sketched in Figure 8.15, according to which the coarsest mesh (mesh 5 of Table 8.3) does not provide a proper solution.

8.2.1 The SWANS model versus DNS analysis

Film thickness spatio-temporal evolutions have been compared with DNS simulations provided by G. Blanchard at ONERA by means of the Slosh code (Chanteperdrix *et al.* [15], Schied *et al.* [75]). Comparison of the film thickness with respect to time is shown in Fig-

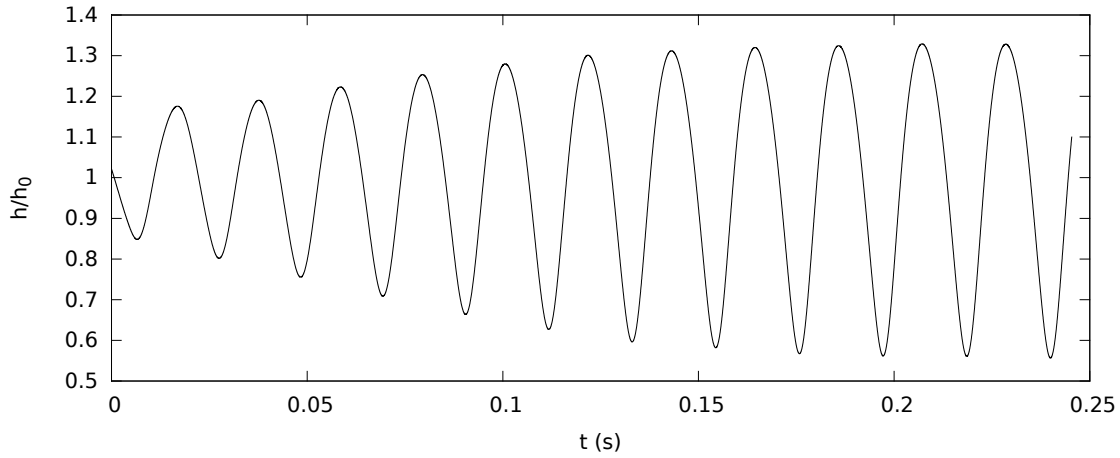

Figure 8.13: Time evolution of normalized film thickness for the vertical flow. Dimensionless numbers: $Re_1 = 16.5$ and $Re_2 = 1972$, $Fr = 5.65$, $We = 0.021$. Uniform flow: $\tau_{i0} = 0.03\ Pa$, $u_0|_h = 0.15\ m\ s^{-1}$.

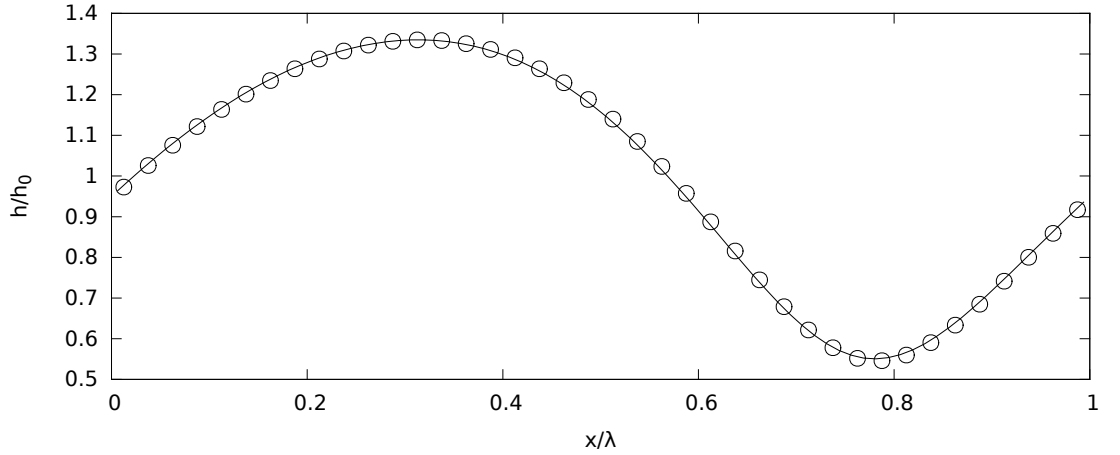

Figure 8.14: Film thickness versus normalized wavelength at $t = 0.235\ s$. Convergence of two different meshes. Solid line: mesh 6 in Table 8.3, circles: mesh 5 in Table 8.3. Physical parameters are detailed in the caption of Figure 8.13.

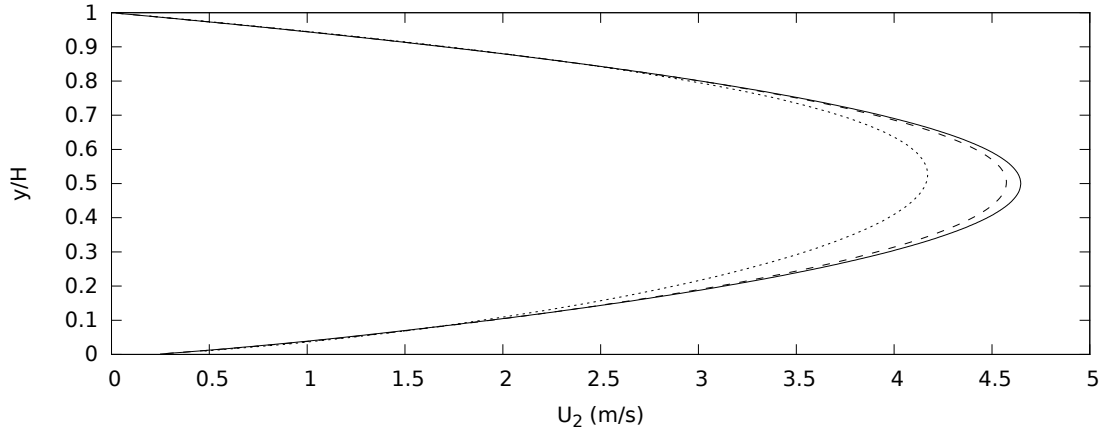

Figure 8.15: Gas velocity profiles at $t = 0.25\ s$. Convergence of three different meshes. Solid line: mesh 7 in Table 8.3; dashed line: mesh 6; dotted line: mesh 5. Physical parameters are detailed in the caption of Figure 8.13.

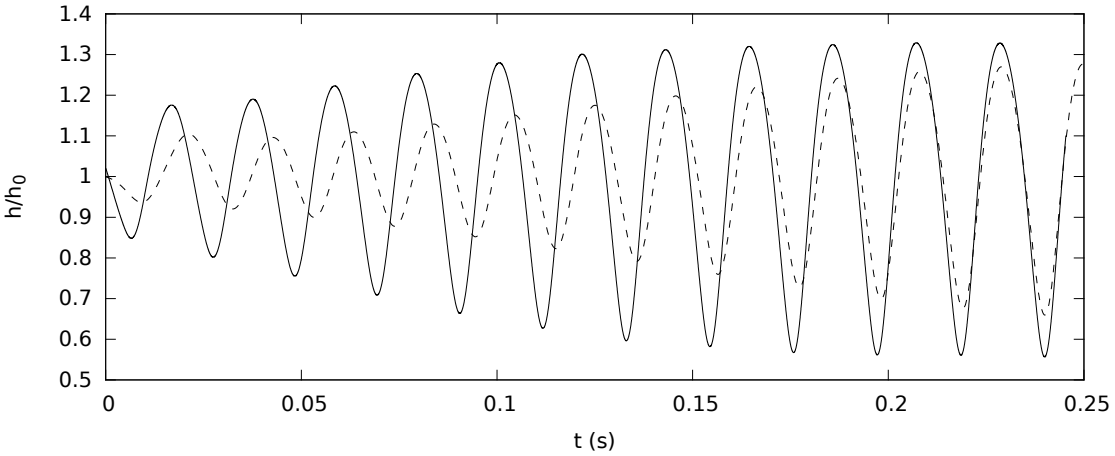

Figure 8.16: Film thickness time evolution. Comparison between SWANS (solid line) and DNS provided by G. Blanchard by means of Slosh (dashed line). Physical parameters are detailed in the caption of Figure 8.13.

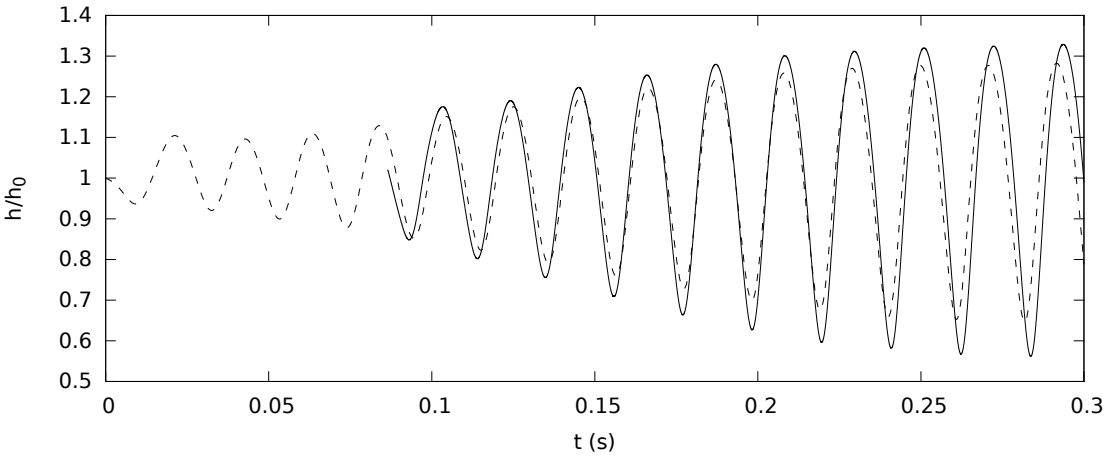

Figure 8.17: Film thickness time evolution after shifting in time the solution of SWANS. Comparison between SWANS (solid line) and DNS provided by G. Blanchard by means of Slosh (dashed line). Physical parameters are detailed in the caption of Figure 8.13.

ure 8.16. Several remarks must be done. Firstly, the two analysis do not start with the same evolution, and the transient is different. Indeed, it emerges that in the DNS evolution, the wave amplitude decreases in the first two periods before increasing again. This is mainly a problem of initial conditions: once the uniform flow is perturbed with a sinusoidal perturbation, only the stream-wise component of velocity is forced to satisfy this initial condition. In other words, $u(t = 0)$ fulfills the local equilibrium, and thus the stream-wise velocity matches to the initial perturbed interface. On the contrary, $v(t = 0) = 0$ and the initial condition is not satisfied. As a consequence, the decreasing beginning wave observed in the DNS simulation, can be explained by the fact that the cross-stream velocity needs time to match the initial condition. A detailed analysis shows that the time required by v to be entirely established in the gas phase is $t_g = H/a \simeq 2 \cdot 10^{-5}\ s$ and $t_f = \lambda/c \simeq 0.02\ s$ in the liquid phase, which corresponds to a few periods of the time evolution of the waves. Instead, in the SWANS approach, the long-wave model of the film respects the compatibility equation $\partial_t h + u|_h \partial_x h = v|_h$ by construction, hence, the cross-stream velocity is directly consistent with the shape of the initial perturbed interface, and does not need time to establish. Therefore, the different transient between DNS and SWANS in Figure 8.16 is due to the time required by the DNS to establish the cross-stream velocity in the liquid

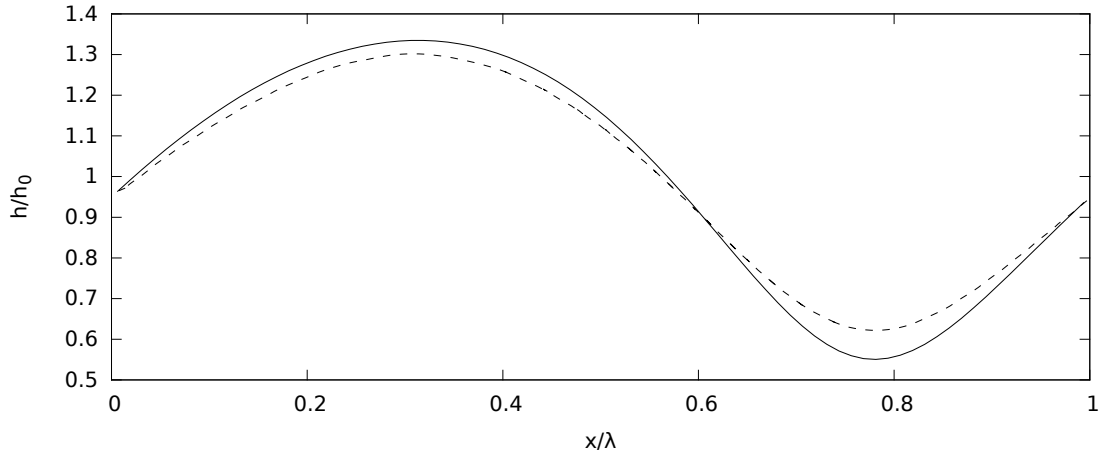

Figure 8.18: Film thickness space evolution of saturated non-linear waves. Comparison between SWANS (solid line) and DNS provided by G. Blanchard by means of Slosh (dashed line). Physical parameters are detailed in the caption of Figure 8.13.

phase.

As a matter of fact, by shifting the time solution, one can notice that the growth rate matches well between SWANS and DNS, as sketched in Figure 8.17.
At this stage, looking at the non-linear saturated waves, the difference between SWANS and DNS consists of two issues: firstly, there exists a gap in the amplitudes of such waves, because those computed by SWANS are higher than DNS's. Secondly, there is a discrepancy in the wave celerity, of about $7 \div 8\%$, meaning that every 15 waves travel, the model misses one. These two differences can be explained by the second-order dissipation missing in the thin film model used here.

Finally, space evolution of saturated non-linear waves in comparing SWANS and DNS are sketched in Figure 8.18, from where the crest of the wave is close to the one provided by the DNS, while the trough is more evident to be lower than the DNS, with an error about the 10%.

8.3 Effect of second-order dissipation in the film model

As final consideration, one aims to study the effect of second-order dissipative terms on the SWANS results previously described. Indeed, Ruyer-Quil & Manneville [69] have shown, for gravity-driven liquid films, that second-order dissipative terms play an important role in the accuracy of long-wave models. Subsequently, Dietze & Ruyer-Quil [25] have used this model (called *simplified second-order model*, because of the addition of only dissipative terms at $\mathcal{O}(\varepsilon^2)$) in the analysis of two-layer channel flows.

By recalling the Navier-Stokes equations (2.16), the x-momentum equation at order two can be manipulated as

$$\begin{aligned} &\partial_t u + u\partial_x u + v\partial_y u = G - \frac{\cos\beta}{Fr}\,\partial_x h + \frac{\sin\beta}{Fr} + \frac{1}{Re}\partial_{yy} u + \frac{1}{We}\partial_{3x} h \\ &+ \frac{1}{Re}\Big(2\partial_{xx} u + \partial_x(\partial_x u|_h) + 2\partial_{xx} h\partial_y u|_h + 2\partial_x h\partial_x(\partial_y u|_h)\Big)\ . \end{aligned} \tag{8.2}$$

This comes after the application of the boundary condition of normal stresses (2.20b) to the y-momentum equation, and the subsequent derivation with respect to x, namely

$$\partial_x p = -G + \frac{\cos\beta}{Fr}\partial_x h - \frac{1}{We}\partial_{3x} h + \frac{1}{Re}\partial_x(\partial_y v|_h + \partial_y v) - \frac{2}{Re}[\partial_{xx} h\partial_y u|_h + \partial_x h\partial_x(\partial_y u|_h)]\ . \tag{8.3}$$

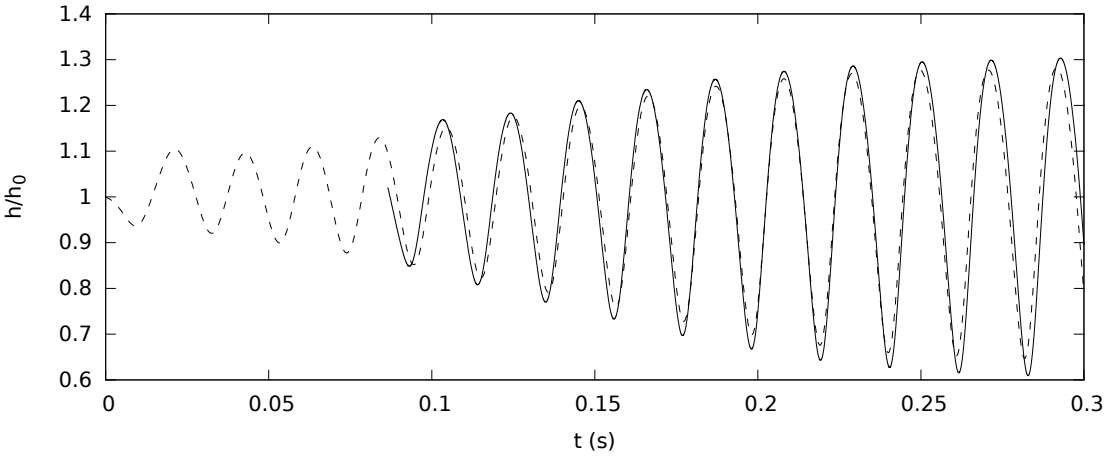

Figure 8.19: Film thickness time evolution. Comparison between SWANS (solid line) by adding the dissipative term $2\partial_{xx}q$, and DNS provided by G. Blanchard by means of Slosh (dashed line). Physical parameters are detailed in the caption of Figure 8.13.

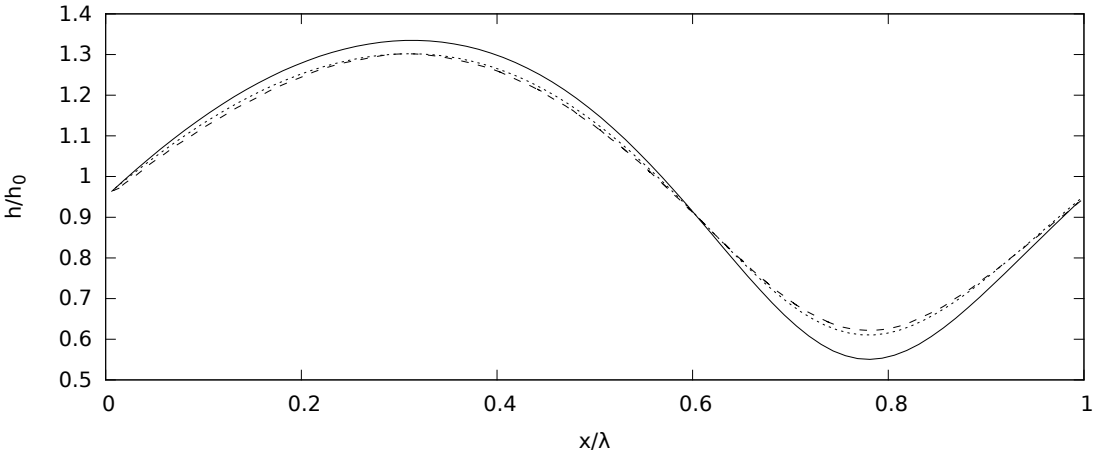

Figure 8.20: Film thickness space evolution of the traveling wave. Comparison between SWANS (dotted line) by adding the dissipative term $2\partial_{xx}q$, and DNS provided by G. Blanchard by means of Slosh (dashed line). Solid line is solution by SWANS without second-order dissipative contribution. Physical parameters are detailed in the caption of Figure 8.13.

The equivalence $\partial_{xy}v = -\partial_{xx}u$ and $\partial_y v|_h = -\partial_x u|_h$ through the continuity equation, has also been used to get (8.2).
Second-order terms of the x-momentum equation (8.2) are those in the second line, and this is clear after comparison with the first-order x-momentum equation (3.14). However, the analysis of the second-order film model is beyond the purpose of this work.* Therefore, in the present analysis only the term $2\partial_{xx}u$ is kept. Indeed, the integration of such a term over the film thickness provides $2\partial_{xx}q$, which plays a dissipative effect. In order to verify whether the differences between SWANS and DNS are given by the omission of second-order dissipative terms, the quantity $2\partial_{xx}q$ has been then added to the film model of order one. Solution of this system are shown in Figure 8.19. The simple addition of such a dissipative term improves the comparison with DNS, as evident from the space evolution of the film thickness of Figure 8.20. The match shows a good agreement, even without adding all other second-order terms. Furthermore, shear stress and pressure gradient evolutions with

*In the case of sheared films, dissipative terms of order two contain also spatio-temporal derivatives of shear stress and pressure gradient, making the problem more complicated and long.

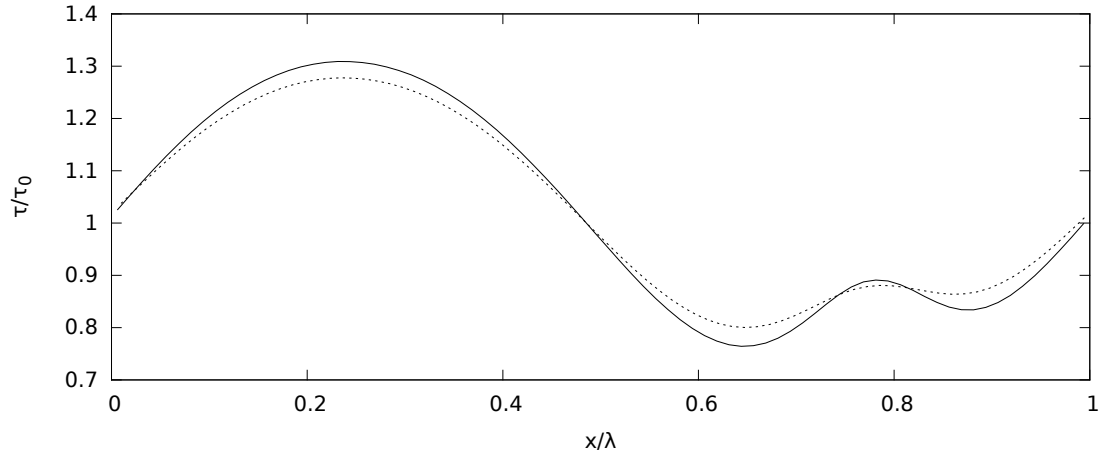

Figure 8.21: Interfacial shear stress space evolution. Comparison between SWANS (dotted line) by adding the dissipative term $2\partial_{xx}q$ and without (solid line). Physical parameters are detailed in the caption of Figure 8.13.

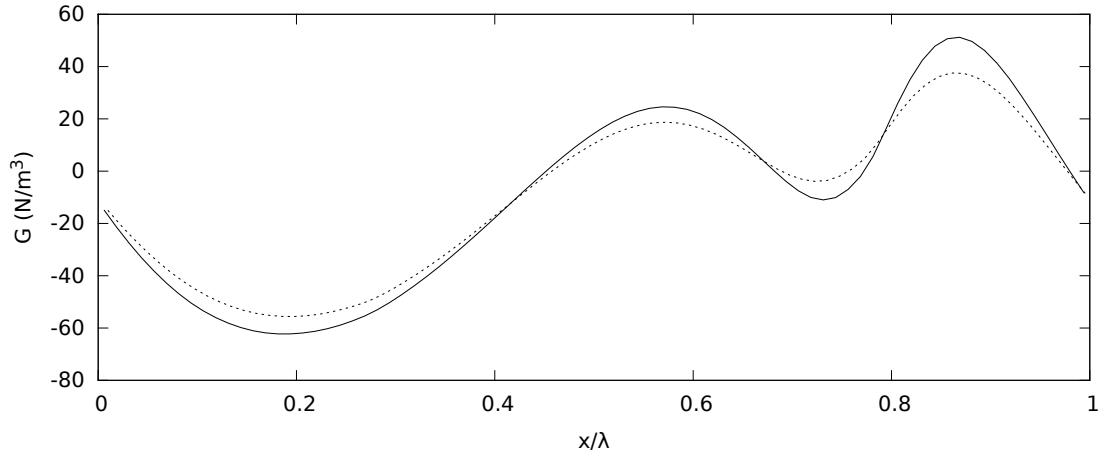

Figure 8.22: Interfacial pressure gradient space evolution. Comparison between SWANS (dotted line) by adding the dissipative term $2\partial_{xx}q$ and without (solid line). Physical parameters are detailed in the caption of Figure 8.13.

respect to the normalized wavelength are shown in Figures 8.21 and 8.22, in the case with and without the dissipative second-order term $2\partial_{xx}q$. There are not DNS data to which compare the results of SWANS. However, it is worthwhile to show that the dissipative term plays a more important role on the shear stress and pressure gradient than the film thickness, and it acts particularly on the small wave structures. One can notice that these small structures are observable only for the stresses, and do not appear in the wave shape. The effect that the shape of the stresses does not strongly influence the wave profile can be explained by the aforementioned mechanism of instability: the inertial terms play a more important role than the stresses.

Finally, by reproducing the horizontal confined test discussed at the beginning by adding the dissipative term $2\partial_{xx}q$, one obtains the traveling wave evolution as in Figure 8.23. It is evident that in this configuration the term $2\partial_{xx}q$ plays less: the peak of the traveling wave has the same amplitude as before, while capillary ripples decrease in amplitude. Indeed, the weight of $\partial_{xx}q$ in the horizontal narrow channel is small, while it is much larger in the vertical large channel because the ratio between film thickness and wavelength is ten times larger: the small parameter ε is ten times bigger for the large channel, see Table 8.1. However, in

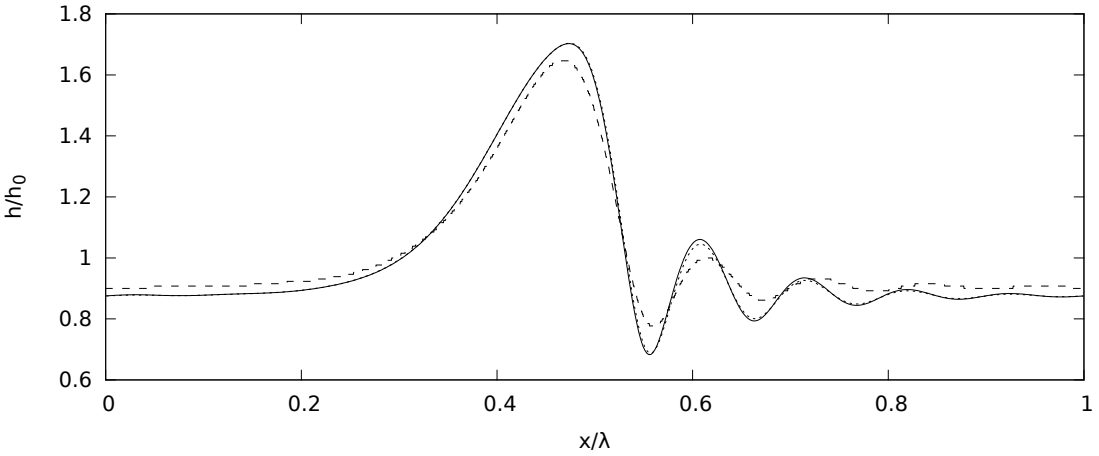

Figure 8.23: Film thickness time evolution of the horizontal two-layer flow. Comparison between SWANS (dotted line) by adding the dissipative term $2\partial_{xx}q$ and DNS provided by Dietze & Ruyer-Quil with OpenFOAM (dashed line). Solid line is solution by SWANS without second-order dissipative contribution. Physical parameters are detailed in the caption of Figure 8.2.

order to study the effect of the second-order dissipation for the two configurations analyzed in this chapter, one should account for all second-order terms when developing the long-wave film model.

9 Conclusions and perspectives

The aim of this Ph.D. work has been to study the dynamics of liquid films sheared by a gas flow. This subject has a wide interest because it is encountered in several industrial applications, such as distillation columns, heat pipes and coolers, as well as in several aerospace configurations. The main issue is the estimation of the influence of the waviness of liquid films over heat and mass transfers.

In order to save the computational cost, the liquid film has been modeled with integral equations rather than the classical Navier-Stokes equations. This low-dimensional film model has been then coupled to Navier-Stokes equations accounting for the gas phase, which gives the possibility to study many engineering configurations (not only channels). This approach represents a compromise between the two existing methods dedicated to two-layer flows: full DNS, i.e. Navier-Stokes equations in both the phases (Frank [27, 28], among the others), and the full long-wave model applied to both the phases (Dietze & Ruyer-Quil [25]).

Therefore, the object of this work has been the physical and numerical coupling between a thin liquid film and a laminar gas flow, which has driven to the development of the SWANS model. The depth-integrated equations used for the liquid phase derive from the integration of the Navier-Stokes equations over the film thickness. The long-wave assumption is an essential ingredient in order to close these integrated equations. Therefore, the liquid film is assumed to be thin compared to the wavelength of interfacial waves. This assumption does not reduce notably the validity of the model since several experiments (Kapitza [41], Liu & Gollub [47], Alekseenko *et al.* [2], Craik [21], Cohen & Hanratty [19]) show that waves which develop at the liquid-gas interface have usually a much larger length than the film thickness. On the other hand, the advantage of using shallow water equations in describing the dynamics of thin liquid films is mainly numerical: the computational cost is greatly reduced compared to the Navier-Stokes analysis. For example, the discretization of shallow water equations needs by construction only one cell in the cross-stream direction.
The long-wave model developed in this work takes into account interfacial shear stress and pressure gradient provided by the gas, and possibly the gravity force. This system of equations has been discretized by means of an augmented system, which accounts for one evolution equation for the surface tension. This prevents from the typical numerical shortcomings deriving by the discretization of the surface tension term. The validity of such a numerical approach has been proven by comparing wave celerities and growth rates

of linear waves to those given by the performed linear stability theory. Furthermore, the comparison of the numerical solution with non-linear waves detected by the experiments of Liu & Gollub [47] has been also performed. However, being accurate at $\mathcal{O}(\varepsilon)$, the developed integral model of shallow water equations misses the dissipative second-order terms, and thus is not able to catch the exact amplitude of periodic waves, as well as amplitude and phase of capillary ripples (Kalliadasis *et al.* [40]).

On the other hand, compressible Navier-Stokes equations have been used to describe a laminar gas flowing on the top of the liquid film. These equations have been discretized through a low-Mach scheme, which allows studying compressible flows at low speeds, such as those adopted in this work. The reason for using compressible equations for the gas phase is due to the aim of solving aerospace applications, in line with the spirit of ONERA. Indeed, in those applications, the gas flows usually at high speeds and compressibility effects cannot be neglected.

The coupling methodology between the above mentioned depth-integrated equations and compressible Navier-Stokes equations represents the main result of this Ph.D. thesis. The coupling has been assured by transferring interfacial stresses from the gas to the film. On the contrary, the liquid film sends back to the gas the interfacial velocities, as well as the position of the interface. Particularly, the implemented ALE technique allows moving the nodes of the gas grid in order to take into account the displacement of the interface. Finally, the integral model and the low-Mach scheme, accounting for the liquid and the gas, respectively, as well as the coupling approach, have been implemented in MATLAB to accomplish the code SWANS. A peer-reviewed publication about this subject is under submission (Lavalle *et al.* [44]).

The validity of SWANS has been then proven by performing comparisons with the DNS for two different test-cases: an air-water flow in (i) a horizontal strictly narrow channel and (ii) a vertical large channel.

In the case of the strictly confined flow, the film thickness evolution has been compared to DNS performed by Dietze & Ruyer-Quil [25]. Indeed, the profile of saturated periodic waves shows a good agreement. Furthermore, interfacial shear stress and pressure gradient have been compared with their full model, because the thinness of the channel allows for using averaged equations for both layers. Results show a good agreement.
In addition, time evolution of the film thickness has been analyzed also with the full integral model developed in Chapter 4. This model, accurate at $\mathcal{O}(\varepsilon)$, has been built by imposing the total flow rate in the channel, and thus leaving the pressure gradient free. On the contrary, all computational simulations have been performed by imposing a pressure drop between the entry and exit sides of the channel. As a consequence, a proper comparison between the code SWANS and the full model developed in this thesis cannot be performed. Nevertheless, although this discrepancy, such a full reduced model is capable to reproduce the periodic waves.

Finally, in the case of the large channel, the film thickness spatio-temporal evolution has been compared with the DNS performed at ONERA by G. Blanchard with the code Slosh. Also in this test, comparisons show a good agreement.

However, as already mentioned, the integral model for the liquid film has been developed at $\mathcal{O}(\varepsilon)$, thus neglecting the dissipative second-order terms. Hence, the code SWANS cannot capture exactly the amplitude and the celerity of periodic waves and capillary ripples. The discrepancy with DNS has been quantified in the range $3\% \div 8\%$. In order to improve such an integral model, second-order terms must be also considered. As final result of this Ph.D work, the second-order dissipative term $2\partial_{xx}q$, which derives from the integration of the term $2\partial_{xx}u$ in the boundary-layer equations, has been added to the first-order model. This is only one of many second-order dissipative terms which come out from the analysis at $\mathcal{O}(\varepsilon^2)$. However, in the large channel test, it has been proven that the only addition

of the dissipative term $2\partial_{xx}q$ improves the solution provided by the code SWANS, in the sense that the amplitude of periodic waves matches better with the DNS analysis. On the contrary, by applying this correction to the strictly confined horizontal configuration, the effect of this dissipative second-order term is much smaller and almost imperceptible.

As perspectives of this work, one can consider again the full reduced model of Chapter 4. As mentioned above, in order to have proper comparisons with the solver SWANS and DNS, the asympotic expansion must be developed in the case of imposed pressure gradient, rather than imposed total flow rate. In addition, one can also analyze the limit of small ratio of viscosities m, in order to greatly simplify the asymptotic fields and the final film model. Indeed, in the liquid-gas applications the viscosity ratio is usually small, i.e. $m = 0.01$. Therefore, all stress and velocity fields can be developed in the limit of vanishing m and thus reduce the complexity of the system of equations.

For what concerns the developed computational method, the main feature to be discussed is the correction of the velocity gradient to account for non-orthogonal meshes in the computation of the shear stress. As already explained in Chapter 6, the diamond method of Coudière [20] can be for example implemented in SWANS as correction of the velocity gradient.

Another perspective for this work regards the film model: it can be pushed up to the second order, with the aim to improve amplitude and celerity of periodic waves and capillary ripples in matching those provided by DNS. However, the so-called *simplified second-order model*, which takes into account only the dissipative terms at $\mathcal{O}(\varepsilon^2)$ and neglecting the inertial ones, should be enough, as shown by Dietze & Ruyer-Quil [25] for their full long-wave model.

There are two other stimulating extensions of this work regarding boundary layers over a wavy liquid film. Firstly, the developed coupling technique can be extended to the case of laminar boundary layers: for example, one can consider a Blasius velocity profile in interaction with a wavy liquid film. In addition, the analysis can move to turbulent boundary layers: the works of Benjamin [8] and Tseluiko & Kalliadasis [90] can be continued by considering liquid films with a certain longitudinal velocity.

Concerning the liquid-gas instabilities, the SWANS model can be used to investigate the instabilities of counter-current flows. Indeed, the work of Tseluiko & Kalliadasis [90] does not contemplate the velocity of the interface and accounts for turbulent flows only, while Dietze & Ruyer-Quil [25] cannot dispose of a wide description of the gas phase. So far, SWANS seems the only tool capable to circumvent the use of full DNS for these flow configurations. In the case, instead, of co-current channel flows, the work of Dietze & Ruyer-Quil [25] can be extended to higher Re in the gas phase. This would allow investigating the instability mechanism and the development of vortex structures in flows where shear stress and pressure effects are comparable.

To conclude, the coupling methodology developed in this work can be implemented into the platform CEDRE at ONERA. Indeed, the CEDRE platform has many numerical tools avalaible, such as a shallow water film solver, the ALE moving mesh and a compressible Navier-Stokes gas solver. However, the implementation into CEDRE cannot be immediate. Effectively, the SWANS model should be extended to more complex two-dimensional geometries, such as aircraft wing profiles, and the prediction of resulting stress and heat transfer coefficients should be quantified. Furthermore, from a numerical point of view, the computational cost related to the mesh refinement must be also analyzed. For example, it has been discussed in this work that SWANS manifests a quicker convergence (in terms of mesh refinement) than the full DNS. It would be then interesting to investigate and compare the time step required by SWANS and DNS.
Finally, the implementation of the surface tension into the shallow water film solver of

CEDRE must be accomplished before the analysis of the coupling with the Navier-Stokes gas solver based on the ALE technique.

A Integration of the boundary-layer equations

The integration of boundary-layer equations (3.14) over the film thickness leads to the integrated equations (3.15). The integration methodology is shown hereby and can also be extended to two-layer systems (4.16) and (4.18).
Leibniz's integration rule reads

$$\frac{d}{dx}\left(\int_a^b f(x,y)\,dy\right) = \int_a^b \partial_x f(x,y)\,dy + f(x,b)\partial_x b - f(x,a)\partial_x a \ . \tag{A.1}$$

Focusing first on the continuity equation, by using the Leibniz's integration rule and the no-slip boundary condition, one obtains

$$\int_0^h \partial_x u\,dy = \partial_x\Big(\int_0^h u\,dy\Big) - u|_h \partial_x h \ . \tag{A.2}$$

Thus the continuity equation $\partial_x u + \partial_y v = 0$ turns into

$$\partial_x\Big(\int_0^h u\,dy\Big) - u|_h \partial_x h + v|_h = \partial_t h + \partial_x q = 0 \ , \tag{A.3}$$

where the definition of y-averaged flow rate, as well as the boundary conditions (3.11c) and (3.10) have been used.

For what concerns the integration of the x-momentum equation, time and cross-stream derivatives develop as in (A.2). On the other hand, in an analogous way as the continuity equation, the term $u\partial_x u + v\partial_y u$ can be integrated as

$$\int_0^h \Big(\partial_x u^2 + \partial_y(uv)\Big)\,dy = \partial_x\Big(\int_0^h u^2\,dy\Big) - u^2|_h \partial_x h + (uv)|_h \ , \tag{A.4}$$

where the assumption of incompressible flow has been used.
Finally, through the boundary condition (3.11c), one obtains equations (3.15).

B Fields of the first-order expansion

In this appendix, the first-order fields related to the two-layer channel flow of Chapter 4 are expressed.
The velocity profile of the film at order one can be computed by double integration of the x-momentum equation of system (4.39). Indeed, the first-order velocity profile of the liquid film reads

$$
\begin{aligned}
u_1^{(1)} = \frac{\partial_x G^{(0)}}{12}\Bigg[\frac{Re}{5}G^{(0)}(y^5-h^5) + \Big(\frac{1}{2}y^3h - \frac{1}{5}y^4 - h^4\Big)(Re\ G^{(0)}h + \tau_i^{(0)})\Bigg]yRe^2 \\
+ \frac{1}{3}\partial_t G^{(0)}\Bigg[-\frac{1}{8}y^3 + \frac{1}{2}y^2h - h^3\Bigg]Re^2y \\
+ \frac{1}{6}\partial_x \tau_i^{(0)}\Bigg[\Big(\frac{1}{4}y^3 - h^3\Big)(Re\ G^{(0)}h + \tau_i^{(0)})\Bigg]yRe \\
+ \frac{1}{2}\partial_t \tau_i^{(0)}\Bigg[\frac{1}{3}y^2 - h^2\Bigg]yRe + \tau_i^{(1)}y \\
+ \partial_x h\Bigg[\Big(\frac{1}{24}y^3 - \frac{1}{6}h^3\Big)(Re\ G^{(0)}h + \tau_i^{(0)})yRe\Bigg] \\
+ \partial_t h\Bigg[\frac{1}{3}y^2 - h^2\Bigg]yRe + G^{(1)}\Bigg[-\frac{1}{2}y + h\Bigg]yRe - \frac{1}{2}\frac{Re}{We}y^2\partial_{3x}h\ .
\end{aligned}
\tag{B.1}
$$

In an analogous way, the first-order velocity profile in the gas yields

$$
\begin{aligned}
u_2^{(1)} = \frac{1-y}{360m^3}\Bigg[\Bigg[& -180Re^2\ G^{(0)}\tau_i^{(0)} r(1-h)^3 + Re^2\ {G^{(0)}}^2 r\ A_1 \\
& + 45Re^2\ G^{(0)} r(1-y)^3\Big(\tau_i^{(0)} - Re\ G^{(0)}(1-h)\Big)\Bigg]\partial_x h \\
& + G^{(0)} r Re^2\ m\ A_2\ \partial_t h + Re^2\ r\ m\ A_5\ \partial_t G^{(0)} \\
& + \Big[Re^2\tau_i^{(0)} A_3 + Re^3 G^{(0)} A_4\Big] r\ \partial_x G^{(0)} \\
& + Re\ r\Big[\tau^{(0)} A_6 + Re\ G^{(0)} A_7\Big]\partial_x \tau_i^{(0)} \\
& + Re\ r\ m\ A_8\ \partial_t \tau_i^{(0)} - 360m^2\tau_i^{(1)} \\
& + \frac{180}{Fr} m^2(1+y-2h)\Big(Re\ G^{(1)} + Re(1-r)\partial_x h\Big)\Bigg]\ ,
\end{aligned}
\tag{B.2}
$$

with

$$
\begin{aligned}
A_1 &= 90(1-h)^4 + 18(1-y)^4\ , \\
A_2 &= -60(1-y)^2 + 180(1-h)^2\ , \\
A_3 &= 120(1-h)^4 + 12(1-y)^4 - 45(1-h)(1-y)^3\ , \\
A_4 &= -60(1-h)^5 + 5(1-y)^5 - 45h(1-h)(1-y)^3 \\
&\quad + 15(1-h)(1-y-3y^2+5y^3-2y^4\ , \\
A_5 &= -120(1-h)^3 - 15(1-y)^3 + 60(1-h)(1-y)^2\ , \\
A_6 &= 45(1-y)^3 - 180(1-h)^3\ , \\
A_7 &= 18(1-y)^4 + 90(1-h)^4 - 45(1-h)(1-y)^3\ , \\
A_8 &= -60(1-y)^2 + 180(1-h)^2\ .
\end{aligned}
$$

These velocity profiles still depend on two unknowns: the pressure gradient $-G^{(1)}(h)$ and the interfacial shear stress $\tau_i^{(1)}$ at order one. The latter can be computed similarly as the order zero. By using the boundary conditions at the interface (4.41c), one obtains

$$
\begin{aligned}
\tau_i^{(1)} = \frac{6}{35}\frac{Q^2 Re(m-1)\big(h^2(m-1)-1+2h\big)}{\big(1+(m-1)(-6h^2+4h^3+4h)+h^4(m-1)^2\big)^5}\Big(& r(h-1)^{16} \\
& - rmh(5h^2-27h-2)(h-1)^{13} \\
& + 2rm^2h^2(5h^4-54h^3+141h^2+18h+16)(h-1)^{10} \\
& - h^4m^3C_1(h-1)^7 + h^5m^4C_2(h-1)^5 - h^7m^5C_3(h-1)^4 \\
& + 2h^{10}m^6C_4(h-1)^2 - h^{13}m^7(5h^2+17h-24)(h-1) + h^{16}m^8\Big)\partial_x h \\
& - \frac{2(h-1)^2 Re\ h^2 m}{\big(1+(m-1)(-6h^2+4h^3+4h)+h^4(m-1)^2\big)}\Big(\frac{6}{35}\frac{r-1}{Fr}\partial_x h + \frac{\partial_{3x} h}{Re\ We}\Big)\ ,
\end{aligned}
\tag{B.3}
$$

with

$$
\begin{aligned}
C_1 &= h^5 + 10rh^5 + 19h^4 - 162rh^4 + 858rh^3 + 127h^3 + 1001h^2 - 2146rh^2 \\
&\quad - 448h + 496rh + 384r - 700 \,, \\
C_2 &= 5rh^6 + 5h^6 + 73h^5 - 103rh^5 + 759rh^4 + 319h^4 + 1535h^3 - 3641rh^3 \\
&\quad + 4020rh^2 - 3304h^2 + 812h - 480rh + 560 \,, \\
C_3 &= rh^5 + 10h^5 + 112h^4 - 24rh^4 + 310h^3 + 213rh^3 - 1506rh^2 \\
&\quad + 444h^2 - 1820h + 2016rh + 560 \,, \\
C_4 &= 5h^4 + 34h^3 + 9h^2 - 158h + 126 \,.
\end{aligned}
$$

The computation of the pressure gradient $-G^{(1)}(h)$, being still unknown, is obtained from the gauge condition (4.30), which states that the sum of first-order flow rates is equal to zero. This gives also the physical explaination that the first-order pressure gradient varies along the channel in a way that the first-order total flow rate is zero. First order flow rates are given by integration of the respective velocities, namely

$$
q_1^{(1)} = \int_0^h u_1^{(1)}\, dy \,, \qquad\qquad q_2^{(1)} = \int_h^H u_2^{(1)}\, dy \,. \tag{B.4}
$$

Finally, by imposing the condition (4.30), as well as by replacing $\partial_t h$ through the mass conservation equation, one finds

$$
\begin{aligned}
G^{(1)}(h) = -\frac{18}{35} &\frac{Q^2(m-1)\big(h^2(m-1)-1+2h\big)}{\big(1+(m-1)(-6h^2+4h^3+4h)+h^4(m-1)^2\big)^5}\Big(3r(h-1)^{15} \\
&- rmh(15h^2-70h+11)(h-1)^{12} \\
&+ 2rm^2h^2(15h^4-140h^3+349h^2-157h-11)(h-1)^9 \\
&- h^3m^3B_1(h-1)^7 + h^5m^4B_2(h-1)^5 - h^7m^5B_3(h-1)^3 \\
&+ 2h^9m^6B_4(h-1)^2 - h^{12}m^7(15h^2+40h-44)(h-1) + 3h^{15}m^8\Big)\partial_x h \\
&+ \frac{(h-1)^2(h^2m-h^2+2h-4hm-1)}{\big(1+(m-1)(-6h^2+4h^3+4h)+h^4(m-1)^2\big)}\left(\frac{18}{35}\frac{r-1}{Fr}\partial_x h - \frac{\partial_{3x}h}{Re\ We}\right) \,,
\end{aligned}
\tag{B.5}
$$

with

$$
\begin{aligned}
B_1 &= 3h^5 + 30rh^5 + 46h^4 - 390rh^4 + 1638rh^3 + 259h^3 + 686h^2 - 2364rh^2 \\
&\quad + 350h + 510rh + 184r \,, \\
B_2 &= 15h^5 + 15rh^5 - 250rh^4 + 175h^4 + 641h^3 + 1491rh^3 - 3830rh^2 \\
&\quad + 707h^2 - 882h + 3230rh - 376r - 280 \,, \\
B_3 &= 3rh^5 + 30h^5 + 240h^4 - 61rh^4 + 378h^3 + 473rh^3 - 1769rh^2 \\
&\quad - 510h^2 - 714h + 2698rh - 1344r + 392 \,, \\
B_4 &= 15h^4 + 80h^3 + 19h^2 - 181h + 56 \,.
\end{aligned}
$$

The first-order wall shear stress in the liquid reads

$$
\begin{aligned}
\tau_{1w}^{(1)} = u_{1,y}^{(1)}|_0 = &-\frac{1}{12}Re^2h^4\Big[\tau_i^{(0)} + \frac{6}{5}Re\ G^{(0)}h\Big]\partial_x G^{(0)} \\
&- \frac{1}{3}Re^2h^3\partial_t G^{(0)} - \frac{1}{2}Re\ h^2\Big[Re\ G^{(0)}\partial_t h + \partial_t\tau_i^{(0)}\Big] \\
&- \frac{1}{6}Re\ h^3\Big(Re\ G^{(0)}\partial_x h + \partial_x\tau_i^{(0)}\Big)\big(Re\ G^{(0)}h + \tau_i^{(0)}\big) \\
&+ \tau_i^{(1)} + Re\ G^{(1)}h + \frac{Re}{We}h\partial_{3x}h \,,
\end{aligned}
\tag{B.6}
$$

while in the gas phase yields

$$\begin{aligned}\tau_{2w}^{(1)} = m u_{2,y}^{(1)}|_1 = &-\frac{1}{2}\frac{r}{m} Re\ h_2^2 (Re\ G^{(0)} \partial_t h + \partial_t \tau_i^{(0)}) \\ &- \frac{1}{2}\frac{r}{m^2} Re\ h_2^2 \Big(\frac{1}{2} Re\ G^{(0)} \partial_x h h_2 + \frac{1}{2} \partial_x \tau_i^{(0)} - \frac{1}{3} Re\ \partial_x G^{(0)} h_2^2 \Big) (Re\ G^{(0)} h_2 - 2\tau_i^{(0)}) \\ &+ \frac{1}{3}\frac{r}{m} Re^2 h_2^3 \partial_t G^{(0)} \\ &+ \tau_i^{(1)} - h_2 Re\ G^{(1)} - \frac{Re}{Fr} h_2 (1-r) \partial_x h\ ,\end{aligned} \tag{B.7}$$

where $h_2 = 1 - h$ is the thickness of the gas layer.

In conclusion, these fields can be greatly simplified by considering that the viscosity ratio m is small for the air-water flows considered in this work.

C Dispersion relation coefficients

Coefficients of the two-layer dispersion relation (5.36) are expressed here. Coefficient D_1 multiplies ik and reads

$$
\begin{aligned}
D_1 = &- \frac{Q^2}{35}\frac{1}{((m-1)^2h^4+4(m-1)h^3H-6(m-1)h^2H^2+4(m-1)hH^3+H^4)^5}\\
&\Big[-r\big[-45(m-1)^7h^{18}+252H(4m-3)(m-1)^6h^{17}+M_1H^2h^{16}+M_2H^3h^{15}\\
&+M_3H^4h^{14}+M_4H^5h^{13}+M_5H^6h^{12}+M_6H^7h^{11}+M_7H^8h^{10}\\
&+M_8H^9h^9+M_9H^{10}h^8+M_{10}H^{11}h^7+M_{11}H^{12}h^6+M_{12}H^{13}h^5+M_{13}H^{14}h^4\\
&+M_14H^{15}h^3+M_{15}H^{16}h^2-18H^{17}(m+6)(m-1)h+9H^{18}(m-1)\big]\\
&-\big[5m^2(7m+2)(m-1)^7h^{18}-4Hm^2(71m-8)(m-1)^6h^{17}+N_1H^2h^{16}\\
&+N_2H^3h^{15}+N_3H^4h^{14}+N_4H^5h^{13}+N_5H^6h^{12}+N_6H^7h^{11}+N_7H^8h^{10}\\
&+N_8H^9h^9+N_9H^{10}h^8+N_{10}H^{11}h^7+N_{11}H^{12}h^6+N_{12}H^{13}h^5\\
&+N_{13}H^{14}h^4+84H^15m^2(-49+39m)h^3+315H^16m^2h^2\big]\Big]\\
&-\frac{1}{h^3((m-1)^2h^4+4(m-1)h^3H-6(m-1)h^2H^2+4(m-1)hH^3+H^4)Fr}\\
&\Big[h^4(H-h)^3(H-h+hm)r+\big[(m-1)h^8+(4-3m)Hh^7+3(m-2)H^2h^6\\
&+\Big(H^3(4-m)+q_0^2Fr(m-1)^2\Big)h^5+\Big(-H^4+4Hq_0^2Fr(m-1)\Big)h^4\\
&-6H^2q_0^2Fr(m-1)h^3+4H^3q_0^2Fr(m-1)h^2+q_0^2FrH^4h\Big]\\
&+\frac{6k}{h^3((m-1)^2h^4+4(m-1)h^3H-6(m-1)h^2H^2+4(m-1)hH^3+H^4)^2Re}\\
&\Big[Q\big[-m(m-1)^3h^8+m(m-1)^2Hh^7-2m(m-1)(3m-7)H^2h^6\\
&+2m(m-1)(m-13)H^3h^5+19m(m-1)H^4h^4-m(6m-5)H^5h^3\big]\\
&+q_0\big[(m-1)^4h^8+8(m-1)^3Hh^7-4(3m-7)(m-1)^2H^2h^6\\
&+8(m-7)(m-1)^2H^3h^5+70(m-1)^2H^4h^4-8(m-1)(6m-7)H^5h^3\\
&+4(m-1)(4m-7)H^6h^2+8(m-1)H^7h+H^8\big]\Big]\,,
\end{aligned}
\tag{C.1}
$$

where coefficients M are defined as

$$
\begin{aligned}
M_1 &= -9(1015m^2 - 1642m + 663)(m-1)^5 \ , \\
M_2 &= 18(2121m^3 - 6506m^2 + 5633m - 1632)(m-1)^4 \ , \\
M_3 &= -9(9555m^4 - 48804m^3 + 77619m^2 - 48022m + 11220)(m-1)^3 \ , \\
M_4 &= 18(6230m^5 - 50127m^4 + 129469m^3 - 142941m^2 + 71169m - 14280)(m-1)^2 \ , \\
M_5 &= -9(9457m^5 - 111937m^4 + 367633m^3 - 472007m^2 + 255346m - 55692)(m-1)^2 \ , \\
M_6 &= 18(1945m^5 - 40406m^4 + 182326m^3 - 286478m^2 + 174213m - 42432)(m-1)^2 \ , \\
M_7 &= -9(m-1)(672m^6 - 36848m^5 + 285943m^4 - 759780m^3 \\
&\qquad + 873609m^2 - 466466m + 102102) \ , \\
M_8 &= -18(m-1)(4517m^5 - 61586m^4 + 220424m^3 - 306768m^2 + 194337m - 48620) \ , \\
M_9 &= 9(m-1)(944m^5 - 33397m^4 + 177220m^3 - 309155m^2 + 249106m - 72930) \ , \\
M_{10} &= 18(m-1)(2490m^4 - 23090m^3 + 51523m^2 - 60515m + 21216) \ , \\
M_{11} &= -9(m-1)(288m^4 - 6744m^3 + 16921m^2 - 43498m + 18564) \ , \\
M_{12} &= -18(m-1)(170m^3 + 1034m^2 + 5579m - 2856) \ , \\
M_{13} &= -9(m-1)(16m^3 - 1797m^2 - 1962m + 1020) \ , \\
M_{14} &= -18m(195m + 119)(m-1) \ , \\
M_{15} &= 9(m-1)(32m^2 + 24m + 51) \ .
\end{aligned}
$$

On the other hand, coefficients N read

$$
\begin{aligned}
N_1 &= m^2(993m^2 - 1162m + 493)(m-1)^5 \ , \\
N_2 &= -2m^2(237m^3 + 192m^2 - 523m - 3362)(m-1)^4 \ , \\
N_3 &= m^2(5880m^3 - 27027m^2 - 4658m + 39917)(m-1)^3 \ , \\
N_4 &= -2m^2(2229m^4 - 32547m^3 + 43527m^2 + 49463m - 66992)(m-1)^2 \ , \\
N_5 &= 3m^2(264m^4 - 26117m^3 + 63223m^2 + 35993m - 94963)(m-1)^2 \ , \\
N_6 &= 12m^2(5554m^3 - 22653m^2 + 424m + 32923)(m-1)^2 \ , \\
N_7 &= -3m^2(m-1)(11168m^4 - 90494m^3 + 134317m^2 + 58864m - 111551) \ , \\
N_8 &= 4m^2(m-1)(1736m^4 - 29789m^3 + 79311m^2 - 15194m - 25696) \ , \\
N_9 &= m^2(m-1)(21568m^3 - 140493m^2 + 148650m - 135817) \ , \\
N_{10} &= 2m^2(m-1)(18955m^2 - 56993m + 112954) \ , \\
N_{11} &= -m^2(m-1)(9408m^2 - 57296m + 172217) \ , \\
N_{12} &= 2m^2(m-1)(1008m^2 - 10017m + 40448) \ , \\
N_{13} &= 7m^2(-3843m + 504m^2 + 3419) \ .
\end{aligned}
$$

Coefficient D_2 instead is relative to k^2 in the dispersion relation (5.36) and yields

$$\begin{aligned} D_2 = & \frac{1}{Re\big((m-1)^2h^4+4(m-1)h^3H-6(m-1)h^2H^2+4(m-1)hH^3+H^4\big)^2h^3} \\ & \Big[6\Big(-m(m-1)^3h^8+m(m-1)^2h^7H-2m(m-1)(3m-7)h^6H^2 \\ & +2m(m-1)(m-13)h^5H^3+19m(m-1)h^4H^4-m(6m-5)h^3H^5\Big)Q \\ & +6\Big((m-1)(m^3-3m^2+3m+3)h^8+8(m-1)^3h^7H-4(3m-7)(m-1)^2h^6H^2 \\ & +8(m-7)(m-1)^2h^5H^3+70(m-1)^2h^4H^4-8(m-1)(6m-7)h^3H^5 \\ & +4(m-1)(4m-7)h^2H^6+8(m-1)hH^7+H^8\Big)q_0\Big] \ . \end{aligned} \tag{C.2}$$

In both the expressions, the dependence from the ratio of viscosities m has been highlighted, in a way that if one neglects m, being very small for air-water flows, these expressions greatly simplify.

D Description of the Newton method

Using the ij notation, and considering $\gamma_e = \gamma_0 = const.$, discrete mass conservation equation (6.32) can be written as

$$
\begin{aligned}
&\Phi(\rho_{ij}^{n+1}, \rho_{i+1,j}^{n+1}, \rho_{i,j+1}^{n+1}, \rho_{i-1,j}^{n+1}, \rho_{i,j-1}^{n+1}) \\
&= \rho_{ij}^{n+1}\Big(1 + \frac{\Delta t}{A_{ij}^{n+1}}(V_{i+1,j}^{n,+} m_{i+1,j} + V_{i,j+1}^{n,+} m_{i,j+1} + V_{i-1,j}^{n,+} m_{i-1,j} + V_{i,j-1}^{n,+} m_{i,j-1})\Big) \\
&- \frac{A_{ij}^{n}}{A_{ij}^{n+1}}\rho_{ij}^{n} + \frac{\Delta t}{A_{ij}^{n+1}}(V_{i+1,j}^{n,-} m_{i+1,j}\rho_{i+1,j}^{n+1} + V_{i,j+1}^{n,-} m_{i,j+1}\rho_{i,j+1}^{n+1} + V_{i-1,j}^{n,-} m_{i-1,j}\rho_{i-1,j}^{n+1} \\
&+ V_{i,j-1}^{n,-} m_{i,j-1}\rho_{i,j-1}^{n+1}) - \frac{\Delta t}{A_{ij}^{n+1}}\gamma_0 a^2\Big[m_{i+1,j}\Big(\rho_E^- \rho_{ij}^{n+1} + \rho_E^+ \rho_{i+1,j}^{n+1}\Big) \\
&+ m_{i,j+1}\Big(\rho_N^- \rho_{ij}^{n+1} + \rho_N^+ \rho_{i,j+1}^{n+1}\Big) + m_{i-1,j}\Big(\rho_W^- \rho_{ij}^{n+1} + \rho_W^+ \rho_{i-1,j}^{n+1}\Big) \\
&+ m_{i-1,j-1}\Big(\rho_S^- \rho_{ij}^{n+1} + \rho_S^+ \rho_{i,j-1}^{n+1}\Big)\Big] = 0 \ ,
\end{aligned}
\tag{D.1}
$$

where $A_i j$ is the surface of the cell (i, j), and n, $n+1$ refer to the time step. Superscripts $+$, $-$ denote $\max[\cdot, 0]$, $\min[\cdot, 0]$ respectively, while $V^n = \mathbf{w}_e^n \cdot \mathbf{n}_{e,K}$. With reference to Figure 6.8b, if one defines the four neighborhood cells with E, N, W and S as the cardinal points, then $\rho_E = \rho_{i+1,j}^{n+1,p} - \rho_{i,j}^{n+1,p}$ and so on.
Furthermore, the explicit form of the linear system (6.35) reads

$$
\begin{aligned}
&\Phi\left(\underline{\rho}^{n+1,p}\right) + \Phi_{\rho_{ij}}\left(\underline{\rho}^{n+1,p}\right)(\delta\rho)_{ij}^{n+1,p} + \Phi_{\rho_{i+1,j}}\left(\underline{\rho}^{n+1,p}\right)(\delta\rho)_{i+1,j}^{n+1,p} \\
&+ \Phi_{\rho_{i,j+1}}\left(\underline{\rho}^{n+1,p}\right)(\delta\rho)_{i,j+1}^{n+1,p} + \Phi_{\rho_{i-1,j}}\left(\underline{\rho}^{n+1,p}\right)(\delta\rho)_{i-1,j}^{n+1,p} \\
&+ \Phi_{\rho_{i,j-1}}\left(\underline{\rho}^{n+1,p}\right)(\delta\rho)_{i,j-1}^{n+1,p} = 0 \ ,
\end{aligned}
\tag{D.2}
$$

where $\delta\rho = \rho^{p+1} - \rho^p$ are the unknowns. Yet, superscript p indicates the step of the Newton method, while superscript n refers to the time step. On the other hand, the derivative of

Φ with respect to $\rho_{i,j}$ leads to

$$\begin{aligned}\Phi_{\rho_{ij}}\left(\underline{\rho}^{n+1,p}\right) &= 1+\frac{\Delta t}{A_{ij}^{n+1}}(V_{i+1,j}^{n,+}m_{i+1,j}+V_{i,j+1}^{n,+}m_{i,j+1}+V_{i-1,j}^{n,+}m_{i-1,j}\\ &+V_{i,j-1}^{n,+}m_{i,j-1})+\frac{\Delta t}{A_{ij}^{n+1}}\gamma_0 a^2\Big[\Big(\rho_{ij}^{n+1,p}(1-\delta(\rho_E))+\rho_E\,\mathrm{sgn}(\rho_E)\Big)m_{i+1,j}\\ &+\Big(\rho_{ij}^{n+1,p}(1-\delta(\rho_N))+\rho_N\,\mathrm{sgn}(\rho_N)\Big)m_{i,j+1}+\Big(\rho_{ij}^{n+1,p}(1-\delta(\rho_W))\\ &+\rho_W\,\mathrm{sgn}(\rho_W)\Big)m_{i-1,j}+\Big(\rho_{ij}^{n+1,p}(1-\delta(\rho_S))+\rho_S\,\mathrm{sgn}(\rho_S)\Big)m_{i,j-1}\Big]\ ,\end{aligned}\tag{D.3}$$

with sgn and $\delta(\cdot)$ representing signum and Kronecker functions, respectively. The derivative of Φ with respect to $\rho_{i+1,j}$ reads instead

$$\Phi_{\rho_{i+1,j}}\left(\underline{\rho}^{n+1,p}\right)=\frac{\Delta t}{A_{ij}^{n+1}}\Big[V_{i+1,j}^{n,-}-\gamma_0 a^2\left(\rho_{ij}^{n+1,p}(1-\delta(\rho_E))+2\rho_E^{+}\right)\Big]m_{i+1,j}\ ,\tag{D.4}$$

while all other derivatives have an analogous form.
Finally, knowing the density field allows for solving the velocity by means of the momentum balance equations (6.33). For example, the first component of velocity can be found through

$$\begin{aligned}\rho_{i,j}^{n+1}u_{i,j}^{n+1} &= \frac{A_{ij}^{n}}{A_{ij}^{n+1}}\rho_{i,j}^{n}u_{i,j}^{n}-\frac{\Delta t}{A_{ij}^{n+1}}\Big[m_{i+1,j}\rho_{i+1,j}^{n+1}u_{i+1,j}^{n}\Big(V_{i+1,j}^{n,-}-\gamma_0 a^2\rho_E^{+}\Big)\\ &+m_{i,j+1}\rho_{i,j+1}^{n+1}u_{i,j+1}^{n}\Big(V_{i,j+1}^{n,-}-\gamma_0 a^2\rho_N^{+}\Big)+m_{i-1,j}\rho_{i-1,j}^{n+1}u_{i-1,j}^{n}\Big(V_{i-1,j}^{n,-}-\gamma_0 a^2\rho_W^{+}\Big)\\ &+m_{i,j-1}\rho_{i,j-1}^{n+1}u_{i,j-1}^{n}\Big(V_{i,j-1}^{n,-}-\gamma_0 a^2\rho_S^{+}\Big)\Big]-\frac{\Delta t}{A_{ij}^{n+1}}\Big[m_{i+1,j}\Big(V_{i+1,j}^{n,+}-\gamma_0 a^2\rho_E^{-}\Big)\\ &+m_{i,j+1}\Big(V_{i,j+1}^{n,+}-\gamma_0 a^2\rho_N^{-}\Big)+m_{i-1,j}\Big(V_{i-1,j}^{n,+}-\gamma_0 a^2\rho_W^{-}\Big)\\ &+m_{i,j-1}\Big(V_{i,j-1}^{n,+}-\gamma_0 a^2\rho_S^{-}\Big)\Big]u_{i,j}^{n}\rho_{i,j}^{n+1}-\frac{1}{2}\frac{\Delta t}{A_{ij}^{n+1}}\Big[m_{i+1,j}\Big(a^2(\rho_{i,j}^{n+1}+\rho_{i+1,j}^{n+1})\\ &+2p_0\Big)n_{i+1,j}^{(x)}+m_{i,j+1}\Big(a^2(\rho_{i,j}^{n+1}+\rho_{i,j+1}^{n+1})+2p_0\Big)n_{i,j+1}^{(x)}+m_{i-1,j}\Big(a^2(\rho_{i,j}^{n+1}\\ &+\rho_{i-1,j}^{n+1})+2p_0\Big)n_{i-1,j}^{(x)}+m_{i,j-1}\Big(a^2(\rho_{i,j}^{n+1}+\rho_{i,j-1}^{n+1})+2p_0\Big)n_{i,j-1}^{(x)}\Big]\ ,\end{aligned}\tag{D.5}$$

where the superscript (x) indicates the x-component of the outward normal to the cell ij.

Bibliography

[1] Alba, K., Laure, P., and Khayat, R. E. Transient two-layer thin-film flow inside a channel. *Physical Review E 84* (Aug. 2011).

[2] Alekseenko, S. V., Nakoryakov, V. Y., and Pokusaev, B. G. Wave Formation on a Vertical Falling Liquid Film. *AIChE Journal 31*, 9 (1985), 1446–1460.

[3] Amaouche, M., Mehidi, N., and Amatousse, N. Linear stability of a two-layer film flow down an inclined channel: A second-order weighted residual approach. *Physics of Fluids 19* (2007), 084106.

[4] Anderson, Jr., J. D. *Hypersonic and High-Temperature Gas Dynamics*, second edi ed. AIAA Education Series, 2006.

[5] Barthelet, P., Charru, F., and Fabre, J. Experimental study of interfacial long waves in a two-layer shear flow. *Journal of Fluid Mechanics 303* (Apr. 1995), 23–53.

[6] Batchelor, G. K. *An Introduction to Fluid Dynamics*. Cambridge University Press, 1970.

[7] Benjamin, T. B. Wave formation in laminar flow down an inclined plane. *Journal of Fluid Mechanics 2* (1957), 554–574.

[8] Benjamin, T. B. Shearing flow over a wavy boundary. *Journal of Fluid Mechanics 6* (1959), 161–205.

[9] Benney, D. J. Long waves on liquid films. *J. Math. Phys. 45* (1966), 150–155.

[10] Binnie, A. M. Experiments on the onset of wave formation on a film of water flowing down a vertical plane. *Journal of Fluid Mechanics* (1957), 551–553.

[11] Boomkamp, P. A. M., and Miesen, R. H. M. Classification of instabilities in parallel two-phase flow. *International Journal of Multiphase Flow 22* (1996), 67–88.

[12] Boutounet, M., Chupin, L., Noble, P., and Vila, J. P. Shallow water viscous flows for arbitrary topography. *Commun. Math. Sci. 6*, 1 (2008), 29–55.

[13] Bringhurst, R. *The Elements of Typographic Style*. Hartley & Marks, 1992.

[14] Chang, H. C. Wave Evolution on a Falling Film. *Annual Review of Fluid Mechanics 26*, 1 (Jan. 1994), 103–136.

[15] Chanteperdrix, G., Villedieu, P., and Vila, J.-P. A Compressible Model for Separated Two-Phase Flows Computations. In *ASME 2002 Joint U.S.-European Fluids Engineering Division Conference* (2002).

[16] Charru, F. *Hydrodynamic Instabilities*. Cambridge University Press, 2011.

[17] Charru, F., and Fabre, J. Long waves at the interface between two viscous fluids. *Physics of Fluids 6*, 3 (1994), 1223–1235.

[18] Charru, F., and Hinch, E. J. 'Phase diagram' of interfacial instabilities in a two-layer Couette flow and mechanism of the long-wave instability. *Journal of Fluid Mechanics 414* (July 2000), 195–223.

[19] Cohen, L. S., and Hanratty, T. J. Generation of Waves in the Concurrent Flow of Air and a Liquid. *AIChE Journal 11*, 1 (1965), 138–144.

[20] Coudière, Y., Vila, J.-P., and Villedieu, P. Convergence rate of a finite volume scheme for a two dimensional convection-diffusion problem. *Mathematical Modelling and Numerical Analysis 33*, 3 (1999), 493–516.

[21] Craik, A. D. D. Wind-generated waves in thin liquid films. *Journal of Fluid Mechanics 26*, 02 (Mar. 1966), 369–392.

[22] Desjardins, O., Moureau, V., and Pitsch, H. An accurate conservative level set/ghost fluid method for simulating turbulent atomization. *Journal of Computational Physics 227*, 18 (Sept. 2008), 8395–8416.

[23] Dietze, G. F., Al-Sibai, F., and Kneer, R. Experimental study of flow separation in laminar falling liquid films. *Journal of Fluid Mechanics 637* (Sept. 2009), 73–104.

[24] Dietze, G. F., Leefken, A., and Kneer, R. Investigation of the backflow phenomenon in falling liquid films. *Journal of Fluid Mechanics 595* (Jan. 2008), 435–459.

[25] Dietze, G. F., and Ruyer-Quil, C. Wavy liquid films in interaction with a confined laminar gas flow. *Journal of Fluid Mechanics 722* (Mar. 2013), 348–393.

[26] Donea, J., Huerta, A., Ponthot, J.-P., and Rodriguez-Ferran, A. Arbitrary Lagrangian-Eulerian Methods, 2004.

[27] Frank, A. M. Shear driven solitary waves on a liquid film. *Physical Review E 74*, 6 (Dec. 2006), 065301.

[28] Frank, A. M. Numerical simulation of gas driven waves in a liquid film. *Physics of Fluids 20*, 12 (2008), 122102.

[29] Fuster, D., Bagué, A., Boeck, T., Le Moyne, L., Leboissetier, A., Popinet, S., Ray, P., Scardovelli, R., and Zaleski, S. Simulation of primary atomization with an octree adaptive mesh refinement and VOF method. *International Journal of Multiphase Flow 35*, 6 (June 2009), 550–565.

[30] Fuster, D., Matas, J.-P., Marty, S., Popinet, S., Hoepffner, J., Cartellier, A., and Zaleski, S. Instability regimes in the primary breakup region of planar coflowing sheets. *Journal of Fluid Mechanics 736* (Nov. 2013), 150–176.

[31] Gjevik, B. Occurrence of Finite-Amplitude Surface Waves on Falling Liquid Films. *Physics of Fluids 13*, 8 (1970), 1918–1925.

[32] Grenier, N., Vila, J.-P., and Villedieu, P. An accurate low-Mach scheme for a compressible two-fluid model applied to free-surface flows. *Journal of Computational Physics 252* (Nov. 2013), 1–19.

[33] Grimley, S. S. Liquid Flow Conditions in Packed Towers. *Trans. Inst. Chem. Eng. 23* (1945), 228–235.

[34] Hanratty, T. J. Interfacial instabilities caused by air flow over a thin liquid layer. In *Waves on Fluid Interfaces*. R. E. Meyer (Academic, New York), 1983, pp. 221–259.

[35] Healey, J. J. Destabilizing effects of confinement on homogeneous mixing layers. *Journal of Fluid Mechanics 623* (Mar. 2009), 241–271.

[36] Henstock, W. H., and Hanratty, T. J. Gas absorption by a liquid layer flowing on the wall of a pipe. *AIChE Journal 25*, 1 (1979), 122–131.

[37] Hirt, C. W., Amsden, A. A., and Cook, J. L. An Arbitrary Lagrangian-Eulerian Computing Method for All Flow Speeds. *Journal of Computational Physics 14* (1974), 227–253.

[38] Joo, S. W., Davis, S. H., and Bankoff, S. G. On falling-film instabilities and wave breaking. *Physics of Fluids 3*, 1 (Jan. 1991), 231–232.

[39] Jurman, L. A., and McCready, M. J. Study of waves on thin liquid films sheared by turbulent gas flows. *Physics of Fluids A 1*, 3 (1989), 522–536.

[40] Kalliadasis, S., Ruyer-Quil, C., Scheid, B., and Velarde, M. G. *Falling Liquid Films*. Springer, 2012.

[41] Kapitza, P. L. Wave flow of a thin viscous fluid layers. *Zh. Eksp. Teor. Fiz. 18*, 1 (1948).

[42] Kelly, R. E., Goussis, D. A., Lin, S. P., and Hsu, F. K. The mechanism for surface wave instability in film flow down an inclined plane. *Physics of Fluids A 1*, 5 (1989), 819–826.

[43] Lavalle, G., Laurent, C., Charru, F., and Vila, J.-P. Study of the linear stability analysis of thin liquid films. In *8th International Conference on Multiphase Flow ICMF 2013* (Jeju, Korea, 2013).

[44] Lavalle, G., Vila, J.-P., Blanchard, G., Laurent, C., and Charru, F. A shallow water and Navier-Stokes coupling for thin liquid films sheared by a gas flow. *Journal of Computational Physics* (2015). (under submission).

[45] Li, J., Renardy, Y. Y., and Renardy, M. A numerical study of periodic disturbances on two-layer Couette flow. *Physics of Fluids 10*, 12 (1998), 3056–3071.

[46] Lin, S. P. Finite-amplitude stability of a parallel flow with a free surface. *Journal of Fluid Mechanics 36* (1969), 113–126.

[47] Liu, J., and Gollub, J. P. Solitary wave dynamics of film flows. *Physics of Fluids 6*, 5 (1994), 1702–1712.

[48] Liu, J., Paul, J. D., and Gollub, J. P. Measurements of the primary instabilities of film flows. *Journal of Fluid Mechanics 250* (Apr. 1993), 69–101.

[49] Liu, J., Schneider, J. B., and Gollub, J. P. Three-dimensional instabilities of film flows. *Physics of Fluids 7*, 1 (1995), 55–67.

[50] Luchini, P., and Charru, F. Consistent section-averaged equations of quasi-one-dimensional laminar flow. *Journal of Fluid Mechanics 656* (2010), 337–341.

[51] Luchini, P., and Charru, F. The phase lead of shear stress in shallow-water flow over a perturbed bottom. *Journal of Fluid Mechanics 665* (Dec. 2010), 516–539.

[52] Malamataris, N. a., Vlachogiannis, M., and Bontozoglou, V. Solitary waves on inclined films: Flow structure and binary interactions. *Physics of Fluids 14*, 3 (2002), 1082–1094.

[53] Matar, O. K., Lawrence, C. J., and Sisoev, G. M. Interfacial dynamics in pressure-driven two-layer laminar channel flow with high viscosity ratios. *Physical Review E 75*, 5 (May 2007).

[54] McCready, M. J., and Hanratty, T. J. Effect of Air Shear on Gas Absorption by a Liquid Film. *AIChE Journal 31* (1985), 2066.

[55] Ménard, T., Tanguy, S., and Berlemont, A. Coupling level set/VOF/ghost fluid methods: Validation and application to 3D simulation of the primary break-up of a liquid jet. *International Journal of Multiphase Flow 33*, 5 (May 2007), 510–524.

[56] Miles, J. W. On the generation of surface waves by shear flows. *Journal of Fluid Mechanics 3*, 02 (Mar. 2006), 185–204.

[57] Noble, P., and Vila, J.-P. Stability theory for difference approximations of some dispersive shallow water equations and application to thin film flows. *arXiv preprint arXiv:1304.3805* (2013).

[58] Nosoko, T., and Miyara, A. The evolution and subsequent dynamics of waves on a vertically falling liquid film. *Physics of Fluids 16*, 4 (2004), 1118–1126.

[59] Nosoko, T., Yoshimura, P. N., Nagata, T., and Oyakawa, K. Characteristics of Two-Dimensional Waves on a Falling Liquid Film. *Chemical Engineering Science 51*, 5 (1996), 725–732.

[60] Nusselt, W. Die Oberflachenkondensation des Wasserdampfes. *VDI-Zeitschrift 60* (1916), 541–546.

[61] Ó Náraigh, L., Spelt, P. D. M., and Shaw, S. J. Absolute linear instability in laminar and turbulent gas–liquid two-layer channel flow. *Journal of Fluid Mechanics 714* (Jan. 2013), 58–94.

[62] Orr, W. M. The stability or instability of the steady motions of a perfect liquid and of a viscous liquid. *Proc. R. Irish Acad. A 27* (1907), 9–68, 69–138.

[63] Park, C. D., and Nosoko, T. Three-dimensional wave dynamics on a falling film and associated mass transfer. *AIChE Journal 49*, 11 (Nov. 2003), 2715–2727.

[64] Popinet, S. An accurate adaptive solver for surface-tension-driven interfacial flows. *Journal of Computational Physics 228*, 16 (Sept. 2009), 5838–5866.

[65] Pumir, A., Manneville, P., and Pomeau, Y. On solitary waves running down an inclined plane. *Journ 135* (1983), 27–50.

[66] Ramaswamy, B., Chippada, S., and Joo, S. W. A full-scale numerical study of interfacial instabilities in thin-film flows. *Journal of Fluid Mechanics 325* (Apr. 1996), 163–194.

[67] Refloch, A., Courbet, B., Murrone, A., Villedieu, P., Laurent, C., Gilbank, P., Troyes, J., Tessé, L., Chaineray, G., Dargaud, J. B., and Vuillot, F. CEDRE Software. *Aerospace Lab*, 2 (2011), 1–10.

[68] Reynolds, W. C., and Potter, M. C. Finite-amplitude stability of a parallel shear flows. *Journal of Fluid Mechanics 27* (1967), 465–492.

[69] Ruyer-Quil, C., and Manneville, P. Modeling film flows down inclined planes. *The European Physical Journal B 6*, 2 (Nov. 1998), 277–292.

[70] Ruyer-Quil, C., and Manneville, P. Improved modeling of flows down inclined planes. *The European Physical Journal B 15* (2000), 357–369.

[71] Ruyer-Quil, C., and Manneville, P. Further accuracy and convergence results on the modeling of flows down inclined planes by weighted-residual approximations. *Physics of Fluids 14*, 1 (2002), 170–183.

[72] Salamon, T. R., Armstrong, R. C., and Brown, R. a. Traveling waves on vertical films: Numerical analysis using the finite element method. *Physics of Fluids 6*, 6 (1994), 2202–2220.

[73] Samanta, A. Shear-imposed falling film. *Journal of Fluid Mechanics 753* (July 2014), 131–149.

[74] Scheid, B., Ruyer-Quil, C., and Manneville, P. Wave patterns in film flows: modelling and three-dimensional waves. *Journal of Fluid Mechanics 562* (Aug. 2006), 183–222.

[75] Schied, N., Villedieu, P., and Vila, J.-P. A Diffuse Interface Model for the Numerical Simulation of Thermocapillary Effects. In *ASME 2009 Fluids Engineering Division Summer Meeting* (2009).

[76] Shkadov, V. Y. Wave Flow Regimes of a Thin Layer of Viscous Fluid subject to Gravity. *Izv. Akad. Nauk SSSR, Mekh. Zhidk. i Gaza 2*, 1 (1967), 43–51.

[77] Sisoev, G. M., Matar, O. K., Sileri, D., and Lawrence, C. J. Wave regimes in two-layer microchannel flow. *Chemical Engineering Science 64*, 13 (July 2009), 3094–3102.

[78] Smith, M. K. The mechanism for the long-wave instability in thin liquid films. *Journal of Fluid Mechanics 217* (Apr. 1990), 469–485.

[79] Smith, M. K., and Davis, S. H. The instability of sheared liquid layers. *Journal of Fluid Mechanics 121* (Apr. 1982), 187–206.

[80] Sommerfeld, A. Ein beitrag zur hydrodynamischen erklaerung der turbulenten fluessigkeitsbewegungen. In *Atti del 4 Congresso Internazionale dei Matematici, Ser. I* (Rome, 1908), pp. 116–124.

[81] Soulaimani, A., Fortin, M., Dhatt, G., and Ouellet, Y. Finite element simulation of two- and three-dimensional free surface flows. *Computer Methods in Applied Mechanics and Engineering 86* (1991), 265–296.

[82] Sussman, M., and Puckett, E. G. A Coupled Level Set and Volume-of-Fluid Method for Computing 3D and Axisymmetric Incompressible Two-Phase Flows. *Journal of Computational Physics 162*, 2 (Aug. 2000), 301–337.

[83] Tilley, B. S., Davis, S. H., and Bankoff, S. G. Linear stability theory of two-layer fluid flow in an inclined channel. *Physics of Fluids 6*, 12 (1994), 3906–3922.

[84] Tilley, B. S., Davis, S. H., and Bankoff, S. G. Nonlinear long-wave stability of superposed fluids in an inclined channel. *Journal of Fluid Mechanics 277* (1994), 55–83.

[85] Tomar, G., Fuster, D., Zaleski, S., and Popinet, S. Multiscale simulations of primary atomization. *Computers & Fluids 39*, 10 (Dec. 2010), 1864–1874.

[86] Toro, E. F. *Riemann Solvers and Numerical Methods for Fluid Dynamics*. Springer, 1997.

[87] Trifonov, Y. Y. Counter-Current Gas-Liquid Wavy Film Flow Between the Vertical Plates Analyzed Using the Navier-Stokes Equations. *AIChE Journal 56*, 8 (2010), 1975–1987.

[88] Trifonov, Y. Y. Counter-current gasliquid flow between vertical corrugated plates. *Chemical Engineering Science 66* (Oct. 2011), 4851–4866.

[89] Trifonov, Y. Y. Stability and bifurcations of the wavy film flow down a vertical plate: the results of integral approaches and full-scale computations. *Fluid Dynamics Research 44*, 3 (June 2012).

[90] Tseluiko, D., and Kalliadasis, S. Nonlinear waves in counter-current gas–liquid film flow. *Journal of Fluid Mechanics 673* (Feb. 2011), 19–59.

[91] Valluri, P., Ó Náraigh, L., Ding, H., and Spelt, P. D. M. Linear and nonlinear spatio-temporal instability in laminar two-layer flows. *Journal of Fluid Mechanics 656*, 2010 (May 2010), 458–480.

[92] Vellingiri, R., Tseluiko, D., Savva, N., and Kalliadasis, S. Dynamics of a liquid film sheared by a co-flowing turbulent gas. *International Journal of Multiphase Flow 56* (Oct. 2013), 93–104.

[93] Whitham, G. B. *Linear and Nonlinear Waves*. Wiley-Interscience, 1974.

[94] Yiantsios, S. G., and Higgins, B. G. Linear stability of plane Poiseuille flow of two superposed fluids. *Physics of Fluids 31*, 11 (1988), 3225–3238.

[95] Yih, C.-S. Stability of Liquid Flow down an Inclined Plane. *Physics of Fluids 6*, 3 (1963), 321–334.

[96] Yih, C.-S. Instability due to viscosity stratification. *Journal of Fluid Mechanics 27* (1967), 337–352.

[97] Zhang, J., Miksis, M. J., Bankoff, S. G., and Tryggvason, G. Nonlinear dynamics of an interface in an inclined channel. *Physics of Fluids 14*, 6 (2002), 1877–1885.

[98] Zuzio, D., Estivalezes, J.-L., Villedieu, P., and Blanchard, G. Numerical simulation of primary and secondary atomization. *Comptes Rendus Mécanique 341*, 1-2 (Jan. 2013), 15–25.

Final abstract

Liquid films sheared by a gas flow are encountered in many industrial devices and aerospace applications, such as heat exchangers and distillation columns, as well as airplane turbines and rocket motors. Owing to pressure gradient and shear stress exerted by the gas, unstable waves can develop at the interface, with relevant consequences on liquid-gas exchanges, like heat and mass transfers.

In general, two-layer flows are numerically investigated by means of the Direct Numerical Simulation (DNS). However, the thinness of the liquid layer suggests that the film can be studied through depth-integrated equations, with the benefit to greatly reduce the computational cost.

Hence, the aim of the present work consists in developing a coupling methodology between depth-integrated equations and Navier-Stokes equations accounting for liquid and gas phases respectively, in order to describe the instabilities of liquid films sheared by a gas flow in confined and large channels. This approach thus represents a compromise between the full DNS and the complete low-dimensional model, and answers the needs of ONERA in creating a coupling technique to be later extended to the CEDRE platform.

In a first step, the reduced model for the liquid phase is developed: by integrating the boundary-layer equations over the film thickness and by assuming that the film is thin compared to the wavelength of traveling waves, a system of consistent shallow water equations is found. The gas flow is treated instead with compressible Navier-Stokes equations, and a low-Mach scheme allows to discretize these equations in the developed finite-volume computational technique. Finally, the coupling between the two layers is assured by the continuity of interfacial velocities and stresses, as well as by the transfer of the interface position. Particularly, an Arbitrary Lagrangian-Eulerian (ALE) method ensures the transfer of the interface position from the liquid to the gas.

In conclusion, the performed computational analysis is validated for the configurations of a strictly confined channel and a large channel: film thickness and interfacial stress evolutions are compared with those provided by the DNS, or avalaible in the literature.

Résumé général

Cette partie de la thèse est un résumé général du travail présenté jusqu'à présent. Ce résumé contient le même nombre de chapitres que la partie en anglais, à laquelle il faut s'adresser pour une description plus complète et exhaustive.

1 Introduction

Les écoulements de films liquides cisaillés sont présents dans de nombreux domaines de l'aérospatial et leur modélisation est un enjeu important pour les industriels chargés de concevoir les nouveaux systèmes. Des problématiques comme l'ingestion d'eau dans les turboréacteurs, le dimensionnement des systèmes d'injection ou le ruissellement sur la voilure d'un avion sont des exemples de configurations industrielles où la présence d'un film avec des instabilités modifie considérablement les transferts à la paroi et pour lesquelles il est nécessaire de développer des modèles capables de reproduire le comportement d'un film en interaction avec un environnement complexe. Par exemple, dans le cas de l'étude d'un système de dégivrage, une mauvaise estimation des coefficients d'échanges entre le film et le gaz peut conduire à sous-estimer le ruissellement et la formation de glace dans des zones non-protégées, ce qui a un impact direct sur les performances aérodynamiques.

Une approche intéressante pour les codes industriels consiste à modéliser les films par une approche eulérienne intégrale (équations de Navier-Stokes intégrées sur l'épaisseur du film), ce sont les approches dites St. Venant ou "shallow water". En effet, la spécificité "écoulement mince" est ainsi directement prise en compte dans la méthode de résolution afin de réduire considérablement les temps de calcul. En contrepartie, certains phénomènes comme les instabilités de surface sont plus difficiles à reproduire avec ces modèles réduits.

Jusqu'à présent, l'étude de ces modèles St Venant s'est surtout concentrée sur les films tombants, sans cisaillement par un écoulement gazeux. Dans ce cas, des modèles consistants ont pu être établis et permettent de prédire de manière très satisfaisante la dynamique non linéaire et le seuil de stabilité linéaire des films soumis à la gravité seule. Ces modèles ont été validés par comparaison avec des DNS et des résultats expérimentaux. Concernant les films cisaillés par un gaz, des modèles réduits ont été développés pour des configurations de conduites confinées où il est possible d'utiliser une approche intégrale à la fois pour le film et le gaz. Ces modèles, intéressant pour certains procédés industriels comme les échangeurs de chaleur, doivent être généralisés pour les configurations rencontrées dans le domaine

aéronautique.

L'objectif de la thèse est donc de développer une méthodologie pour coupler un modèle réduit de film avec un solveur gaz compressible couramment utilisé par les codes industriels. Le choix a été fait d'utiliser une méthode ALE pour réaliser ce couplage qui a été implémenté dans un code baptisé SWANS (Shallow Water ALE Navier-Stokes). Pour ce travail, seuls les écoulement gazeux laminaires ont été considérés.

Dans le chapitre 3, un modèle réduit basé sur l'hypothèse d'ondes longues a été développé pour un film liquide mince soumis à la gravité avec un cisaillement interfacial et un champ de pression gaz imposés. Dans le chapitre 4, ce modèle a été étendu au cas d'un écoulement diphasique en conduite. Le chapitre 5 est consacré à l'étude de la stabilité linéaire de ces deux modèles réduits, afin de les valider par rapport aux données de la littérature. Dans le chapitre 6, le modèle de film du chapitre 3 a été couplé aux équations de Navier-Stokes pour la partie gaz : la méthodologie de couplage ainsi que le code de calcul SWANS (Shallow Water ALE Navier-Stokes) développé au cours de cette thèse sont présentés. Le chapitre 7 décrit des cas-tests de validation de chacune des modules du code SWANS, en comparant les résultats numériques à des solutions exactes ou bien à des expérience de la littérature. Enfin, le chapitre 8 traite de la résolution numérique de la dynamique non linéaire des ondes se développant sur un film cisaillé. Ce chapitre montre la comparaison de SWANS avec des résultats de DNS disponibles dans la littérature pour un cas de conduite fortement confinée où une approche basée sur un double St. Venant est possible et des résultats de DNS produits à l'ONERA pour une configuration en canal large où seul un couplage avec Navier-Stokes est possible.

2 État de l'art

Ce chapitre donne un aperçu des travaux portant sur la modélisation des films liquides minces et l'analyse de stabilité linéaire. Une revue de la littérature est d'abord présentée afin de décrire l'état de la recherche sur le sujet. Ensuite, certains travaux sélectionnés sont décrits plus en détails, notamment les modèles réduits issus de la littérature afin de les comparer à ceux développés dans la thèse. Enfin, les résultats de travaux portant sur la stabilité linéaire des films liquides à partir des équations de Navier-Stokes ou des modèles réduits sont présentés.

Les expériences sur les films liquides tombants et cisaillés montrent la présence de vagues à grande longueur d'onde par rapport à l'épaisseur du film. Cela a permis de développer des modèles de film basé sur l'hypothèse de l'existence d'un petit paramètre $\varepsilon = h/\lambda$, où h est l'épaisseur du film et λ la longueur d'onde. Les modèles obtenus sont dits consistants si ils sont capables de retrouver le bon seuil de stabilité prédit par l'analyse de linéaire des équations de Navier-Stokes (Orr-Sommerfeld, cf. travaux de Benjamin [7] et Yih [95] pour les films tombants et Smith [78] pour les films tombants avec un cisaillement imposé). Dans le cadre d'un film tombant, Benney [9] développe dans les années soixante un modèle réduit à une seule équation. Ce modèle, basé sur la seule équation de conservation de la masse, est consistant mais n'est valide qu'aux très petits nombre de Reynolds comme dans le cadre de la théorie de la lubrification. Pour s'affranchir de cette limitation, Shkadov [76] propose un modèle à deux équations qui résout en plus l'équation intégrale de conservation de la quantité de mouvement. Le défaut de ce modèle est d'être non consistant. Finalement, Ruyer-Quil & Manneville [69, 70] propose un modèle de film tombant à deux équations qui est consistant et permet de reproduire la dynamique des ondes non linéaires observées dans l'expérience de Liu & Gollub [47]. Pour ce qui concerne la modélisation bi-couche des écoulements de films cisaillés fortement confinés (double St. Venant), les premiers modèles réduits ont été fournis par Tilley *et al.* [84] en utilisant l'approche de Benney [9].

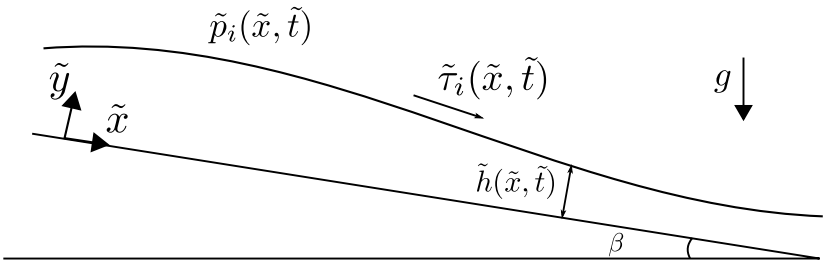

Figure FR1: Film liquide mince, soumis à la gravité et un champs imposé pour le cisaillement et la pression.

Récemment, Dietze & Ruyer-Quil [25] ont également développé un modèle ondes longues qui traite le film et le gaz avec des équations intégrales. Les résultats de ce modèle sont consistants et en accord avec la théorie linéaire de Yih [96]. La dynamique non-linéaire a été validée par comparaison avec des DNS. Toutefois, l'utilisation d'équations intégrales pour la couche gazeuse est contraignante, car celle-ci doit être suffisamment mince par rapport à la longueur d'onde, ce qui n'est pas le cas dans la plupart des applications aérospatiales visées.

3 Modèle d'ondes longues d'un film liquide mince

Dans ce chapitre, on va développer des équations intégrales d'ondes longues pour étudier la dynamique d'un film liquide mince, soumis à la gravité et un champs imposé pour le cisaillement et la pression, comme le montre la Figure FR1. Ces champs sont décrits par des fonctions de l'espace et du temps. Le modèle d'ondes longues est obtenu à partir de l'intégration des équations de Navier-Stokes sur l'épaisseur du film. Toutefois, ces équations intégrées doivent être fermées. Le film étant très mince par rapport à la longueur d'onde, un développement asymptotique des équations de Navier-Stokes par rapport au petit paramètre ε permet dans une première étape d'obtenir la vitesse du film à l'ordre souhaité. Cette expression est ensuite utilisée pour fermer les équations. Cette méthodologie permet d'obtenir un modèle consistant à l'ordre 1.

L'hypothèse de film mince permet d'utiliser les équations de couche-limite pour l'intégration. Ces équations s'écrivent

$$\begin{cases} \partial_x u + \partial_y v = 0 \\ \partial_t u + u\partial_x u + v\partial_y u = -\partial_x p + \dfrac{1}{Fr}\sin\beta + \dfrac{1}{Re}\partial_{yy} u \\ 0 = -\dfrac{1}{Fr}\cos\beta - \partial_y p \end{cases} ,$$

avec les conditions de non-glissement à la paroi

$$u = 0 \ , \qquad v = 0 \ .$$

et la continuité à l'interface

$$\begin{gathered} p|_h = p_i(x,t) - \frac{1}{We}\partial_{xx} h \ , \\ \partial_y u|_h = \tau_i(x,t) \ , \\ \partial_t h + u|_h \partial_x h = v|_h \ . \end{gathered}$$

Finalement, suivant les étapes décrites précédemment, le modèle d'ondes longues se met

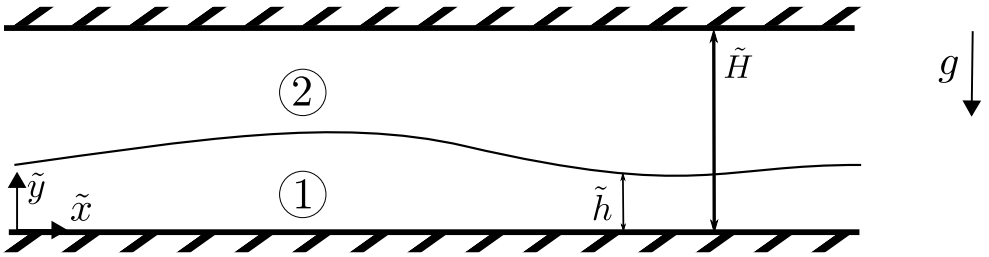

Figure FR2: Écoulement bi-couche dans une conduite étroite.

sous la forme

$$\partial_t h + \partial_x q = 0 \ ,$$
$$\partial_t q + \partial_x\Big(\frac{q^2}{h} + P\Big) = \frac{1}{Re}\Big[\Lambda h - \frac{3q}{h^2} + \frac{3}{2}\tau_i - T\Big] + \frac{1}{We} h \ \partial_{3x} h \ ,$$

où P et T sont définis comme

$$P = \frac{2}{225}\Lambda^2 h^5 + \frac{1}{15}\Lambda\tau_i h^4 + \frac{1}{12}{\tau_i}^2 h^3 + \frac{1}{2}\frac{h^2}{Fr}\cos\beta \ ,$$
$$\begin{aligned} T =& \frac{1}{240} h^3 Re(3\Lambda h + 14\tau_i) \ \partial_x \tau_i \\ &+ Re^2 h^4\Big(\frac{3}{175}\Lambda h + \frac{1}{24}\tau_i\Big) \ \partial_x G \\ &+ \frac{1}{15} Re^2 h^3 \ \partial_t G + \frac{1}{8} h^2 Re \ \partial_t \tau_i \ . \end{aligned}$$

Pour toutes informations supplémentaires, ainsi pour la définitions des différents termes, on renvoie le lecteur à la version anglaise.

4 Modèle d'ondes longues d'un écoulement bi-couche

L'objectif de ce chapitre est d'étendre le résultat du chapitre 3 au cas d'un écoulement bi-couche se développant dans une conduite étroite, comme le montre la Figure FR2. Un modèle d'ondes longues permettant d'étudier la dynamique et les interactions entre le film et le gaz est donc établi. En se basant sur le même hypothèse de travail que Tilley *et al.* [84], le débit total (somme des débits liquide et gazeux) est supposé constant et uniforme dans la conduite. La démarche pour développer ce modèle est la même que dans le chapitre précédent : les équations de Navier-Stokes sont intégrées sur l'épaisseur du film et du gaz et une méthode de développement asymptotique permet d'obtenir un modèle bi-couche consistant à l'ordre 1. Finalement, le modèle s'écrit

$$\partial_t h + \partial_x q_1 = 0 \ ,$$
$$\partial_t q_1 + \partial_x\Big[\frac{6}{5}\frac{q_1^2}{h} + \Pi_1\Big] = Gh + \frac{1}{Re}\Big(\tau_i - \tau_{w1}\Big) + \frac{1}{We} h \partial_{3x} h \ ,$$
$$\partial_t h - \partial_x q_2 = 0 \ ,$$
$$\partial_t q_2 + \partial_x\Big[\frac{6}{5}\frac{q_2^2}{H-h} + \Pi_2\Big] = \frac{G}{r}h + \frac{1}{Re}\frac{1}{r}\Big(\tau_{w2} - \tau_i\Big) \ ,$$

où les différentes variables sont définies dans la partie anglaise.

5 Stabilité linéaire des modèles ondes longues

Dans ce chapitre, la stabilité linéaire des modèles ondes longues développés précédemment est étudiée, l'objectif étant de montrer que les modèles établis sont effectivement consistants.

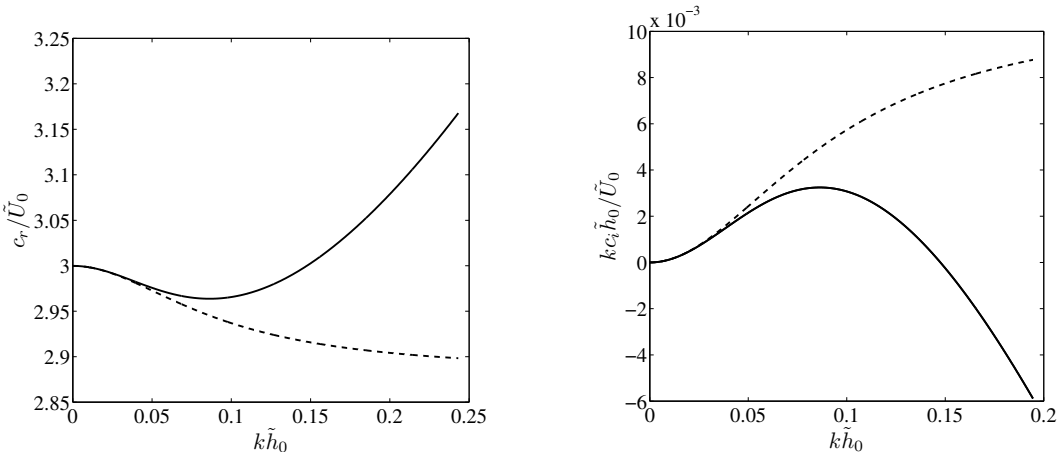

(a) *Vitesse de propagation.* (b) *Taux de croissance.*

Figure FR3: Solution de la relation de dispersion pour un film d'eau-glycerine tombant le long d'un plan incliné de $\beta = 6.4°$. Nombres adimensionnés : $Re = 8.5$, $Fr = 0.316$, $We = 0.048$. Courbes avec tension de surface (ligne en traits pleins) et sans (ligne en pointillés).

La relation de dispersion, qui lie le nombre d'onde k à la vitesse d'onde $c = c_r + ic_i$, est obtenue par la méthode des petites perturbations. Cette relation permet donc de calculer la vitesse de propagation c_r des ondes longues linéaires et le taux de croissance kc_i. La Figure FR3 illustre l'évolution de la vitesse et du taux de croissance en fonction du nombre d'onde, en présence et en absence de tension de surface, pour un film tombant le long d'un plan incliné. Cela montre le rôle de la tension de surface qui stabilise les petites longueurs d'ondes. Le limite de stabilité des ondes longues est donnée par un taux de croissance kc_i qui s'annule. Pour un film tombant, ce seuil est

$$Re_{cr} = \frac{5}{6}\cot\beta \ , \qquad Fr_{cr} = \frac{5}{18} \ ,$$

tandis que pour un film tombant liquide soumis à un cisaillement constant, ce seuil vaut

$$Re_{cr} = \frac{5/6\cot\beta}{1-\tau_i/6} \ , \qquad Fr_{cr} = \frac{5/18}{(1-\tau_i/2)(1-\tau_i/6)} \ .$$

Ces résultats montrent que les modèles d'ondes longues étudiés sont consistants à l'ordre 1 car le seuil de stabilité et la vitesse de propagation des ondes est la même que celle obtenue par la théorie linéaire d'Orr-Sommerfeld (Benjamin [7] et Yih [95] pour les films tombants et Smith [78] pour les films tombants soumis à un cisaillement constant). La même analyse pour le modèle bi-couche montre que le modèle développé dans le chapitre 4 permet également de retrouver le seuil de stabilité et la vitesse de propagation obtenus par Yih [96] à partir d'Orr-Sommerfeld.

6 Couplage entre le modèle ondes longues de film et les équations de Navier-Stokes pour le gaz : le code SWANS

Ce chapitre est consacré au développement d'un outil numérique pour coupler le modèle d'ondes longues de film (chapitre 3 avec les équations de Navier-Stokes pour le gaz. Cette approche permet de garder les avantages de la modélisation du film liquide mince sans se limiter à des configurations de canalisations où le gaz est fortement confiné. Afin d'évaluer cette méthode, un code simplifié a été développé sous MATLAB. Il s'agit d'un code 2D avec des conditions d'entrée-sortie périodiques traitant la configuration d'un écoulement

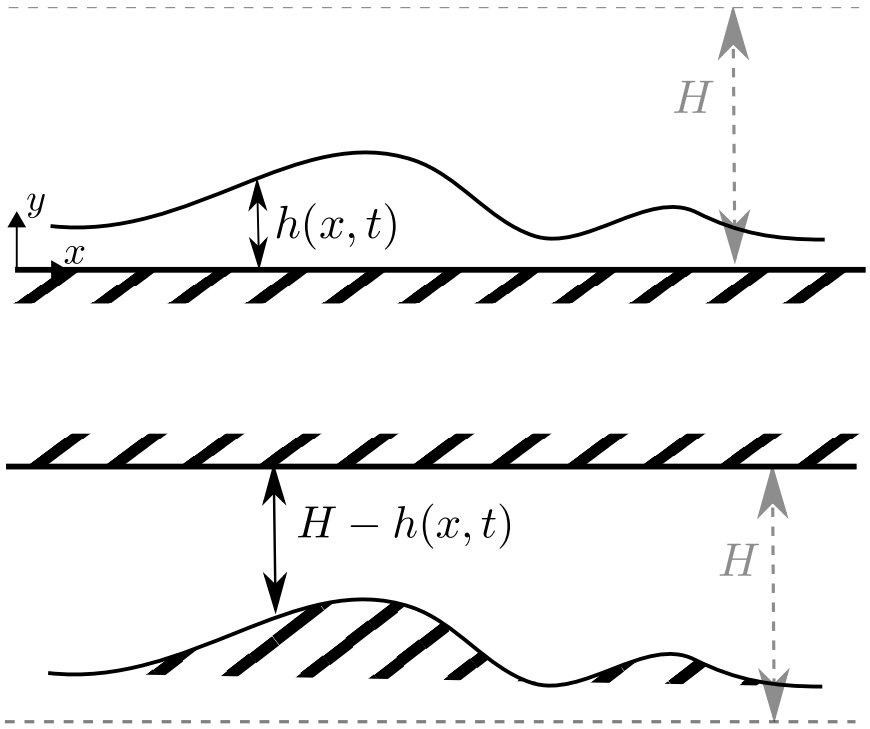

Figure FR4: Représentation de la géométrie du code film (en haut) et du code gaz (en bas). La ligne en pointillés sur le fond illustre la configuration de base.

liquide-gaz entre deux parois. Ce code couple deux modules, l'un pour le film et l'autre pour le gaz en faisant appel à une méthode ALE (Arbitrary Lagrangian-Eulerian). Pour le gaz, le film se comporte comme une paroi qui bouge au cours du temps (cf Figure FR4). Le couplage du gaz vers le film se fait à travers l'échange des contraintes à l'interface et celui du film vers le gaz par la vitesse et la position de l'interface que voit le gaz. La méthode ALE est utilisée pour déplacer les noeuds du maillage de façon à suivre le mouvement de l'interface. Finalement, le système d'équations couplé résolu par la méthode SWANS est le suivant :

$$\partial_t \tilde{h} + \partial_x \tilde{q}_1 = 0 \ ,$$
$$\partial_t \tilde{q}_1 + \partial_x \Big(\frac{\tilde{q}_1^2}{\tilde{h}} + \tilde{P} \Big) = \tilde{\Lambda} \tilde{h} - \frac{1}{\rho_1} \Big[\mu_1 \frac{3\tilde{q}_1}{\tilde{h}^2} + \frac{3}{2} \tilde{\tau}_i - \tilde{T} \Big] + \frac{\gamma}{\rho_1} \tilde{h} \ \partial_{3x} \tilde{h} \ ,$$

et

$$\begin{cases} \partial_t \tilde{\rho}_2 + \nabla \cdot (\tilde{\rho}_2 \tilde{\mathbf{u}}_2) = 0 \\ \partial_t (\tilde{\rho}_2 \tilde{\mathbf{u}}_2) + \nabla \cdot (\tilde{\rho}_2 \tilde{\mathbf{u}}_2 \otimes \tilde{\mathbf{u}}_2) = -\nabla \tilde{p}_2 + \tilde{\mathbf{F}}_2 + \nabla \cdot \tilde{\mathbf{T}}_2 \end{cases} .$$

Les conditions aux limites sont données par :

$$\tilde{\tau}_i = \mu_2 \partial_y \tilde{u}_2|_{\tilde{h}} \ ,$$
$$\tilde{G} = -\partial_x \tilde{p}_2|_{\tilde{h}} \ .$$

pour le transfert du gaz vers le film, et par

$$\tilde{u}_2|_{\tilde{h}} = \tilde{u}_1|_{\tilde{h}} \ ,$$
$$\tilde{v}_2|_{\tilde{h}} = \tilde{v}_1|_{\tilde{h}} \ ,$$
$$\partial_t \tilde{h} + \tilde{u}|_h \partial_x \tilde{h} = \tilde{v}|_h \ ,$$

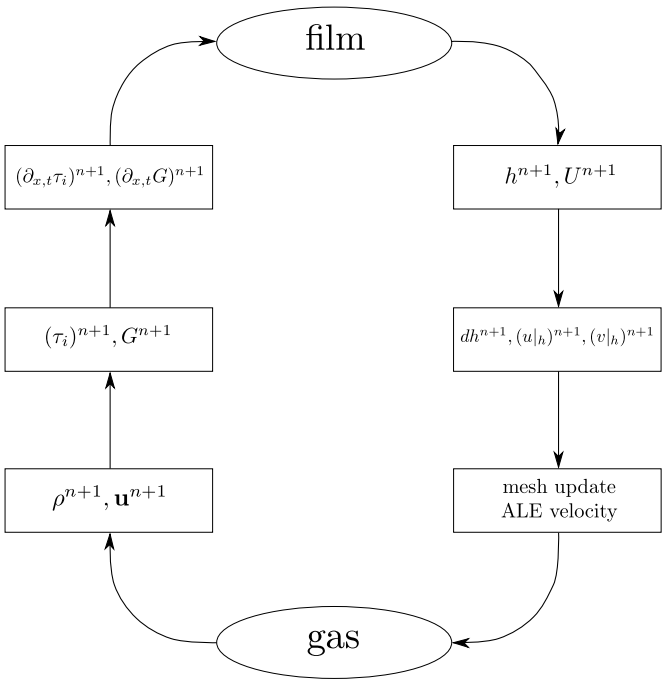

Figure FR5: Représentation de la méthodologie de couplage et progression en temps $n \longrightarrow n+1$.

pour le transfert du film vers le gaz. La vitesse longitudinale à l'interface est celle du développement asymptotique d'ordre zéro :

$$\tilde{u}_1|_{\tilde{h}} = \frac{3}{2}\frac{\tilde{q}_1}{\tilde{h}} + \frac{1}{4}\tilde{\tau}_i\tilde{h} \ ,$$

tandis que la vitesse verticale est déterminée par l'équation de compatibilité. En effet, la prise en compte de l'ordre un dans les modèles est déterminante sur la forme de l'interface mais négligeable sur les champs. Ceci implique que le point clé dans la méthodologie de couplage est de donner la bonne forme d'interface au gaz (calculée par la modèle à l'ordre un) tandis que le champs de vitesse peut être approximé par l'ordre zéro.

Concernant les méthodes numériques de résolution des équations, les équations de film ont été discretisées avec la méthode de Noble & Vila [57], qui consiste à ajouter une équations de transport pour la tension de surface afin de réduire l'ordre de dérivation du système. Pour le code Navier-Stokes compressible, les équations ont été résolues avec un schéma bas-Mach (cf. Grenier *et al.* [32]). Le couplage numérique entre ces deux modules est représenté dans la Figure FR5.

7 Validation de la méthode numérique SWANS

Ce chapitre est dédié à la validation numérique de SWANS. Plusieurs tests ont été effectués, afin de tester le code film, le code gaz et la stratégie de couplage.

Pour valider le code film, un test de stabilité linéaire a été fait dans la configuration d'un film tombant. La comparaison des résultats numériques et théoriques (chapitre 5) donne un très bon accord. Le code film a été aussi validé par rapport aux expériences de Liu & Gollub [47] pour la dynamique non-linéaire.

Pour valider le code gaz, un écoulement de Poiseuille sur maillage fixe et mobile a été étudié. Les résultats montrent que dans le cas du maillage mobile, on obtient la convergence pour des maillages très raffinés. Cela peut être expliqué par le fait que les termes visqueux

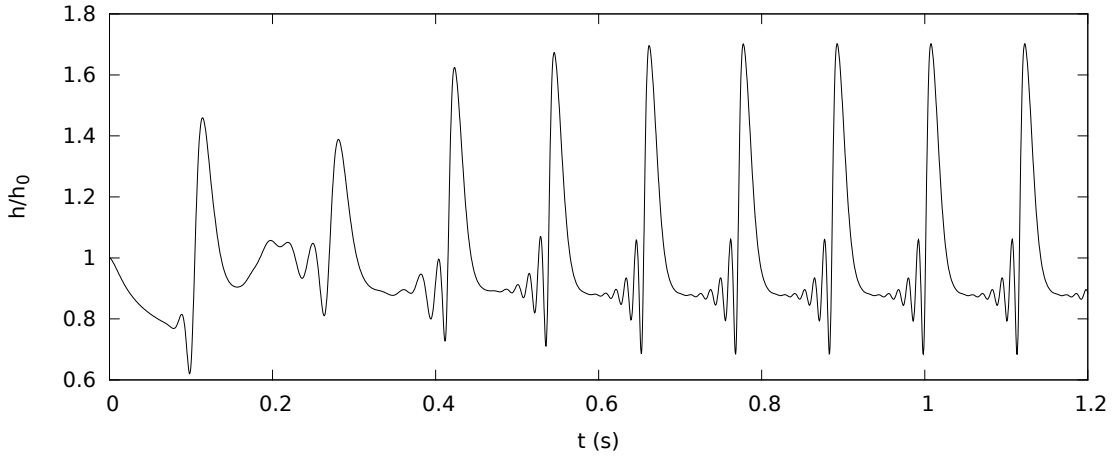

Figure FR6: Evolution temporelle de l'épaisseur du film normalisé avec l'état uniforme. Nombres adimensionnés : $Re_1 = 4.48$, $Re_2 = 36.8$, $We = 2 \cdot 10^{-3}$. Gradient de pression et cisaillement uniforms : $G_0 = -\Delta p/L = 2461.5\ Pa\ m^{-1}$, $\tau_{i0} = 0.32\ Pa$.

ne sont pas corrigés en présence d'un maillage non orthogonale. Afin de s'affranchir de cette limitation, une méthode de type "cellule diamant" pour calculer les gradients sur un maillage quelconque pourrait être utilisée.

Pour conclure, la validation de la méthode de couplage a été réalisée sur un écoulement bi-couche en comparant les résultats de SWANS avec le développement asymptotique du chapitre 4.

8 Dynamique non linéaire d'un écoulement bi-couche : résultats SWANS et comparaison avec DNS

Ce chapitre permet de valider l'approche SWANS sur deux configurations bi-couche pour lesquelles on dispose de DNS. La première configuration issue de la littérature (Dietze & Ruyer-Quil [25]) est celle d'un écoulement film-gaz dans une conduite très étroite, de façon que le gaz soit aussi mince vis-à-vis de la longueur d'onde. Ce type d'écoulement peut ainsi être étudié avec un double St Venant film-gaz, comme celui du chapitre 4. La deuxième configuration traite un écoulement film-gaz se développant dans une conduite large. Le gaz ne peut plus être modélisé avec des équations intégrales, et une méthode de type SWANS devient nécessaire.

Dans le premier test, la conduite est horizontale et l'écoulement film-gaz est piloté par le gradient de pression. Un différentiel de pression est imposé entre l'entrée et la sortie de la conduite. Les conditions initiales sont celles de l'état d'équilibre perturbé. L'évolution temporelle de l'interface obtenue avec SWANS est représentée sur la Figure FR6. Après le transitoire, des ondes stationnaires sont observable.
La Figure FR7 montre la comparaison entre SWANS et la DNS de Dietze & Ruyer-Quil [25]. Les deux courbes sont en bon accord. Enfin, le gradient de pression et le cisaillement à l'interface donnés par SWANS ont été comparés au modèle intégrale bi-couche de Dietze & Ruyer-Quil (Figure FR8 et FR9). L'interprétation de ces résultats est détaillée dans la version anglaise.

Cette configuration a également été simulée avec le double St Venant du chapitre 4 (voir version anglaise). La dynamique globale est retrouvée mais des écarts apparaissent sur l'amplitude et la fréquence des ondes périodiques. Cela peut s'expliquer par le fait que dans le modèle du double St. Venant, le débit total est imposé, tandis que dans le code

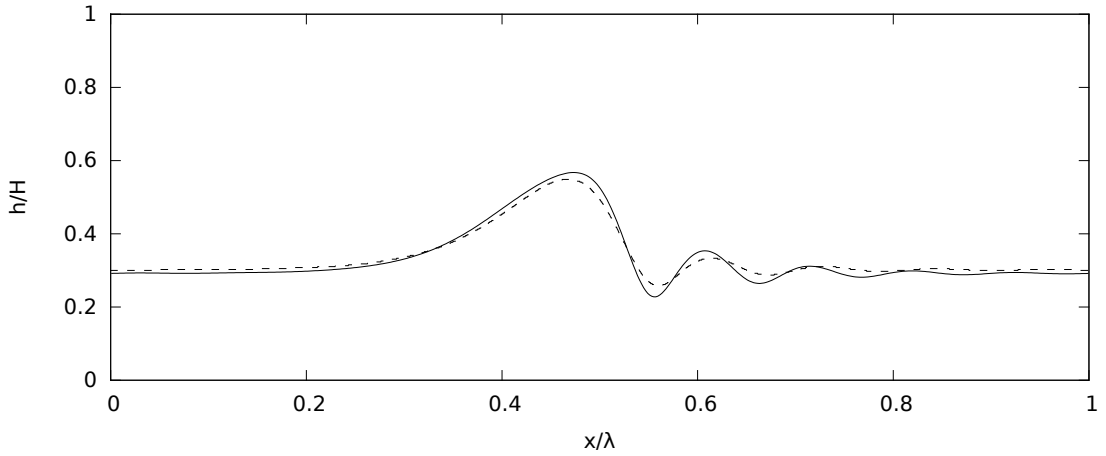

Figure FR7: Épaisseur du film dans la conduite. Comparaisons entre la DNS de Dietze & Ruyer-Quil (ligne en pointillés), Figure 7(a) de [25], et SWANS (ligne en traits pleins). La description des paramètres physiques se trouve dans la Figure FR6.

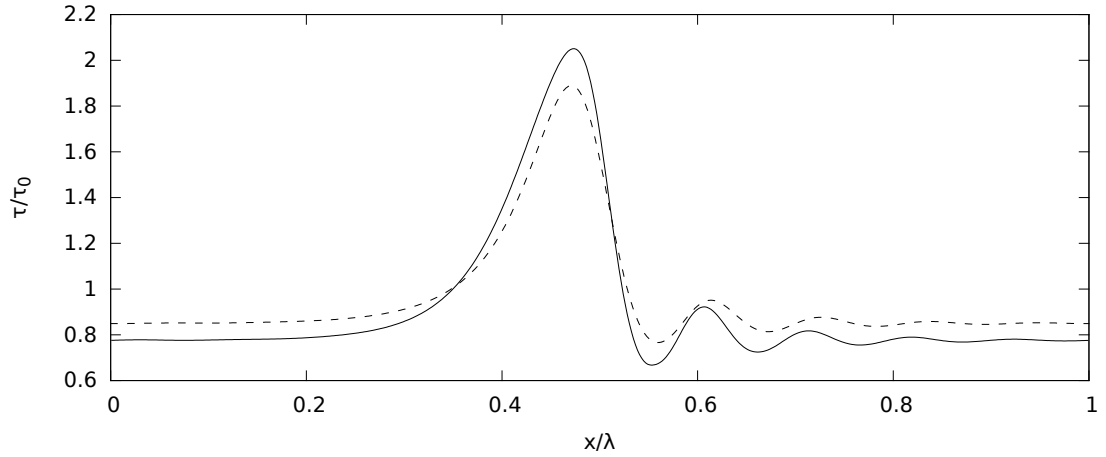

Figure FR8: Évolution spatiale du cisaillement. Comparaisons entre le modèle double St. Venant de Dietze & Ruyer-Quil (ligne en pointillés), Figure 8(c) de [25], et SWANS (ligne en traits pleins). La description des paramètres physiques se trouve dans la Figure FR6.

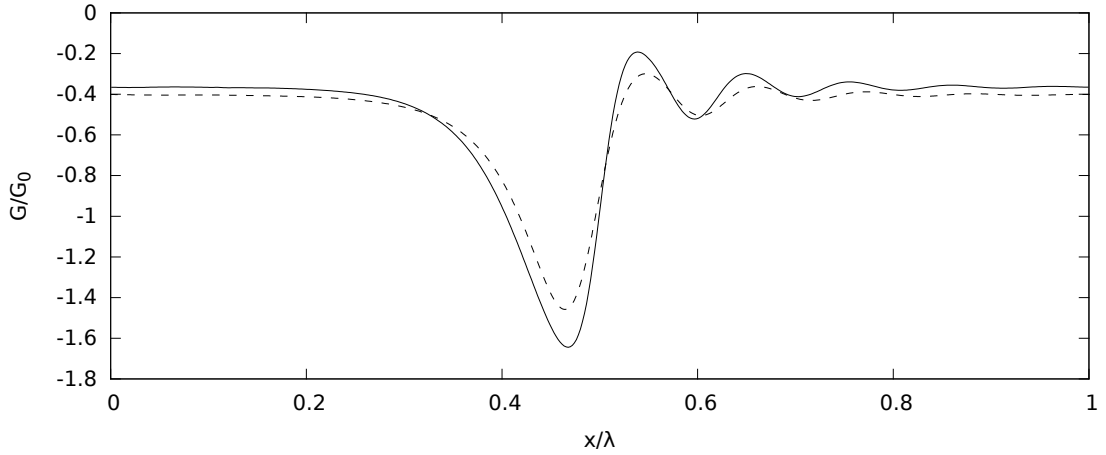

Figure FR9: Évolution spatiale du gradient de pression. Comparaisons entre le modèle double St. Venant de Dietze & Ruyer-Quil (ligne en pointillés), Figure 8(b) de [25], et SWANS (ligne en traits pleins). La description des paramètres physiques se trouve dans la Figure FR6.

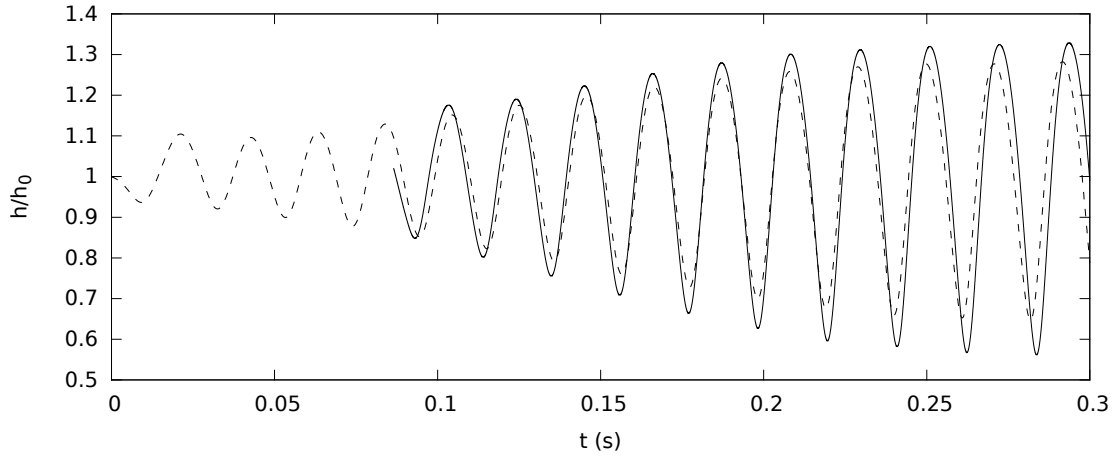

Figure FR10: Évolution temporelle de l'interface après décalage de la solution SWANS. Comparaison entre la DNS de G. Blanchard avec le code Slosh (ligne en pointillés), et SWANS (ligne en traits pleins). Nombres adimensionnés : $Re_1 = 16.5$ et $Re_2 = 1972$. État uniforme : $\tau_{i0} = 0.03\ Pa$, $u_0|_h = 0.15\ m\ s^{-1}$.

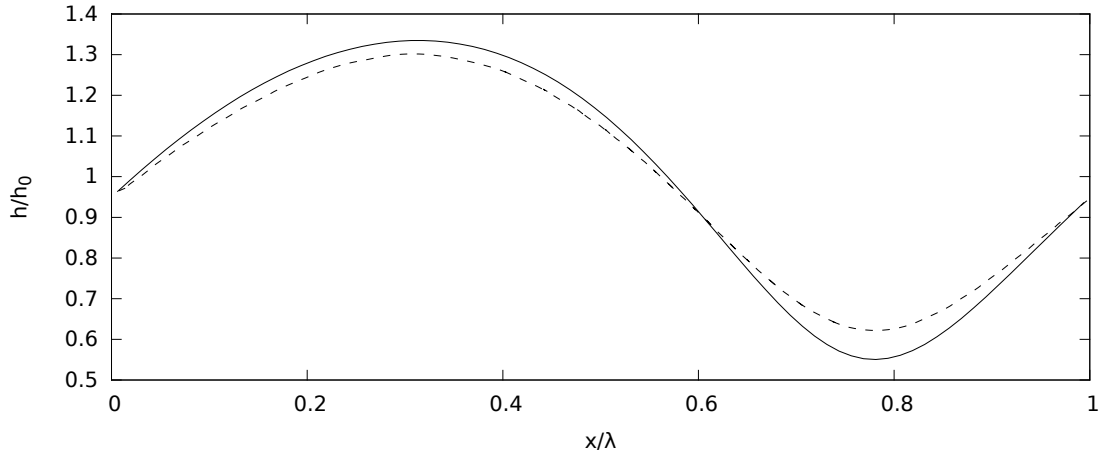

Figure FR11: Évolution spatiale de l'onde périodique. Comparaison entre la DNS de G. Blanchard avec le code Slosh (ligne en pointillés), et SWANS (ligne en traits pleins). La description des paramètres physiques se trouve dans la Figure FR10.

SWANS et la littérature, c'est la différence de pression entre l'entrée et la sortie qui est imposée.

Le deuxième test est un écoulement film-gaz vertical, donc piloté par la gravité, dans une conduite large. La Figure FR10 montre la comparaison de l'évolution temporelle pour SWANS et la DNS fournie à l'ONERA par G. Blanchard. Afin de comparer les deux courbes, la solution SWANS a du être déplacée en temps. En effet, dans la DNS, la vitesse verticale v a besoin d'un certain temps pour s'établir en accord avec la condition initiale perturbée. Cela vaut pour la DNS parce que le film est résolu avec des équations de Navier-Stokes, mais pas pour SWANS, où le modèle film satisfait par construction la relation de compatibilité sur la vitesse v. Enfin, la Figure FR11 montre un bon accord entre le code SWANS et le code DNS sur l'évolution spatiale de l'onde périodique.

9 Conclusions

L'objectif de cette thèse a été de développer une méthode de couplage entre un modèle St Venant pour le film et les équations de Navier-Stokes pour le gaz. L'intérêt de ce couplage est de pouvoir traiter des configurations industrielles avec un modèle peu coûteux pour le film et un modèle générique pour le gaz.

Pour cela, un modèle de film ondes longues a été développé pour un film liquide tombant soumis à un champs de cisaillement et de pression imposés. Ce modèle est consistant (seuil de stabilité et vitesse des ondes linéaires corrects) et permet également de décrire la dynamique non-linéaire du film. Ce modèle a ensuite été couplé numériquement avec les équations de Navier-Stokes compressible en utilisant une approche ALE. Cette méthode a été implémentée dans le code SWANS. Finalement, le code SWANS a été validé en analysant la dynamique non linéaire de deux configurations en conduite (horizontale très étroite et verticale large). Les comparaisons avec les résultats de DNS ont montré un bon accord. Cette méthode semble donc prometteuse pour la simulation de la dynamique non-linéaire des films liquides cisaillés sur des cas académiques. Dans le cas d'écoulement gazeux à grands nombres de Reynolds (écoulements turbulents), cette étude doit être poursuivie pour tester la faisabilité de la méthode. Enfin, pour évaluer la possible implémentation de cette méthode dans le code CEDRE de l'ONERA, il faudrait tester le couplage SWANS sur des configurations plus complexes, comme par exemple un profil d'aile d'avion. Il s'agirait d'évaluer la faisabilité du calcul des instabilités de film sur ce type de configuration, de vérifier que les coûts de calcul ne sont pas prohibitifs et de voir si cette méthode permet de retrouver les corrélations expérimentales couramment utilisées pour les coefficients d'échanges.